



The
University
Of
Sheffield.

Purification and characterisation of the FNR-cy***t***₆*f* supercomplex in plants

Federica Pastorelli

Faculty of Science
School of Bioscience

A thesis submitted for the degree of Doctor of Philosophy
September 2023

Abstract

In photosynthesis, light energy drives the linear electron transfer (LET) from water to NADP⁺, generating NADPH and ATP to power CO₂ fixation in the dark reactions. In addition to LET, alternative electron transport pathways and regulatory mechanisms exist in the chloroplast. In angiosperms, a key regulatory mechanism is cyclic electron transfer (CET). CET around PSI plays an important role in photosynthesis and in the development of the plant. It contributes to the photoprotection of the photosynthetic machinery, and it balances the ATP/NADPH ratio for metabolic demands. In angiosperms, CET is dominated by the PGR5-dependent antimycin A-sensitive pathway, which utilises ferredoxin to reduce plastoquinone. Despite the fact that this pathway was discovered nearly 70 years ago the identity of the ferredoxin-plastoquinone reductase (FQR) complex remains unclear. Ferredoxin-NADP⁺ reductase (FNR) was previously found to bind cytochrome *b₆f* leading to the suggestion that this interaction may facilitate FQR activity, yet the interaction is weak and unstable leading to suggestions that it represents an artefact.

In this thesis, a novel purification approach is described for the successful isolation of cytochrome *b₆f* with FNR. The purified sample includes also the CET effector proteins PGR5, PGRL1, TROL, Tic62, NdhS and TSP9. The extreme fragility of the interactions among the various proteins did not enable us to structurally characterise the FNR-cytochrome *b₆f* supercomplex by cryo-EM. However, the purified supercomplex possesses enhanced FQR activity relative to pure cytochrome *b₆f*; this provides another evidence of the interactions between the CET effector proteins to the cytochrome *b₆f* complex and their key role in promoting the enzyme activity.

Furthermore, we demonstrate that FNR binds to cytochrome *b₆f* and prevents the binding of the stromal PetP subunit of the cyanobacterial cytochrome *b₆f*. In addition, recombinant PGR5 is also able to pull down the FNR-cytochrome *b₆f* supercomplex from solubilised thylakoid membranes. Cross-linkers were used for the stabilisation of the interactions among the proteins; these were then identified and analysed by mass spectrometry. A structural model of the FNR-cytochrome *b₆f* supercomplex based on the cross-linking data is here presented and new potential mechanisms of CET are proposed. Finally, measurements of CET

using chlorophyll fluorescence and absorption spectroscopy were performed on Arabidopsis plants to understand the relevance of FNR binding to the thylakoid membrane to CET *in vivo*.

Acknowledgments

Firstly, I would like to thank my supervisor, Matt, for giving me the opportunity to undertake this PhD. Your guidance and immense support over the last four years has been invaluable to me. Thank you for your encouragement, enthusiasm and for keeping me motivated throughout the project. For your patience and for being not only an amazing supervisor but also a great life mentor, and for that, I will always be extremely grateful.

I would also like to thank all the past and present members of the Hunter/Johnson/Hitchcock lab for being a lovely bunch of people. In particular, I would like to thank Matt Proctor for your valuable advice over the years and for your help in this project, as well as to Katherine Richardson for the contribution to this work with the activity assays. I would also like to thank Phil Jackson for the immense help with mass spectrometry. I will never forget our lovely long chats about the worst crimes against Italian food. These certainly made our afternoons spent analysing data so much more enjoyable. I would also like to thank Frederick Hawkings for being a great companion in this project and for the countless cryo-EM grids made to attempt to get the structure of this fascinating supercomplex. Thank you for being just a lovely friend and the best conference bud in NZ and US. Special thanks also to Gustaf Degen, for helping me with the Walz equipment, for keeping our Arabidopsis plants alive and for being an amazing friend. A huge thanks also to Mo Brindley, for your kindness and unwavering support throughout these years.

Away from work, I would like to thank my wonderful friends. To Carolina and Riccardo from Napoli Centro, for the laughter, infinite support, and unforgettable moments we have shared in Sheffield. You guys made me feel at home when I needed it most. To Luca, Francesca, Anda, Areti, Mattia and Adam for the fantastic times we have had in Sheffield, the memorable holidays and for being such incredibly supportive friends.

Lastly, but most importantly, to my family. To my parents, Stefania and Cosimo, to my sister, Maria, and to Claudia, thank you for your unconditional love and encouragement. Words cannot describe how grateful I am to have you in my life and for your constant support. Without you, I would have never made it this far.

Contents

1. Introduction.....	1
1.1 Oxygenic photosynthesis	1
1.2 The dark reactions of photosynthesis.....	1
1.3 The light reactions of photosynthesis.....	3
1.3 Photosynthetic components of the thylakoid membrane	6
1.3.1 Pigments	6
1.3.2 Light harvesting complexes.....	6
1.3.3 Photosystem II	7
1.3.4 Plastoquinone pool	8
1.3.5 Cytochrome <i>b₆f</i>	9
1.3.6 The modified Q-cycle in <i>cytb₆f</i>	11
1.3.6 Plastocyanin	14
1.3.7 Photosystem I	14
1.3.8 Ferredoxin	16
1.3.9 Ferredoxin:NADP ⁺ oxidoreductase.....	16
1.3.10 ATP synthase.....	18
1.3.11 Heterogeneous distribution of protein complexes within the thylakoid membranes.....	20
1.4 Regulation in photosynthesis.....	21
1.4.1 Photoprotective mechanisms	21
1.4.2 Flexible regulation in photosynthetic reactions.....	22
1.4.3 Alternative electron transfer pathways	23
1.5 Cyclic Electron Transport	24
1.5.1 NDH-dependent pathway	24
1.5.2 PGRL1/PGR5-dependent pathway	28
1.5.3 The elusive CET supercomplex?	31
1.6 Outstanding questions.....	32
2. Materials and methods	33
2.1 Materials.....	33
2.2 Buffers and reagents.....	33
2.3 Preparation of thylakoid membranes	33
2.3.1 <i>Spinacia oleracea</i>	33

2.3.2	Thylakoid preparation for the purification of <i>cytb_{6f}</i> at pH 7.5	33
2.3.3	Thylakoid preparation for the purification of <i>cytb_{6f}</i> at pH 6.5	34
2.3.4	Chlorophyll concentration	34
2.4	Cytochrome <i>b_{6f}</i> purification techniques	35
2.4.1	Solubilisation	35
2.4.2	Ammonium sulfate precipitation	36
2.4.3	Protamine sulfate precipitation	37
2.4.4	DTT oxidation and reduction	37
2.4.5	Sucrose gradients	38
2.4.6	Ceramic Hydroxyapatite (CHT) Chromatography	38
2.4.7	Size Exclusion Chromatography	38
2.5	Biochemical analysis of purified proteins	38
2.5.1	Sodium Dodecyl Sulfate PAGE	38
2.5.2	Blue Native PAGE	39
2.5.3	Immunoblotting	39
2.5.4	Absorbance spectroscopy	40
2.6	Cross-linking	40
2.7	Mass spectrometry and protein identification	40
2.7.1	Thylakoid membrane protein extraction and proteolytic digestion	40
2.7.2	Analysis by mass spectrometry and protein identification	41
2.7.3	In-gel proteolytic digestion and protein identification	42
2.8	Negative stain transmission electron microscopy (TEM)	42
2.8.1	Grid preparation and negative staining	42
2.8.2	Imaging	42
2.9	Single particle Cryo-TEM	42
2.9.1	Single particle Cryo-TEM of sample purified in LMNG	42
2.9.2	Single particle Cryo-TEM of sample purified in GDN	43
2.9.3	Single particle Cryo-TEM of sample purified in A8-35	44
2.9.4	Single particle Cryo-TEM of DSS cross-linked sample in GDN	44
2.10	Purification of PetP and pull-down	45
2.10.1	Overexpression and purification of PetP	45
2.10.2	PetP pull-down	45
2.11	Purification of PGR5 and pull-down	46

2.11.1 SUMO-PGR5-ApoA1 purification.....	46
2.11.2 Purification of SUMO and 3C proteases.....	46
2.11.3 Digestion	47
2.11.4 PGR5 Pull-down	47
2.12 Activity assays.....	48
2.13 Chlorophyll fluorescence	49
2.13.1 Plant material.....	49
2.13.2 Chlorophyll fluorescence	49
2.13.3 Electrochromic shift measurements	50
3. Purification of the FNR-cyt b_6f supercomplex	51
3.1 Introduction.....	51
3.2 Initial purification of cytb $6f$ and FNR.....	53
3.3 Optimisation of ammonium sulphate concentration	55
3.4 Thylakoid membranes treated with dithiothreitol	57
3.5 Isolation of thylakoid membranes at different pH.....	59
3.6 Hydroxyapatite column	60
3.7 Protamine sulfate precipitation	60
3.8 Screening of detergents for FNR-cyt b_6f purification.....	62
3.9 Optimization of LMNG concentration	63
3.10 Biochemical characterisation of cytb $6f$ sample in LMNG.....	65
3.11 Discussion	69
4. Structural characterisation of the FNR-cyt b_6f supercomplex.....	70
4.1 Introduction.....	70
4.2 Preparation of the FNR-cyt b_6f supercomplex sample for cryo-EM.....	72
4.3 Structural determination of FNR-cyt b_6f supercomplex in LMNG	74
4.3.1 Negative Stain EM analysis.....	74
4.3.2 Cryo-EM analysis.....	74
4.4 Reconstitution of the FNR- cytb $6f$ supercomplex in amphipols	76
4.5 Stabilisation of the labile interactions using cross-linkers	81
4.5.1 Detergent exchange of the cross-linked sample from LMNG to GDN	84
4.5.2 Cryo-EM analysis of cross-linked sample in GDN	84
4.7 Structural model of the cross-linked FNR-cyt b_6f supercomplex.....	85
4.8 PetP pulldown.....	97

4.9 PGR5 pulldown	98
4.10 FQR activity of the FNR- <i>cytb₆f</i> supercomplex	99
4.11 Discussion	101
5. Relevance of FNR binding to the thylakoid membrane for photosynthesis and CET <i>in vivo</i>	106
5.1 Introduction	106
5.1.1 Chlorophyll fluorescence	108
5.1.2 Electrochromic shift.....	112
5.2 A new <i>Arabidopsis thaliana</i> phenotype lacking CET	113
5.3 Analysis of the growth phenotype of CET mutants	114
5.4 Effects of light fluctuations in CET	117
5.4.1 Fluctuating light effects on PSII photochemistry	119
5.4.2 Effects of fluctuating light on PSI photochemistry	121
5.4.3 Effects of fluctuating light on Fd and PC absorption changes.....	124
5.5 Effects of light fluctuations on <i>ECS</i> signal	126
5.6 <i>In vivo</i> analysis of P700 oxidation activity	128
5.7 Discussion	130
6. Concluding remarks.....	133
7. Bibliography.....	138
Appendix	151

Figures

Figure 1.1 Overview of the main interactions between the photosynthetic electron transfer chain (PETC) (light reactions) and Calvin-Benson-Bassham cycle (dark reactions) in the chloroplast.	3
Figure 1.2 Light dependent reaction of photosynthesis.....	4
Figure 1.3 Z-scheme of Linear Electron Transport.....	5
Figure 1.4 LHCII- PSII supercomplex.	8
Figure 1.5 Plastoquinone-9 structure.....	9
Figure 1.6 Cytochrome <i>b₆f</i> complex.....	10
Figure 1.7 The modified Q-cycle of <i>cyt_{b₆f}</i>	13
Figure 1.8 PSI-LHCI-LHCII supercomplex.....	15
Figure 1.9 Structure of FNR and Fd.....	17
Figure 1.10 Schematic illustration of the catalytic pathway.....	17
Figure 1.11 Structure of ATP synthase.....	19
Figure 1.12 Organisation of the thylakoid membrane system.....	20
Figure 1.13 Alternative electron pathways in angiosperms.....	24
Figure 1.14 Structure of the NDH-complex.....	27
Figure 1.15 Schematic model of CET involving NDH-PSI and <i>cyt_{b₆f}</i>	28
Figure 1.16 Model of PSI oxidation and <i>cyt_{b₆f}</i> reduction by PGRL1.....	30
Figure 3.1 Initial purification of <i>cyt_{b₆f}</i>	54
Figure 3.2 Effect of different ammonium sulphate concentrations on the purity of <i>cyt_{b₆f}</i> ...56	
Figure 3.3 Purification of <i>cyt_{b₆f}</i> using 40% ammonium sulphate saturation.	57
Figure 3.4 Purification of <i>cyt_{b₆f}</i> from thylakoid isolated with 2mM oxidised and reduced DTT.	58
Figure 3.5 Purification of <i>cyt_{b₆f}</i> from thylakoid isolated at pH 6.5 with 2mM oxidised and reduced DTT.....	59
Figure 3.6 Ceramic Hydroxyapatite column chromatography of samples collected from sucrose gradients at pH 6.5.	60
Figure 3.7 Protamine sulfate precipitation.....	61
Figure 3.8 Detergents screening.....	63
Figure 3.9 Optimisation of LMNG concentration.	64
Figure 3.10 Purity of <i>cyt_{b₆f}</i> in the samples harvested from the sucrose gradients.....	64
Figure 3.11 Characterisation of <i>cyt_{b₆f}</i> sample in LMNG.....	66
Figure 3.12 Identification of copurified proteins by western blots.	68
Figure 3.13 Comparison of FNR- <i>cyt_{b₆f}</i> supercomplex purified from thylakoid membranes isolated with and without NaBr.	69
Figure 4.1 Chemical structures of commonly used detergents for protein purification and stabilisation.	71
Figure 4.2 Size exclusion chromatography of the sample purified in LMNG.....	73
Figure 4.3 Negative stain analysis of the FNR- <i>cyt_{b₆f}</i> supercomplex in LMNG.....	74
Figure 4.4 Cryo-EM micrographs of the FNR- <i>cyt_{b₆f}</i> supercomplex.....	76
Figure 4.5 Workflow of the reconstitution in amphipols A8-35.	77

Figure 4.6 Size exclusion chromatography of the sample reconstituted in amphipols A8-35.	77
Figure 4.7 Negative stain analysis of the FNR-cytb _{6f} supercomplex in A8-35.	78
Figure 4.8 Cryo-EM micrographs of the FNR-cytb _{6f} supercomplex in A8-35.....	79
Figure 4.9 3D structural model generated from particles extracted from the FNR-cytb _{6f} supercomplex cryo grids overlaid to cryo-EM cytb _{6f} published structure.	80
Figure 4.10 Chemical cross-linking with the reagent DSS.....	82
Figure 4.11 Optimisation of the concentration of DSS.....	83
Figure 4.12 Size exclusion chromatography of the cross-linked sample reconstituted in GDN	84
Figure 4.13 Cryo-EM micrographs of the cross-linked FNR-cytb _{6f} supercomplex in GDN.....	85
Figure 4.14 Total proteins analysis of the sample purified in LMNG by MS.	86
Figure 4.15 Cross-linking between FNR and subIV.	88
Figure 4.16 Cross-linking between PGR5 and subIV.	89
Figure 4.17 Cross-linking between PGR5 and FNR.	90
Figure 4.18 Cross-linking between subIV and PGRL1a.	91
Figure 4.19 Cross-linking between PGRL1a and FNR.....	92
Figure 4.20 Cross-linking between TROL and FNR.....	94
Figure 4.21 Cross-linking between FNR and Tic62	96
Figure 4.22 PetP pulldown of cytb _{6f} complex from different photosynthetic organisms.	97
Figure 4.23 Testing the interaction of the cytb _{6f} -FNR supercomplex with PetP.	98
Figure 4.24 PGR5 pulldown.	99
Figure 4.25 FQR activity of the FNR- cytb _{6f} supercomplex.....	101
Figure 5.1 Chlorophyll fluorescence.	109
Figure 5.2 Differential model plot (DMP) of P700, PC and Fd.	110
Figure 5.3 Overview of the photosynthetic electron transport chain and the quantum yields of PSI.	111
Figure 5.4 Schematic illustration of the ECS decay.....	113
Figure 5.6 Growth analysis of the genotypes under control and high light conditions.....	116
Figure 5.7 Chlorophyll <i>a</i> fluorescence measurement.....	118
Figure 5.8 PSII photochemistry.....	120
Figure 5.9 PSI photochemistry.	123
Figure 5.10 Redox state of Pc and Fd.	125
Figure 5.11 Proton motive force (<i>pmf</i>), proton conductivity (gH ⁺) and proton flux (vH ⁺).....	127
Figure 5.12 P700 oxidation for CET determination.	129
Figure 5.13 vH ⁺ versus LET.....	130
Figure 6.1 Cryo-EM structure of the PetP-cytb _{6f} and structural model of the FNR-cytb _{6f} complex.....	135
Figure 6.2 Possible model of the regulation of the FNR-cytb _{6f} supercomplex formation.....	137

Tables

Table 2.1 List of buffers used for the thylakoid preparation.	34
Table 2.2 Outline of the detergents used in this study.....	35
Table 2.3 Plant material.....	49

1. Introduction

1.1 Oxygenic photosynthesis

Photosynthesis is the biological process that sustains life on Earth, providing oxygen and biomass by converting light energy (photons) from the Sun into chemical energy. Oxygenic photosynthesis is carried out by plants, algae and cyanobacteria and is characterised by light-dependent (“light”) reactions and light-independent (“dark”) reactions. In the light reactions, water is broken down into protons, electrons and oxygen, while in the dark reactions CO₂ is converted into carbohydrates (Figure 1.1). In eukaryotic oxygenic phototrophs, including land plants, the light and dark reactions occur in a small organelle known as the chloroplast. The chloroplast is composed of a double membrane (envelope), enclosing an aqueous medium (stroma) in which resides an extensive internal membrane structure (thylakoid) in turn enclosing another aqueous space (lumen). The light reactions take place within the thylakoid, where chlorophylls and carotenoids absorb light energy and through coupled proton and electron transfers ultimately generate chemical energy in the form of adenosine triphosphate (ATP) and nicotinamide adenine dinucleotide phosphate (NADPH). The dark reactions take place in the stroma, which contain the enzymes involved in carbon fixation via the Calvin-Benson-Bassham (CBB) cycle. In 1937 Robert Hill first discovered that the “light” reaction operates independently from the “dark” reaction, since broken chloroplasts (lacking the envelope) were able to evolve O₂ in absence of CO₂. The overall reaction of photosynthesis can be summarised with the equation:



1.2 The dark reactions of photosynthesis

In plants, the Calvin-Benson-Bassham (CBB) cycle consumes ATP and NADPH molecules generated during the light reaction to fix CO₂ into carbohydrate. In the first step of the reactions of the cycle, CO₂ is combined with ribulose-1,5- biphosphate (RuBP) by ribulose biphosphate carboxylase (Rubisco). The reaction generates an unstable 6-carbon intermediate which is split into two 3-carbon molecules of 3-phosphoglycerate (3-PGA). 3-PGA is then phosphorylated by 3-phosphoglycerate kinase, using ATP, into 1,3-bisphosphoglycerate (BPGA). BPGA is then converted into glyceraldehyde 2-phosphate (GAP)

by the enzyme glyceraldehyde 3-phosphate dehydrogenase (GAPDH) using NADPH. In each CBB cycle, for every 3 molecules of CO₂, 6 molecules of GAP (3C sugar) are generated. Only one molecule of GAP is used in several biosynthetic pathways, while the other 5 are required for the regeneration of RuBP, with further ATP consumption (Figure 1.1).

It is also well known that the activity of the enzymes involved in the CBB cycle is regulated by light through a ferredoxin/thioredoxin (Fd/TRX)-dependent reduction of disulfide bonds. The Fd/TRX system is indeed involved in also numerous reactions occurring in the chloroplast regulating photosynthesis for the avoidance of over reducing conditions. In the dark where oxidising conditions prevail, most of the enzymes are inactive. Upon light illumination, the Fd pool becomes more reduced and CBB enzymes are activated by the TRX system (Michelet et al., 2013). Another TRX system, known as NADPH-dependent thioredoxin reductase C (NTRC), exists and utilises NADPH as reductant for redox regulation. NTRC also plays a role in regulating ATP synthesis by reducing the γ subunit of the chloroplast ATP synthase (CF₁ γ). Previous studies have shown that overexpression of NTRC enhances photosynthetic yield at low light intensity and it is involved in the regulation of redox poise also during changes in light conditions (Nikkanen et al., 2016., 2018).

Thus, there is indeed a tight correlation between the intracellular redox state and CBB enzymes; this redox control allows a fine regulation between CBB cycle and the light-driven photosynthetic electron transport.

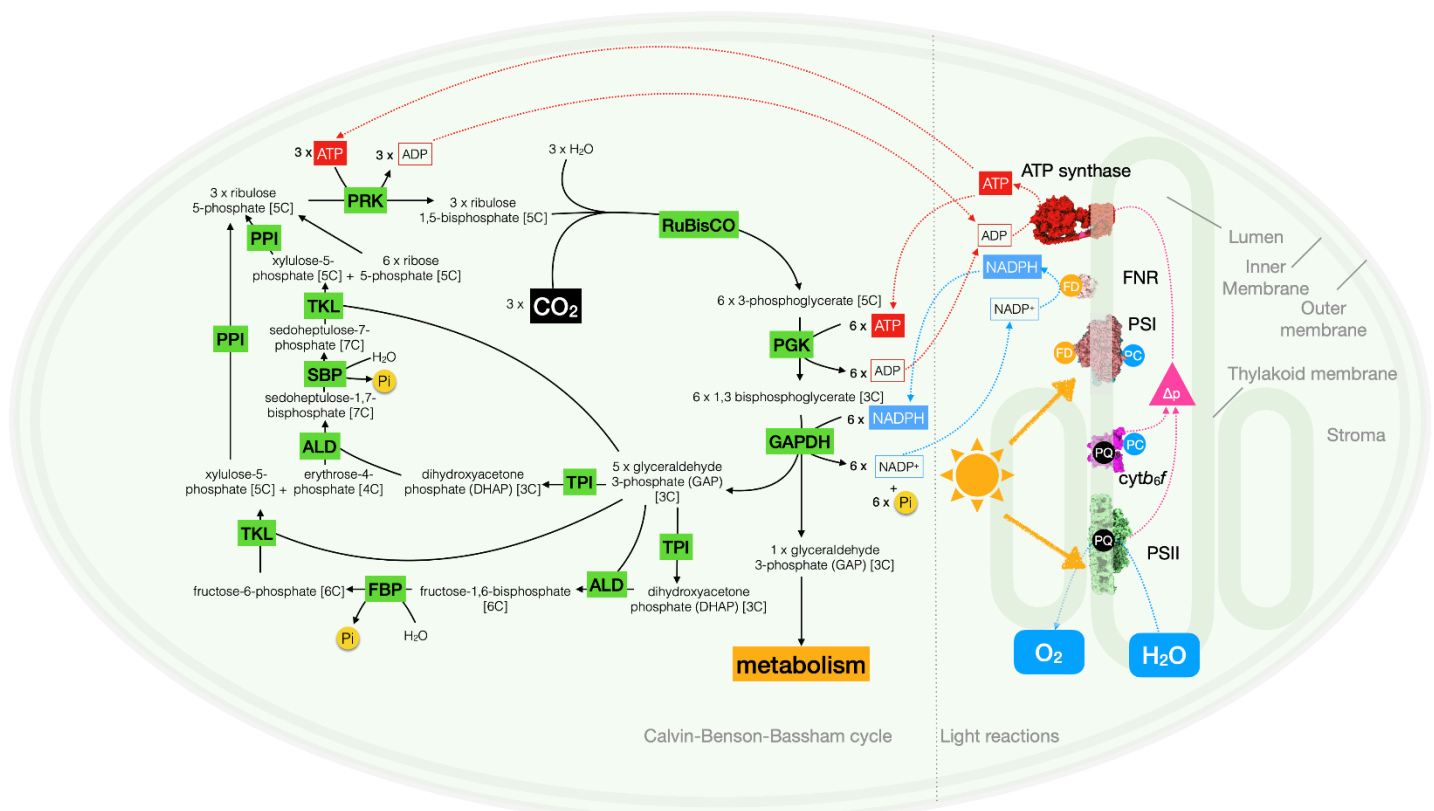


Figure 1.1 | Overview of the main interactions between the photosynthetic electron transfer chain (PETC) (light reactions) and Calvin-Benson-Bassham cycle (dark reactions) in the chloroplast.

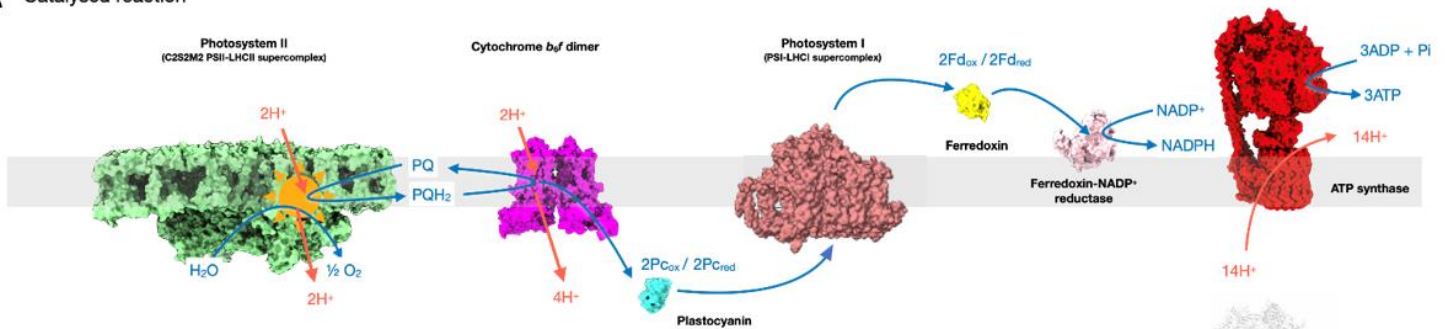
In the light reaction, light-powered PSII oxidises water to oxygen, releasing H^+ into the lumen and passing e^- to PQ, *cytb₆f* oxidises PQH₂ and reduces Pc releasing H^+ into the lumen, light powered PSI oxidises PC and reduces FD, FD reduces NADP⁺ to NADPH via FNR. The transmembrane proton motive force (Δp) is utilised by ATP synthase to synthesise ATP from ADP and Pi. The CBB cycle consumes ATP and NADPH regenerating NADP⁺ and ADP and Pi for the PETC, fixing CO₂ into GAP in the process. PETC complexes are shown as their dominant supercomplexes; PSII (Protein Data Bank (PDB): 5XNM), *cytb₆f* (PDB: 6RQF), PSI (PDB: 5L8R), FNR (PDB: 1GAQ) and ATP synthase (PDB: 6FKF), the electron carriers PC, FD and PQ are shown as coloured circles. Abbreviations for the CBB cycle enzymes are: RuBisCO (rubulose 1,5-bisphosphate carboxylase/ oxygenase), PGK (phosphoglycerate kinase), GAPDH (glyceraldehyde 3-phosphate dehydrogenase), TPI (triose phosphate isomerase), ALD (aldolase), FBP (fructose 1,6 bisphosphatase), TKL (transketolase), SBP (sedoheptulose 1,6- bisphosphatase), PPI (phosphopentose epimerase), PRK (phosphoribulose kinase).

1.3 The light reactions of photosynthesis

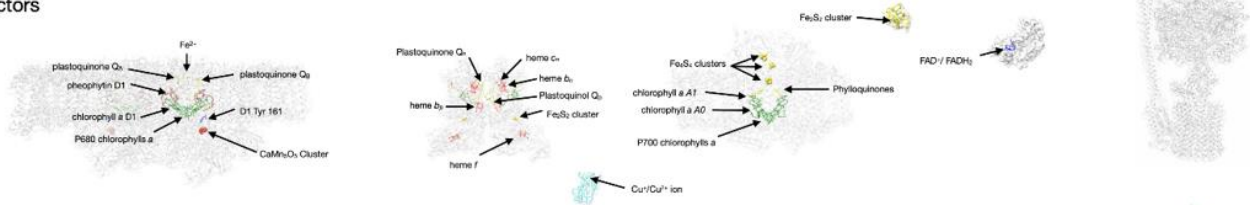
Light energy conversion is driven by two separate multi-protein complexes, photosystem II (PSII) and photosystem I (PSI) composed of a peripheral antenna system, known as light harvesting antenna complexes (LHCs) and a core complex containing the reaction centre (RC). Light energy is captured in the antenna system mainly by chlorophylls and carotenoids. The excitation energy is transferred towards a “special pair” of chlorophylls molecules residing in PSII RC and PSI RC, known as P680 and P700 respectively. Here, an electron will be transferred to another species, resulting in the formation of an oxidised special pair and a reduced acceptor; this process is known as charge separation.

PSII catalyses the initial water oxidation into oxygen, protons and electrons. The electrons are then transferred from the RC to the lipid carrier molecule plastoquinone (PQ), forming plastoquinol (PQH₂) (Nelson and Ben-Shem, 2004). Here, via the quinol (Q) cycle cytochrome *b₆f* (cyt *b₆f*) oxidises PQH₂ and, via electron bifurcation, the Cu²⁺ centre of plastocyanin (Pc), and plastoquinone (PQ) are reduced at two separate sites; this is coupled to a proton translocation across the thylakoid membrane into the lumen (Mitchell, 1975). This leads to the formation of an electric potential difference across the thylakoid membrane ($\Delta\Psi$), and proton concentration gradient (ΔpH), which together constitute the proton motive force (*pmf*) that allows ATP synthase to make ATP. Light absorption in PSI drives the oxidation of P₆₈₀ and the reduction of ferredoxin (Fd), a water- soluble iron-containing protein in the stroma. Then, Fd is used by the enzyme Ferredoxin NADP(H) oxidoreductase (FNR) for the reduction of NADP⁺ to NADPH. This electron transfer pathway is known as linear electron transfer (LET) (Figure 1.2) or Z-scheme (Figure 1.3).

A Catalysed reaction



B Co-factors



C Subunit composition

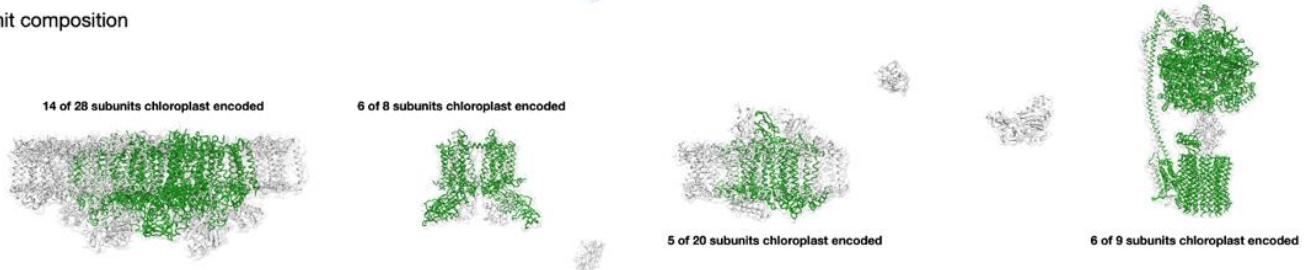


Figure 1.2 | Light dependent reaction of photosynthesis.

(A) The key components of the linear electron transport chain are illustrated. In LET, Fd transfers electrons to FNR, which reduces NADP⁺ to NADPH. Protons translocation into the lumen lead to the formation of *pmf* driving ATP synthesis. Blue arrows represent the electron transfer in LET, while proton transfer is shown in red. Catalysed reactions are shown as well. PQ, plastoquinone; PQH₂,

plastoquinol; $P_{C_{ox}}/P_{C_{red}}$, plastocyanin oxidised/ reduced; Fd_{ox}/Fd_{red} , ferredoxin oxidised/reduced; $NADP^+/NADPH$ nicotinamide adenine dinucleotide phosphate oxidised/ reduced forms; H^+ , proton; ADP, adenosine diphosphate; ATP, Adenosine triphosphate. (B) Cofactors involved in the electron transfer chain are highlighted in each complex. $CaMn_4O_5$, calcium-manganese-oxygen cluster; Tyr_{161} , redox active tyrosine in PSII; Fe^{2+} , iron ion in PSII; Cu^{2+}/Cu^+ , oxidised/ reduced forms of copper cofactor in plastocyanin; Fe_2S_2 , two iron two sulfur cluster; Fe_4S_4 , four iron four sulfur cluster; $FAD^+/FADH_2$, oxidised/ reduced forms flavin adenine dinucleotide. (C) Structural properties of the photosynthetic complexes. Plastid encoded subunits shown in green and nuclear encoded subunits in grey.

The Z-scheme illustrates the electron transfer from the water-oxygen couple (+820mV) through a series of redox carriers to $NADP^+/NADPH$ (-320mV). Since electrons are typically transferred from redox couples with lower potentials, which are good reductants, to those with higher potentials, which are good oxidants, this process is considered exergonic. However, also two endergonic steps occur at PSII and PSI, when light energy excites electrons within the chlorophyll molecules to a higher energy level for the reduction of acceptors in the electron transport chain.

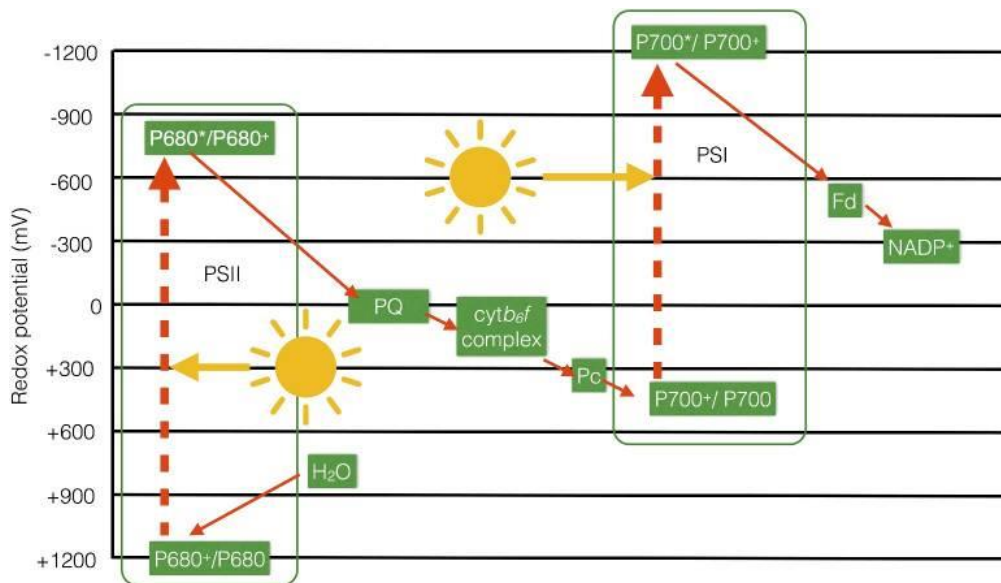


Figure 1.3 | Z-scheme of Linear Electron Transport.

The key components of LET are illustrated according to redox potential. Electron transfer occurs from the water-oxygen couple (+820mV) through a series of redox carriers to $NADP^+/NADPH$ (-320mV). Light energy reaches the reaction centres of PSII (P680) and is used to power the endergonic oxidation of water, generating oxygen, protons and electrons. Oxygen is released and into the atmosphere and protons are translocated into the lumen. Electrons are transferred to the PQ pool and subsequently to $cytb_6/f$, which catalyses the oxidation of QH_2 and reduces PC. Light energy promotes the oxidation of PC and reduction of Fd. Fd is then oxidised by FNR, for the generation of NADPH.

1.3 Photosynthetic components of the thylakoid membrane

1.3.1 Pigments

In plants, the initial absorption of light is performed primarily by chlorophylls in the antenna system. Chlorophyll consists of a chlorin ring with a central magnesium ion and a long hydrophobic phytol tail allowing stable protein binding; the series of single and double carbon bonds creates a conjugated π - system with 24 delocalised electrons enabling light absorption.

All electrons can be excited upon absorption of photons from a ground state (S_0) to an excited state (S_1 or S_2). Upon absorption of a red photon (~600-700 nm), electrons will be promoted to S_1 state, showing an absorption peak in the Qy peak in the spectrum. Upon absorption of a blue photon (~400-500nm), electrons will jump to the S_2 state and resulting in an absorption peak in the blue region of the electromagnetic spectrum called Soret peak. (Reviewed in Johnson, 2016). Electrons excited in the S_2 state lose their energy very quickly (picoseconds) by internal conversion reaching S_1 state. This excitation energy then, can either be transferred directly to another pigment if within ~1 nm distance through exciton coupling or via Förster-type excitation transfer (FRET) if distance is greater (1-7 nm) or lost as heat by internal conversion, or emitted as fluorescence (Reviewed in Lamb et al., 2018).

Two types of chlorophyll exist in plants, *a* and *b*, that have slightly different structures; C7 of chlorophyll *a* (Chl *a*) has a methyl group (-CH₃), whereas chlorophyll *b* (Chl *b*) a formyl group (-CHO). Consequently, their absorption spectra show some differences: Chl *b* is red-shifted in the Soret band compared to Chl *a*, and blue-shifted in the Qy peak compared to Chl *a*.

1.3.2 Light harvesting complexes

Chlorophylls and carotenoids are embedded in LHCs, where light is absorbed, and excitation energy is transferred to the reaction centres of either PSI or PSII where charge separation occurs.

PSII receives excitation energy by LHCII, a heterotrimeric complex and the most dominant antenna protein in plants. Each LHCII monomer binds to a total of 14 chlorophyll molecules, 8 Chl *a* and 6 Chl *b* and they are coordinated by three transmembrane helices. LHCII monomers are always bound to PSII, while LHCII trimers bind to PSII and to PSI to modulate

the energy flux between the two photosystems when PSII is disproportionately excited. LHCI is the antenna system associated to PSI and presents similar features to LHCII monomers (Liu et al., 2004).

1.3.3 Photosystem II

PSII is a supramolecular complex that oxidises water and reduces the bound PQ. The core complex of PSII is composed of more than 20 subunits, of which 14 are encoded within the chloroplast genome. The RC is composed of heterodimeric D1 and D2 proteins tightly bound to the antenna proteins CP47 and CP43 and α and β subunit of cytb_{559} . Each monomer is flanked by one LHCII trimer and the monomeric minor LHC proteins CP24, CP26 and CP29 (Figure 1.4B) (Su et al., 2017; Van Bezouwen et al., 2017; Wei et al., 2016). In PSII resides a special pair of Chl *a* known as P680, due to their 680 nm absorption peak. Upon absorption of light, this excitation energy is transferred from the antenna proteins to P680, which is excited and results in a transient intermediate P680* that undergoes charge separation. An electron is transferred to a pheophytin molecule and then to acceptor quinones (Q_A and Q_B). Two photochemical cycles are required for the full reduction of the plastoquinone at the Q_B binding site, which takes two protons from the stroma resulting in formation of PQH_2 ; the PQH_2 molecule dissociates from PSII and diffuses into the lipid bilayer. P680⁺ is reduced by a tyrosine residue, Tyr 161, which acts as wire for electrons from the catalytic water splitting Mn_4CaO_5 cluster, known as the oxygen evolving complex (OEC), formed by the c-termini of CP43 and D1 and the membrane extrinsic subunit PsbO, PsbP and PsbQ in plants. Through a four-step reaction, two water molecules are oxidised, releasing 4 protons and one molecule of oxygen into the lumen (Joliot et al., 1969).

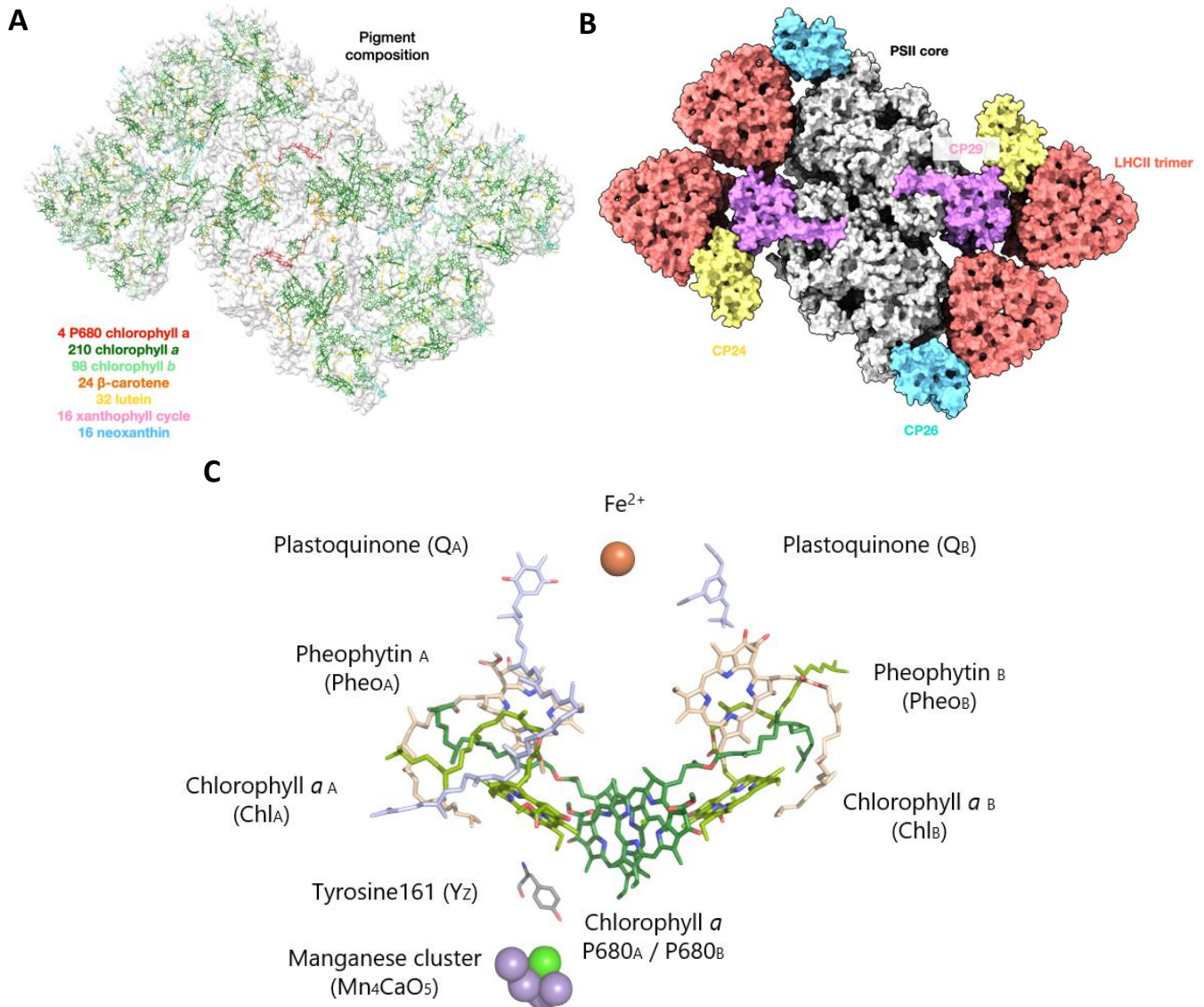


Figure 1.4 | LHCII- PSII supercomplex.

LHCII-PSII supercomplex viewed perpendicular to the membrane plane from the stroma. (A) Arrangement of the pigments in the LHCII- PSII supercomplex. (B) PSII core, with the monomeric LHCII subunits CP24, CP26 and CP29 and LHCII trimers (PDB ID: 5XNM). PSII and the antenna form a homodimeric supercomplex (C) PSII RC chromophores and additional components within the D1 and D2 proteins. The RC comprises the central P680_A/P680_B “special pair”, flanked by two Chl *a* molecules, Chl_A and Chl_B, and two pheophytin molecules, Pheo_A and Pheo_B. The RC receives the excitation energy from the LHCII systems and CP43 and CP47. Following excitation and charge separation, P680* is generated and water is oxidised at the OEC. P680* is reduced by Tyr 161 (Y_Z), which in turn is reduced by the catalytic water splitting Mn₄CaO₅ cluster. One electron is transferred to Pheo_A molecule and then sequentially to acceptor plastoquinones (Q_A and then Q_B).

1.3.4 Plastoquinone pool

PQ is a lipid-soluble charge carrier and an essential component in photosynthesis. The general structure of a PQ is a benzoquinone ring attached to a polyisoprenoid side chain. In nature

several forms of PQ molecules exist; the main form of PQ in plants is the PQ-9 which is characterised by a nonaprenyl side chain (Havaux, 2020). Reduction of PQ occurs by the uptake of 2 electrons and 2 protons for the generation of two hydroxyl groups (Figure 1.5).

The PQ-9 content in plants is responsive to changes in the environmental conditions. Previous studies have documented an augmentation of PQ-9 production in plants grown under high light conditions compared to low light conditions (Szymańska & Kruk, 2010; Zbierzak et al., 2010).

Around 50% of the PQ-9 pool in plants is located in the thylakoid membranes where it carries electrons in LET, from PSII to *cytb₆f*, and involved also in alternative electron transport pathways. In addition, PQs may not diffuse homogenously in the photosynthetic membranes and there is evidence that they are compartmentalised in distinct regions providing “local” PQs pools, in the appressed and non-appressed regions of the thylakoid (reviewed in Alric, 2015).

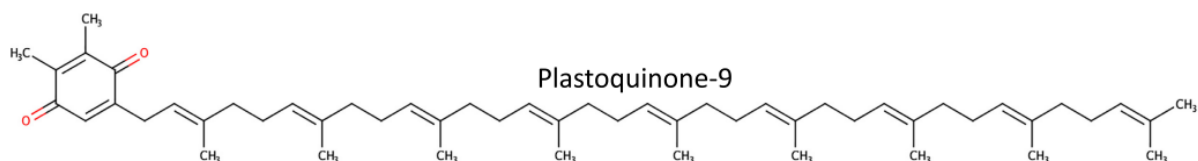


Figure 1.5 | Plastoquinone-9 structure.

Chemical structure of PQ-9 molecule characterised by a benzoquinone ring attached to a nonaprenyl side chain. Upon reduction of the molecule, two hydroxyl groups are generated from ketone groups (highlighted in red).

1.3.5 Cytochrome *b₆f*

The *cytb₆f* complex is a homodimeric complex of ~220kDa that links the electron transfer between PSII and PSI by oxidising PQH₂ and reducing the luminal electron carrier PC (Kurusu et al., 2003; Stroebel *et al.*, 2003). In vascular plants *cytb₆f* is composed of 8 subunits of which 6 are encoded within the chloroplast genome. Each *cytb₆f* monomer consists of four main subunits: cytochrome *f* (PetA), cytochrome *b₆* (PetB), Rieske iron-sulphur protein (PetC) and subunit IV (PetD). These subunits are stabilised by four minor subunits PetG, PetL, PetM, PetN (Figure 1.6A-B). In the green alga *Chlamydomonas reinhardtii* (Chlamydomonas), *cytb₆f* has an additional transmembrane subunit known as PetO (Buchert et al., 2018; Lemaire et al., 1986), while in *Synechocystis* sp. PCC6803 (*Synechocystis*), a small protein known as PetP interacts to the stromal side of *cytb₆f* (Proctor et al., 2022).

The *cytb₆f* complex shows high similarity with the bacterial and mitochondrial *cytbc₁* complex (respiratory complex III), with conserved redox components bound to the core four-helix bundle of the *cytb₆* subunit (Cramer et al., 2011). In *cytb₆f*, this subunit binds to two highly conserved *b*-type haems (haems *b_n* and *b_p*) and *c*-type haem (haem *c_n*). The ISP and *cyt_f* subunits consist of two transmembrane single helices which tether the two soluble domains protruding into the thylakoid lumen. Here, an iron sulphur cluster (2Fe-2S) and the *c*-type haem *f* are coordinated by the ISP and *cyt_f* subunit respectively. In addition, *cytb₆f* also contains one chlorophyll *a* and one β -carotene pigment per monomer; their function is still unknown (Figure 1.6C).

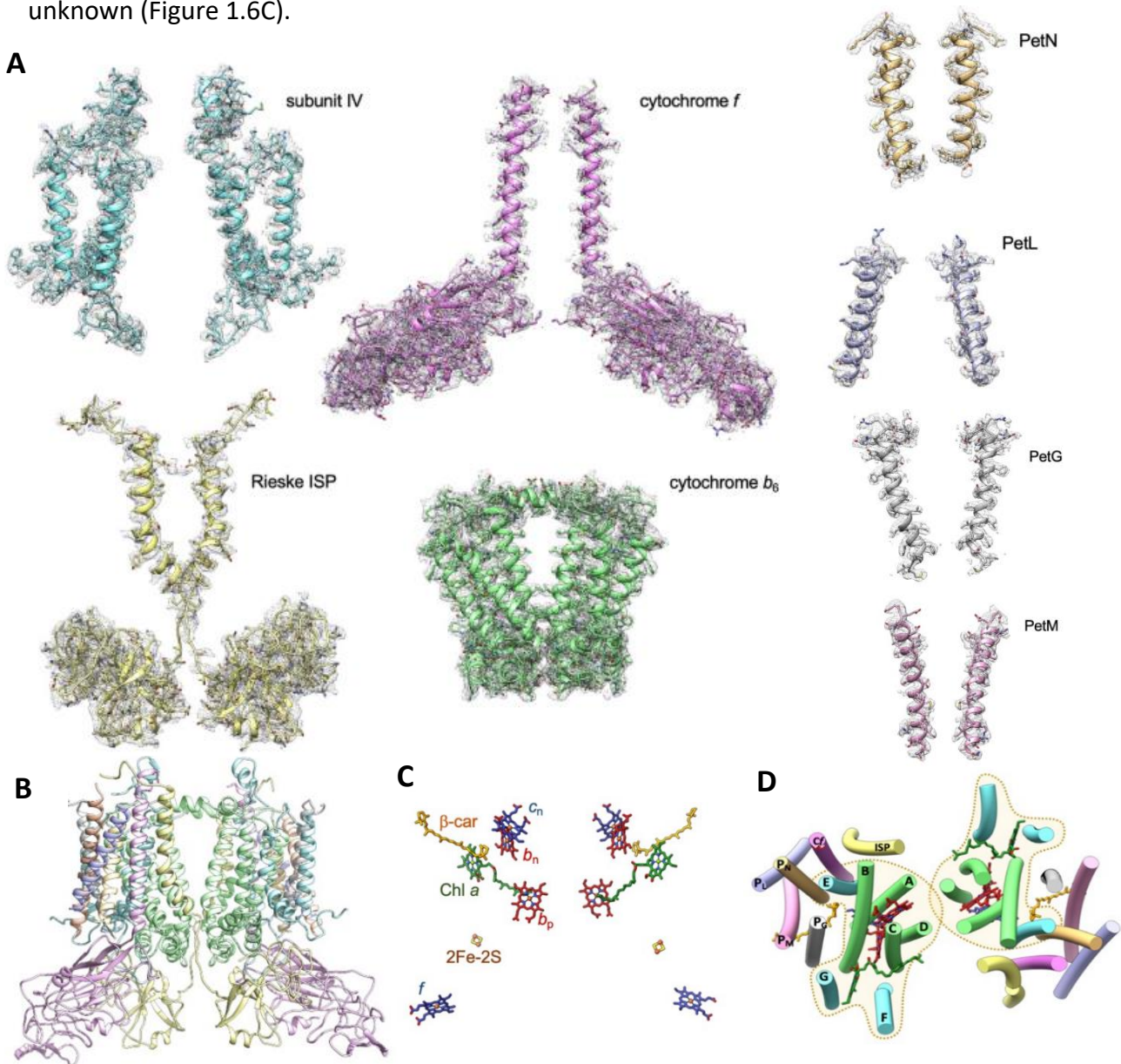


Figure 1.6 | Cytochrome *b₆f* complex.

(A) Cryo-EM density and structural models of the *cytb₆f* subunits (PDB: 6RQF). (B) View of the structure of *cytb₆f* in the plane of the membrane (PDB: 6RQF). (C) Arrangement of prosthetic groups within the

complex; c-type haems (f and c_n in dark blue), b-type haems (b_p and b_n in red), Chl a (in dark green), β -carotene (in orange) and the 2Fe-2S cluster (S in yellow and Fe in dark orange). (D) Arrangement of transmembrane helices of the subunits within $cytb_6f$ viewed perpendicular to the membrane plane from the lumenal side.

1.3.6 The modified Q-cycle in $cytb_6f$

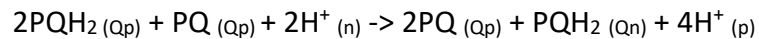
$Cytb_6f$ complex is the major site of proton translocation (4 of the $6H^+$ transferred per NADPH formed) in the electron transport chain and therefore it greatly contributes to the generation of pmf . In both $cytb_6f$ and $cytbc_1$ complexes, a large protein-free cavity is found between the monomeric units, and both perform quinol oxidation following a mechanism of electron bifurcation according to the modified Q-cycle (Mitchell, 1975b, 1975a; Crofts *et al.*, 1983). In $cytb_6f$, this internal cavity provides the space for the sequestration of a pool of PQ/PQH₂; oxidation of quinols and reduction of quinones are coordinated at two catalytic sites, one near the p-side of the complex (Q_p) and one near the n-side of the complex (Q_n) respectively (Malone *et al.*, 2019). The overall process of the modified Q-cycle occurs in two half cycles; each half cycle results in the translocation of two protons into the lumen and the transfer of two electrons from a two-electron carrier plastoquinol molecule to a soluble single electron carrier (Figure 1.7).

1st half cycle

In the first half-cycle, one PQH₂ molecule diffuses into the complex at the Q_p site, where it is oxidised and electron bifurcation occurs; here, one electron is transferred into the high potential chain (2Fe-2S and haem f , and while the other is transferred to the low-potential chain (haems b_p , b_n and c_n). In the high potential chain, 2Fe-2S cluster (+310 mV) receives an electron from the PQ/PQH₂ couple, which is then transferred to the haem f (+355 mV) and in turn to a Pc molecule (+370 mV). In the low potential chain, one electron from the semiquinone (PQ/PQ⁻ couple, -280 mV) is transferred to the haem b_p (-150 mV), to the haem b_n (-85 mV) and then to the haem c_n (+100 mV). However, according to the recent work carried by Szwalec *et al.*, the redox potentials of the haem b_p and b_n are -85mV and -150mV respectively, implicating a uphill step between the two haems (Szwalec *et al.*, 2022). Two protons are released into the thylakoid lumen which contribute to the pmf .

2nd half cycle

In the second half reaction, at the Q_p site another PQH₂ molecule is oxidised leading to the reduction of a second Pc molecule at the high potential chain; the second electron is transferred to the low potential chain, leading to the reduction of both haems *b_n* and *c_n*. Two electrons and two protons are then transferred to ultimately reduce the PQ molecule at the Q_n site. The overall reaction can be summarised as follows:



According to this mechanism described above, upon oxidation of a PQH₂ molecule at the Q_p site, one electron is transferred to the high potential chain to the 2Fe-2S cluster and finally to the haem *f*. However, according to the last high-resolution structures of the *cytb₆f* complex the distance between the two cofactors is of ~26 Å, representing a large distance for a transfer estimated to occur in 2-5 ms; this implies that a conformational change in the extrinsic domain of the ISP is induced to facilitate the rapid transfer of electrons (Darrouzet et al., 2000; Sarewicz et al., 2023; Yan & Cramer, 2003). In the high potential chain, electrons are transferred to Pc and subsequently to PSI (Figure 1.7C)

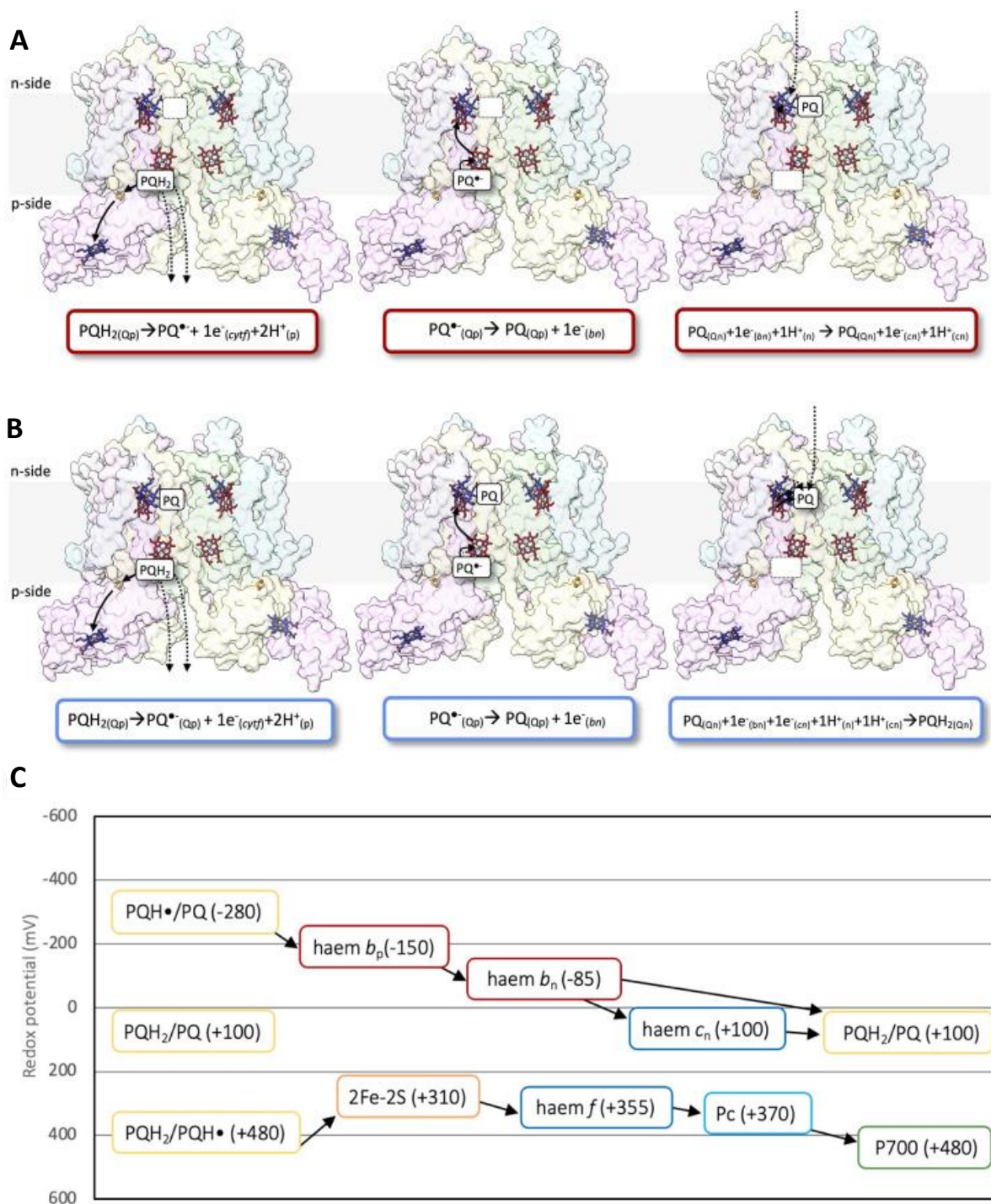


Figure 1.7 | The modified Q-cycle of *cytb₆f*.

Schematic illustration of the modified Q-cycle illustrating electron and proton transfer through the *cytb₆f* complex. The cycle is split into two half-cycles: (A) first half of the cycle is summarised in the red boxes, (B) while the second half of the cycle in blue boxes. Solid black arrows indicate electron transfer, while dotted black arrows indicate proton transfer. (C) Prosthetic groups and proteins are coloured as in figure 1.6. Redox potentials of the cofactors are also here shown. However, according to the recent work carried by Szwalec *et al.*, the redox potentials of the haem *b_p* and *b_n* are -85mV and -150mV respectively.

1.3.6 Plastocyanin

Plastocyanin (Pc) is a small soluble copper-metalloprotein of ~11 kDa and it is one electron carrier responsible for the transfer of electrons from the *cyt_b6/f* complex to PSI (Haehnel 1986). Oxidised Pc (Cu^{2+}) binds to the luminal side of *cyt_b6/f* while reduced Pc (Cu^+) interacts with the PsaF subunit of PSI. Pc represents the primary electron donor to the PSI RC's special pair of chlorophylls, P700 (Caspy et al., 2021) (Figure 1.8C).

1.3.7 Photosystem I

Photosystem I (PSI) is a multi-subunit protein complex able to oxidise Pc in the lumen (PSI donor side) and reduce Fd in the stroma (PSI acceptor side) by using light energy (Nelson & Junge, 2015). The structure of plant PSI is characterised by a core of 12 subunits (PsaA-L), of which 5 are encoded within the chloroplast genome, with a peripheral antenna composed of 4 light harvesting proteins, Lhca1-4 (Mazor et al., 2015, 2017; Pan et al., 2018) (Figure 1.8). The reaction centre composed of the subunits PsaA/PsaB bind the special pair of Chl *a* with an absorption at 700 nm. Upon absorption of light, the excitation energy is channelled from LHCI to the RC P700, giving rise to the transient intermediate P700*. P700* undergoes charge separation and the electron is transferred to modified Chl *a* molecule. The electron transfer can occur in either side of the RC. A phylloquinone molecule is then reduced and then the electron is transferred through a series of 4Fe-4S centres, F_x , F_A and F_B coordinated by the subunits PsaA/B and PsaC. Reduction of Fd on the stromal site is coordinated by PsaC, D and E (Mazor et al., 2017). PSI can also bind LHCI trimers at the PsaH/L, when LHCI subunits are phosphorylated by STN7 kinase, to balance the energy absorption between the photosystems in a process known as state transitions (Pan *et al.*, 2018; Erik et al., 2007).

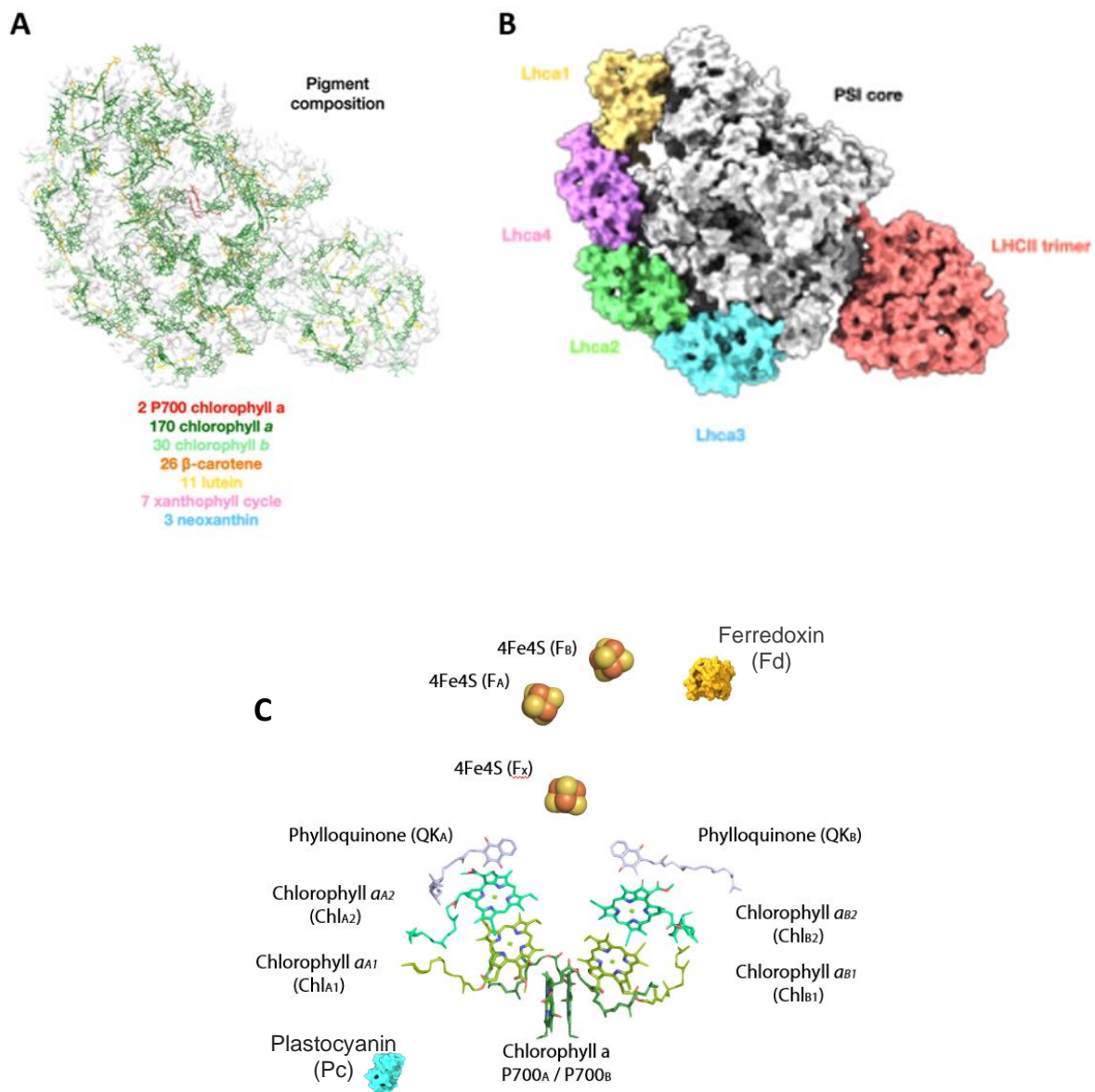


Figure 1.8 | PSI-LHCI-LHCII supercomplex.

PSI-LHCI-LHCII supercomplex viewed perpendicular to the membrane plane from the stroma. (A) Arrangement of the pigments in the PSI-LHCI-LHCII supercomplex. (B) PSI core, with Lhca 1-4 subunits arranged a belt around the core and LHCII trimer. (PDB ID: 5ZJI). (C) PSI RC chromophores and additional components within PsaA and PsaB. PC delivers one electron to PSI. Upon excitation of light, the excited P700 will reduce one of the nearby chl molecules in either side of the PSI RC coordinated by each monomer. A phylloquinone molecule is then reduced. The routes converge at a cluster of 4Fe-4S centres (F_X , F_A and F_B), by which the electron is transferred to Fd on the stromal side of the membrane.

1.3.8 Ferredoxin

Fd is a small, soluble electron carrier protein located in the stroma of ~10 kDa. It contains a 2Fe-2S cluster, possessing a negative redox potential of -430 mV (Tagawa et al., 1963). It accepts electrons from PSI and donates them to the enzyme Ferredoxin:NADP⁺ oxidoreductase (FNR), for the final reduction of NADP⁺.

1.3.9 Ferredoxin:NADP⁺ oxidoreductase

Leaf-type FNR is a flavin adenine dinucleotide (FAD)-containing enzyme of ~35 kDa. FNR is a hydrophilic protein localised in the stroma and it binds sequentially two Fd molecules to receive two electrons for the reduction of NADP⁺ to NADPH in the last step of LET. NADPH provides reducing power in many metabolic pathways, such as nitrogen fixation and the CBB cycle. The enzyme is characterised by two domains: the N-terminus binds the FAD cofactor, with the isoalloxazine ring system stacked between the aromatic side chains of two tyrosine residues, while the C-terminus binds NADP⁺. The C-terminal domain can be further divided into two subdomains, one rigid and one flexible; the flexible subdomain shows conformational changes at higher stromal pH (6-8) upon illumination, increasing the affinity for NADP⁺ molecule (Y. H. Lee et al., 2007). Fd binds in the concave surface at the N-terminus, so that the FAD domain is close for efficient electron transfer. The interaction between Fd and FNR is dependent on the surface charge of the two proteins; Fd possesses a negatively charged surface with mainly glutamate and aspartate residues, and FNR has a positively charged surface with exposed arginine and lysine residues. Co-crystallization of the complex structure of Fd and FNR confirm the presence of five intermolecular salt bridges (Kurusu et al., 2001) (Figure 1.9). These interactions between the two proteins favour the correct orientation of the redox-active sites of the proteins to allow efficient electron transfer. Hydrophobic interactions and the removal of water molecules from the interface strengthen this interaction further. From the crystal structure of the maize leaf Fd-FNR complex, the FAD in FNR is 6Å from the FE1 atom of the 2Fe-2S cluster in Fd, a sufficiently close distance for the direct transfer of electrons (Kurusu et al., 2001)

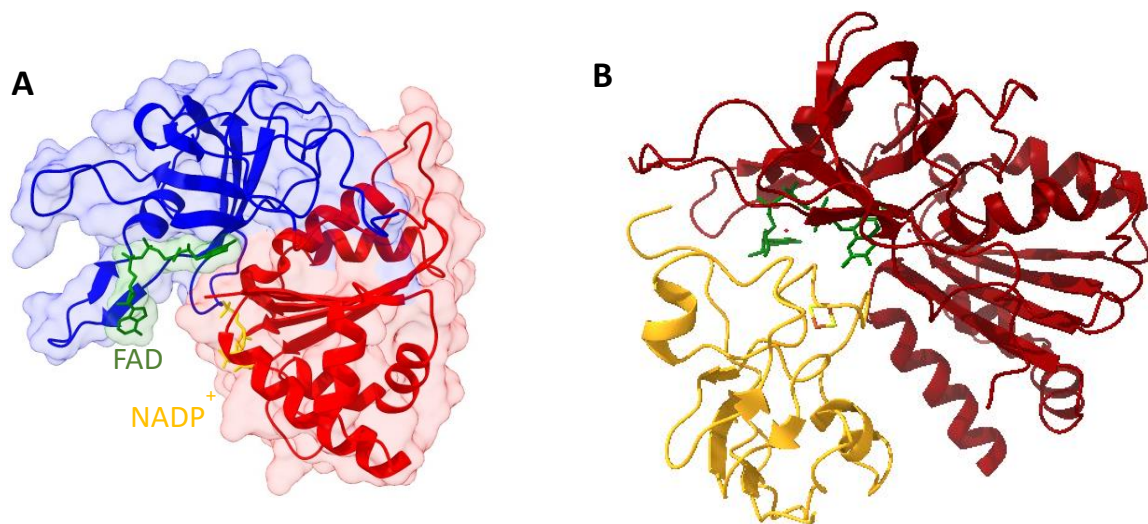


Figure 1.9| Structure of FNR and Fd.

(A) Structure of FNR illustrating the two main domains of the protein; FAD binding domain in blue (residues 1-153), NADP⁺ binding domain in red (residues 154-314). FAD (green) and NADP⁺ (yellow) are indicated. (FNR PDB ID: 1FNC). (B) Structure of maize leaf Fd-FNR complex. FNR (dark red) and Fd (yellow). FAD (green) and 2Fe-2S cluster (dark orange and yellow) are also shown. PDB ID: 1GAQ.

To reduce one molecule of NADP⁺ (two electron acceptor) two molecules of reduced Fd (a one electron donor) sequentially bind to FNR and transfer the electrons. In the catalytic mechanism, NADP⁺ binds to FNR, followed by reduced Fd (Figure 1.10). In fact, the affinity of FNR for reduced Fd is 30x higher than for oxidised Fd in the presence of NADP⁺ (Batie & Kamins, 1984a, 1984b; Carrillo & Ceccarelli, 2003). Thus, FNR would control energetically the binding of Fd. The conformational flexibility of the c-terminus of FNR also allows the entry and release of NADP⁺ and NADPH at the active site (Y. H. Lee et al., 2011; Paladini et al., 2009).

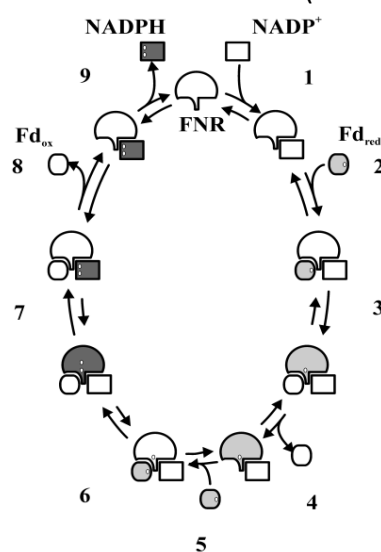


Figure 1.10| Schematic illustration of the catalytic pathway.

The pathway here shown was proposed by Batie and Kamin (Batie & Kamins, 1984a, 1984b). NADP⁺ binds to FNR (step 1) and reduced ferredoxin binds the complex (step 2) transferring one electron (step 3). Oxidised Fd dissociates from the complex (step 4) and a second reduced Fd binds to FNR (step 5).

6) and resulting in the full reduction of FNR (step 7). NADP⁺ is instantly reduced to NADPH and oxidised Fd dissociates (step 8) and NADPH is released (step 9). Adapted from Carrillo and Ceccarelli, 2003.

In *Arabidopsis thaliana* (*Arabidopsis*) two leaf isoforms exist, FNR1 and FNR2 (Hanke et al., 2005). In *Arabidopsis*, previous studies have shown the ability of the two FNR isoforms to form a complex with the proteins Tic62 and TROL. Tic (translocon at the inner envelope of the chloroplast) complex guide several proteins into the organelle and one of the 7 subunits of this complex, Tic62, interacts with FNR at its C-terminus serine/proline rich (Benz et al., 2009). TROL (thylakoid rhodanese-like protein) is a nuclear encoded protein of 66 kDa, characterised by two transmembrane helices and an inactive rhodanese domain; its C-terminal domain interacts with FNR, as well as Tic62 (Jurić et al., 2009). While *Arabidopsis* mutants lacking Tic62 do not show a strong phenotype, plants lacking TROL showed some defects in LET efficiency in extremely high light (due to photodamage). It has been suggested that the tethering of the FNR to the membrane by Tic62 is pH dependent and the interaction is stronger in acidic conditions (Alte et al., 2010).

1.3.10 ATP synthase

The chloroplastic ATP synthase (CF₁F₀) is a large multi subunit protein and it is located in the stromal lamellae of the thylakoid membrane. The complex can catalyse either the phosphorylation of ADP plus Pi to ATP or the reverse reaction. The synthesis of ATP is powered by the *pmf* generated by the proton translocation at PSII and *cytb₆f*.

The chloroplastic ATP synthase is monomeric, in contrast to the mitochondrial dimeric version of the complex. However, they share common structural characteristics: the membrane intrinsic rotor F₀ and the F₁ domain protruding in the stroma with the catalytic head, precluding the complex from entering the stacked grana. F₀ is composed of a ring rotor of 14 α helical c-subunits characterised by protonatable glutamate residues allowing the proton uptake from the lumen and subunit a. F₁ contains 11 subunits; three α , three β of the catalytic head, a central stalk of subunits γ , ϵ attached to the F₀, and a peripheral stalk of δ , b and b' subunits (Figure 1.11) (Hahn et al., 2018).

The central stalk rotation is driven by the *pmf* and it causes conformational changes of α and β subunits. At each catalytic site of α/β subunit, ATP generation occurs by a three-step

rotational mechanism of 120° each; one rotation allows the ADP and Pi binding to the catalytic site, the second rotation bring ADP and Pi in close proximity resulting in ATP, and the last one allows the release of the ATP molecule in the stroma. In total, three catalytic sites are present in each complex, resulting in the generation of three molecules of ATP per 360° rotation of the head group and translocation of 14 protons, giving a H^+/ATP ratio for the complex of 4.67. Thus, the $6H^+$ coupled to LET can provide $6/4.67 = 1.28$ ATP per NADPH formed (Boyer, 2000; Stock et al., 1999). In the γ subunit, the plant cF_1F_0 present 40 residues that are involved in the regulation of ATP synthase in the dark. Upon illumination, thioredoxins reduce thiol-regulatory Cys residues, leading to the formation of disulfide bond (Arana & Vallejos, 1982; Junesch & Gräber, 1987; Nalin & McCarty, 1984).

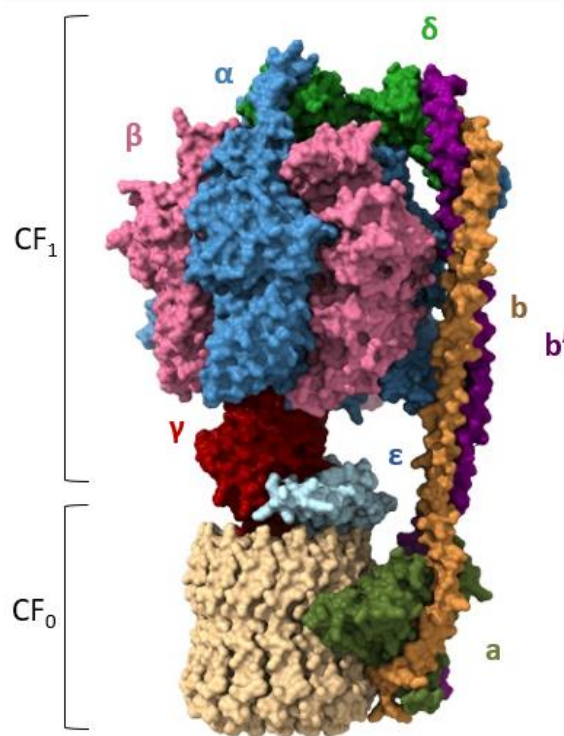


Figure 1.11 | Structure of ATP synthase.

Structure of the chloroplast ATP synthase from *Spinacia Oleracea* (PDB ID:6FKI). The membrane intrinsic rotor CF_0 and the CF_1 domain are indicated. CF_0 is composed of a ring rotor of 14 α helical c-subunits (light pink) and subunit a (light green). F_1 contains 11 subunits; three α (blue), three β (pink) of the catalytic head, a central stalk of subunits γ (red), ϵ (light blue) attached to the F_0 , and a peripheral stalk of δ (green), b (orange) and b' subunits (violet).

1.3.11 Heterogeneous distribution of protein complexes within the thylakoid membranes

The thylakoid membrane can be separated into the appressed grana, forming a cylindrical stack, and the interconnecting non-appressed stromal lamellae. A lateral heterogeneity in the distribution of the photosynthetic complexes can be observed in the thylakoid membrane. PSII-LHCII supercomplexes are found mainly in the appressed grana and LHCII-LHCII interactions induce the grana formation and have a role in increasing the grana size, while PSI-LHCI and ATP synthase are sterically excluded from the grana stack because of stromal protrusions (M. P. Johnson & Wientjes, 2020). Therefore, PSI and ATP synthase complexes are mainly found in the stromal lamellae (Figure 1.12). This compartmentation of the thylakoid membrane could also reduce the spillover of the excitation energy from PSII to PSI (Trissl & Wilhelm, 1993). *Cytb₆f* complex instead is equally distributed among them, receiving electrons from PSII via PQH₂ in the grana stacks, and delivering them via PC to PSI in the stromal lamellae (Anderson, 1982; Cox & Andersson, 1981). It has been also shown that net area of stacked and unstacked thylakoid membranes can be finely modulated in a process known as dynamic thylakoid stacking.

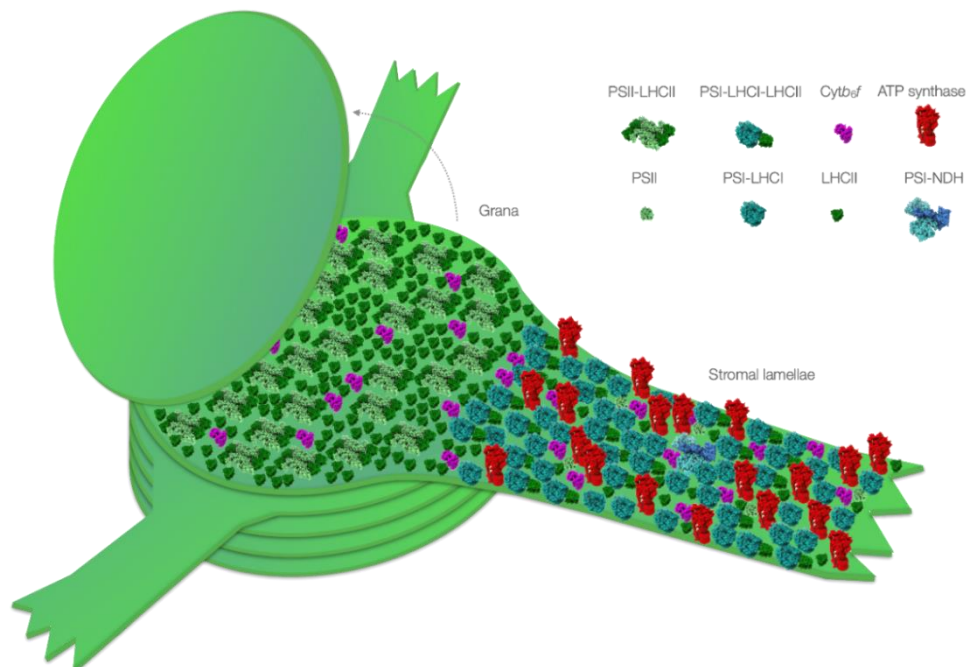


Figure 1.12 | Organisation of the thylakoid membrane system.

All the key components involved in LET and CET are illustrated. The stacked grana membranes contain PSII-LHCII supercomplexes, PSII monomers and loosely bound LHCII trimers and *cyt_b*6*f*, while in the stromal lamellae membranes contain mainly PSI, loosely bound LHCII trimers, PSII monomers, ATP synthase and PSI-NADH-dehydrogenase like Complex (NDH).

1.4 Regulation in photosynthesis

In nature, plants are exposed to multiple stresses, including frequent changes in light intensity, temperature or drought and they require an apparatus that is flexible and able to adjust the energy utilisation to meet the metabolic requirements. Photoexcitation of PSII and PSI needs to be finely regulated to ensure a high photosynthetic efficiency and avoid photodamage. Thus, plants have evolved short- and long-term adaptive responses to environmental changes. Short-term responses can occur in a timescale of seconds to few minutes; plants effectively manage the excess of light energy and modulate the NADPH:ATP ratio for metabolic demands. In long-term responses, dynamic acclimation occurs which leads to substantial changes in the thylakoid membrane composition (Flannery et al., 2021)

1.4.1 Photoprotective mechanisms

As mentioned above, plants have developed several strategies to cope with light intensity fluctuations in nature. For instance, excess absorbed light energy can lead to damage of the photosynthetic machinery. In the PSII RC, the special P680 chl pair is excited to P680*, and electrons are transferred to pheophytin, to the quinone molecules Q_A and Q_B, and finally to PQ molecules. An excess of energy can lead to the over-reduction of the PQ pool, which can promote P680 charge recombination, resulting in the regeneration of P680*. The extension of the lifetime of P680* can result in intersystem crossing to the P680 triplet state which can transfer excitation to ³O₂ to form singlet oxygen (¹O₂); furthermore, O₂ can be reduced to superoxide O₂^{•-} at the iron-sulphur clusters of PSI. Both molecules are reactive oxygen species (ROS) and lead to photo-oxidative damage and photoinhibition.

Thus, photoprotective mechanisms developed including non-photochemical quenching (NPQ), involving the dissipation of the excess of light energy into heat. NPQ is triggered by excess proton translocation across the membrane which causes the acidification of the thylakoid lumen and the protonation of glutamate residues of PsbS protein and activation of violaxanthin de-epoxidase (VDE), transforming LHCII bound violaxanthin into zeaxanthin. Together PsbS and zeaxanthin bring about conformational changes in LHCII which trigger qE (the rapidly-relaxing component of NPQ) and dissipation of the excess of energy into heat (Ruban, 2016).

Acidification of the thylakoid lumen also downregulates the electron transport rate at *cytb₆f*, in a process called photosynthetic control (Jahns et al., 2002; Nishio & Whitmarsh, 1993; Rumberg & Siggel, 1969). Lumenal pH below 6.2 causes the protonation of His129 of the ISP coordinating 2Fe-2S, which act as H-bond acceptor of PQH₂, inhibiting its oxidation and slowing down the Q-cycle. Thus, protonation of this His129 would control the rate of PQH₂ oxidation at Q_p site, causing feedback downregulation of LET and protect PSI from over reducing conditions (Malone et al., 2021). Since electron transport to PSI is restricted at its donor side, the oxidation of P700 represents a method to monitoring photosynthetic control (Harbinson and Hedley, 1989).

1.4.2 Flexible regulation in photosynthetic reactions

In addition to the photoprotective mechanisms evolved to prevent the accumulation of reactive oxygen species (ROS) or reduced intermediates, regulatory mechanisms have evolved to give flexibility to the system to respond rapidly to environmental changes and meet metabolic demands.

LET can only provide a fixed ratio of ATP:NADPH. For every two electrons liberated upon photolysis of a water molecule at PSII and passed along the LET chain via PSI to NADP⁺, 6 protons are moved from the stroma to the thylakoid lumen, 2 at the water splitting complex of PSII itself and a further 4 via the Q-cycle at *cytb₆f*. ATP synthase consumes this proton gradient in the synthesis of ATP. Since, the structure of the chloroplast ATP synthase has revealed that there are 14 proton binding c-subunits for every 3 ATP forming catalytic sites giving a H⁺/ATP ratio for the complex of 4.67. Thus, the 6H⁺ coupled to LET can provide $6/4.67 = 1.28$ ATP per NADPH formed. Yet in the CBB cycle the ATP/NADPH ratio required per turn of the cycle and generation of one molecule of glyceraldehyde 3-phosphate is $9/6 = 1.5$ (Allen, 2003).

Thus, in simple terms LET is not able to fulfil the ATP requirement of the CBB cycle. However, a range of other metabolic pathways exist alongside the CBB cycle in the chloroplast, and these consume ATP and NADPH in varying amounts. For instance, NO₂⁻ reduction to NH₄⁺ in the chloroplasts would lower the required ATP/NADPH ratio since it requires more reductant than ATP, while photorespiration elevates the required ATP/NADPH ratio (Noctor & Foyer, 2000). Therefore, the metabolic and developmental state of the plant can vary the required

ATP/NADPH ratio substantially. Thus, flexibility in the ability to produce ATP relative to NADPH is required (D. M. Kramer & Evans, 2011).

1.4.3 Alternative electron transfer pathways

Several mechanisms exist to ensure the supply of extra ATP in the chloroplast (Figure 1.13). One of the most studied mechanisms is photosynthetic cyclic electron transport (CET), by which electrons are reinjected from reduced Fd back to the PQ/PQH₂ pool forming a cyclic flow of around *cytb₆f* and PSI. CET generates additional *pmf* without forming net NADPH and can therefore provide flexibility to adjust the NADPH/ ATP ratio. In addition, the augmentation of ΔpH by CET can trigger downregulation of LET by photosynthetic control and light harvesting by qE which help plants cope with environmental stresses, such as drought, extreme temperatures and high light conditions (G. N. Johnson, 2011; Yamori & Shikanai, 2016).

Alternatively to CET, in the water-water cycle (WWC), also called the Mehler peroxidase reaction or pseudocyclic electron transfer, electrons are instead transferred from Fd and NADPH to reduce O₂ to the superoxide anion radical O₂⁻. The superoxide is then converted to H₂O₂ by the enzyme superoxide dismutase and then detoxified to H₂O by ascorbate peroxidase. These reactions require NADPH, resulting in a net gain in ATP (Asada, 1999). In cyanobacteria, green algae, mosses and liverworts the reduction of O₂ to water is instead catalysed by flavodiiron proteins (FLV), which are not found in angiosperms. The reasons of this are still unclear, however it is thought that CET around PSI substituted completely their function, leading to their loss during evolution.

Excess NADPH is also consumed by the enzyme NADP-malate dehydrogenase (NADP-MDH) to reduce oxaloacetate (OAA) to malate, regenerating NADP⁺ via the so-called 'malate valve' (Scheibe, 2004). NADP-MDH is activated by reduced thioredoxins and inactivated by NADP⁺. Malate is then exported to the cytosol where it can be oxidised back to OAA, generating NADPH. Alternatively, it can be exported to the mitochondrion via the oxaloacetate/malate transporters where it can be used a substrate for ATP synthesis or in case of excess of NADPH in the chloroplast, hence providing a short term regulatory response (Voss et al., 2013).

1.5 Cyclic Electron Transport

The major pathway for the augmentation of the ATP production in angiosperms is CET. CET was discovered in 1955, when Daniel Arnon and his group found that light-driven synthesis of ATP could occur in intact chloroplasts without the evolution or consumption of O_2 (Whatley et al., 1955). CET involves the reinjection of electrons from Fd into the PQ pool thus cycling electrons between PSI and *cyt_bf* (Tagawa et al., 1963). In angiosperms, PSI cyclic electron flow can occur through two pathways: a main route depending on the Proton Gradient Regulation 5 (PGR5) and PGR5-like photosynthetic phenotype 1 (PGRL1) proteins (DalCorso et al., 2008; Munekage et al., 2002) and a minor route depending on NADH dehydrogenase-like (NDH) complex (Endo et al., 1997).

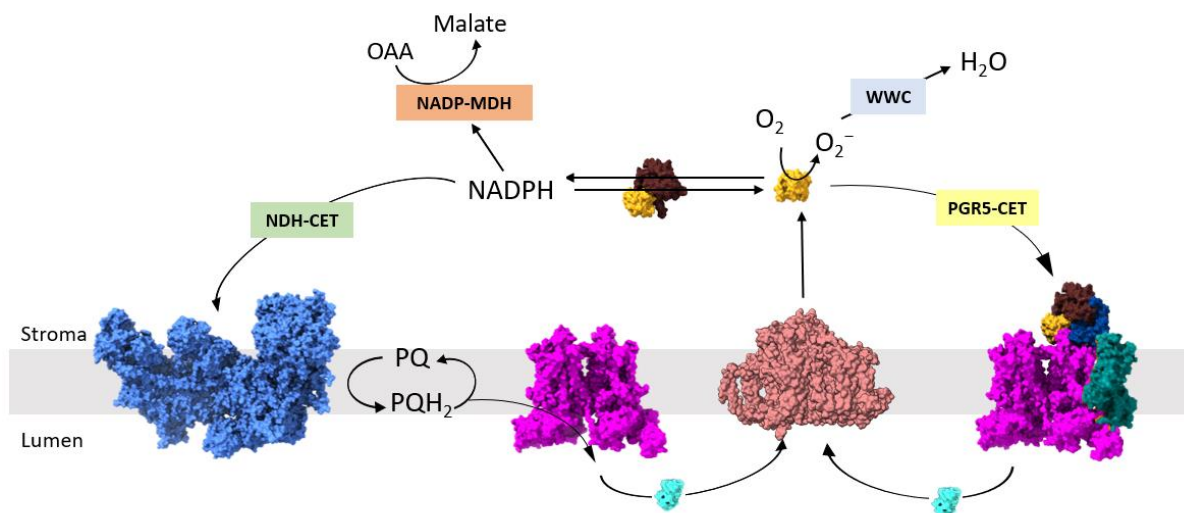


Figure 1.13 | Alternative electron pathways in angiosperms.

LET can provide just a fixed ratio of ATP:NADPH. However CBB cycle requires a ratio of 1.5 ATP:NADPH. This shortfall of ATP is provided by alternative electron pathways which contribute to the augmentation of ATP to NADPH. CET is well known for the photoprotection of PSI and for generating extra ATP without net production of NADPH, by the NDH complex or via the PGR5/PGRL1 pathway. NDH forms a supercomplex with PSI-LHCI, facilitating the electron transfer from Fd to the NDH complex; PGR5/PGRL1 complex instead could act as binding site for Fd-FNR at *cyt_bf*. Both act as ferredoxin-plastoquinone reductase (FQR) complexes reinjecting electrons in the PQ pool between PSI and *cyt_bf*. Ferredoxin instead could also donate electrons to O_2 leading to generation of O_2^- , detoxified by the WWC. In addition, NADPH can be used for the reduction of OAA to malate.

1.5.1 NDH-dependent pathway

Genetic and biochemical evidences showed that NDH complex is involved in CEF around PSI (Endo et al., 1997), returning electrons from Fd to the PQ pool and subsequently to PSI via

cytb₆f; simultaneously, NDH complex pumps two additional protons into the lumen per electron shuttled (Ifuku et al., 2011; Strand et al., 2016) (Figure 1.15).

In the chloroplast, the NDH complex possesses more than 30 subunits and its sequence shows a high homology to the bacterial and respiratory type I NADH:quinone reductase Complex I sequence (Friedrich et al., 1995; Shinozaki et al., 1986). The complex is characterised by a L-shaped skeleton and can be subdivided into five subcomplexes; transmembrane subcomplexes “A” (SubA) and “B” (SubB), the membrane arm involved in the proton translocation “M” (SubM), a luminal subcomplex “L” (SubL) and an electron donor subcomplex “E” (SubE) (Figure 1.14B)(Su et al., 2022) .

In angiosperms SubA contains the NDH subunits NdhH-O and represent the hydrophilic arm of the complex (Figure 1.14A). NdhL is the only membrane subunit of SubA and it is necessary for its stabilisation. All the subunits of Arabidopsis SubA show a very high similarity to *Thermosynechococcus elongatus* NDH-1L (TeNDH-1L) and to *Hordeum vulgare* NDH (HvNDH) in the sequence and overall fold. The subunit NdhO, absent in the recent structure of NDH-PSI from *Hordeum vulgare*, was previously shown as essential for the assembly and function of the NDH complex (Rumeau & Peltier, 2005; Shen et al., 2022; Su et al., 2022). NdhO may be involved in Fd binding, as previously suggested for TeNdhO (Laughlin et al., 2020; C. Zhang et al., 2020). Three 4Fe-4S clusters involved in the electron transfer pathway of the NDH complex are located in SubA, specifically two in subunit NdhI and one in NdhK (Laughlin et al., 2019).

The SubB comprises the subunits PnsB1-PnsB5, and it represents the second hydrophilic arm of the Arabidopsis NDH complex. PnsB4 and PnsB5 are embedded in the membrane, while PnsB1-3 are located at the stromal side of the complex (Figure 1.14A). PnsB3 contains a 2Fe-2S cluster, which was shown to be redox active suggesting that it could be involved in sensing the redox state of the stroma or in electron transfer (Su et al., 2022; Takabayashi et al., 2009).

SubM is composed of the subunits NdhA to NdhG and it is the membrane-embedded arm of the NDH complex; these are homologous to the transmembrane subunits from the multiple resistance and pH (Mrp) Na⁺/H⁺ antiporter complex (Berrisford et al., 2016; Schuller et al., 2019).

Subunits PnsL1-PnsL5 are part of SubL and are all soluble proteins located on the luminal side of the complex.

SubE is responsible for the binding Fd (NdhS-V). NdhS-U-V were not observed in both HvNDH and AtNDH cryo-EM structures (Shen et al., 2022; Su et al., 2022) The chloroplast NDH complex differs from the mitochondrial complex I as it lacks the NADH binding molecule. Therefore, two electron donations occur at SubE from two reduced Fd molecules for the reduction of a PQ molecule in the complex (Yamamoto et al., 2011). SubE is involved in the formation of the supercomplex with PSI (Reviewed in Peltier et al., 2016).

The NDH complex has been found to associate to PSI forming the NDH-PSI supercomplex. The association of PSI with NDH helps in the stabilization of the NDH complex and is required especially under stress conditions, as in high light conditions (Peng & Shikanai, 2011). In plants, recent structures have been resolved of the PSI-NDH-1 supercomplex (Shen et al., 2022; Su et al., 2022). One NDH complex is able to bind to two copies PSI; in the recent structure of NDH-PSI supercomplex is possible to observe that the PSI complexes are associated with NDH through LHCI belt, specifically via Lhca5 and Lhca6 (Figure 1.14C) (Su et al., 2022).

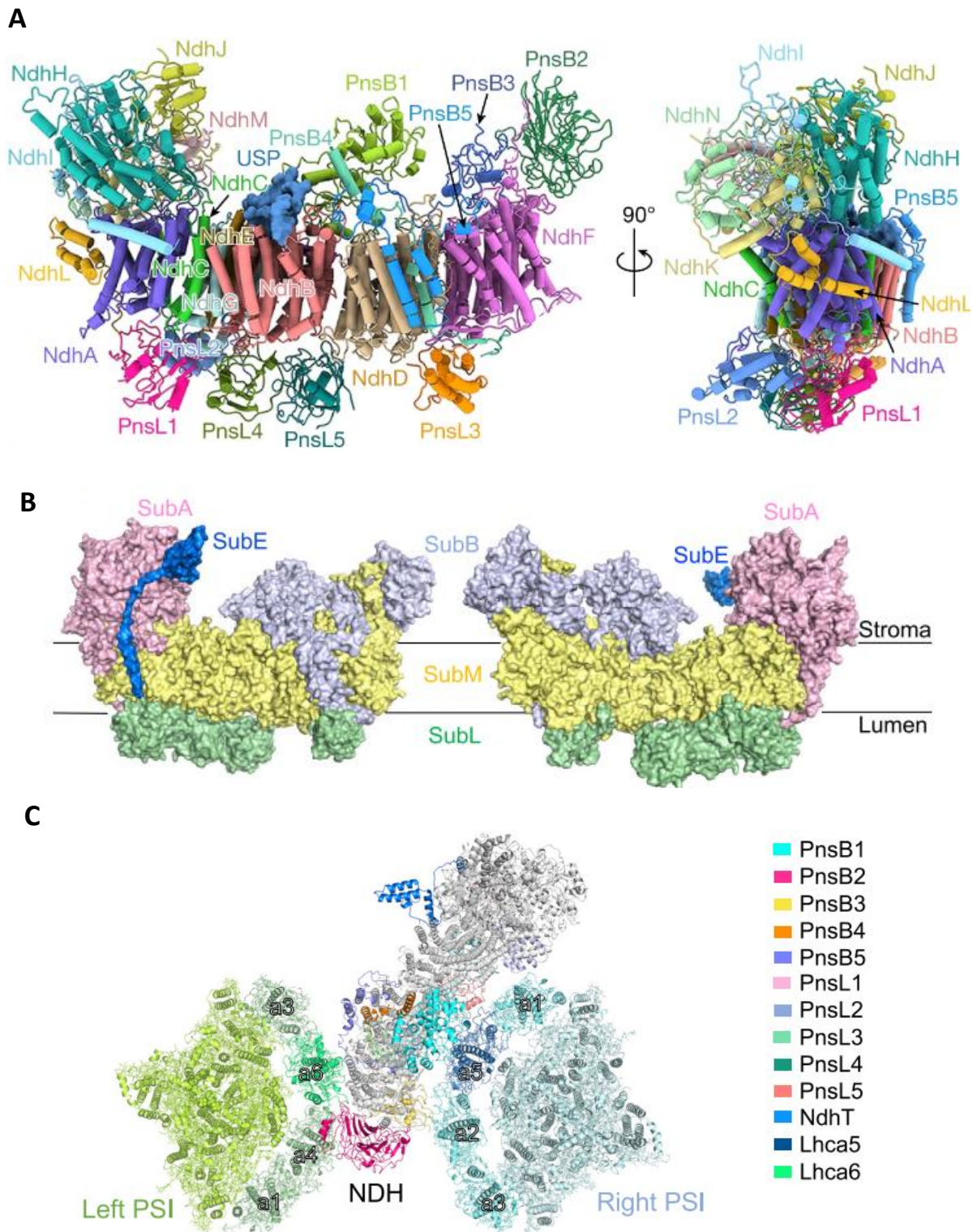


Figure 1.14 Structure of the NDH-complex.

The complex can be subdivided into five subcomplexes; transmembrane subcomplexes “A” (NdhH-O) and “B” (PnsB1-PnsB5), the membrane arm involved in the proton translocation “M” (NdhA-G), a luminal subcomplex “L” (PnsL1-PnsL5) and an electron donor subcomplex “E” responsible for the binding Fd (NdhS-V) (A) View of the overall structure of the HvNDH complex in the plane of the membrane with a 90° rotation. All the subunits are indicated. (PDB:7EU3) Figure adapted from Shen *et al.*, 2022. (B) surface representation of the structure of AtNDH complex in the plane of the membrane. The five subcomplexes are indicated (PDB: 7WFD). Figure adapted from (Su *et al.*, 2022). (C) Overall structure AtNDH-PSI supercomplex viewed perpendicular to the membrane plane from the stroma (PDB: 7WG5). Figure adapted from (Su *et al.*, 2022).

The NDH complex has a crucial function in cyanobacteria as mutants without NDH activity do not survive, or others with partial NDH activity show a much slower growth compared to the wild-type in normal air CO₂ concentration (He et al., 2016; He & Mi, 2016). In Arabidopsis, NDH defective mutants show only a slight reduction in *pmf* generation.

The chloroplast NDH complex differs from the mitochondrial complex I as it lacks the NADH binding molecule. Therefore, two electron donations occur at SubE from two reduced Fd molecules for the reduction of a PQ molecule in the complex (Yamamoto et al., 2011).

In Arabidopsis NDH forms a supercomplex with two copies of PSI via the Lhca5 and Lhca6 subunits. This supercomplex could enable a fast transfer of electrons from PSI to NDH, therefore enhancing CET (Su et al., 2022) (Figure 1.15).

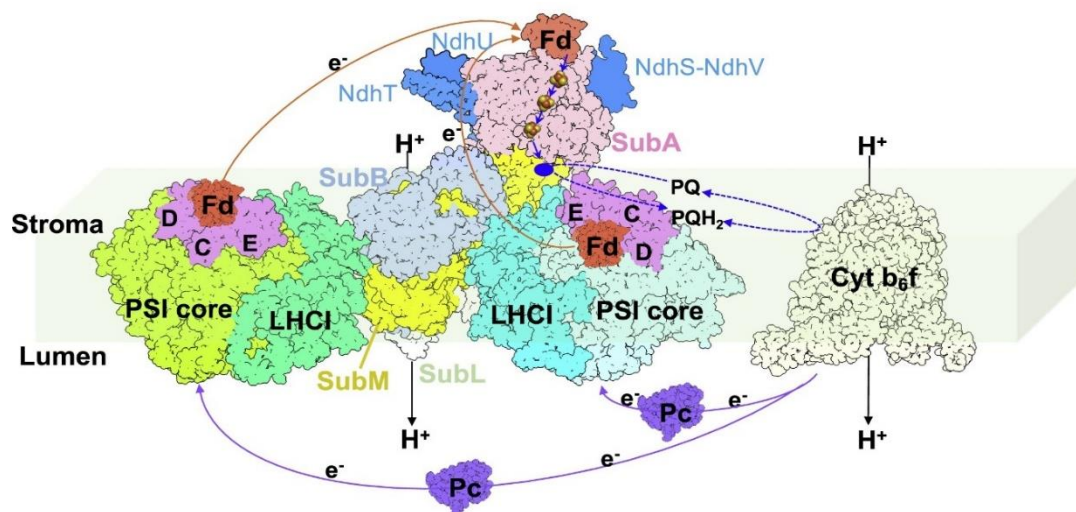


Figure 1.15 Schematic model of CET involving NDH-PSI and *cytb₆f*.

Schematic model adapted from Su *et al.*, 2022 illustrating CET involving NDH-PSI supercomplex, which receives electrons from reduced Fd for the reduction of PQ molecules. Pc molecules are reduced by *cytb₆f* and oxidised by PSI complexes.

1.5.2 PGRL1/PGR5-dependent pathway

The major CET pathway in Arabidopsis is the PGRL1/PGR5 dependent pathway, which involves the small protein PGR5 and the transmembrane protein PGRL1. This pathway is also known as being sensitive to the poison Antimycin A (AA), however the mechanisms are still unclear (Tagawa *et al.*, 1963).

AA is an antibiotic isolated from *Streptomyces* species (Nakayama et al., 1956) and it has been widely used as electron inhibitor in mitochondria and chloroplast. Initially, AA was found to inhibit in mitochondrial *cytb_{c1}* by binding to the quinone reduction site Q_i, blocking its reduction by the closely located haem b_H and therefore causing the generation of ROS (Crowther and Hind, 1980). However, the *cytb_{6f}* was shown to be not targeted by AA and the NDH-dependent pathway is also insensitive to this poison (Endo et al., 1997), suggesting another ferredoxin-plastoquinone oxidoreductase 'FQR' activity must exist (Moss & Bendall, 1984). The AA-sensitive pathway utilised Fd as an electron donor, similar to the NDH pathway, but it also involved the FNR (Joliot & Johnson, 2011; Mills et al., 1979)(Mills et al., 1979; Johnson and Joliot., 2011).

A major leap in knowledge occurred with the discovery of the PGR5 protein in 2002 (Munekage et al., 2002). Arabidopsis plants lacking PGR5 showed an absence of photosynthetic control and diminished qE due to a lower steady state level of ΔpH (Munekage et al., 2004). PGR5 is a small membrane extrinsic protein associated with the stromal side of the thylakoid without any obvious metal or ET co-factor binding site (DalCorso et al., 2008; Munekage et al., 2004). The absence of PGR5 resulted in the loss of the major AA-sensitive CET activity but since it was a small protein and bound no ET co-factors it seemed unlikely to represent the FQR in isolation. In the study conducted by Sugimoto et al in 2013, FQR activity was shown to be resistant to antimycin A in ruptured chloroplast and leaves from Arabidopsis expressing Pinus taeda PGR5 protein (PtPGR5). PtPGR5 and Arabidopsis PGR5 (AtPGR5) sequences differentiate in eight amino acids; in order to define which alteration would confer an antimycin A resistance, a series of *pgr5* mutants were generated. Results showed that a single amino acid mutation (valine to lysine) in AtPGR5 would induce resistance to the antibiotic. Thus, antimycin A may inhibit directly PGR5 function (Sugimoto et al., 2013).

A very similar phenotype to the *pgr5* mutant was found in Arabidopsis plants lacking the PGRL1 (DalCorso et al., 2008). PGRL1 is an integral thylakoid protein, characterised by two transmembrane domains divided by a loop of 19 amino acids. In Arabidopsis, PGRL1 is encoded by the two homologous genes PGRL1A (At4g22890) and PGRL1B (At4g11960); plants lacking entirely these two genes (*pgrl1ab* double mutants) showed no PGR5 accumulation, whereas in *pgr5* mutants PGRL1 expression is not inhibited (DalCorso et al., 2008). PGR5-PGRL1 heterodimers have been previously observed through co-Immunoprecipitation studies

(DalCorso *et al.*, 2008); these intermolecular interactions involve inter-molecular disulphide bridges between cysteine residues in PGRL1 and PGR5 protein sequences (Hertle *et al.*, 2013). Interestingly, PGRL1 was able to bind an iron co-factor via several of the conserved cysteine residues and showed AA-sensitive FQR activity in vitro when combined with NADPH, FNR and Fd (Hertle *et al.*, 2013). Thus, it was proposed that PGRL1 protein is the elusive FQR in CET, reducing the PQ pool (Figure 1.16).

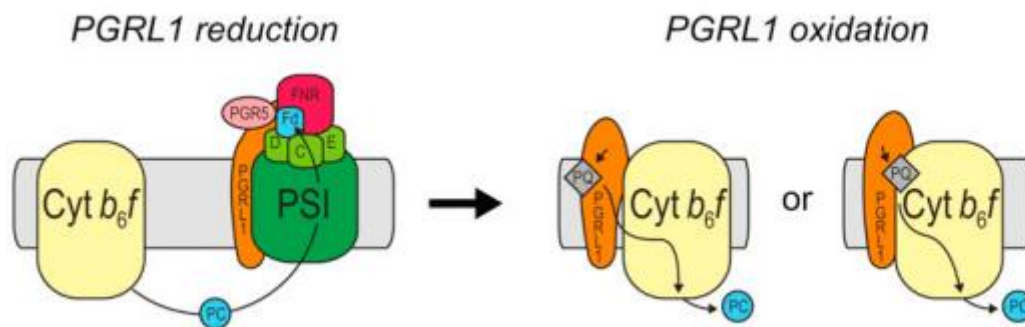


Figure 1.16 Model of PSI oxidation and *cyt*_{b6f} reduction by PGRL1.

Schematic model adapted from (Hertle *et al.*, 2013) illustrating CET via PGRL1. PGRL1 would interact with PSI, FNR and PGR5 and accept the electrons from Fd. Subsequently, PGRL1 would interact with *cyt*_{b6f}, transferring electrons from PQ to PC.

However, a recent study showed that *pgr1* mutant in *Chlamydomonas* possessed a similar maximal rate of CET compared to the wild type (Nawrocki, Bailleul, Cardol, *et al.*, 2019). Supporting this, it has been shown that in *Arabidopsis* PGRL1 function is to protect PGR5 by degradation by PGRL2. *Arabidopsis* plants lacking PGRL2 do not show any marked physiological effect and the molecular mechanisms of how PGRL2 is triggered for degradation of PGR5 remain elusive. Interestingly, a single amino acid mutation in PGR5 (PGR5_{G130S}) inhibits its interaction with PGRL1, leading to its degradation by PGRL2. Furthermore, *Arabidopsis* mutant lacking both PGRL1 and PGRL2 show a high accumulation of “free” PGR5, resulting in high CEF but also in an impairment of electron flow in low light. Therefore, both PGRL1 and PGRL2 are necessary for regulating PGR5 abundance and activity in the photosynthetic electron transport chain (Rühle *et al.*, 2021).

Although PGR5 is important for proper regulation of AA-sensitive CET in *Arabidopsis*, there is some evidence it may not play a direct role. For instance, the *pgr5* *Arabidopsis* mutant was

still capable of performing CET and thus forming NPQ under low CO₂ conditions (Nandha et al., 2007). This leads to the idea that a PGR5/PGRL1 complex might play a regulatory role in CET and the FQR activity might reside elsewhere such as in *cytb₆f* or in FNR/Fd.

Since early *cytb₆f* purifications from spinach FNR was found in substoichiometric levels to the complex (Clark et al., 1984; H. Zhang et al., 2001). This led to the hypothesis that FNR could interact with *cytb₆f* and by donating electrons to the Q_n site of the complex it would contribute to CET (Shahak et al., 1981). Despite the fact that many studies have identified FNR in *cytb₆f* purifications, no structural findings have been published to this day confirming the interaction between the two proteins leading to the idea that FNR could only be a contaminant owing to its hydrophobic nature (Sarewicz et al., 2023). Recently, isothermal titration calorimetry (ITC) was used to study the interaction between FNR and *cytb₆f* however no interaction was observed (Zakharov et al., 2020).

1.5.3 The elusive CET supercomplex?

Recently, PGR5 was found to interact with *cytb₆f* and also affected the tethering of FNR to the membrane (Wu et al. 2021; Mosebach et al. 2017); renewing speculation that PGR5 could act as a binding site for FNR/Fd complex on *cytb₆f* (Malone et al., 2021). Indeed, FNR associated with *cytb₆f* in spinach was able to reduce PQ in the presence of NADPH (Szymańska & Kruk, 2010).

Moreover, a supercomplex involving PSI, LHCII, *cytb₆f*, PGRL1 and FNR has been isolated from *Chlamydomonas* (Iwai et al., 2010), though subsequently proved highly unstable (Buchert et al., 2018).

Recently in *Chlamydomonas* Fd was suggested to act as a direct electron donor to PQ bound at the reducing site (Q_n) via haem c_n (Nawrocki et al., 2019), in a manner consistent with the original Q-cycle proposed by Peter Mitchell in 1975 (Mitchell, 1975). Consistent with a regulatory role, PGR5 was shown to affect the redox state of the low potential chain in *cytb₆f* under anoxia (CET promoting conditions) in *Chlamydomonas* (Buchert et al., 2020).

Several studies have been conducted to investigate the role of FNR and its interaction with TROL and Tic62. While TROL/Tic62/FNR interaction was thought to protect FNR from proteolytic degradation during photosynthetic inactivity, recent studies show instead that this

interaction would regulate the partitioning of LET/CET. In the light the interaction of TROL and Tic62 with FNR is weakened, enabling FNR to reduce NADP⁺ and favouring LET over CET. Instead, in the dark TROL and Tic62 would tether FNR to the stromal lamellae promoting CET activity (Alte et al., 2010; Benz et al., 2009; M. Kramer et al., 2021). FNR could interact with other proteins in a yet uncharacterised mechanism to increase CET and represent the FQR complex with *cytb₆f*.

1.6 Outstanding questions

Despite the many genetical and biochemical evidences showing the involvement of FNR and other protein complexes in CET, the mechanisms of this pathway are still unknown.

The key outstanding questions are:

1. Which proteins are involved in the AA-sensitive CET in angiosperms?
2. Does AA-sensitive CET involve FNR binding to *cytb₆f*?
3. How does the FNR tethering to the membrane regulate AA-sensitive CET?

This thesis attempts to answer these questions about AA-sensitive CET in photosynthesis in angiosperms. The first aim of the thesis focuses on the development of a protocol for the purification of the CET supercomplex in Spinach to understand which proteins are involved in the AA- sensitive pathway.

The second aim was to attempt the structural characterisation of the supercomplex by using chemical crosslinking and mass spectrometry analysis for a better understanding of the structural interconnections between the CET proteins. Furthermore, it was to assess spectroscopically the FQR activity of the purified supercomplex.

The third aim was to understand the relevance of FNR binding to the thylakoid membrane to CET *in vivo* in Arabidopsis.

2. Materials and methods

2.1 Materials

All chemicals and reagents used were of analytical grade purity supplied by Sigma-Aldrich Company Ltd. or Thermo Fisher Scientific UK Ltd unless stated otherwise.

2.2 Buffers and reagents

All buffers were prepared using distilled water purified via a Milli-Q Integral Water Purification System. All buffers were adjusted to their required pH using HCl or NaOH/KOH. Buffers used in chromatography were additionally filtered in a vacuum pump with 0.2µM filter. Buffers containing detergents were filtered prior to their addition from stocks.

2.3 Preparation of thylakoid membranes

2.3.1 *Spinacia oleracea*

All the *S.oleracea* used in this study was purchased from a local supermarket the same day of use.

2.3.2 Thylakoid preparation for the purification of *cytb₆f* at pH 7.5

The following protocol is adapted from Hurt and Hauska, 1981. All buffers used are outlined in Table 2.1.

Fresh spinach leaves were homogenised in ice-cold Buffer 1. The homogenate was filtered through two layers of muslin and then through two layers of muslin wrapped around absorbent cotton wool. The cell lysate was centrifuged at 4000 x g for 15 minutes at 4 °C. The supernatant was discarded and the pellet was resuspended in Buffer 2 and centrifuged at 4000 x g for 15 minutes, 4 °C. The resultant pellet was resuspended in Buffer 3 and incubated on ice for 15 minutes before diluting 2-fold with ice cold milliQ water and centrifuged at 4000 x g for 15 minutes, 4 °C. The resultant pellet was resuspended again in Buffer 3 and incubated on ice for 15 minutes and then diluted 2- fold with milliQ water and centrifuged at 4000 x g

for 15 minutes, 4 °C. The pellet was resuspended in Buffer 2 and centrifuged at 4000 x g for 15 minutes, 4 °C. The final pellet was resuspended in a small volume of Buffer 4.

Table 2.1| List of buffers used for the thylakoid preparation.

Buffers	Components
Buffer 1a	50 mM Tris pH 7.5 200 mM Sucrose 100 mM Sodium Chloride
Buffer 2a	10 mM Tricine pH 8 150 mM Sodium Chloride
Buffer 3a	10 mM Tricine pH 8 2M Sodium Bromide 300 mM Sucrose
Buffer 4a	30 mM Tris pH 7.5 5 mM Magnesium Chloride 5 mM Potassium Chloride 50 mM Sodium Chloride 1 mM Ethylenediaminetetraacetic acid

2.3.3 Thylakoid preparation for the purification of *cytb6f* at pH 6.5

Thylakoids were purified as stated in section 2.3.2, however Tris and Tricine were substituted with MES pH 6.5 at the same concentration.

2.3.4 Chlorophyll concentration

Chlorophyll concentrations were measured according to Porra et al., (1989). 4 ul of thylakoid sample was added to 2 ml of 80% (w/v) acetone. The solution was then vortexed and

centrifuged at 14 000 rpm for 3 minutes in a benchtop microcentrifuge to remove precipitates prior to spectrophotometric analysis. The absorption readings at 750 nm, 663 nm and 646 nm were taken on a Cary 60 UV-Vis Spectrophotometer (Agilent Technologies, USA). The total chlorophyll content ([Chl a] + [Chl b]) in mg ml⁻¹ were calculated using the following equations:

$$[Chl\ a] = 12.25\ A_{663}^* - 2.55\ A_{646}^*$$

$$[Chl\ b] = 20.31\ A_{646}^* - 4.91\ A_{663}^*$$

$$Chl\ a\ (A_{663}^*) = A_{663} - A_{750}$$

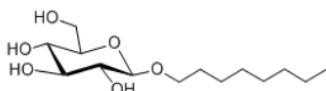
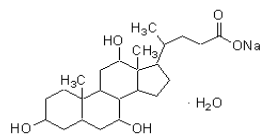
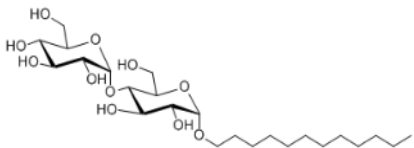
$$Chl\ b\ (A_{646}^*) = A_{646} - A_{750}$$

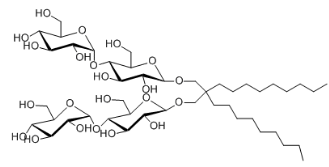
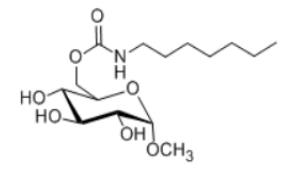
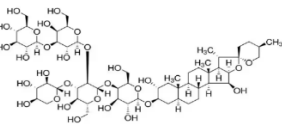
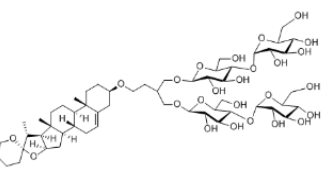
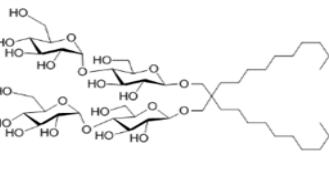
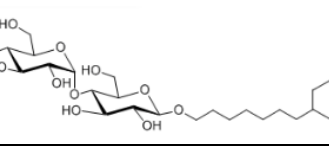
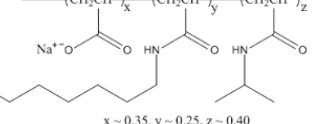
2.4 Cytochrome *b₆f* purification techniques

2.4.1 Solubilisation

All the detergents used to solubilise membranes in this study are outlined in Table 2.2. Solubilisation was carried out on freshly purified thylakoid membranes. Concentrations of the detergents and incubation time and temperature are described in the relevant results section.

Table 2.2| Outline of the detergents used in this study.

Detergent	Synonym	CMC (mM)	MW (g/mol)	Supplier	Molecular structure
n-Octyl-β-D-Glucopyranoside	OG	18-20	292.4	Anatrace	
Sodium Cholate	Cholic acid	14	448.57	Sigma-Aldrich	
n-Dodecyl-α-D-Maltopyranoside	αDDM	0.152	510.6	Anatrace	

Undecyl Maltose Neopentyl Glycol	UMNG	-	977.14	Anatrace	
6-O-(N-Heptylcarbamoyl)-Methyl- α -D-Glucopyranoside	HECAMEG	19.5	335.4	Anatrace	
Digitonin	Digitin	0.25	1229.3	Sigma-Aldrich	
Glyco-diosgenin	GDN	0.018	1165.31	Anatrace	
2,2-didecylpropane-1,3-bis- β -D-maltopyranoside	LMNG	0.01	1005.19	Anatrace	
7-Cyclohexyl-1-Heptyl- β -D-Maltoside	CYMAL 7	0.19	522.5	Anatrace	
Amphipol 8-35	A835	2	9000	Anatrace	

2.4.2 Ammonium sulfate precipitation

Solubilised thylakoids were ultracentrifuged at 227,220 x g for 40 minutes in a Beckman Ti50.2 rotor. The supernatant was collected and solid ammonium sulfate was added to reach 40% saturation. The ammonium sulfate saturation was calculated using the following equation:

$$\text{Weight(g)} = (G_{\text{sat}} (S_2 - S_1)) / (1 - (PS_2))$$

Where G_{sat} is the grams of $(\text{NH}_4)_2\text{SO}_4$ contained in 1 litre of saturated solution, in this case at 20°C G_{sat} is 536.49. S_2 and S_1 are the final and initial saturation of ammonium sulfate respectively. P is the specific volume of ammonium sulfate in a saturate solution multiplied per G_{sat} and divided per 1000 (Wingfield, 2016). Samples were then stirred at room

temperature for 20 minutes and then ultracentrifuged at 184,048 x g for 30 minutes to pellet and discard the precipitated proteins. The supernatant was then concentrated Amicon Ultra Centrifugal filter unit MWCO 100 kDa and loaded onto continuous sucrose gradients.

2.4.3 Protamine sulfate precipitation

Solubilised thylakoids were ultracentrifuged at 227,220 x g for 40 minutes in a Beckman Ti50.2 rotor to remove any unsolubilised material. A stock of 2mg/ml of protamine sulfate was prepared and added to the solubilised thylakoid sample to reach the final concentration of 0.02%. The samples were incubated on ice for 1 hour and then centrifuged for 10 minutes at 26,267 x g. The supernatant was then concentrated using Amicon Ultra Centrifugal filter unit MWCO 100 kDa and loaded onto sucrose gradients.

2.4.4 DTT oxidation and reduction

To obtain fully reduced DTT, 400 mM sodium borohydride (Sigma) was added to 200mM DTT solution and allowed to react for 1 hour on ice and swirled every 10 minutes. The reaction was then quenched with HCl to remove unreacted sodium borohydride and incubated for 30 minutes on ice. The pH of the solution was then adjusted to pH 7.6 with NaOH and further diluted to 50 mM DTT concentration. To obtain a fully oxidised DTT solution, 200mM DTT solution was exposed to air at room temperature for one week. The reduction and oxidation of the DTT solution was monitored by the disappearance or appearance of a 283nm signal in the absorption spectra respectively.

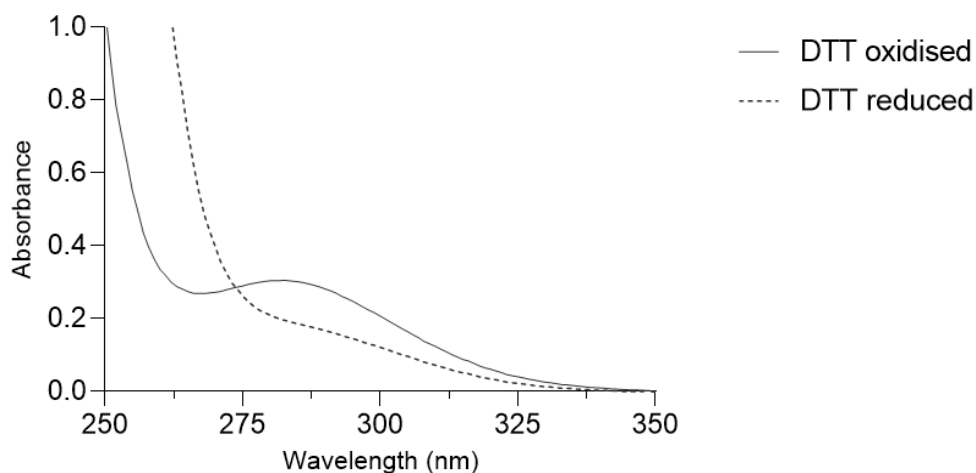


Figure 2.1 | Absorption spectra of DTT oxidised and reduced.

Fully oxidised DTT is characterised by a 283 nm signal in the absorption spectra. This signal disappears when DTT is instead fully reduced.

2.4.5 Sucrose gradients

Continuous sucrose gradients were prepared in SW41 or SW32 rotor tubes by freezing a solution of 0.65M sucrose, 20 mM HEPES (pH7.5) and 0.06% glycol-diosgenin (GDN), unless stated otherwise in the relevant results sections. The sucrose gradients were then left thawing slowly at 4°C. A sample volume of 0.5 to 1.5 ml was carefully loaded onto the gradients depending on their size. Gradients were then ultracentrifuged for 18 hours at 221,831 x g at 4°C when SW41 rotor was used, and for 21 hours at 174,587 x g at 4°C when SW32 rotor was used, unless stated otherwise. Bands were collected using a Gilson Minipuls 3 Peristaltic pump.

2.4.6 Ceramic Hydroxyapatite (CHT) Chromatography

Sample collected from sucrose gradients was loaded onto a 5ml Bio-scale Mini Type CHT 40 µm column (Bio-Rad). The column was equilibrated with 20 mM Tricine pH 8 and sample was loaded at a flow rate of 2 ml/min. The column was then washed with 25ml 100 mM ammonium phosphate pH 8 and eluted with 25ml 400 mM ammonium phosphate pH 8.

2.4.7 Size Exclusion Chromatography

Samples collected from sucrose gradients were concentrated using Amicon Ultra Centrifugal filter unit MWCO 100 kDa and then loaded onto a Superdex 200 Increase 10/300 GL (Cytiva) connected to an ÄKTA purification system (GE Healthcare Life Sciences). The column was equilibrated with 20mM HEPES (pH 7), 20mM NaCl. Details on the detergent chosen and its concentration is described in the relevant results section.

2.5 Biochemical analysis of purified proteins

2.5.1 Sodium Dodecyl Sulfate PAGE

Purified protein samples were mixed with NuPAGE® LDS sample buffer 4x loading dye (Thermo Fisher) or Laemmli buffer 2x (Bio-Rad). 10 µl of Precision Plus Protein Unstained Standards (Bio-Rad) was loaded into a well in every gel. The sample was then loaded into pre-cast Novex™ 12% Bis-Tris polyacrylamide gels (Thermo Fisher) and run in MES SDS running buffer at 180V for 45 minutes to 1 hour. To separate well low molecular weight proteins, as PGR5, Novex™ 10 to 20% Tricine gel (Thermo Fisher) were chosen and were run in Tricine SDS running buffer at 120V for 1 hour.

Gels were then stained in Coomassie Brilliant Blue G-250 for 20 minutes and then destained in milliQ water overnight. Gels were imaged using an Amersham™ Imager 600 (GE Healthcare).

2.5.2 Blue Native PAGE

Purified protein samples were incubated with loading mix containing 125mM Tris pH 6.8, 30% (v/v) glycerol, 0.01% (w/v) bromophenol blue. Samples were then loaded on pre-cast NativePAGE™ 3-12% polyacrylamide Bis-Tris gels (Thermo Fisher) and were run at 160 V for 120 minutes in NativePAGE™ running buffer. 2ml of Coomassie Brilliant Blue G-250 was added into the Cathode buffer prior running.

Gels were stained in Coomassie Brilliant Blue G-250 and then destained in milliQ water overnight. Gels were imaged using an Amersham™ Imager 600 (GE Healthcare).

2.5.3 Immunoblotting

SDS-PAGE was carried out as described in section 2.5.1, however Precision Plus Proteins™ Prestained Standards Dual colour (Bio-Rad) was used. Blue Native PAGE or SDS PAGE gels were not stained and proteins were transferred onto polyvinylidene difluoride (PVDF) membranes, 0.2µm pore size using a Power Blotter System (Invitrogen) by semi-dry transfer. PVDF membranes activated for 1 minute in methanol and then incubated in Power Blotter 1-Step™ transfer buffer. For transfer of proteins between 25kDa to 150kDa from SDS PAGE, the western blot was performed at 1.3 Amps for 7 minutes, whereas for proteins smaller than 25kDa the transfer was performed for 5 minutes.

Following the proteins transfer, membranes were blocked in Blocking buffer (50mM Tris pH 7.6, 150 mM Sodium Chloride, 0.2% (w/v) tween 20, 5% (w/v) skimmed milk powder) for 1 hour at RT. The membranes were then washed in Antibody buffer (50mM Tris pH 7.6, 150 mM Sodium Chloride, 0.05% (w/v) tween 20) and incubated in antibody buffer containing the appropriate primary antibody overnight at 4 °C with gentle agitation. Membranes were then washed three times for 5 minutes with antibody buffer and then incubated with the secondary antibody diluted in antibody buffer for 1 hour with gentle agitation. If the secondary antibody used was conjugated to horse radish peroxidase (HRP), membranes were washed three times for 5 minutes in antibody buffer before incubation in WESTAR SUN chemiluminescence reagents (Cyanagen) for 5 minutes. Membranes were then imaged using

Amersham™ Imager 600 (GE Healthcare) in chemiluminescence mode. If the secondary antibody used was conjugated to a fluorescent dye (Alexa Fluor™ 488, Thermo Fisher) the membrane was washed in milliQ water and imaged in fluorescence mode using Amersham™ Imager 600 (GE Healthcare).

2.5.4 Absorbance spectroscopy

UV/Vis absorbance spectra were recorded using a Cary60 spectrophotometer (Agilent) at room temperature. Redox-difference spectra were obtained by first fully oxidising the redox active groups with a few grains of potassium ferricyanide. Then, a few grains of sodium D-isoascorbate monohydrate to reduce *c*-type haem *f* and a few grains of dithionite to fully reduce *c*-type haem *f* and *b*-type haems *b_n* and *b_p*.

2.6 Cross-linking

Disuccinimidyl suberate (DSS) was used for the crosslinking of *cytb_{6f}* samples. Final concentration of 1mM DSS was added to 5 μM *cytb_{6f}* in 25mM sodium phosphate buffer pH 7.4. The sample was incubated at 22 °C for 45 minutes and the reaction was then quenched with 50mM Tris pH 7.4.

2.7 Mass spectrometry and protein identification

Mass spectrometry was performed by Dr Phil Jackson.

2.7.1 Thylakoid membrane protein extraction and proteolytic digestion

Proteins were extracted from 100 μL of the LMNG-solubilised DSS-crosslinked *cytb_{6f}* complex by precipitation using a 2-D clean-up kit (Cytiva) according to the manufacturer's instructions and recovered by centrifugation at 15,700 x *g* for 10 min. The pellet was redissolved in 10 μL 8 M urea, 100 mM Tris-HCl pH 8.5 (freshly prepared) and protein concentration estimated by Nanodrop. A volume containing 50 μg protein was adjusted to 10 μL and, after adding 1 μL 100 mM tris(2-carboxyethyl) phosphine-HCl, incubated at 37°C for 30 min to reduce any disulphide bonds. Cysteine thiol groups were converted to dithiomethane to prevent subsequent disulphide bond formation by the addition of 1 μL 200 mM S-methyl methanethiosulphonate in 100 mM Tris-HCl pH 8.5 and incubation at room temperature for 10min.

Proteins were digested according to Hitchcock *et al.*, 2016 with 2 µg pre-mixed trypsin/endoproteinase Lys-C (Promega) for 2 h at 37°C, followed by dilution with 75 µL 50 mM Tris-HCl pH 8.5, 10 mM CaCl₂ and the incubation at 37°C continued for a further 16 h. The digest was cooled on ice and 5 µL 10% trifluoroacetic acid (TFA) then added to stop proteolysis. The peptides were desalted using a C18 spin column (Thermo Fisher Scientific) according to the manufacturer's protocol and dried by vacuum centrifugation before storage at -20°C.

2.7.2 Analysis by mass spectrometry and protein identification

Analysis by nano-LC-MS/MS was performed according to Flannery *et al.* 2021 with minor modifications. The dried peptides were dissolved in 0.5% TFA, 3% acetonitrile and 400 ng was analysed in triplicate by injection onto an EASY-Spray PepMap RSLC C18 column (Thermo Fisher Scientific, 50 cm x 75 µm ID, 2 µm particle diameter at 40°C). Separation was achieved using the following gradient profile delivered at 300 nL min by a Dionex RSLCnano chromatography system (Thermo Fisher Scientific): 97% solvent A (0.1% formic acid in water) to 10% solvent B (0.08% formic acid in 80% acetonitrile) over 5 min, then 10% to 50% solvent B over 3 h. The nanoLC was directly coupled to a Q Exactive HF hybrid quadrupole-Orbitrap mass spectrometer (Thermo Fisher Scientific) programmed for data-dependent acquisition with centroid full MS scans at 120,000 resolution and a maximum of ten centroid product ion scans at 30,000 resolution per cycle.

Protein and crosslink identification were performed by searching the peptide mass spectra against multiple edited versions (see below) of the *Spinacia oleracea* reference proteome database (www.uniprot.org/proteomes/UP000054095) downloaded on 6 February 2023 using Byonic (v. 2.3.17, Protein Metrics). All parameters were as per default except that fixed and variable modifications were set to methylthio-Cys and Met sulphoxide respectively and the crosslink option was set to DSS with FASTA proteins specified as '1,2,3'. Accordingly, a series of reference proteome database versions was created with selected crosslink target proteins moved to the top three positions. This approach of dividing the crosslink target proteins into groups of three and performing multiple searches was employed to manage potential computer processing limitations that would be exceeded by selecting a greater number of potential crosslink target proteins in a single search.

2.7.3 In-gel proteolytic digestion and protein identification

After staining with Coomassie Blue, protein bands were excised and subjected to in-gel proteolytic digestion according to Pandey, Andersen and Mann, 2000 except that reduction, thiol derivatization and digestion were carried out with the reagents and proteases specified above.

Analysis by nanoLC-MS was performed as described above except that the gradient from 10% to 50% solvent B was delivered over 75 min. Protein identification by database searching was as described above.

2.8 Negative stain transmission electron microscopy (TEM)

2.8.1 Grid preparation and negative staining

Carbon-coated 400 mesh Cu grids (Agar Scientific, UK) were subjected to glow discharge for 30 seconds using a Cressington Carbon Coater. 5 μ l of purified protein samples were diluted to a suitable concentration with appropriate buffer and applied to the grids and incubated for 1 min. Grids were then blotted with filter paper (Whatman No. 1) to remove excess protein sample then washed and blotted with 10 μ l milliQ. This step was repeated twice, and grids were blotted with 10 μ l 0.75 % (w/v) uranyl formate stain. Subsequently, grids were incubated in the same stain for 45 seconds, blotted and stored in the dark.

2.8.2 Imaging

The grids were imaged at room temperature using a Philips CM100 Transmission Electron Microscope (TEM) operating at 80 kV. Images were recorded at between 25,800 and 73,000 X nominal magnification and defocus value between 500-1,200 nm on a Gatan Multiscan 794 1K x 1K CCD.

2.9 Single particle Cryo-TEM

2.9.1 Single particle Cryo-TEM of sample purified in LMNG

Sample was normalised to 14 μ M, and 5 μ l was applied to a Quantifoil 1.2/1.3 400 mesh Cu grid (EM Resolutions Ltd.) which has been plasma-treated for 25 seconds. Following a 15

second incubation and a 5 second blot, the sample was vitrified in liquid ethane at -178 °C using an EM GP plunge freezer (Leica).

52,701 movies were collected on a Titan Krios (Thermo Fisher Scientific Inc.) operating at 300 kV in AFIS mode, equipped with a K3 direct electron detector (operating in super-resolution mode) and energy filter set to 20 eV (Gatan, Inc.). The nominal magnification was 130,000 X, yielding a calibrated pixel size of 0.653 Å and a final dose of 1 electron/ Å²/frame. Movies were collected at defocus values of -0.8 um to -2.3 um, iterating in steps of 0.3 um.

Following motion corrected (UCSF MotionCor2) and CTF estimation (CTFFIND4), a model for particle picking was trained in crYOLO using approximately 2,000 manually picked candidates from a subset of 10 corrected micrographs. This model was used to pick 2,811,993 candidates from the entire dataset, which were classified into 300 2D classes using unsupervised 2D classification in RELION 3.1.

2.9.2 Single particle Cryo-TEM of sample purified in GDN

Sample was normalised to 14 uM, and 5 ul was applied to a Quantifoil 1.2/1.3 300 mesh Cu grid (EM Resolutions Ltd.) which has been plasma-treated for 15 seconds. Following a 5 second incubation and a 3 second blot, the sample was vitrified in liquid ethane at -178 °C using an EM GP plunge freezer (Leica).

19,869 movies were collected on a Titan Krios (Thermo Fisher Scientific Inc.) operating at 300 kV in AFIS mode, equipped with a Falcon IV direct electron detector and Selectris X energy filter set to 10 eV (Thermo Fisher Scientific Inc.). The nominal magnification was 215,000 X, yielding a calibrated pixel size of 0.576 Å and a final dose of 1 electron/ Å²/frame. Movies were collected at defocus values of -0.8 um to -2.4 um, iterating in steps of 0.4 um.

Following motion corrected (UCSF MotionCor2) and CTF estimation (CTFFIND4), a model for particle picking was trained in crYOLO using approximately 2,000 manually picked candidates from a subset of 10 corrected micrographs. This model was used to pick 842,466 candidates from the entire dataset, which were classified into 300 2D classes using unsupervised 2D classification in RELION 4.0.

2.9.3 Single particle Cryo-TEM of sample purified in A8-35

Sample was normalised to 14 μM , and 4 μl was applied to a Quantifoil 1.2/1.3 400 mesh Cu grid (EM Resolutions Ltd.) which has been plasma-treated for 12 seconds. Following a 10 second incubation and a 3 second blot, the sample was vitrified in liquid ethane at -178°C using an EM GP plunge freezer (Leica).

15,525 movies were collected on a Titan Krios (Thermo Fisher Scientific Inc.) operating at 300 kV in AFIS mode, equipped with a K3 direct electron detector (operating in super-resolution mode) and energy filter set to 20 eV (Gatan, Inc.). The nominal magnification was 130,000 X, yielding a calibrated pixel size of 0.645 \AA and a final dose of 1 electron/ $\text{\AA}^2/\text{frame}$. Movies were collected at defocus values iterating through -0.8 μm , -1.0 μm , -1.2 μm , -1.5 μm , -1.8 μm , -2.0 μm , -2.2 μm , -2.5 μm .

Following motion corrected (UCSF MotionCor2) and CTF estimation (CTFFIND4), a model for particle picking was trained in Topaz using approximately 2,000 manually picked candidates from a subset of 8 corrected micrographs. This model was used to pick 1,919,959 candidates from the entire dataset, which were classified in 2D and 3D, following which a refined map was resolved to a nominal resolution of 4.2 \AA with a final selection of 156,000 particles. All processing after particle selection was carried out in RELION 4.0.

2.9.4 Single particle Cryo-TEM of DSS cross-linked sample in GDN

Sample was normalised to 14 μM , and 5 μl was applied to a Quantifoil 1.2/1.3 400 mesh Cu grid (EM Resolutions Ltd.) which has been plasma-treated for 25 seconds. Following a 15 second incubation and a 5 second blot, the sample was vitrified in liquid ethane at -178°C using an EM GP plunge freezer (Leica).

56,795 movies were collected on a Titan Krios (Thermo Fisher Scientific Inc.) operating at 300 kV in AFIS mode, equipped with a K3 direct electron detector (operating in super-resolution mode) and energy filter set to 20 eV (Gatan, Inc.). The nominal magnification was 130,000 X, yielding a calibrated pixel size of 0.651 \AA and a final dose of 1 electron/ $\text{\AA}^2/\text{frame}$. Movies were collected at defocus values of -0.8 μm to -2.4 μm , iterating in steps of 0.4 μm .

Following motion corrected (UCSF MotionCor2) and CTF estimation (CTFFIND4), a model for particle picking was trained in crYOLO using approximately 2,000 manually picked candidates

from a subset of 10 corrected micrographs. This model was used to pick 3,216,452 candidates from the entire dataset, which were classified into 300 2D classes using unsupervised 2D classification in RELION 4.0.

2.10 Purification of PetP and pull-down

Cloning and overexpression of the protein PetP was carried out by Dr M. Proctor.

2.10.1 Overexpression and purification of PetP

The *Synechocystis* petP gene (ssr2998) was codon optimized for expression in *Escherichia coli* and cloned into the NdeI and XhoI sites of pET28a(+) (Novagen). Production of N-terminally hexa-Histidine (His)-tagged PetP (His-PetP) was performed in *E. coli* BL21(DE3) (ThermoFisher Scientific). To initiate expression, a 5 ml LB starter culture was added to 1 L autoinduction media (Formedium) at 37°C with 220 rpm shaking until it reached an optical density (OD) at 600 nm of 0.6. The temperature was lowered to 18°C and the culture was incubated for further 16 hours. The cells were harvested by centrifugation at 4696×g for 15 min at 4°C and resuspended in buffer E (25 mM sodium phosphate pH 7, 10 mM MgCl₂, 300 mM NaCl). DNase I (Sigma–Aldrich) and a cOmplete EDTA-free protease inhibitor tablet (Roche) were added before breakage by two passes through French pressure cell at 18,000 psi. The cell lysate was centrifuged at 75,600×g for 30 min at 4°C and imidazole was added to a final concentration of 10 mM before application to a 5 ml HisTrap column (GE Healthcare) pre-equilibrated in buffer E. The column was washed with 10 volumes of buffer E supplemented with 10, 20 or 50 mM imidazole prior to elution of His-PetP with 400 mM imidazole. The eluate containing PetP was concentrated to 2.5 ml using a 3 kDa MWCO protein spin concentrator (Amicon) and buffer exchanged into buffer D (25 mM sodium phosphate pH 7.6, 10 mM MgCl₂, 150 mM NaCl, 0.02% (w/v) GDN) using a PD-10 Desalting column (GE Healthcare).

2.10.2 PetP pull-down

His-PetP was re-bound to a 300 ml Ni²⁺-NTA agarose immobilized metal affinity chromatography (IMAC) column (Qiagen) and washed with 5 ml buffer D. Spinach thylakoid purified as described in section 2.3.2 were solubilised at 2mg/ml in 2% GDN for 1 hour at 4°C. Unsolubilised material was pelleted and the supernatant was applied to columns with and without PetP, as negative control. After washing the column with 10 ml of buffer D, a

significant amount of *cytb_{6f}* was retained by the column and co-eluted with PetP in buffer D supplemented with 100 mM L -Histidine (Sigma–Aldrich).

The purified FNR-*cytb_{6f}* complex was also loaded onto the column and washed with 10 ml of buffer D. The wash was collected and a small amount of *cytb_{6f}* was retained by the column and co-eluted with PetP in buffer D supplemented with 100 mM L -Histidine (Sigma–Aldrich).

2.11 Purification of PGR5 and pull-down

Cloning and overexpression of the protein PGR5 was carried out by Dr M. Proctor.

2.11.1 SUMO-PGR5-ApoA1 purification

pET28a::His₁₀SUMO-PGR5-Strep-3C-ApoA1-His₁₀ was transformed into BL21 (DE3) cells and selected on Kan 30 mg/ml LB plates. Two colonies were selected and grown in 2x 10 mL LB overnight at 37°C. This was used to inoculate 2 L of autoinduction media and incubated at 37°C, 300 rpm of shaking until the OD₆₀₀ reached 0.6 at which point the temperature was lowered to 18 C for overnight incubation. Cells were harvested the following morning by centrifugation at 7000 x g, 10 mins and cell pellets were resuspended in 25 mM Tris-HCl, pH 7.4, 0.15M NaCl with 1 tablet of EDTA-free protease inhibitors and DNase prior to cooling on ice and cell breakage by 2x passes through a French press at 18000 psi. The cells lysate was centrifuged at 48,400xg for 30 mins and the supernatant filtered through a 0.2 µm unit. 10 mM imidazole was added to the supernatant and then it was applied to a 4 mL Ni IMAC column twice. The column was then washed with 50 mL buffer +10, 20 and 50 mM imidazole each before elution in 400 mM imidazole. The sample was buffer exchanged into 25 mM Tris-HCl, pH 7.4, 0.15M NaCl, 1 mM DTT and 0.02% βDDM by PD10 column.

2.11.2 Purification of SUMO and 3C proteases

pET28a::Ulp (SUMO protease) and pET28a:: IM9-H3C (3C protease) plasmids were transformed into BL21 (DE3) cells. A colony from each plate was selected and grown in 10 mL LB overnight and used the next day to inoculate 2x 500 mL baffled flasks with LB (1 L final per protease). The cells were grown at 37°C with 300 rpm shaking. The cells were induced with 1mM IPTG until the OD₆₀₀ reached 0.6 at which point the temperature was lowered to 30°C overnight. The cells were harvested the following day and resuspended in 25 mM Tris-HCl, pH

7.4, 0.15M NaCl. DNase was added. The cells were broken by 1x pass through French press at 18000 psi and the cell lysate was centrifuged at 48,400 × g. The supernatant was filtered through a 0.2 μm filter units. 0.3M NaCl and 10mM imidazole were added to the supernatant and poured down to 3 mL His columns. The column was then washed with 50 mL of 25 mM Tris-HCl, pH 7.4, 0.15M NaCl. The column was then washed with the same buffer supplemented with 10mM, 20 mM, 50 mM imidazole subsequentially before eluting with 400 mM imidazole. The eluted sample was then pelleted and the supernatant was retained. A portion of the eluate was buffer exchanged using a PD10 column (GE Healthcare) into 0.15M NaCl, 25 mM Tris-HCl, pH 7.4. The sample was pelleted and supernatant was retained. The sample was buffer exchanged by PD10 columns (GE Healthcare) into 50 mM Tris-HCl pH8, 0.3 M NaCl, 1 mM EDTA and 1 mM DTT. Glycerol was added to a final concentration of 50% and the protein was frozen in aliquots of 100 μL before storage at -80°C.

2.11.3 Digestion

His₁₀-SUMO-PGR5-Strep-3C-ApoA1-His₁₀ protein was incubated with 1/10th concentration of SUMO and 3C protease overnight at 4°C with rotation. The next morning the PGR5 digest mixture was re-applied to the Ni IMAC column and the Flow through collected. His₁₀-SUMO and 3C-ApoA1-His₁₀, which had been cleaved from the PGR5-Strep, bound to the column whereas the PGR5-Strep passed through the column.

2.11.4 PGR5 Pull-down

Spinach thylakoids were prepared as described previously. GDN was added to the sample to a final concentration of 0.8% at 1 mg/ml Chl. The sample was incubated for 1 hour at 4° C with rotation before being centrifuged at 48,400 × g for 10 mins to pellet insoluble debris. The sample was filtered through a 0.2 μm syringe filter unit and diluted 2-fold in buffer TM (10 mM Sodium Phosphate pH 7.4, 5 mM MgCl, 10 mM NaCl, 10 mM NaF, 200 mM sucrose). The sample was then split in half into 2x 50 mL dark falcon tubes. SpPGR5 was buffer exchanged into this buffer by PD10 column and passed through a 400 μL StrepTrap 2x. The FT from this column was added to one of the falcon tubes along with strep resin. 400 μL of strep resin that had not been incubated with PGR5 was added to the second falcon as a negative control. The samples were incubated overnight at 4° C with rotation.

The following morning the resin was collected and washed with 10 mL Spinach TM buffer +0.02% GDN. The +PGR5 column was visibly green-brown and while the -PGR5 column returned to white. Both resins were washed again in Syn TM buffer (25 mM Sodium Phosphate pH7.4, 10 mM MgCl, 20 mM NaCl, 0.02% GDN) and eluted in the same buffer + 50 mM biotin. Both elates were concentrated in 3000 MWCO spin concentrators.

2.12 Activity assays

The assay was performed in 20 mM HEPES pH 7, 50 mM NaCl, 10 mM KCl, 2mM MgCl₂ buffer (Huang et al., 1994) in 1 ml quartz cuvette on FluoroLog FL3-22 spectrofluorometer. 200 μM decyl-plastoquinone (dPQ) was prepared in 0.15% asolectin/CHAPS, followed by the addition *cytb₆f* or *cytb₆f* supercomplex. Where indicated Fd was added at an equimolar concentration to *cytb₆f* (10 μM). NADPH was added to the measurements at a final concentration of 200 μM. Decyl-plastoquinol (dPQH₂) formation was monitored using excitation 290 nm (5 nm slit width) and emission at 330 nm (5 nm slit width). After data was collected 5 ml of ethyl acetate was added to the sample and vortexed. It was immediately dried under nitrogen gas followed by resuspension in 200 μl of ethanol, followed by centrifugation at 21,000g. 10 μl of sample was loaded onto a Fortis 5 μM UniverSil C18 HPLC column (150 x 10 mm) in 3:1 acetonitrile:ethanol at 0.75 ml/min. The percentage of reduced dPQH₂ in the sample was determined from the area of the corresponding peaks in the chromatograms to the same sample fully reduced by addition of 1 μl NaBH₄. dPQ and dPQH₂ standards were used to determine the elution volumes of the peaks, and concentrations were determined using $\epsilon_{255} = 17.94 \text{ mM}^{-1} \text{ cm}^{-1}$ for PQ and $\epsilon_{290} = 3.39 \text{ mM}^{-1} \text{ cm}^{-1}$ for PQH₂ both in absolute ethanol (Kruk & Karpinski, 2006). The extinction coefficient for PQH₂ used for the calculation of the rate of PQ reduction is $2.7116 \text{ mM}^{-1} \text{ cm}^{-1}$ (determined by Katherine Richardson). Rate of PQ reduction was calculated by dividing the change in counts in the first 60 seconds of the measurement by the extinction coefficient and then adjusted to the concentration of *cytb₆f* or *cytb₆f* supercomplex (2.8 μg).

2.13 Chlorophyll fluorescence

2.13.1 Plant material

Table 2.3 | Plant material

Strain	Description
Col-0	Columbia ecotype
<i>fnr1</i>	T-DNA insertion in exon in AT5G66190
<i>ndho</i>	T-DNA insertion in intron in AT1G74880
<i>pgr5</i>	point mutation in AT2G05620
<i>pgr5 ndho</i>	double mutant generated by crossing <i>pgr5</i> with <i>ndho</i>

Arabidopsis plants were grown in a controlled-environment chamber for 6 weeks with day/night temperatures 21/15°C, 60% rel. humidity with 8-hour photoperiod and light intensity 200 $\mu\text{mol m}^{-2} \text{s}^{-1}$.

2.13.2 Chlorophyll fluorescence

Chlorophyll fluorescence yield and redox changes of Pc, P700 and Fd were measured using Dual PAM/KLAS NIR spectrophotometer (Heinz Walz GmbH, Effeltrich, Germany). This system allows the measurement of four dual-wavelength difference signals in the near-infrared (NIR) of the spectrum; the redox changes of Fd, P700 and Pc are deconvoluted from the difference signals measured at the wavelengths pairs 785 - 840 nm, 810 - 870 nm, 870 - 970 nm respectively; an additional wavelength pair is also used, 795 - 970 nm, and it covers all the differential changes of all components. Arabidopsis plants were dark-adapted for 1 hour and NIR measuring beans were zeroed and calibrated. For each Arabidopsis genotype, a differential model plot was generated according to the manufacturer's protocol and used for spectral deconvolution of the signals for P700, PC and Fd. Maximum reduction of Fd and oxidation of P700 and Pc were measured before each measurement by using the NIRmax routine, consisting of 3 s pulse illumination with actinic light, 30 ms of MT (multiple turnover flash) leading to the reduction of Fd, followed by 4 s of darkness and 10 s of FR light (255 $\mu\text{mol photons m}^{-2} \text{s}^{-1}$) and a MT pulse to achieve fully oxidation of P700 and Pc. NIRmax signals were normalised by using the "Get Max Values" option. Dark fluorescence yield (F_0) of PSII in the

dark state and maximum fluorescence (F_m) were determined at the beginning of each measurement. Red actinic light and far-red light intensities are specified in the relative results section. Saturation pulses were applied during the measurements to allow the assessment of plastoquinone pool reduction ($1-qP$), non-photochemical quenching (NPQ), PSII and PSI quantum yields and related photosynthetic parameters. These parameters were calculated as follows: $qP = (F_m' - F_s) / (F_m' - F_o')$, $NPQ = (F_m - F_m') / F_m'$, $Y(II) = (F_m' - F_s) / F_m'$, $Y(I) = (P_m' - P) / P_m$, $Y(NA) = (P_m - P_m') / P_m$, $Y(ND) = (P - P_o) / P_m$. F_s is the steady fluorescence and F_m' is the maximum fluorescence levels during actinic light illumination. CET determination in each Arabidopsis genotype was assessed by observing the rate of P700 oxidation during the NIRmax routine; half-time of P700 oxidation was determined by fitting an allosteric sigmoidal function (Graphpad Prism, 9.1.1).

2.13.3 Electrochromic shift measurements

Electrochromic shift was measured using P515/535 emitter/detector module of the Dual-PAM (Pulse-Amplitude-Modulation) system (Heinz Walz GmbH, Effeltrich, Germany). Arabidopsis plants were dark adapted for at least 1 hour prior measurements. Continuous illumination of dark-adapted leaves causes absorbance changes in the green region of the spectra, 500-550 nm. Proton translocation across the thylakoid membrane leads to changes in the electric field and causes electrochromic shift of absorption of various pigments at 515-520 nm. Measurements of the proton motive force (pmf), proton flux (νH^+) and proton conductivity (gH^+) were made following the dark interval relaxation kinetics (DIRK) analysis. Pmf was calculated by fitting a single exponential decay to the first 300 ms of the dark interval to determine the amplitude of the span of the decay (ECS_t) and normalised by dividing it by the 50 μ s ST flash. Proton conductivity (gH^+) was calculated as $1/\tau \times 1000$ and proton flux (νH^+) was calculated multiplying pmf per gH^+ .

3. Purification of the FNR-cyt_{b₆f} supercomplex

3.1 Introduction

Despite the fact that the antimycin A-sensitive cyclic electron transport in plants was discovered nearly 70 years ago (Whatley et al., 1955), the identity of the ferredoxin plastoquinone reductase (FQR) complex remains unclear. Early studies on CET activity in chloroplasts found it was inhibited by disulfodisalicylidene propane-1,1-diamine (sulfo-DSPD) an inhibitor of FNR (Shahak et al., 1981). The finding that FNR could be co-purified with cytochrome *b₆f* in spinach led to the suggestion that interaction between the two complexes may facilitate FQR activity (Clark *et al.*, 1984, Zhang *et al.*, 2001). In these preparations, cytb₆f was isolated according to a method developed by Hurt and Hauska in 1981. In this procedure, 2M of the chaotropic agent NaBr was added to wash buffers during the thylakoid purification to facilitate the removal of the head domain (CF₁) of ATP synthase and other peripheral membrane proteins which otherwise contaminated the preparation of cytb₆f (Kamienietzky & Nelson, 1975). A mixture of octyl-β-D-glucopyranoside (OG) and sodium cholate was used for a selective purification of cytb₆f from the NaBr washed thylakoids. Ammonium sulphate was then used to precipitate more contaminating proteins and then cytb₆f was separated using propyl-agarose column, a form of hydrophobic interaction chromatography (HIC). Cytb₆f was further separated from other photosynthetic complexes by sucrose density gradient (SDG) ultracentrifugation. Using this approach FNR was present in the final purified sample at stoichiometric level to cytochrome *f* subunit.

Dietrich and Kühlbrandt in 1999, used a modified purification method to obtain specific enrichment of cytb₆f from spinach. In this method, the OG/sodium cholate solubilisation step was instead performed by the detergent HECAMEG and sucrose density ultracentrifugation step was replaced by Ceramic hydroxyapatite (CHT) chromatography. Biomolecules interact with the hydroxyapatite (Ca₁₀(PO₄)₆(OH)₂) matrix in multiple ways, as cation exchange (amine groups interacting with negatively charged phosphate groups), metal affinity (carboxyl groups interacting with positively charged calcium ions) or electrostatic repulsion. Typically, proteins

bind to the column in phosphate buffer with low ionic strength and then are eluted by altering the ionic conditions.

Recently, *cytb_{6f}* prepared by Malone et al., (2019), using a modification of the method of Dietrich and Kuhlbrandt (1999) involving detergent exchange from HECAMEG to 4-trans-(4-trans-propylcyclohexyl)-cyclohexyl α -maltoside (tPCC α M) to increase complex stability, was also devoid of FNR. The data suggested that FNR was lost at the stage of the CHT chromatography step due to the high affinity of FNR for the matrix, similarly a high affinity of FNR for HIC matrix has been described (Sarewicz et al., 2023; Zakharov et al., 2020). These results have cast doubt on whether FNR is a true interactor of *cytb_{6f}* and led to the suggestion that it may instead represent a contaminant (Sarewicz et al., 2023; Zakharov et al., 2020). Similarly, reports of FNR association with a *cytb_{6f}*-PSI supercomplex in *Chlamydomonas* (Iwai et al., 2010; Takahashi et al., 2013) have proved difficult to recapitulate (Buchert et al., 2018).

It was reasoned that a high-resolution structure of the FNR-*cytb_{6f}* complex could provide further insight into the nature of the association, while an improved preparation could also allow its relevance to CET to be functionally tested. In this chapter, several methods for the purification of the FNR-*cytb_{6f}* complex have been tested. Starting from the original Hurt and Hauska method to the development of a new purification procedure, involving LMNG solubilisation and preservation in amphipols.

3.2 Initial purification of *cytb₆f* and FNR

Initial attempts to purify the FNR-*cytb₆f* supercomplex focused on the broad approach of Clark et al., 1984, with the modification that following solubilisation in OG/ sodium cholate samples were then exchanged into glyco-diosgenin (GDN) on the SDGs. This modification was used since GDN has been previously shown to better preserve the native dimeric structure of *cytb₆f* (Mayneord et al., 2019). Thylakoid membranes were purified as described in section 2.3.2; this protocol included a wash step in which buffers contained the chaotropic agent NaBr for the removal of peripheral membrane associated proteins and the F₁ portion of ATP synthase (HURT & HAUSKA, 1981). Briefly, thylakoid membranes were solubilised at 2mg/ml of Chl with a mix of 0.82% OG and 0.2% sodium cholate for 20 minutes at RT and then ultracentrifuged. Solid ammonium sulphate was then added to the supernatant until 35% salt saturation was reached. The sample was stirred for 20 minutes at RT and then ultracentrifuged. The supernatant was then concentrated and loaded on continuous sucrose gradients and further ultracentrifuged (section 2.4.5).

The resultant SDG is illustrated in figure 3.1A. Two main fractions indicated by the arrows were harvested and further analysed by SDS-PAGE (Figure 3.1B). Both samples showed typical *cytb₆f* banding pattern of the main four subunits: *cytf* (31kDa), *cytb₆* (24kDa) and Rieske Iron Sulfur Protein (ISP) (20kDa) (which resolve as a single broad band) and Subunit IV (17kDa). To confirm the presence of the complex, a western blot was performed using anti-Rieske ISP antibody (Figure 3.1C). In addition to these *cytb₆f* related bands a number of other potential contaminant proteins were observed in the preparation including bands at ~60kDa consistent with α and β subunits of ATP synthase and/or PsaA/B of PSI and CP43/47 (~43-47kDa) and D1/D2 (~30 kDa) of PSII (Figure 3.1B). In contrast, only a sub-stoichiometric amount of FNR at ~37 kDa was observed. To verify the oligomeric state of the isolated complexes, both samples were further analysed by BN-PAGE (Figure 3.1D). Fraction 2 contained a mixture of high molecular weight complexes at ~480 kDa, including a band at ~220kDa corresponding to dimeric *cytb₆f*. Whereas fraction 1 was dominated by a lower molecular weight band at ~100kDa, corresponding to monomerised *cytb₆f*.

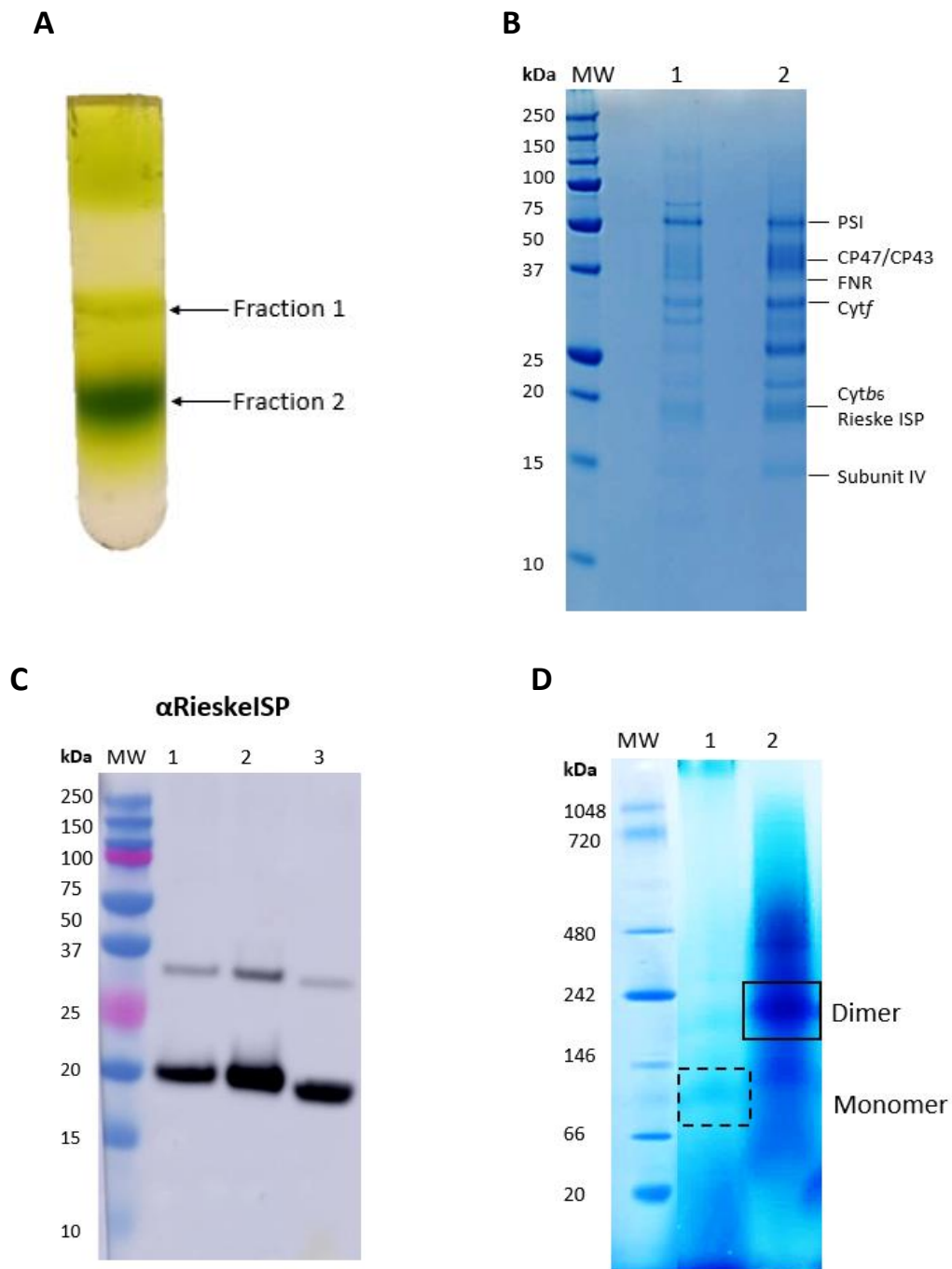


Figure 3.1 | Initial purification of *cytb₆f*.

(A) Sucrose gradient of the supernatant following 35% ammonium sulphate precipitation. The two fractions indicated by the arrows were harvested. (B) SDS PAGE analysis of the two samples collected from the sucrose gradient. Lanes: MW) ladder, 1) fraction 1 collected from the gradient, 2) fraction 2 collected from the gradient. (C) Western blot of the SDS PAGE using a Rieske ISP antibody, showing the presence of *cytb₆f* in both bands. Lanes: MW) ladder, 1) fraction 1, 2) fraction 2, 3) spinach thylakoid membrane (positive control). (D) Blue Native page of the samples harvested. Lanes: MW) ladder 1) fraction 1, 2) fraction 2. *cytb₆f* harvested from the top fraction is monomeric, while from the bottom fraction is dimeric.

3.3 Optimisation of ammonium sulphate concentration

Following the previous experiment, we tested whether a different ammonium sulphate concentration would increase the precipitation of the putative contaminating proteins. The thylakoid solubilisation step was carried out as previously described and the concentration of ammonium sulphate was varied from 30% to 45%. The samples were then ultracentrifuged, and absorption spectra of the supernatant were taken (Figure 3.2A). The amount of *cytb₆f* in the sample was measured by observing the ratio between the absorbance signal at 421nm (Soret band of haems) and 668nm (Q_y absorption band of Chl*a*)(Figure 3.2B), and the purity of *cytb₆f* was assessed by measuring the ratio of 421nm and 440nm (chlorophyll signal from other photosynthetic complexes) (Figure 3.2C)(Dietrich & Kühlbrandt, 1999). The results showed that the ratio of *cytb₆f* relative to the putative contaminants does not change significantly when varying the ammonium sulphate concentration. However, when the sample was saturated with 45% ammonium sulphate, the purity of *cytb₆f* appeared to slightly decrease, which could be related to destabilisation of the complex in excess salt. Therefore, 40% ammonium sulphate saturation was selected for further study.

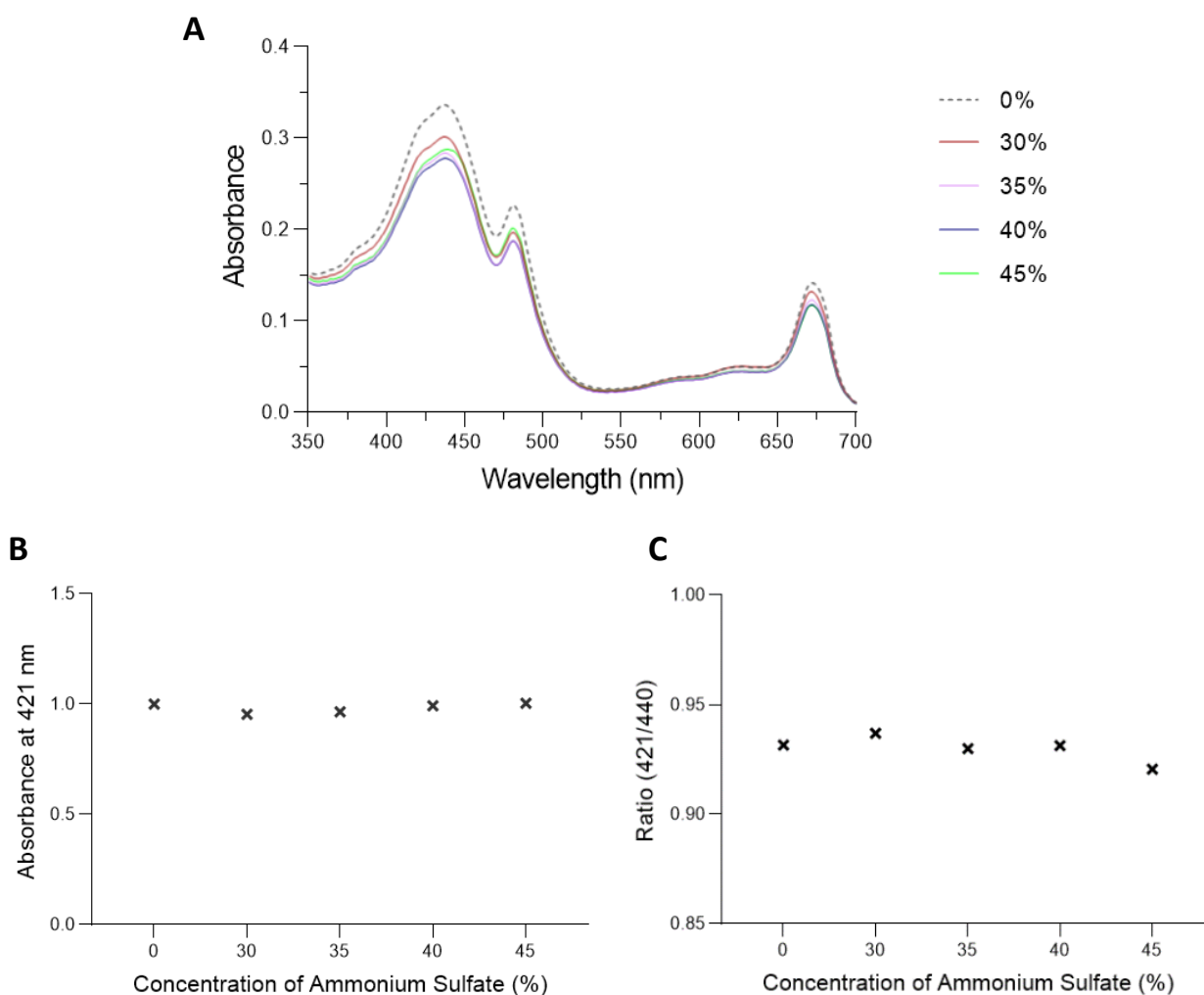


Figure 3.2| Effect of different ammonium sulphate concentrations on the purity of *cytb_{6f}*.

(A) Absorption spectra of the supernatant collected after the precipitation of contaminants with different ammonium sulphate concentrations. (B) Relative amount of *cytb_{6f}* measured from a ratio between the absorbance signals at 421nm and 668nm (Q_y absorption band of Chl a). (C) Ratio between the absorbance signal at 421nm, corresponding to the Soret band of haems, and the absorbance at 440nm (Soret absorption band of Chl a).

Supernatant from the 40% ammonium sulfate treated sample was collected and concentrated as described above. The sample was then loaded onto a sucrose gradient containing 0.06% GDN and ultracentrifuged. The resultant gradient illustrated in Figure 3.3A showed two main fractions which were harvested and further analysed by SDS PAGE (Figure 3.3B). Compared to the SDG in Figure 3.1, both fractions 1 and 2 here were further enriched in *cytb_{6f}* subunits, while the contaminants at 43-47 kDa and 30 kDa are now largely absent. Moreover, only fraction 1 showed the presence of the ~60 kDa contaminant.

A ~37 kDa band consistent with FNR was observed although only in fraction 1. Immunoblotting with an anti-FNR antibody confirmed the band identity (Figure 3.3C). Hence, the modification of the procedure to increase the ammonium sulphate precipitation to 40% resulted in a *cytb₆f* sample with increased purity and it did not improve the FNR:*cytb₆f* stoichiometry in the preparation.

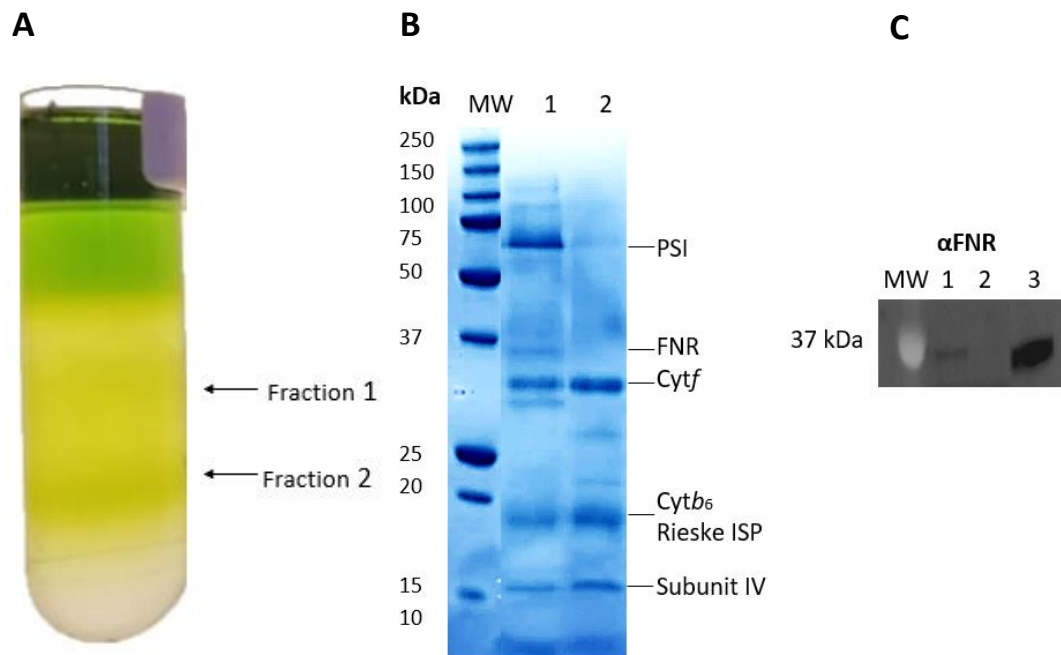


Figure 3.3 | Purification of *cytb₆f* using 40% ammonium sulphate saturation.

(A) sucrose gradient of the supernatant following 40% ammonium sulphate precipitation. The two fractions indicated by the arrows were collected. (B) SDS PAGE analysis of the two samples harvested from the sucrose gradient. Lanes: MW) ladder, 1) fraction 1 collected from the gradient, 2) fraction 2 collected from the gradient. (C) Western blot using FNR antibody. Lanes: MW) ladder, 1) fraction 1, 2) fraction 2, 3) pure FNR protein (Sigma) as a positive control.

3.4 Thylakoid membranes treated with dithiothreitol

As shown in the previous experiment, the amount of FNR copurified with *cytb₆f* is low, suggesting that either the interaction is very weak or that specific conditions are required to promote the association. Previously AA-sensitive CET activity in spinach chloroplasts was shown to be promoted by inclusion of reduced DTT in all buffers during the isolation procedure (Strand et al., 2016).

To investigate whether reducing conditions could enhance the interaction of FNR with *cytb₆f*, oxidised and reduced DTT was added to all buffers used throughout the protein purification procedure.

Final concentration of 2mM DTT oxidised or reduced was then added to all the buffers used in this experiment while otherwise following the approach used in figure 3.3.

The resultant gradients are shown in Figure 3.4A. Two main fractions in each gradient were harvested and further analysed by SDS PAGE (Figure 3.4B). No clear differences could be observed between the samples purified with reduced and oxidised DTT. The amount of FNR purified was again substoichiometric relative to *cyt_f* in fraction 1 and absent in fraction 2. As in figure 3.3 fraction 1 was again contaminated with the 65kDa bands, while fraction 2 was somewhat purer. The superior resolution of the gel relative to figure 3.3B suggests the major contaminant in fraction 1 is ATP synthase, with the 60kDa bands corresponding to α and β subunits, a band at 100 kDa corresponding to the c- ring and lower molecular weight bands at 15-13kDa corresponding to b' and ϵ subunits (Akiyama *et al.*, 2023).

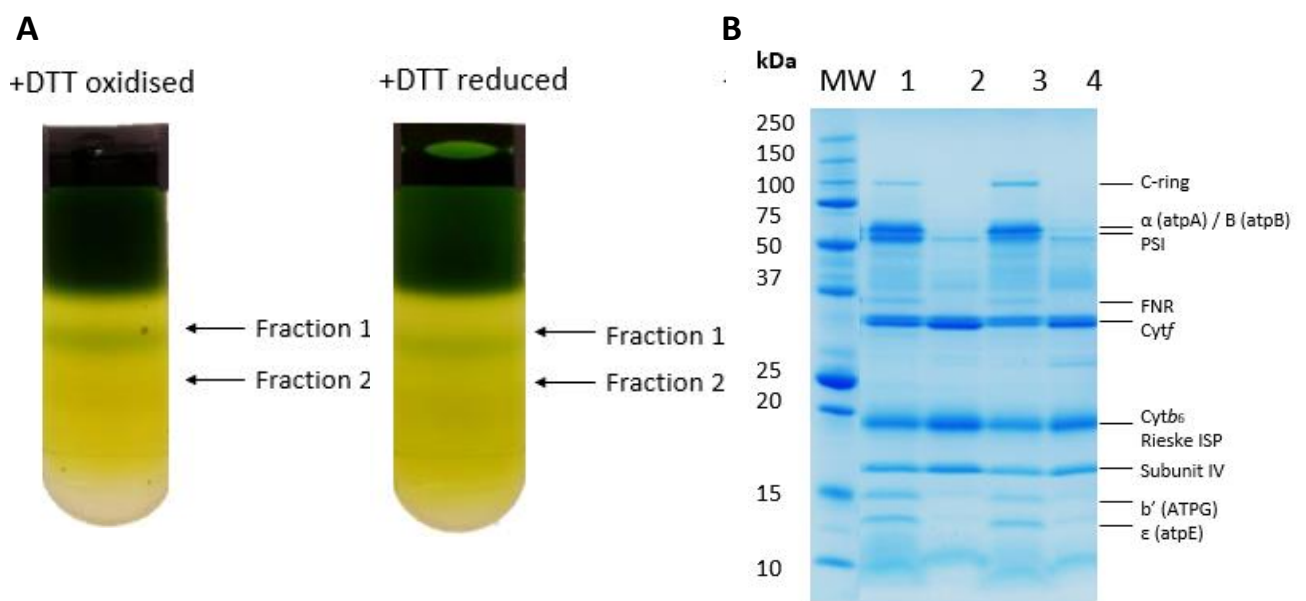


Figure 3.4 | Purification of *cyt_{b6f}* from thylakoid isolated with 2mM oxidised and reduced DTT.

(A) sucrose gradient of the supernatant following 40% ammonium sulphate precipitation. The indicated fractions were harvested. (B) SDS PAGE analysis of the fractions harvested from the sucrose gradients. Lanes: MW) ladder, 1) fraction 1 from gradient with oxidised DTT, 2) fraction 2 from the gradient with oxidised DTT, 3) fraction 1 from gradient with reduced DTT, 4) fraction 2 collected from the gradient with reduced DTT.

3.5 Isolation of thylakoid membranes at different pH

Further improvements to the protocol were necessary to better preserve the interaction between FNR and *cytb₆f*. In February 2020, an abstract of a poster was published where isothermal calorimetry (ITC) was used to quantify the strength of FNR-*cytb₆f* interactions. In this study, FNR-*cytb₆f* interactions were found to be pH dependent; favoured at pH 6.5 relative to pH 8.0 (Zakharov et al., 2020).

With this in mind, the isolation buffers used were adjusted from pH 8.0 to pH 6.5, while otherwise following the procedure in figure 3.4. The resultant gradients are shown in figure 3.5A and the two main fractions were collected and further analysed by SDS PAGE (Figure 3.5B). In contrast to the pH 8.0 procedure in figure 3.4, at pH 6.5 both fractions 1 and 2 appeared to contain FNR. Moreover, the ratio of FNR to *cyt_f* was increased in fraction 1 at pH 6.5 relative to pH 8.0. However, the contamination in both fractions 1 and 2 was significantly increased at pH 6.5 relative to pH 8.0, as shown by the complex banding pattern in figure 3.5.

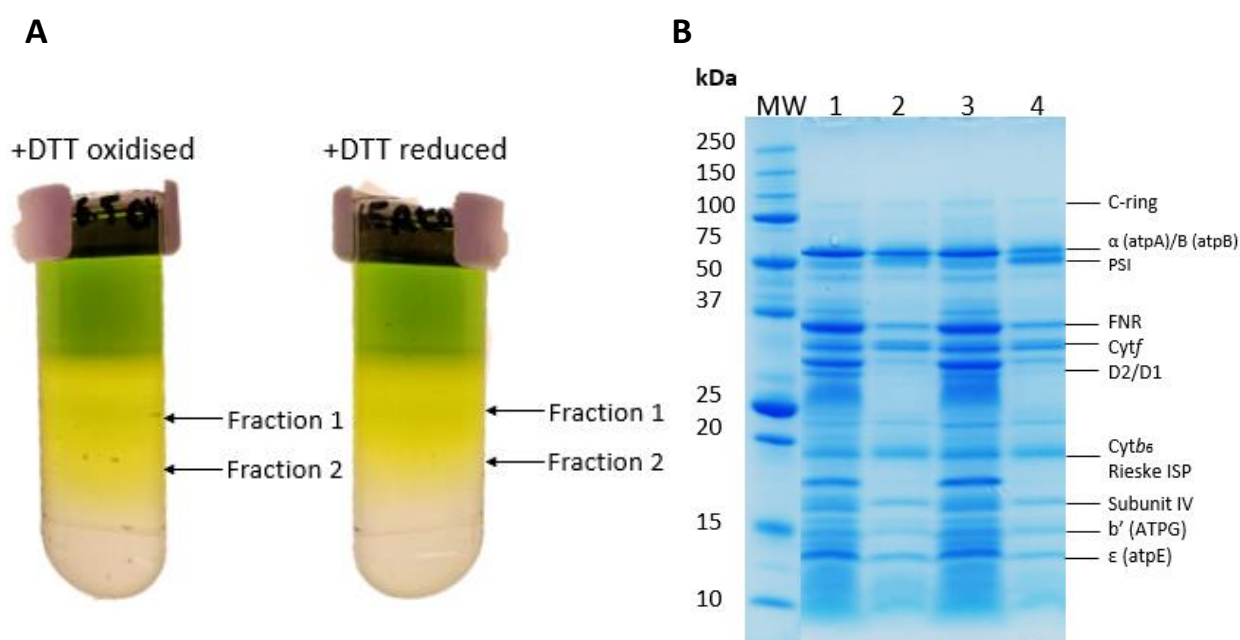


Figure 3.5 | Purification of *cytb₆f* from thylakoid isolated at pH 6.5 with 2mM oxidised and reduced DTT.

(A) Sucrose gradient of the supernatant following 40% ammonium sulphate precipitation. Fractions indicated were collected. (B) SDS PAGE analysis of the fractions harvested from the sucrose gradients. Lanes: MW) ladder, 1) fraction 1 from gradient with oxidised DTT, 2) fraction 2 from the gradient with oxidised DTT, 3) fraction 1 from gradient with reduced DTT, 4) fraction 2 collected from the gradient with reduced DTT.

3.6 Hydroxyapatite column

The samples previously collected from the sucrose gradients were combined and applied on a ceramic hydroxyapatite (CHT) column in an attempt to remove the contaminating proteins (details in section 2.4.6). The eluate was analysed by SDS PAGE (Figure 3.6A); the CHT column did not effectively remove all the contaminants. Furthermore, the sample was analysed by BN-PAGE to investigate whether the complex was still intact. A main band appeared to be present at 66kDa (lane 1), suggesting that the exposure to high concentration of ammonium phosphate during CHT chromatography affected the stability of the complex. In comparison, the sample directly harvested from the sucrose gradients (lane 1) showed to be dimeric (~220kDa) (Figure 3.6B).

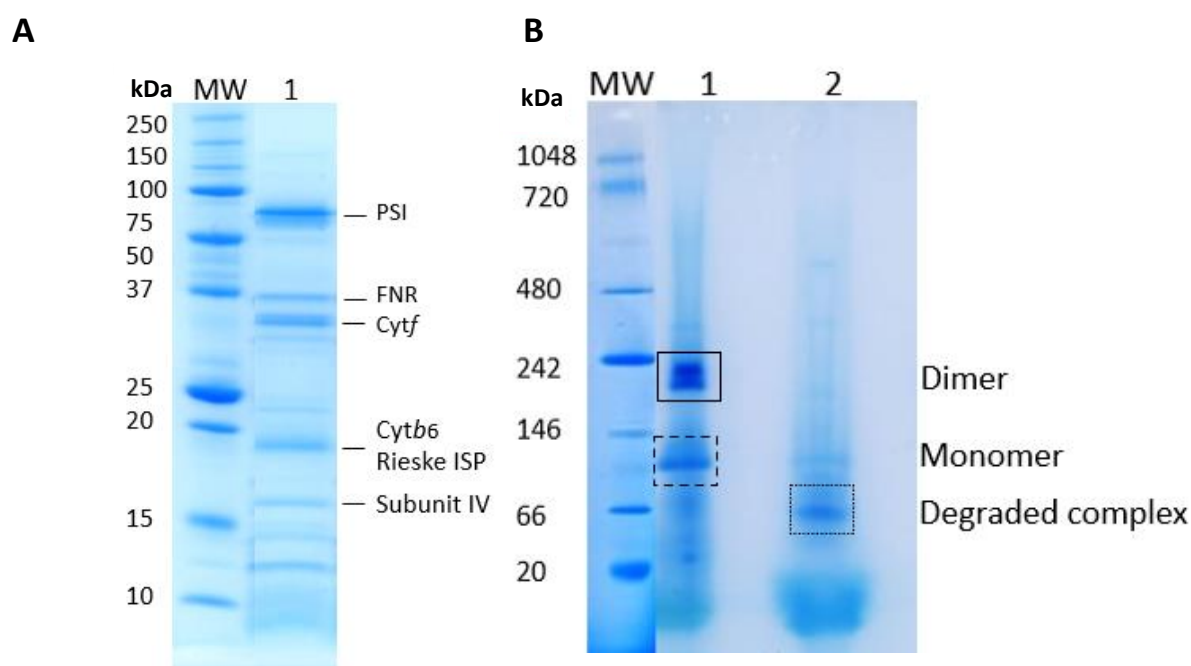


Figure 3.6 | Ceramic Hydroxyapatite column chromatography of samples collected from sucrose gradients at pH 6.5.

(A) SDS PAGE analysis of eluate from the CHT column. (B) Blue Native PAGE analysis of the fractions harvested from the sucrose gradients and eluate from CHT. Lanes: MW) ladder, 1) sample before CHT, 2) eluate from CHT.

3.7 Protamine sulfate precipitation

In an attempt to further improve stability, purity and FNR content of the cytb6f sample protamine sulfate was trialled as an alternative to ammonium sulfate precipitation step.

Protamine sulfate is a small arginine rich cationic peptide. In previous studies it has been observed to have high efficiency in the precipitation of different proteins (Denison et al., 1984; Kim et al., 2013, 2015) including *cytb₆f* (Nelson & Neumann, 1972). Thylakoid membranes were prepared as described in section 2.3.2 and solubilised as described previously. Solubilised thylakoids were ultracentrifuged and 0.02% final concentration of protamine sulfate was added to the sample. This was incubated for 1 hour on ice and subsequently centrifuged to pellet contaminants. The supernatant was then concentrated before loading onto a continuous sucrose gradient in 0.06% GDN and then ultracentrifuged.

The resultant gradient is shown in Figure 3.7A; four fractions were carefully collected and analysed by SDS PAGE (Figure 3.7B). Fractions 2, 3 and 4 from the sucrose gradient were enriched in *cytb₆f*, while fraction 1 showed a high content of FNR. Compared to figures 3.5 and 3.6 the improvement in *cytb₆f* purity with protamine sulphate is clear however it does little to improve the ratio of FNR:*cytb₆f* in the sample. Moreover, fraction 2 that contained some FNR in addition to *cytb₆f* was the most contaminated by the recurrent high molecular weight band at ~50kDa.

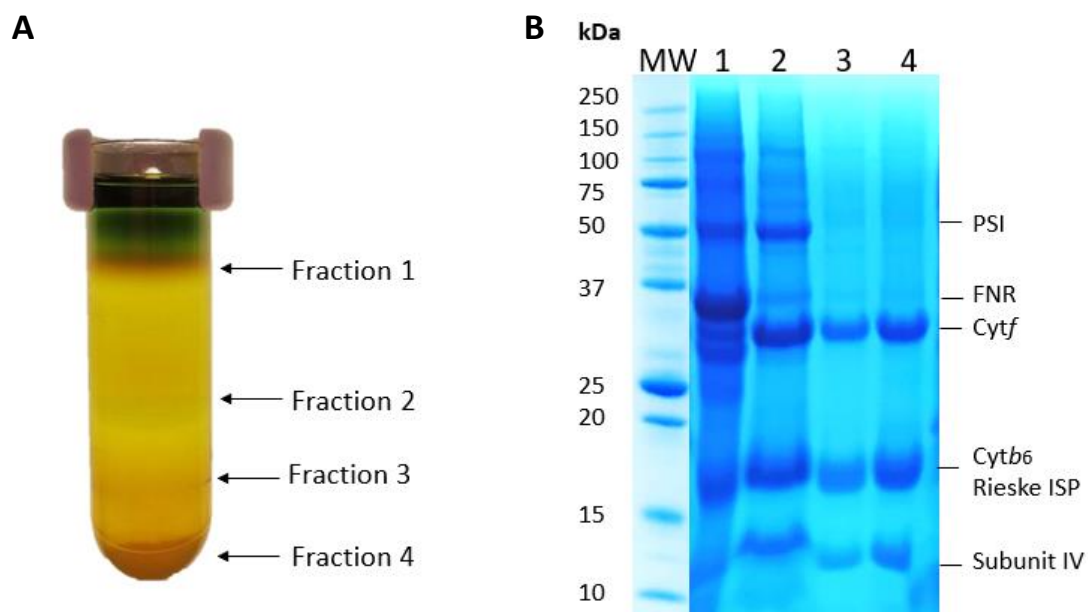


Figure 3.7 | Protamine sulfate precipitation.

(A) Sucrose gradient of the concentrated supernatant following protamine sulfate precipitation. (B) SDS PAGE analysis of the bands collected from the sucrose gradient. Lanes: MW) ladder, 1) fraction 1, 2) fraction 2, 3) fraction 3. 4) fraction 4 collected from the sucrose gradient.

3.8 Screening of detergents for FNR-cyt_b₆f purification

The previous experiments described in this chapter resulted in the copurification of many putative contaminants with cytb₆f or eventually in the loss of stability of the complex and/or the interaction with FNR. Therefore, a series of more alternative non-ionic detergents were next tested in an effort to better preserve the stability of the FNR-cytb₆f supercomplex.

Detergents can be generally classified in three major classes: ionic (cationic and anionic), zwitterionic and nonionic detergents. Nonionic detergents are considered mild and not denaturing; in fact, they are commonly used to preserve protein-protein interactions. Nonionic detergents with bulkier and longer chains are preferred for a much gentler solubilisation and greater stabilisation of protein complexes (H. J. Lee et al., 2022). Many membrane proteins in the last few years have been purified and structurally characterised using lauryl maltose-neopentyl glycol (LMNG) (Bous et al., 2021; Kampjut & Sazanov, 2020). This detergent is characterised by two hydrophobic chains and two hydrophilic maltoside groups joined at a tetrahedral carbon atom and displays an incredible ability to solubilise and stabilise challenging and fragile membrane proteins (Kampjut & Sazanov, 2020).

Thylakoid membranes were prepared as previously described and solubilised at 2mg/ml final chlorophyll concentration with a range of non-ionic detergents: 2% α DDM, 2% UMNG, 2% HECAMEG, 2% digitonin, 2% LMNG and 2% CYMAL-7 for 20 minutes at room temperature. The solubilised material was carefully loaded onto continuous sucrose gradient containing 0.06% GDN and ultracentrifuged at 221,831 x g for 18 hours. Following this step, 12 fractions of 1ml were collected from the top to the bottom of each gradient (Figure 3.8A). The samples were further analysed by haem blots and the cytf content was determined by band quantification using ImageJ. The amount of cytf in each fraction was then plotted (Figure 3.8B). Fractions with the highest content of cytf from each gradient were further analysed by western blot using an FNR antibody to identify which detergent was able to preserve best the interaction of FNR to cytb₆f. Samples purified using LMNG showed the highest FNR content compared to the other detergents (Figure 3.8C). Therefore, LMNG was selected for further analysis.

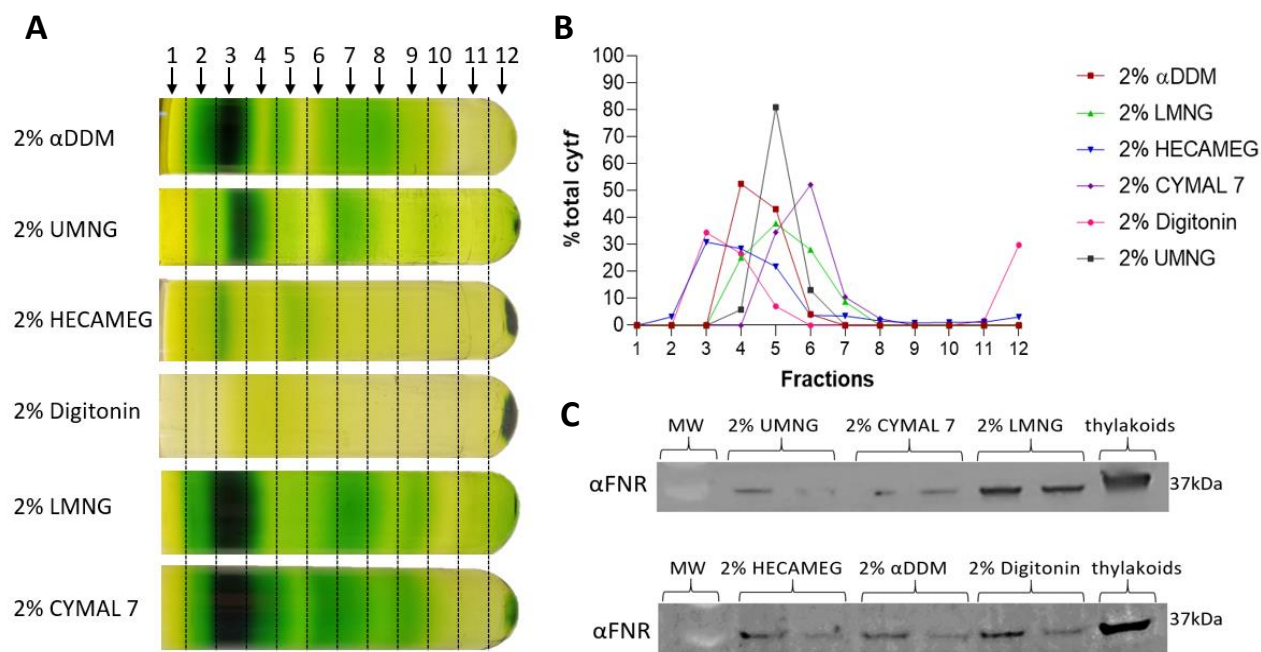


Figure 3.8 | Detergents screening.

Several detergents were tested for the purification of a stable FNR-cyt_b₆f complex. (A) Sucrose gradients of thylakoid membranes solubilised with 2% αDDM, 2% UMNG, 2% HECAMEG, 2% digitonin, 2% LMNG and 2% CYMAL-7. Fractions of 1 ml were carefully harvested from each gradient and analysed by haemblots (B) to determine the cytf content of each sample. C, two fractions with the highest cytf content were western blotted for FNR.

3.9 Optimization of LMNG concentration

While in the previous experiment 2% LMNG was used to solubilise all the thylakoid membranes, it was considered desirable to selectively purify cytb₆f with a low LMNG concentration. This would avoid the isolation of contaminating proteins and therefore extra purification steps.

Thylakoids membranes were isolated as previously described. These were solubilised with 0.35%, 0.65%, 1% LMNG for 20 minutes at room temperature and then carefully loaded onto continuous sucrose gradients (Figure 3.9A). Fractions of 1ml were harvested from the top to the bottom of the gradients and the amount of cytf was quantified as described in section 3.8 and then plotted (Figure 3.9B).

LMNG showed the ability to effectively extract cytb₆f from thylakoid membranes at a very low concentration.

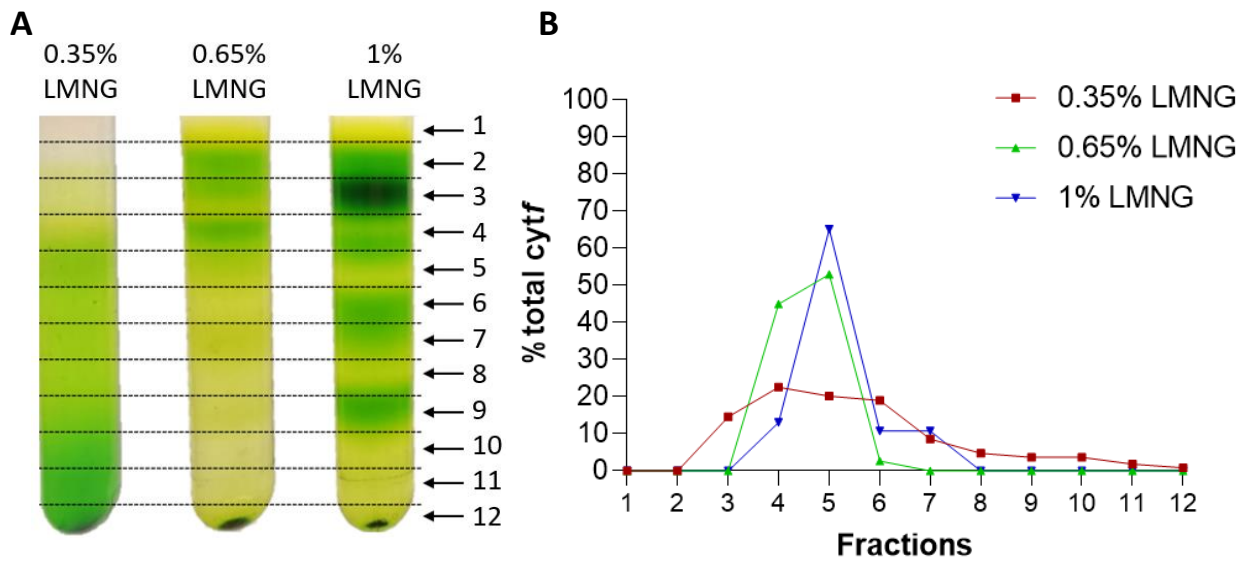


Figure 3.9 | Optimisation of LMNG concentration.

(A) Sucrose gradients of thylakoid membranes solubilised with 0.35%, 0.65% and 1% LMNG. Fractions of 1 ml were carefully harvested from each gradient and analysed by haemblots (B) to determine the amount of *cytf* in each fraction.

Fractions with the highest *cytf* content were identified and the purity of *cytb₆f* was assessed by measuring the ratio of 421nm and 440nm (Figure 3.10). The samples purified using 0.35% LMNG exhibited the highest purity.

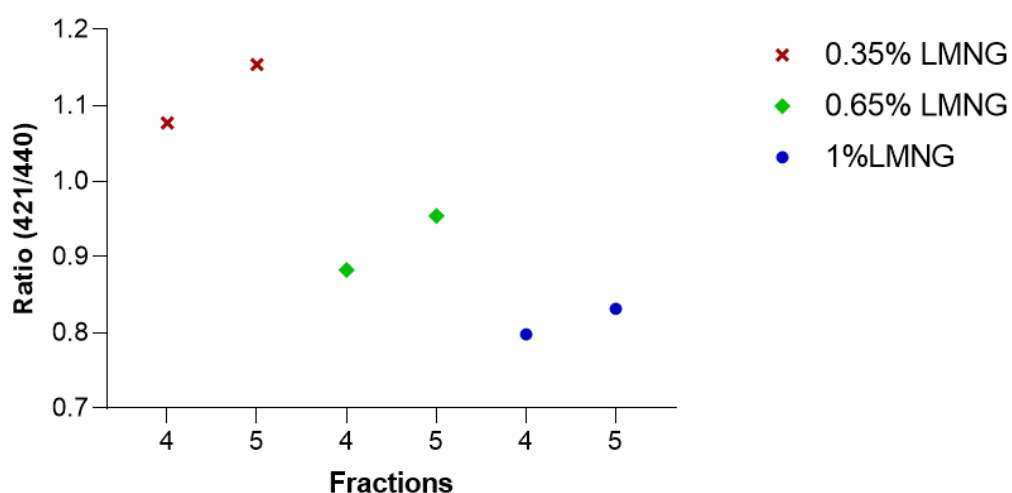


Figure 3.10 | Purity of *cytb₆f* in the samples harvested from the sucrose gradients.

Two fractions with the highest *cytf* content from each gradient were identified and ratio of 421/440 nm was measured to assess the purity of the material (n=1) .

3.10 Biochemical characterisation of *cytb_{6f}* sample in LMNG

The sample purified with 0.35% LMNG was further investigated by SDS PAGE. The four main subunits of *cytb_{6f}* are indicated in figure 3.11A, and the FNR content was almost stoichiometric to the *cytb_{6f}* subunits. LMNG was able to selectively purify *cytb_{6f}* and preserve the labile association with FNR. The absorption spectra of the 0.35% LMNG purified *cytb_{6f}* was characterised by the 421 nm peak corresponding to the Soret band of haems and peak at 554 nm corresponding to the c-type haems of *cytf*. A small peak at 485 nm corresponds to carotenoids bound to the complex.

Redox difference spectra are shown in the inset panel. The sample was first fully oxidised with potassium ferricyanide and then c-type haems of *cytf* were reduced with sodium ascorbate. Finally, sodium dithionite was added to the sample to fully reduce c-type haems of *cytf* and b-type haems (*b_n* and *b_p*). Ascorbate minus ferricyanide spectra (dashed line) show peaks at 523 nm and 554 nm, confirming the presence of c-type haems of *cytf*. Dithionite minus ascorbate spectra (dotted line) show peaks at 534 nm and 564 nm corresponding to *b_n* and *b_p* of *cytb_{6f}*.

BN PAGE analysis of the sample was also performed (Figure 3.11B) and the complex showed to be dimeric and very stable. In fact, when the sample was treated with 1% triton for 1 hour, the complex did not monomerise completely, suggesting that LMNG confers great stability to the complex.

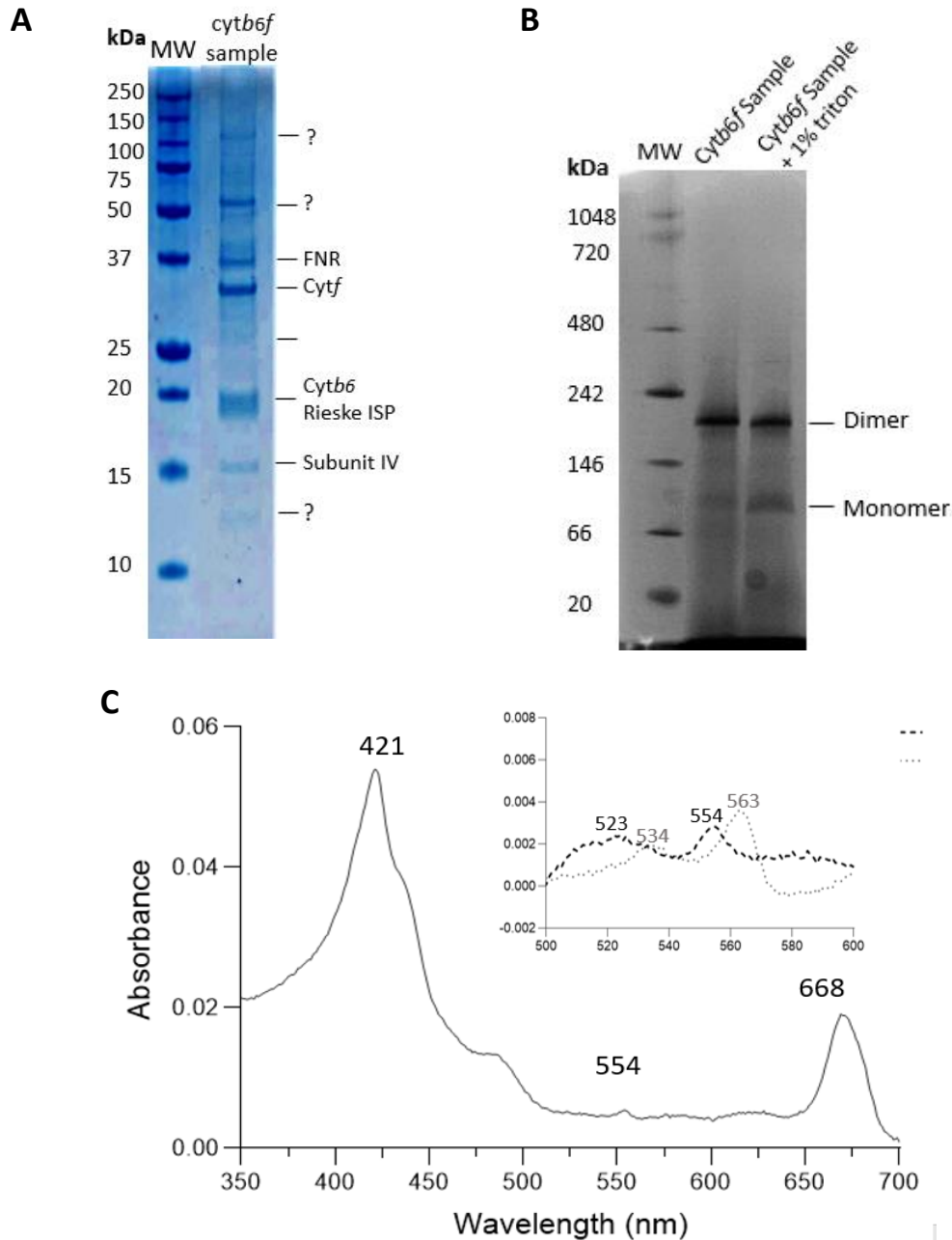


Figure 3.11 | Characterisation of *cytb_{6f}* sample in LMNG.

(A) SDS PAGE analysis of the sample. (B) BN PAGE analysis of the purified sample and 1% triton treated sample. (C) absorption spectra showing the purity of the *cytb_{6f}*. Redox difference spectra are shown in the inset panel. Ascorbate minus ferricyanide spectra (dashed line) show peaks at 523 nm and 554 nm, confirming the presence of *c*-type haems of *cyt_f*. Dithionite minus ascorbate spectra (dotted line) show peaks at 534 nm and 564 nm corresponding to *bn* and *bp* of *cytb_{6f}*.

Although the *cytb_{6f}* complex was dimeric and intact and the FNR interaction has been preserved, the recurrent band at around 50 kDa is still visible and it could correspond to either PSI or ATP synthase contamination. However, this band appears almost at

stoichiometric level to the other proteins and the absorption spectrum of the sample does not reveal any clear contamination from PSI (Figure 3.11C). The Chl *a* peak in the Q_y region of the spectra at 668 nm would be red shifted and no peak is observed at around 440 nm. Other faint additional bands can be observed in the SDS PAGE; at around 100kDa, 25kDa, and smaller molecular weights.

ATP synthase is a common contaminant in *cytb₆f* purifications (Hurt and Hauska, 1981), therefore a western blot for the β subunit was carried out but no signal appeared in the sample lane (Figure 3.12A). In the literature, two chloroplast proteins, TROL and Tic62, have been shown to strongly interact with FNR (Jurić et al., 2009; Benz et al., 2009; K uchler et al., 2002). TROL has a molecular weight of 66kDa and Tic62 has a similar molecular weight, however it displays a different mobility and is often found at around 100kDa (Benz et al., 2010). Western blots for TROL and Tic62 were performed and both proteins were detected in the purified sample (Figure 3.12B-C).

PGRL1 and PGR5 proteins have been previously proposed to form the FQR complex (Hertle et al., 2013), while PGR5 has previously been shown to affect the tethering of FNR to the thylakoid membrane in *Chlamydomonas* (Mosebach et al., 2017). Furthermore, PGRL1 was previously found in the PSI- *cytb₆f* CET supercomplex in *Chlamydomonas* (Iwai et al., 2010) and PGR5 was found to interact with *cytb₆f* in cucumber leaves (Wu et al., 2021) and by yeast two hybrid studies (DalCorso et al., 2008). To investigate whether these proteins were in the LMNG purified FNR- *cytb₆f* sample, western blots were carried out and both PGRL1a and PGR5 were detected (Figure 3.12.D-E).

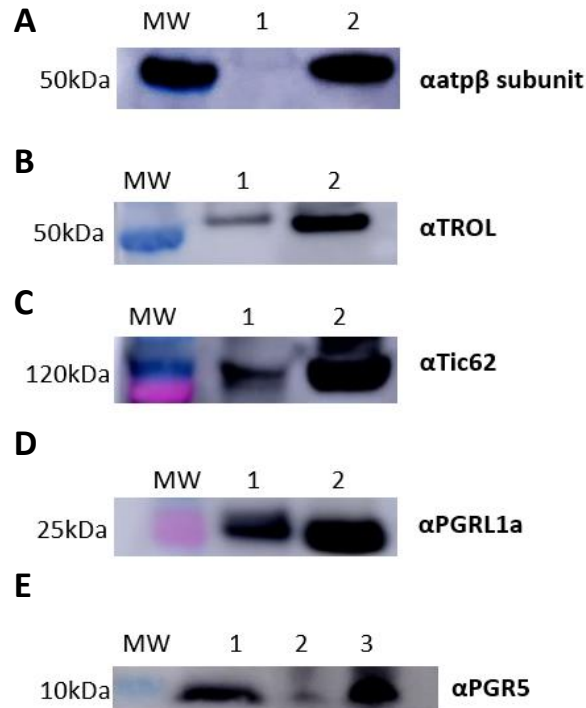


Figure 3.12 | Identification of copurified proteins by western blots.

(A) Western blot for ATP synthase β subunit. Lanes: MW) ladder, 1) purified sample, 2) thylakoid membranes purified from spinach. (B) Western blot for TROL. Lanes: MW) ladder, 1) purified sample, 2) thylakoid membranes purified from spinach. (C) Western blot for Tic62. Lanes: MW) ladder, 1) purified sample, 2) thylakoid membranes purified from spinach. (D) Western blot for PGRL1a. Lanes: MW) ladder, 1) purified sample, 2) thylakoid membranes purified from spinach. (E) Western blot for PGR5. Lanes: MW) ladder, 1) purified sample, 2) thylakoid purified from a *pgr5* mutant *Arabidopsis* plant, as negative control, 3) thylakoid membranes purified from spinach.

To investigate whether the chaotropic agent NaBr would have any effect during the thylakoid purification and if it was causing the removal of contaminants, the experiment was repeated without NaBr washes. From SDS PAGE analysis of the resulting sample it can be observed that additional bands are present in the sample, compared to the complex purified thylakoid washed with NaBr (Figure 3.13). At 30 kDa it can be observed a thick band corresponding to PsbA and PsbD (D1 and D2), core components of PSII.

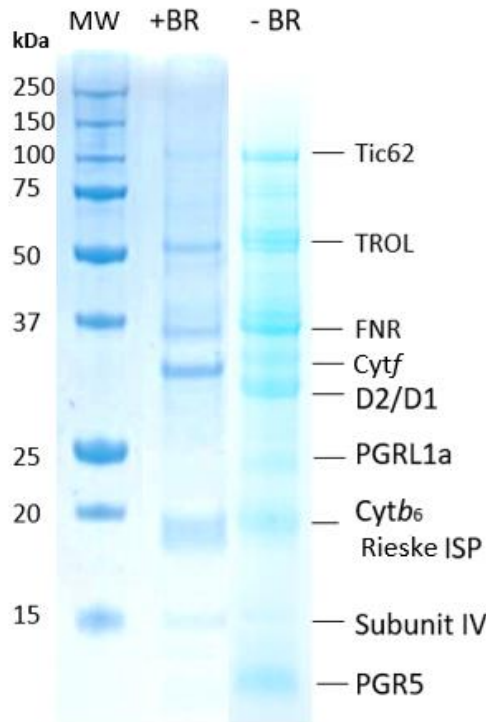


Figure 3.13 | Comparison of FNR-cyt_{b6f} supercomplex purified from thylakoid membranes isolated with and without NaBr.

SDS PAGE analysis of the FNR-cyt_{b6f} supercomplex purified with 0.35% LMNG solubilised thylakoid membranes. Thylakoids were isolated separately with or without NaBr.

3.11 Discussion

In this chapter, successful purification procedure has been developed to purify the FNR-cyt_{b6f} supercomplex from spinach. The detergent LMNG conferred great stability to this multicomponent complex resulting in a dimeric cytb_{6f} and in the preservation of several interactions with stromal proteins (FNR and PGR5) and transmembrane proteins (TROL, Tic62 and PGRL1).

In Chapter 4 the homogeneity of the sample will be further investigated through negative stain EM and Cryo-EM. The FNR-cyt_{b6f} supercomplex will also be assessed spectroscopically to investigate its putative CET activity.

4. Structural characterisation of the FNR-cytb_{6f} supercomplex

4.1 Introduction

As discussed in the previous chapter, the spinach supercomplex purified is characterised by the presence of *cytb_{6f}* and the CET effector proteins FNR, PGRL1, PGR5, Tic62 and TROL. In Chapter 4 the crucial role of detergents in the purification of membrane proteins, their stabilisation and structural determination was discussed. Indeed, the correct choice of detergent is especially important for the structural determination of supercomplexes by cryo-EM, given their fragility. Previous studies have demonstrated that LMNG is markedly effective at stabilising a wide range of membrane proteins (Chae et al., 2010) and in better preserving their activity than dodecyl maltoside (DDM) (Kampjut & Sazanov, 2020). The biochemical advantage of LMNG may reside with its very low critical micellar concentration (CMC), which allows it to stabilise proteins with a minimal background level of detergent. CMC is the concentration above which micelles are formed spontaneously. Compared to the widely used detergent DDM (CMC = 0.007%), LMNG has a much lower CMC (0.001%) (Chung et al., 2012) (Fig 4.1A, B). Nevertheless, detergents with extremely low CMC values, such as LMNG, can be problematic for cryo-EM. It has been observed that cryo-EM grids prepared using LMNG purified samples exhibit a substantial background in the micrographs and poor-quality ice. This issue is caused by the presence of empty detergent micelles, even at concentrations below the CMC and the effects on the surface tension of the buffer. This phenomenon interferes with the particle picking process and consequently the subsequent image processing for the final structural determination of the complexes (Hauer et al., 2015; Li, 2022; Singh & Sigworth, 2015).

Several new polymers have been developed to assist membrane protein purification, including amphipathic polymers (Amphipols). Amphipols are a new class of surfactants and one of the most extensively studied is A8-35, comprised of a mix of short amphipathic polymers. These polymers have polyacrylate backbone and two types of side chains: about 25% of A8-35 have hydrophobic octylamine side chains, around 40% an isopropylamine groups and 35% underivatized carboxylate (Popot, 2010) (Figure 4.1C). Recently, A8-35 has been used

successfully for the stabilisation of the PSII-LHCII (Watanabe et al., 2019) and unsuccessfully in the case of a putative *cytb₆f* complex associated to the CET effector proteins PetO and anaerobic response 1 (ANR1) protein in *Chlamydomonas* (Buchert et al., 2018).

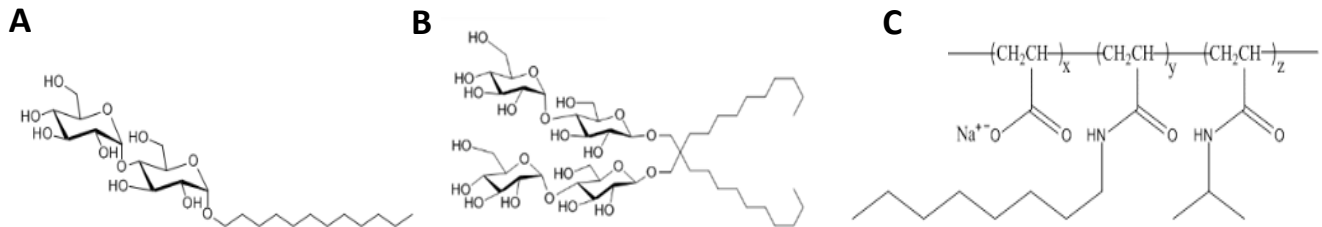


Figure 4.1| Chemical structures of commonly used detergents for protein purification and stabilisation.

(A) Structure of n-Dodecyl- α -D-Maltopyranoside (α DDM). (B) Structure of lauryl maltose neopentyl glycol (LMNG). (C) Structure of the amphipol A8-35, characterised by a polyacrylate backbone and ~35% underivatized carboxylate (x), ~25% hydrophobic octylamine side chains (y), ~40% isopropylamine groups.

Despite the effectiveness of amphipols in stabilising various types of complexes (Charvolin et al., 2014; Chen et al., 2016; Le Bon et al., 2018; Watanabe et al., 2019), preserving labile interactions between proteins for cryo-EM structural analysis remains extremely challenging. In the study carried out by Buchert et al., in 2018, the amphipol approach was combined with mass spectrometry and cross-linking for the characterization of the interactions between the *cytb₆f* complex and the CET effector proteins in *Chlamydomonas*.

Cross-linking mass spectrometry is a structural proteomics technique, which can provide structural information about the topology of protein complexes and protein-protein interactions. The principle of this technique is that the residues of nearby proteins can be cross-linked together. Subsequently, the whole proteome is digested, and the cross-linked peptides are identified. A key challenge of this technique is that crosslinked proteins are inefficiently cleaved by trypsin. Moreover, crosslinked peptides are less efficiently ionised and have lower flyability. Therefore, cross-linked peptides represent only a small percentage of the total peptides present within the analysed sample (K. Lee & O'Reilly, 2023).

In this chapter, the characterization of the FNR-*cytb₆f* supercomplex purified in LMNG and subsequently stabilised in the amphipol A8-35 by cryo-EM is described. In addition, a characterization of the supercomplex by mass-spectrometry is presented which describes the protein composition and protein-protein interactions within the sample. The putative

interactions are tested using a biochemical pulldown approach. Finally, FQR activity of the FNR- *cytb₆f* supercomplex was also assessed.

4.2 Preparation of the FNR-*cytb₆f* supercomplex sample for cryo-EM

The FNR-*cytb₆f* supercomplex sample prepared as described in chapter 3 was concentrated and loaded onto a Superdex 200 Increase 10/300 GL gel filtration column to remove excess of detergent, sucrose, and any remaining protein contaminants in a buffer containing 0.002% LMNG (2x CMC). The complex eluted at around 10ml and two fractions of the peak were pooled and concentrated (Figure 4.2A). The sample was then analysed by SDS-PAGE to confirm the presence of all protein constituents of the complex. The peak eluting at 10 ml contained Tic62 at 120kDa, TROL at 50kDa, FNR at 37kDa, the four main subunits of *cytb₆f* (*cyt_f* at ~31kDa, *cytb₆* ~ 24 kDa, the Rieske ISP ~ 20 kDa and subIV ~ 17 kDa), PGRL1 at 25kDa and PGR5 at 10kDa (Figure 4.2B), suggesting the complex remains stable in LMNG.

Given the problems associated with LMNG described in the introduction, we also assessed the stability of the FNR-*cytb₆f* supercomplex in the detergent, glyco-diosgenin (GDN), which was successfully used to obtain the high resolution structure of the *Synechocystis cytb₆f* complex (Proctor et al., 2022). Therefore, the sample purified from the sucrose gradient in LMNG was subjected to gel filtration in a buffer containing 0.006% GDN (3x CMC). The gel filtration trace pattern exhibited a major peak at around 10 ml with an additional smaller peak at around 13 ml indicating the disassembly of the fragile complex (Figure 4.2C). SDS-PAGE analysis confirmed the presence of *cytb₆f* with its four main subunits in the 10 ml peak fraction, unlike in LMNG no additional proteins were visible (Figure 4.2D).

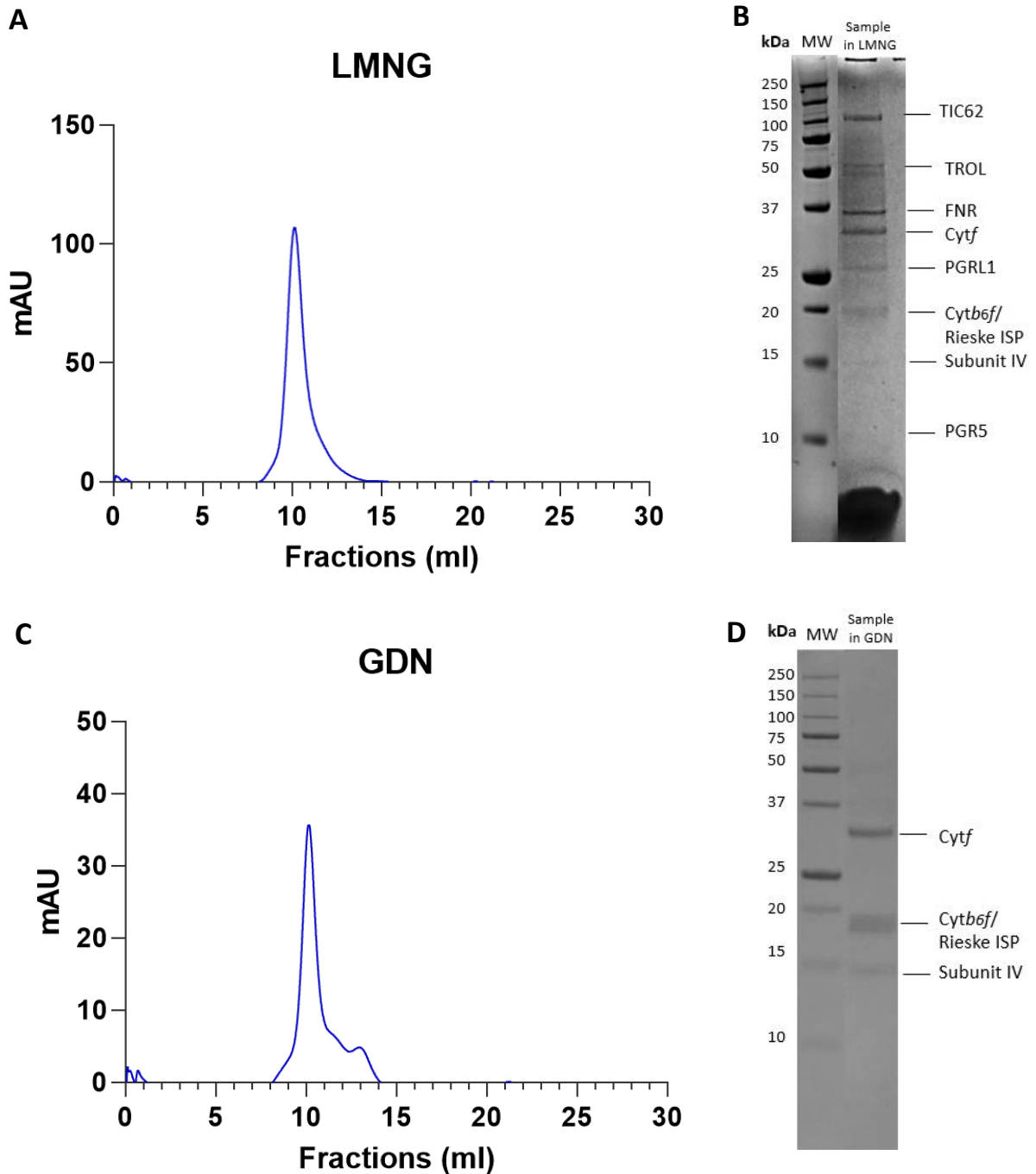


Figure 4.2 | Size exclusion chromatography of the sample purified in LMNG.

(A) Size exclusion elution profile of the FNR-cyt_{b6f} sample previously harvested from 10-35% continuous sucrose gradient. The buffer used during gel filtration contained 25 mM HEPES, 25 mM NaCl and 0.002% LMNG. (B) The eluted fractions around 10 ml were pooled and concentrated for cryo-EM preparation. Based on the SDS-PAGE analysis, the cytb_{6f} sample looked stable with no loss of proteins from the supercomplex. (C) The cytb_{6f} sample harvested from the sucrose gradient was gel filtered in 25 mM HEPES pH7.5, 25 mM NaCl and 0.006% GDN. (D) SDS-PAGE analysis of the sample collected from the major peak revealed the loss of FNR and the other interacting proteins from the supercomplex; the four main subunits of the cytb_{6f} complex can be observed.

4.3 Structural determination of FNR-cyt_bf supercomplex in LMNG

4.3.1 Negative Stain EM analysis

The cytb₆f sample in LMNG was analysed by negative stain EM (details in method section 2.8) to assess sample homogeneity and to estimate an initial concentration suitable for the cryo-EM grid preparation. To achieve optimum particle distribution the sample was diluted 10x reaching the final concentration of ~0.3μM.

Particles of dimeric cytb₆f complex are expected to be of a length of ~11.75 nm and height of ~8.25nm and therefore we expected the size of our supercomplex to be larger. Analysis of negative stain images revealed that the sample is considerably heterogenous, featuring particles of various sizes, varying from 11 nm to 14 nm (Figure 4.3B). Hence, the supercomplex might have disassembled before or during the negative stain preparation.

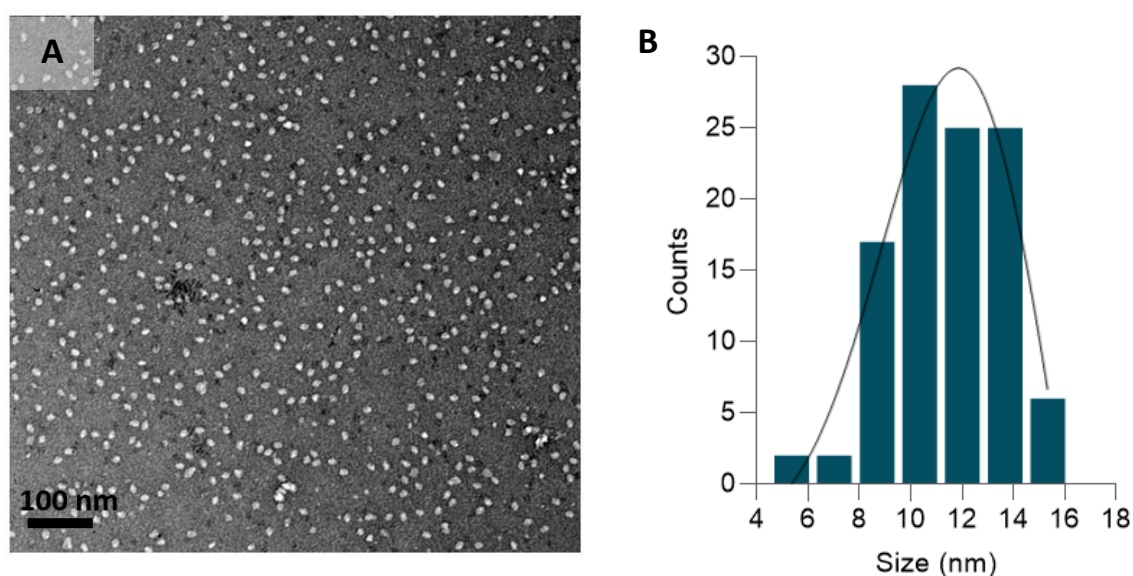


Figure 4.3 | Negative stain analysis of the FNR-cyt_bf supercomplex in LMNG.

(A) Negative stain images of the purified supercomplex; the sample was 10-fold diluted to obtain optimal particles distribution. (B) Histogram showing the particle sizes measured from negative stain micrographs using imageJ.

4.3.2 Cryo-EM analysis

Despite the heterogeneity of the sample observed in the negative stain images, we proceeded with the cryo-EM grid preparation to attempt the structural characterisation of the

supercomplex in LMNG. Our aim was to potentially differentiate the particle sizes during the initial screening stages and select those with a larger diameter (at least >16 nm).

The purified protein sample with a concentration of 14 μ M was applied on Quantifoil R1.2/1/3 400 mesh Cu grids and subsequently screened (details in the method section 2.9).

Grids prepared with the sample solubilised in LMNG exhibited a general lack of good contrast between the particles and the background in the obtained micrographs; some higher contrast features can be observed in the Figure 4.4A which were potentially LMNG artefacts or ethane contamination. Cryo-EM grids were also prepared with the *cytb_{6f}* reconstituted in GDN and it can be observed instead that particles were homogeneously distributed and there was an absence of detergent artefacts (Figure 4.4B).

We proceeded with particle picking on the LMNG grids; approximately 2,000 particles were manually picked and a model for particle picking was trained in crYOLO. This model was used to pick 2,811,993 candidates from the entire dataset, which were classified into 300 2D classes using unsupervised 2D classification in RELION 3.1. A representative subset of the 2D classes is shown in Figure 4.4C. 2D classes from the particles picked from the LMNG sample micrographs were poorly defined and did not display any obvious *cytb_{6f}*-like features.

Another model for particle picking was trained in crYOLO by manually picking around 2,000 particles from the GDN reconstituted sample micrographs. This model was used to pick 842,466 candidates from the entire dataset, which were classified into 300 2D classes using unsupervised 2D classification in RELION 4.0. In figure 4.4D a representative subset of 2D classes from the GDN reconstituted sample is shown, displaying characteristic features of the *cytb_{6f}* complex only, as expected.

To achieve better grids with the detergent LMNG, several conditions were tested: different buffers, lowering LMNG concentration and addition of secondary detergent with a high CMC (e.g. n-Octyl- β -D-Glucopyranoside, CHAPS). Addition of high CMC detergent that arrange themselves at the air-water interface, can prevent denaturation of the sample at the air water interface and result in better dispersion of the particles within the vitreous ice (Kampjut & Sazanov, 2020). However, no improvements in the grid optimisation were achieved by applying these approaches to the samples purified in LMNG.

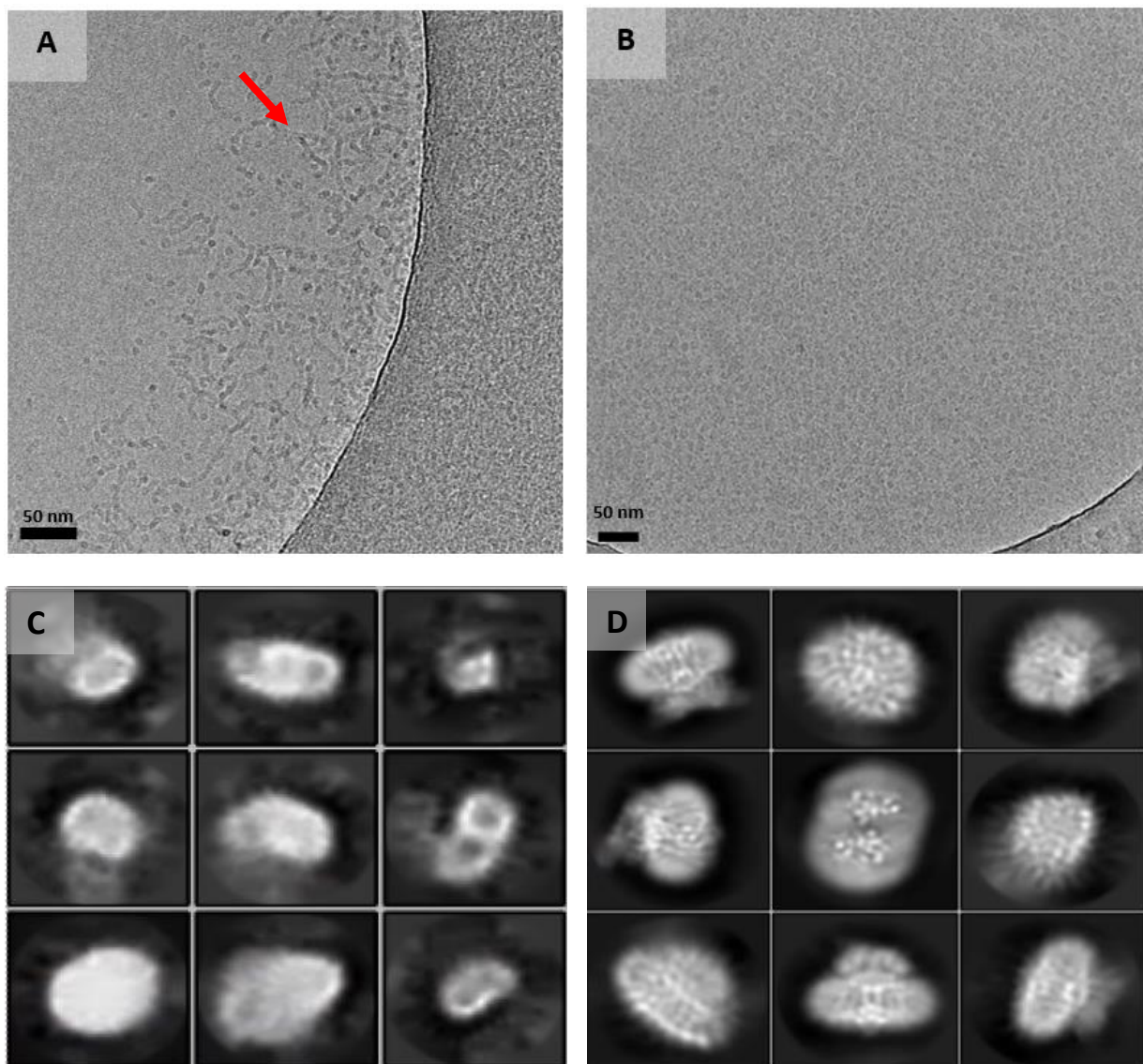


Figure 4.4 | Cryo-EM micrographs of the FNR-*cytb_{6f}* supercomplex.

(A) FNR-*cytb_{6f}* supercomplex purified in LMNG was applied on cryo-EM grids. It can be observed a lack of contrast between particles and the background and detergent artefacts (indicated by a red arrow). In comparison, on the grids prepared with the sample reconstituted in GDN and containing only *cytb_{6f}*, good particles distribution and contrast can be observed (B). Representative subset of selected 2D classes of particles picked from micrographs prepared with sample in LMNG (C) and in GDN (D).

4.4 Reconstitution of the FNR- *cytb_{6f}* supercomplex in amphipols

As an alternative approach, the LMNG sample was reconstituted into amphipols A8-35, in an attempt to better preserve the sample during the cryo-EM grid making and to achieve higher quality grids. To this end, thylakoid membranes prepared as described in Chapter 3 were solubilised in 0.35% LMNG and the unsolubilized material was then removed via

centrifugation. Amphipol A8-35 was then added at a final concentration of 1% and incubated for 10 min on ice, before the sample was loaded onto a 10-35% sucrose density gradient. Following ultracentrifugation, the FNR-cyt_b₆f complex was harvested and gel filtered in 25 mM HEPES pH 7.5, 25 mM NaCl in the absence of additional amphipols or detergents (Figure 4.5).

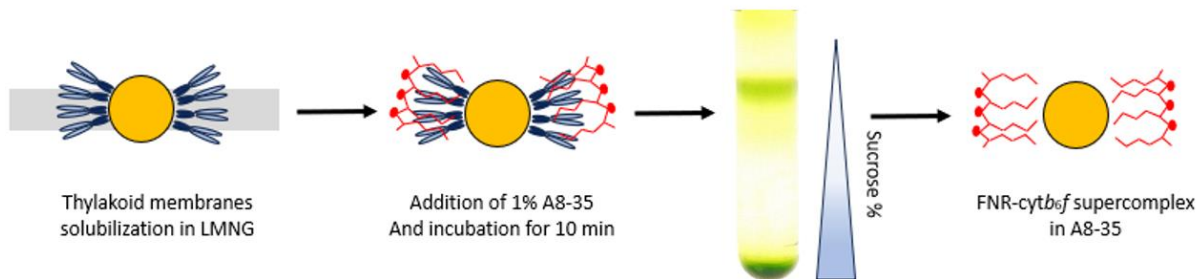


Figure 4.5 | Workflow of the reconstitution in amphipols A8-35.

Thylakoid membranes were solubilised in LMNG and unsolubilized material was removed by centrifugation. The supernatant was mixed with 1% final concentration of A8-35 and incubated for 10 min before being loaded on a 10-35% sucrose density gradient. Gradients were ultracentrifuged and the FNR-cyt_b₆f supercomplex was harvested.

The stability of the FNR-cyt_b₆f supercomplex in A8-35 was assessed by subjecting the sample to size exclusion chromatography. The elution profile displayed a single asymmetric peak at around 10ml as previously observed in the elution profile of samples in LMNG (Figure 4.6A). SDS-PAGE analysis indicated the presence of all the components of the FNR-cyt_b₆f supercomplex, except Tic62 within the 10 ml peak fraction (Figure 4.6B).

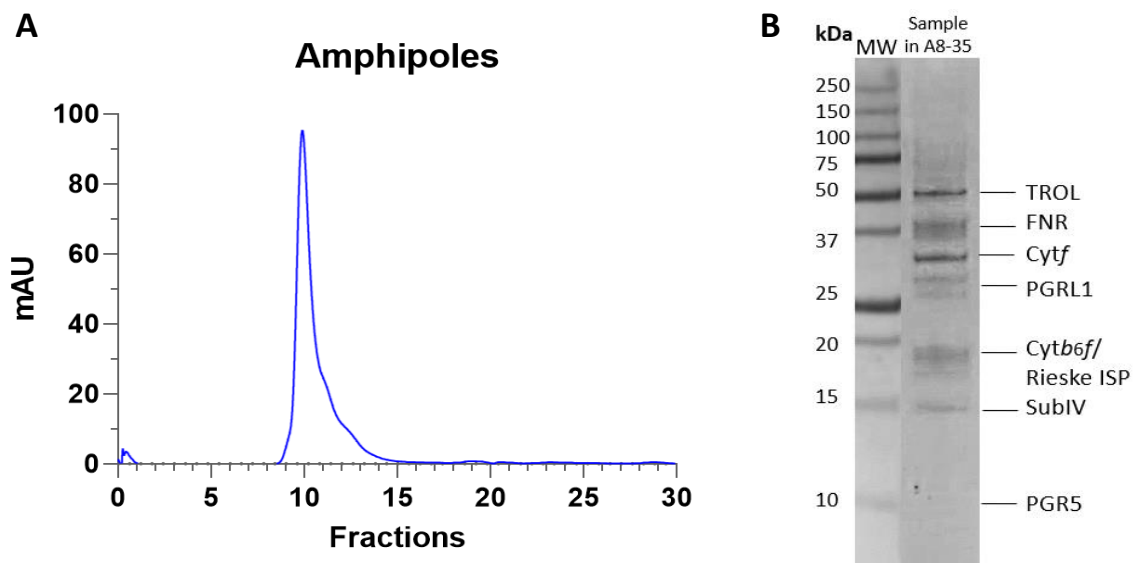


Figure 4.6 | Size exclusion chromatography of the sample reconstituted in amphipols A8-35.

(A) Size exclusion elution profile of the sample previously harvested from 10-35% continuous sucrose gradient with 1% final concentration of A8-35. The buffer used during gel filtration contained 25 mM HEPES, 25 mM NaCl. (B) The eluted fractions around 10 ml were pooled and concentrated for cryo-EM

preparation. Based on the SDS-PAGE analysis, the protein Tic62 dissociated from the FNR-cytb₆f supercomplex.

Negative stain EM was carried out to confirm the sample homogeneity. Analysis of the recorded images revealed that the sample is highly homogenous with particles displaying similar shape and size. However, most of the particle's size is of around 11.61 nm suggesting that the majority of the supercomplex particles disassembled (Figure 4.7). Despite this, we proceeded with the cryo-EM grid preparation with the aim of distinguishing the surviving large supercomplex particles from the smaller cytb₆f only particles.

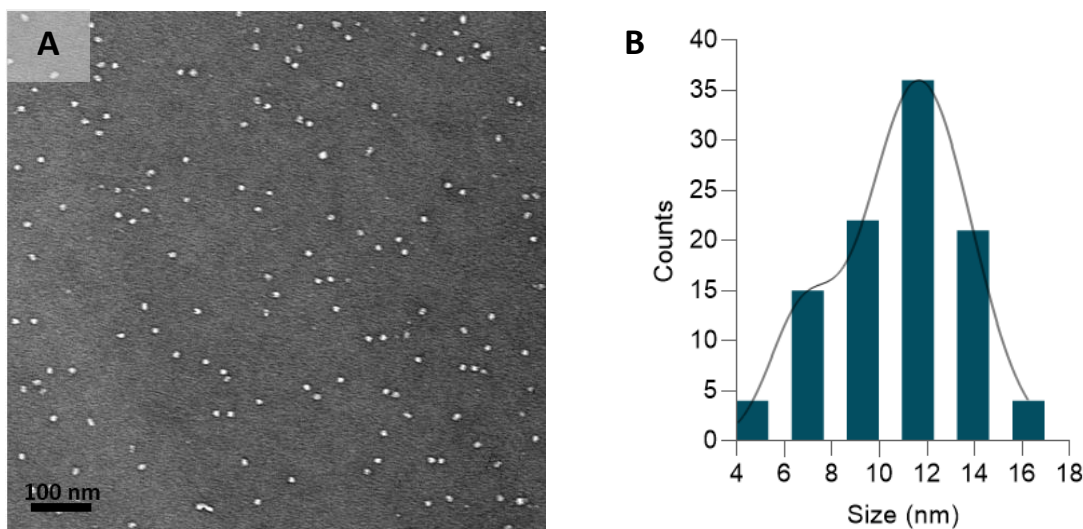


Figure 4.7 | Negative stain analysis of the FNR-cytb₆f supercomplex in A8-35.

(A) Negative stain images of the purified supercomplex reconstituted in A8-35 which confirmed the sample homogeneity. (B) Histogram showing the particle sizes measured from negative stain micrographs using imageJ.

The sample in A8-35 was applied on Quantifoil R1.2/1/3 400 mesh Cu grids at a final concentration of 14 μ M. Screening of the obtained micrographs revealed an optimal particle distribution of roughly similar sizes, absence of detergent artefacts and good contrast between the particles and the background (Figure 4.8A-B). 1,919,959 particles were picked with a semi-automated approach and subjected to 2D classification. A representative subset of the 2D classes obtained is shown in figure 4.8C revealing several views of the cytb₆f complex in different orientations. Several classes were characterised by an unusual asymmetric top-view of the cytb₆f complex, indicating potentially the presence of extra proteins associated with the cytb₆f complex (Figure 4.8C). A refined map was resolved to a nominal resolution of 4.2 \AA with a final selection of 156,000 particles; the processing was carried out in RELION.

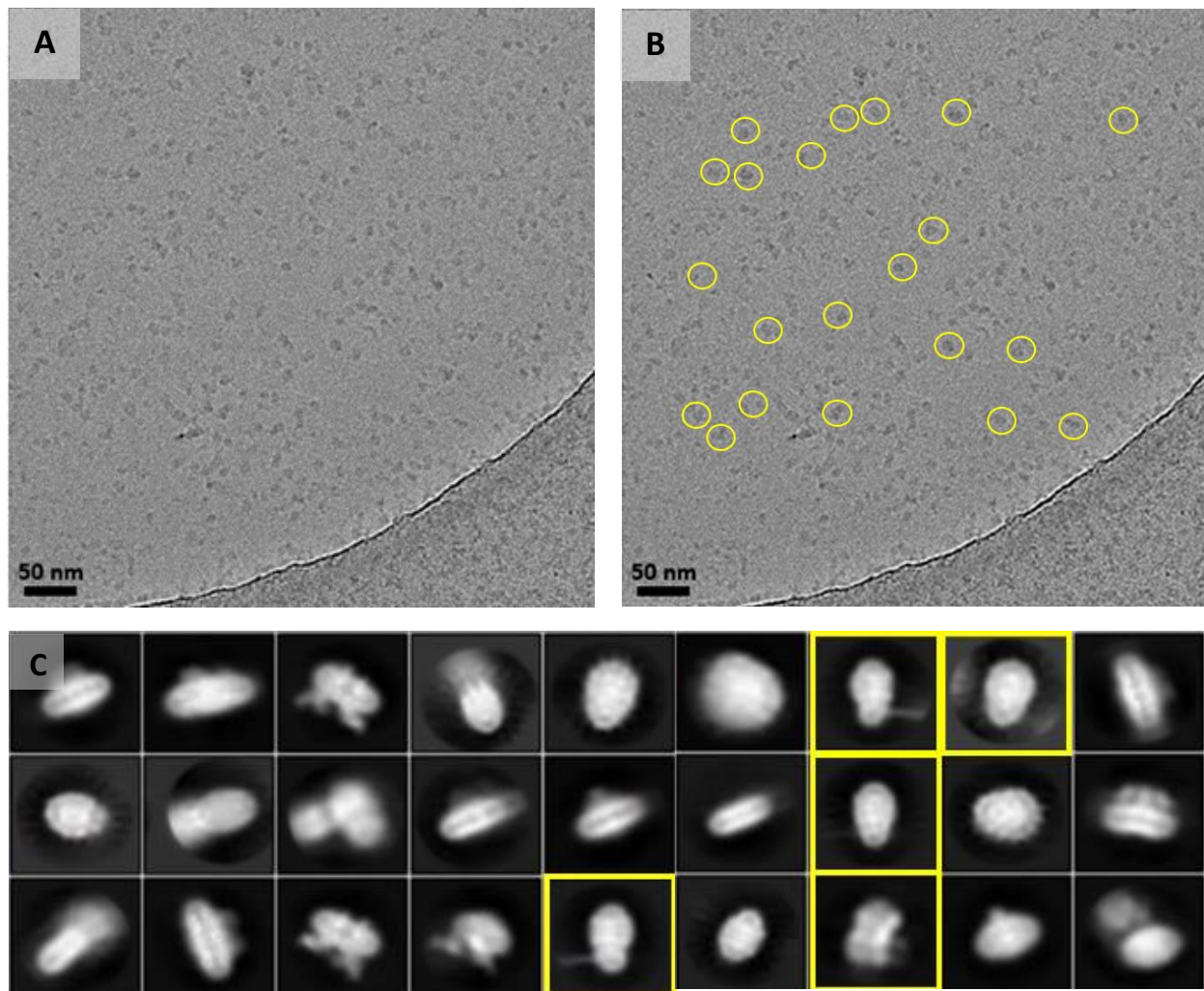


Figure 4.8 | Cryo-EM micrographs of the FNR-*cytb₆f* supercomplex in A8-35

(A) FNR-*cytb₆f* supercomplex reconstituted in A8-35 was applied on cryo-EM grids. It can be observed a good particle distribution and high contrast with the background. (B) Example of particles picked for the 2D classification are circled in yellow. (C) Representative subset of selected 2D classes is shown. Several classes exhibited characteristic feature of the *cytb₆f* complex, however others revealed unusual shapes potentially indicating the presence of the FNR-*cytb₆f* supercomplex (highlighted in yellow).

The resultant model displayed the general *cytb₆f* complex features as observed in previous recent cryo-EM structures (Malone et al., 2019; Sarewicz et al., 2023). No extra densities of proteins interacting with the complex were detected from the overlay of the generated model onto the recent published cryo-EM *cytb₆f* complex structure (Sarewicz et al., 2023)(Figure 4.9). Notably, the resolution of the ISP subunit in our model is quite low (Figure 4.9A). This might be attributed to an increased movement of the ISP head domain to facilitate the electron transfer from the 2Fe-2S cluster to haem *f* of *cyt_f*, resulting from the interaction of the *cytb₆f* complex with other proteins in our sample.

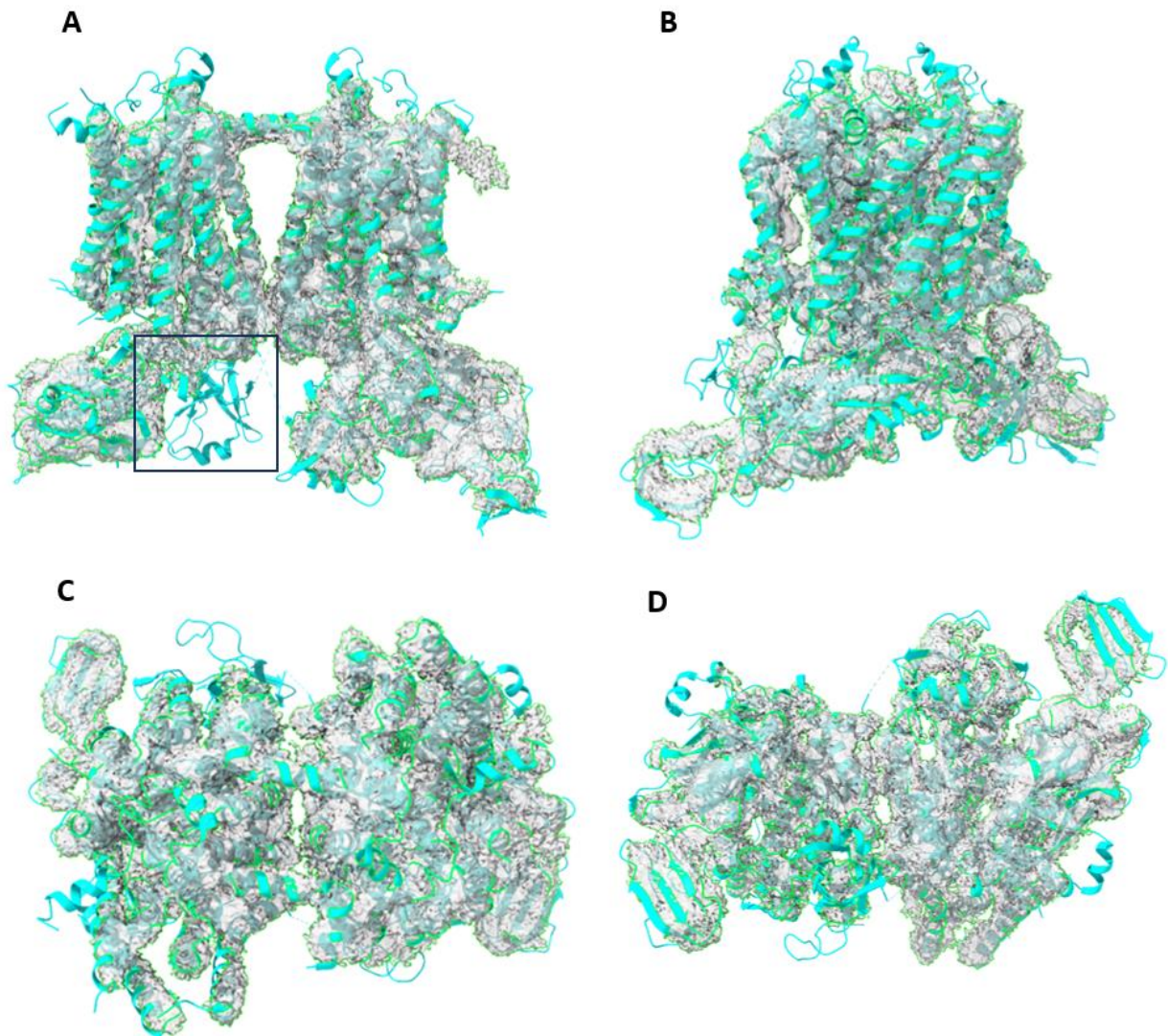


Figure 4.9 | 3D structural model generated from particles extracted from the FNR-*cytb₆f* supercomplex cryo grids overlaid to cryo-EM *cytb₆f* published structure.

Particles extracted from cryo grids prepared with the FNR-*cytb₆f* supercomplex reconstituted in A8-35 were used for the generation of an initial 3D structural model. The model (in grey) was overlaid to a previous 3D model of spinach *cytb₆f* (in cyan) PDB ID: 7ZYV. (A) View in the plane of the membrane. ISP subunit is indicated by a square; the resolution of the subunit in our model is very low possibly due to an increased movement of the ISP head domain to facilitate the electron transfer from the 2Fe-2S cluster to haem *f* of *cyt_f*. (B) Tilted lateral view of the complex. (C) View perpendicular to the membrane from the stromal side. (D) View perpendicular to the membrane from the luminal side.

4.5 Stabilisation of the labile interactions using cross-linkers

As shown above, and consistent with previous work in *Chlamydomonas* (Buchert et al., 2018; Steinbeck et al., 2018), the preservation of the interactions between the components of the FNR-*cytb_{6f}* supercomplex is a major challenge.

Buchert et al., (2018) investigated the use of cross-linkers to stabilise the assembly of the FNR-*cytb_{6f}* supercomplex, specifically the homo-bifunctional disuccinimidyl suberate (DSS) and thiol cleavable DSP (dithiobis(succinimidyl propionate)). In this study, the protein PetO was successfully cross-linked with subIV of the *cytb_{6f}* complex (Buchert et al., 2018).

Therefore, in order to stabilise interactions between the CET effector proteins within our supercomplex we tested DSS, a non-cleavable common cross-linker which uses N-hydroxy succinimide (NHS) esters as the reactive groups (Figure 4.10). NHS esters are highly reactive with the ϵ -amino group of lysine (K) residues and N-termini of amino acids, forming strong amide bonds. To a lesser extent some activity of NHS esters has also been observed with serine (S), threonine (T) and tyrosine (Y) residues. DSS is also a membrane permeable cross-linker and hence enables cross-linking events among transmembrane proteins (K. Lee & O'Reilly, 2023).

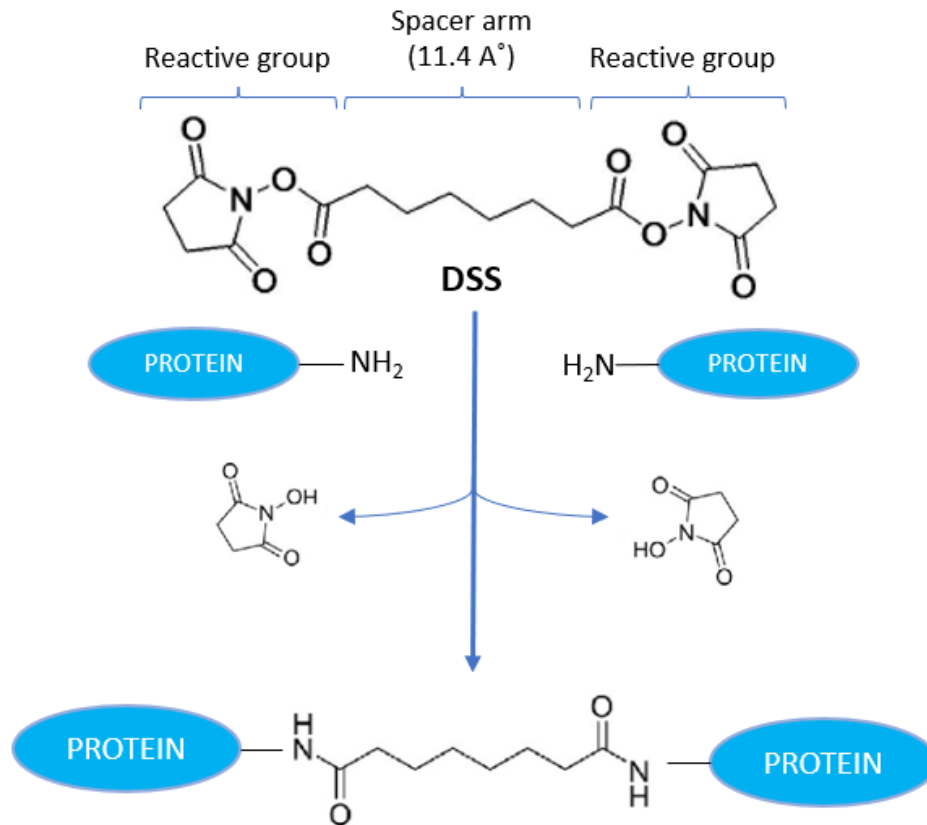


Figure 4.10| Chemical cross-linking with the reagent DSS.

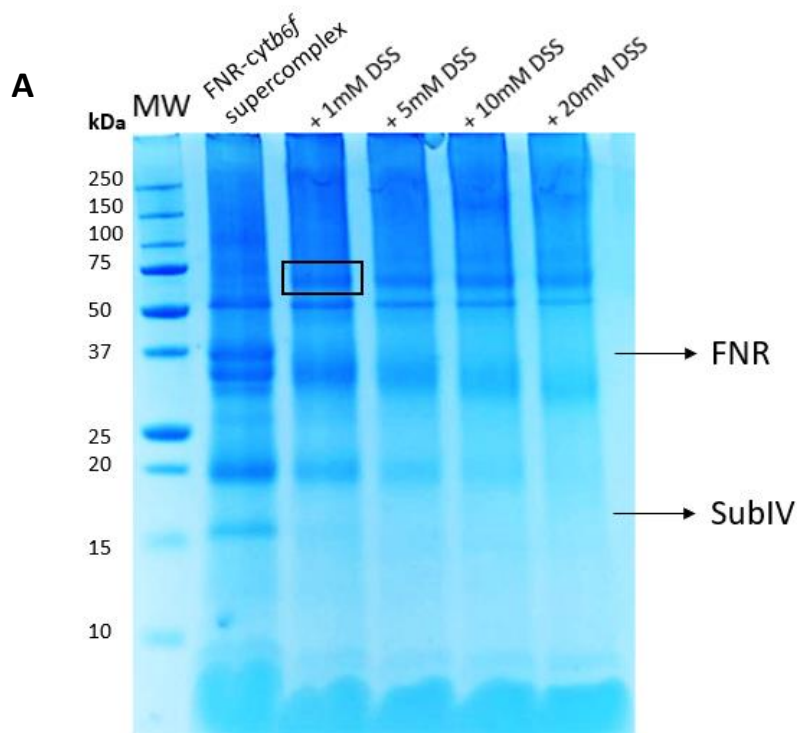
Chemical structure of the cross-linker DSS, characterised by a spacer arm of 11.4 Å. NHS esters react with the amines on the protein resulting in the formation of stable amide bonds and the release of the reactive groups.

To determine the optimum concentration of DSS for successful cross-linking of proteins, varying concentrations were tested (1- 20 mM) and incubated with 5 µM of FNR- *cytb_{6f}* sample prepared in LMNG as described in the method section 2.6.

Initial investigation of the cross-linking events was assessed by analysis of the cross-linked samples by SDS-PAGE (Figure 4.11A). It can be observed that increasing concentrations of DSS lead to a progressive loss of intensity for all bands, suggesting successful cross-linking and a failure of the crosslinked proteins to enter the gel matrix. Interestingly however, at the lowest concentration (1 mM) the FNR and subIV bands, at 35kDa and 15kDa respectively, are lost while most other bands remain present. These changes occur in parallel with the appearance of an additional band at around 50kDa. The additional band was carefully extracted and analysed by mass spectrometry (MS) for protein identification. The quantification strategy chosen in this study is intensity-based absolute quantification (iBAQ). The iBAQ abundance

score¹ is a valid estimation of molar amount for comparisons between analyses. The technique is susceptible to idiosyncratic tryptic cleavage patterns and peptide ionisation properties. The IBAQ value is determined by calculating the sum of the MS intensities of all the tryptic peptides belonging to a protein divided by the number of theoretically observable tryptic peptides of 6-30 amino acid residues and compensates for protein sequence length (Schwanhäusser et al., 2011).

Analysis by MS of the extracted band revealed the presence of both FNR and subIV (Figure 4.11B).



B

IBAQ	N: Unique peptides	N: Unique sequence coverage [%]	T: Fasta headers
52347000	7	50.6	sp P00166 PETD_SPIOL Cytochrome b6-f complex subunit 4 OS=Spinacia oleracea GN=petD
1.53E+08	27	63.1	tr A0A0K9QGT7 A0A0K9QGT7 SPIOL Ferredoxin--NADP reductase, chloroplast OS=Spinacia oleracea GN=SOVF

Figure 4.11 | Optimisation of the concentration of DSS.

(A) Several concentrations of DSS (1-20mM) were tested to determine the optimal one for the crosslinking event to occur. SDS-PAGE analysis shows the disappearance of the FNR band (35 kDa) and subIV (15 kDa) after sample treatment with 1mM DSS, and the appearance of an additional band at around 50 kDa. (B) The 50 kDa band was then carefully extracted and analysed by mass-spectrometry, revealing the presence of both FNR and subIV. IBAQ value, number of peptides found, and % of sequence coverage are also shown.

4.5.1 Detergent exchange of the cross-linked sample from LMNG to GDN

Since the cross-linking event between the *cytb_{6f}* complex and FNR was at least partially successful, we explored whether the cross-linked FNR-*cytb_{6f}* supercomplex would remain stable in GDN instead of LMNG with the aim of improving the quality of the resultant cryo-EM grids. The crosslinked sample was gel filtered in 25 mM HEPES pH 7.5, 25 mM NaCl and 0.006% GDN. The elution profile exhibited several peaks, potentially suggesting the separation of non-cross-linked proteins from the complex and the removal of excess of crosslinkers (Figure 4.12A). The major peak eluting at 8 ml (indicated by a grey arrow), was found to contain the components of the intact FNR-*cytb_{6f}* supercomplex and these were pooled and concentrated for cryo-EM (Figure 4.12B).

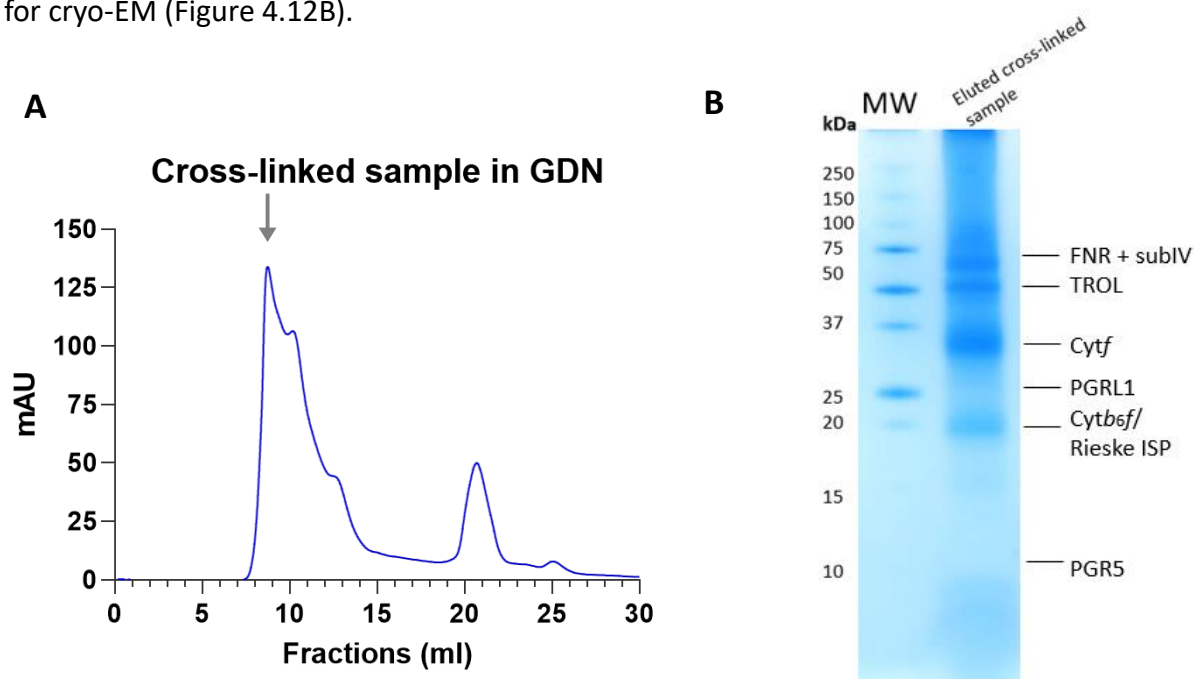


Figure 4.12 | Size exclusion chromatography of the cross-linked sample reconstituted in GDN.

(A) Size exclusion elution profile of the cross-linked sample exchanged into 0.006% GDN. The eluted fractions around 8 ml, indicated by a grey arrow, were pooled, and concentrated for cryo-EM preparation. The elution profile exhibits several peaks which could correspond to proteins that were not cross-linked and excess of cross-linkers. (B) SDS-PAGE analysis, the sample analysed contains the expected bands.

4.5.2 Cryo-EM analysis of cross-linked sample in GDN

The cross-linked FNR-*cytb_{6f}* supercomplex in GDN was applied on Quantifoil R1.2/1/3 400 mesh Cu grids at a final concentration of 14 μ M. Initial screening of the obtained micrographs displayed a good particle distribution and ideal contrast between the particles and the background (Figure 4.13A). 3,216,452 particles were extracted for data processing and around

300 2D classes were generated; unfortunately, none of them exhibited any noticeable *cytb_{6f}* complex features and were poorly defined as shown in a representative subset in Figure 4.13B.

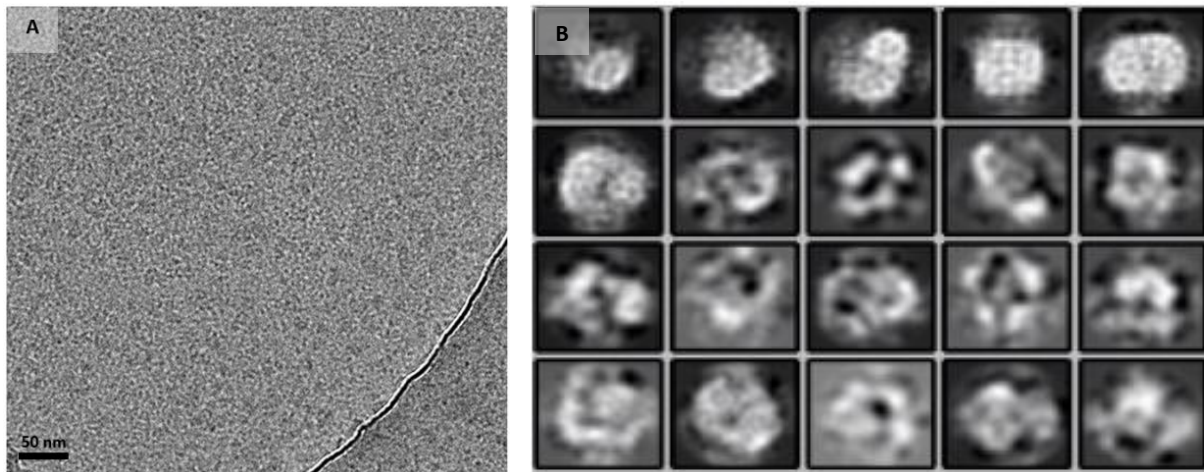


Figure 4.13 | Cryo-EM micrographs of the cross-linked FNR-*cytb_{6f}* supercomplex in GDN.

(A) FNR-*cytb_{6f}* supercomplex cross-linked with DSS and reconstituted in GDN was applied on cryo-EM grids. It can be observed optimum particles distribution and good contrast with the background. (B) Representative subset of selected 2D classes is shown; no *cytb_{6f}* complex features were recognisable and the 2D classes were poorly defined.

4.7 Structural model of the cross-linked FNR-*cytb_{6f}* supercomplex

Following several attempts to structurally characterize the FNR-*cytb_{6f}* supercomplex by cryo-EM, an alternative approach using MS to investigate the protein-protein interactions preserved by cross-linking was employed.

Firstly, all the proteins present in the sample purified in LMNG were identified by MS and their abundance was investigated (Supplementary Figure 1). The quantification strategy chosen in this study is iBAQ and based on this method, the four major subunits of *cytb_{6f}*, along with FNR and TROL, were found among the 40 most abundant proteins within the entire sample. Furthermore, within the 75 most abundant proteins, PGRL1A, PGR5, Tic62 and TSP9 were also detected (Figure 4.14). NdhS, a small subunit of the NDH complex was also found in the sample with a relative lower abundance compared to the other proteins (Supplementary Figure 1).

iBAQ 1	iBAQ 2	iBAQ 3	iBAQ median	N: Unique peptides	N: Unique sequence coverage [%]	T: Fasta headers
1	1.131E+08	1.77E+08	1.13E+08	4	100	sp P69447 ATPH_SPIOL ATP synthase subunit c, chloroplastic OS=Spinacia oleracea GN=atpH
2	1.19E+08	1.28E+08	1.21E+08	22	66.9	sp P16013 CYF_SPIOL Cytochrome f OS=Spinacia oleracea GN=petA
3	92281000	91617000	84088000	14	52.1	tr A0A0K9R361 A0A0K9R361_SPIOL PsbP domain-containing protein OS=Spinacia oleracea GN=SOVF_111890
4	79595000	86727000	82111000	13	68.7	tr A0A0K9QH2 A0A0K9QH2_SPIOL plastocyanin-plastocyanin reductase OS=Spinacia oleracea GN=SOVF_178790
5	64567000	70504000	75906000	9	37.2	sp P00165 CYB6_SPIOL Cytochrome b6 OS=Spinacia oleracea GN=petB
6	61175000	67469000	64566000	8	32.3	tr A0A0K9QLR5 A0A0K9QLR5_SPIOL CAAD domain-containing protein OS=Spinacia oleracea GN=SOVF_164650
7	57942000	63098000	56985000	16	64.7	tr A0A0K9QB7 A0A0K9QB7_SPIOL PAP_fibrillin domain-containing protein OS=Spinacia oleracea GN=SOVF_204200
8	51296000	55434000	50658000	28	66.1	tr A0A0K9QGT7 A0A0K9QGT7_SPIOL Ferredoxin-NADP reductase, chloroplastic OS=Spinacia oleracea GN=SOVF_180280
9	41695000	44107000	40888000	17	35.9	sp P06003 PSB_C_SPIOL Photosystem II CP43 reaction center protein OS=Spinacia oleracea GN=psbC
10	40450000	45360000	40934000	12	57.7	tr A0A0K9RYX2 A0A0K9RYX2_SPIOL PAP_fibrillin domain-containing protein OS=Spinacia oleracea GN=SOVF_018780
11	34540000	39158000	36427000	18	43.3	sp P04160 PSB_SPIOL Photosystem II CP47 reaction center protein OS=Spinacia oleracea GN=psbB
12	32221000	35670000	29852000	7	34.6	tr A0A0K9RVH9 A0A0K9RVH9_SPIOL Photosystem I reaction center subunit III OS=Spinacia oleracea GN=SOVF_023270
13	29575000	32488000	30861000	17	59	tr A0A0K9QUQ7 A0A0K9QUQ7_SPIOL Chlorophyll a-b binding protein, chloroplastic OS=Spinacia oleracea GN=SOVF_146400
14	25641000	31886000	27897000	9	27.8	sp P06005 PSB_SPIOL Photosystem II D2 protein OS=Spinacia oleracea GN=psbD ;tr A0A0K9QC54 A0A0K9QC54_SPIOL Photosystem II D2 protein OS=Spinacia oleracea GN=SOVF_195980
15	26451000	28750000	26213000	4	37.3	sp P69383 PSB_SPIOL Cytochrome b559 subunit alpha OS=Spinacia oleracea GN=psbE
16	25350000	28171000	25815000	9	45.5	tr A0A0K9RJ64 A0A0K9RJ64_SPIOL CAAD domain-containing protein OS=Spinacia oleracea GN=SOVF_060860
17	24877000	26225000	25454000	16	33.8	tr A0A0K9QV97 A0A0K9QV97_SPIOL Rhodanese-like domain-containing protein 4, chloroplastic OS=Spinacia oleracea GN=SOVF_137670
18	22243000	25344000	22535000	8	92.5	tr A0A0K9QGV6 A0A0K9QGV6_SPIOL PGM PMM I domain-containing protein (Fragment) OS=Spinacia oleracea GN=SOVF_215110
19	21074000	22421000	22042000	3	16.3	tr A0A0K9R687 A0A0K9R687_SPIOL Uncharacterized protein OS=Spinacia oleracea GN=SOVF_108060
20	21168000	24333000	21412000	31	68	tr A0A0K9RNN0 A0A0K9RNN0_SPIOL geranylerynyl diphosphate reductase OS=Spinacia oleracea GN=SOVF_046270
21	19170000	21101000	18971000	19	54.7	tr A0A0K9S3L2 A0A0K9S3L2_SPIOL Oxygen-evolving enhancer protein 1, chloroplastic OS=Spinacia oleracea GN=SOVF_003050
22	14764000	18142000	17083000	7	59.2	tr A0A0K9QC55 A0A0K9QC55_SPIOL Carbonic anhydrase OS=Spinacia oleracea GN=SOVF_195830 ;tr A0A0K9QE98 A0A0K9QE98_SPIOL Carbonic anhydrase OS=Spinacia oleracea GN=SOVF_1958
23	13492000	18284000	15901000	3	33.8	tr A0A0K9R9C3 A0A0K9R9C3_SPIOL CAAD domain-containing protein OS=Spinacia oleracea GN=SOVF_042570
24	13722000	15230000	14005000	49	64.7	tr A0A0K9Q9Z1 A0A0K9Q9Z1_SPIOL Glycine cleavage system P protein OS=Spinacia oleracea GN=SOVF_202800
25	12722000	15716000	11364000	12	54.9	sp P06453 ATP_SPIOL ATP synthase subunit b, chloroplastic OS=Spinacia oleracea GN=atpF
26	12457000	14070000	12590000	15	64.5	tr A0A0K9RSV6 A0A0K9RSV6_SPIOL Rhodanese domain-containing protein OS=Spinacia oleracea GN=SOVF_109900
27	11511000	13474000	11829000	17	68.9	tr A0A0K9R856 A0A0K9R856_SPIOL Arginase 1, mitochondrial OS=Spinacia oleracea GN=SOVF_086490
28	10714000	13965000	11528000	3	97.4	sp P60128 PSB_SPIOL Cytochrome b559 subunit beta OS=Spinacia oleracea GN=psbF
29	11485000	11305000	11575000	18	58.4	tr A0A0K9RX22 A0A0K9RX22_SPIOL Serine hydroxymethyltransferase OS=Spinacia oleracea GN=SOVF_019040
30	10466000	12618000	11057000	7	37.9	tr A0A0K9RQK4 A0A0K9RQK4_SPIOL Oxygen-evolving enhancer protein 3-2, chloroplastic OS=Spinacia oleracea GN=SOVF_156430
31	10923000	11180000	10570000	10	24.9	sp P69560 PSA_SPIOL Photosystem II protein D1 OS=Spinacia oleracea GN=psbA
32	10602000	12161000	10737000	15	53.3	tr A0A0K9REI8 A0A0K9REI8_SPIOL PAP_fibrillin domain-containing protein OS=Spinacia oleracea GN=SOVF_075760
33	10289000	11197000	10030000	8	43.1	tr A0A0K9R1K7 A0A0K9R1K7_SPIOL Chlorophyll a-b binding protein, chloroplastic OS=Spinacia oleracea GN=SOVF_123890
34	10011000	11160000	9809300	14	55.6	tr A0A0K9QFF9 A0A0K9QFF9_SPIOL Fructose-bisphosphate aldolase OS=Spinacia oleracea GN=SOVF_190580
35	8572700	9713100	11300000	9	32	tr A0A0K9QQW2 A0A0K9QQW2_SPIOL ATP synthase subunit b, chloroplastic OS=Spinacia oleracea GN=SOVF_151500
36	9377700	8006000	10127000	8	50.6	sp P00166 PETD_SPIOL Cytochrome b6-f complex subunit 4 OS=Spinacia oleracea GN=petD
37	7990400	8899300	8853500	11	37.2	tr A0A0K9RFL8 A0A0K9RFL8_SPIOL Chlorophyll A-B binding protein OS=Spinacia oleracea GN=SOVF_182080
38	8369800	9530100	8688100	26	68.6	tr A0A0K9R2G3 A0A0K9R2G3_SPIOL Hydroperoxide lyase OS=Spinacia oleracea GN=SOVF_120600
39	7711400	9479300	7750400	14	62	tr A0A0K9R9P0 A0A0K9R9P0_SPIOL Rieske domain-containing protein (Fragment) OS=Spinacia oleracea GN=SOVF_044140
40	12260000	4897700	7957500	2	31.7	tr A0A0K9Q8Y8 A0A0K9Q8Y8_SPIOL Photosystem II core complex proteins psbY, chloroplastic OS=Spinacia oleracea GN=SOVF_202020
41	7338900	8189700	7444100	2	17.2	tr A0A0K9RD37 A0A0K9RD37_SPIOL Ribulose biphosphate carboxylase small subunit, chloroplastic OS=Spinacia oleracea GN=RBC5
42	6530200	7141800	7414800	19	48.4	sp P00875 RBL_SPIOL Ribulose biphosphate carboxylase large chain OS=Spinacia oleracea GN=rbcl
43	6684200	7113900	6960900	2	10.7	tr A0A0K9RSQ7 A0A0K9RSQ7_SPIOL Uncharacterized protein OS=Spinacia oleracea GN=SOVF_038190
44	6661900	7137400	6338500	18	42.3	tr A0A0K9RKG9 A0A0K9RKG9_SPIOL NAD(P)-bd dom domain-containing protein OS=Spinacia oleracea GN=SOVF_056230
45	6495200	6907100	6587700	12	50	tr A0A0K9R7D6 A0A0K9R7D6_SPIOL PGR5-like protein 1A, chloroplastic OS=Spinacia oleracea GN=SOVF_098540
46	6354200	7297500	6418500	30	54.5	tr A0A0K9RFL8 A0A0K9RFL8_SPIOL AAA domain-containing protein OS=Spinacia oleracea GN=SOVF_078600
47	5699900	6326700	6313300	35	61.8	tr A0A0K9RD58 A0A0K9RD58_SPIOL AAA domain-containing protein OS=Spinacia oleracea GN=SOVF_080200
48	5782300	47317	6389200	2	20	tr A0A0K9QIU2 A0A0K9QIU2_SPIOL Protein proton gradient regulation 5, chloroplastic-like OS=Spinacia oleracea GN=SOVF_174260
49	5145800	6386600	5693000	2	14.3	tr A0A0K9QYCA A0A0K9QYCA_SPIOL Photosystem II 10 kDa polypeptide, chloroplastic OS=Spinacia oleracea GN=SOVF_132650
50	4540000	5334300	5350400	13	55.8	tr A0A0K9RMD5 A0A0K9RMD5_SPIOL NAD(P)-bd_dom domain-containing protein OS=Spinacia oleracea GN=SOVF_050360
51	4943800	5877300	5259200	28	45.2	tr A0A0K9RCY3 A0A0K9RCY3_SPIOL Rhodanese domain-containing protein OS=Spinacia oleracea GN=SOVF_080110
52	5130600	2754200	5955800	2	24	tr A4F3R4 A4F3R4_SPIOL Chlorophyll a-b binding protein, chloroplastic OS=Spinacia oleracea GN=lhcb1.1
53	4467000	4873000	4713800	17	54.9	tr A0A0K9QG33 A0A0K9QG33_SPIOL PEROXIDASE 4 domain-containing protein OS=Spinacia oleracea GN=SOVF_183170
54	4683600	5303500	4449800	14	42.5	tr A0A0K9R8K2 A0A0K9R8K2_SPIOL ADP/ATP translocase OS=Spinacia oleracea GN=SOVF_057030
55	4077600	4577200	4415500	11	44.2	tr A0A0K9RHM3 A0A0K9RHM3_SPIOL Transmembrane protein OS=Spinacia oleracea GN=SOVF_070480
56	4114900	4693700	4340200	7	37.4	tr A0A0K9RS47 A0A0K9RS47_SPIOL Photosynthetic NDH subcomplex L 2 OS=Spinacia oleracea GN=SOVF_040740
57	4326900	4805300	4326900	14	44.3	tr A0A0K9Q7C4 A0A0K9Q7C4_SPIOL Thylakoid membrane protein slr0575 OS=Spinacia oleracea GN=SOVF_212350
58	4020100	4254300	4234400	3	56.7	tr A0A0K9RWE4 A0A0K9RWE4_SPIOL ATP synthase subunit e, mitochondrial OS=Spinacia oleracea GN=SOVF_022370
59	4136600	5123800	4114700	7	38.6	tr A0A0K9PQP7 A0A0K9PQP7_SPIOL Light-harvesting complex-like protein OHP2, chloroplastic OS=Spinacia oleracea GN=SOVF_156410
60	4047600	3814400	4218200	12	70.8	tr A0A0K9QKH5 A0A0K9QKH5_SPIOL Malate dehydrogenase OS=Spinacia oleracea GN=SOVF_175150
61	3996700	4201800	3984800	20	41.2	tr A0A0K9QQT1 A0A0K9QQT1_SPIOL NAD(P)-bd_dom domain-containing protein OS=Spinacia oleracea GN=SOVF_142800
62	3719000	4619400	3971600	15	61.2	tr A0A0K9QLX6 A0A0K9QLX6_SPIOL Chlorophyll a-b binding protein, chloroplastic OS=Spinacia oleracea GN=SOVF_164340 ;tr A0A0K9Q7Q8 A0A0K9Q7Q8_SPIOL Chlorophyll a-b binding protein
63	3560100	3924400	3854000	19	63.3	tr A0A0K9R5H4 A0A0K9R5H4_SPIOL Glutamate dehydrogenase OS=Spinacia oleracea GN=SOVF_104730
64	3729300	4300900	3843300	28	73.8	tr A0A0K9QAND A0A0K9QAND_SPIOL Amino oxidase domain-containing protein OS=Spinacia oleracea GN=SOVF_206180
65	3700800	4208800	3798900	19	57	tr A0A0K9RF78 A0A0K9RF78_SPIOL PAP_fibrillin domain-containing protein OS=Spinacia oleracea GN=SOVF_073610
66	3733400	3762400	3341900	13	61.3	tr A0A0K9RW58 A0A0K9RW58_SPIOL Chlorophyll a-b binding protein, chloroplastic OS=Spinacia oleracea GN=SOVF_028050
67	3585400	4040300	3397700	21	66	tr A0A0K9S1H1 A0A0K9S1H1_SPIOL Aldo ket red domain-containing protein OS=Spinacia oleracea GN=SOVF_005330
68	3424000	3988900	3577000	12	38.7	tr A0A0K9RYJ2 A0A0K9RYJ2_SPIOL Peptidase_S26 domain-containing protein OS=Spinacia oleracea GN=SOVF_058090
69	3258100	4110100	3342700	1	10.9	tr D2T2F7 D2T2F7_SPIOL Chlorophyll a-b binding protein, chloroplastic OS=Spinacia oleracea GN=lhcb1.4 ;tr A4F3R3 A4F3R3_SPIOL Chlorophyll a-b binding protein, chloroplastic OS=Spinacia oleracea
70	3052500	3565100	3339300	30	58.8	tr A0A0K9RIA9 A0A0K9RIA9_SPIOL Tyrosinase Cu-bd domain-containing protein OS=Spinacia oleracea GN=SOVF_068770
71	3259200	3649600	3305400	8	35	tr A0A0K9QT57 A0A0K9QT57_SPIOL Photosystem II 22 kDa protein, chloroplastic OS=Spinacia oleracea GN=SOVF_144080
72	3172900	3268100	3259100	15	61	tr A0A0K9QW03 A0A0K9QW03_SPIOL Mg-por_mtrn C domain-containing protein OS=Spinacia oleracea GN=SOVF_135020
73	3019200	3345000	2710900	18	60.6	tr A0A0K9RV67 A0A0K9RV67_SPIOL PSII_BNR domain-containing protein OS=Spinacia oleracea GN=SOVF_031790
74	2966700	3134800	2848200	7	26.3	tr A0A0K9RH46 A0A0K9RH46_SPIOL Ubiquitin-like domain-containing protein OS=Spinacia oleracea GN=SOVF_067260
75	2713400	3655100	2772600	2	20.4	tr Q8GT36 Q8GT36_SPIOL Thylakoid soluble phosphoprotein OS=Spinacia oleracea GN=tsp9

Figure 4.14| Total proteins analysis of the sample purified in LMNG by MS.

Proteins identified in the sample purified in LMNG are here displayed based on their relative abundance in the sample. The order of the proteins in the table was based on the median of the iBAQ values from triplicate analyses. Proteins that are part of the FNR-cytb₆f supercomplex are highlighted in yellow.

The cross-links between the different proteins identified by MS were then identified and analysed by using Byonic. Mono-links and intra-protein cross-links were excluded, and we proceeded with the analysis of only inter-protein cross-links between the CET effector proteins by performing multiple searches in the database.

Following this approach, the cross-links detected in the sample were investigated and the building of a structural model of the FNR-cyt b_6f supercomplex was attempted to gain new insights into the potential interactions among the CET effector proteins. The structural model was constructed on UCSF ChimeraX (v 1.6) by constraining distances between the cross-linked residues to 11Å or less while avoiding steric clashes.

Cross-links were found between FNR and subIV of the cytb $6f$ complex (Figure 4.15A). The peptide “FNGLAWLFLGVPTSSSLYKEEFK” of the NADP⁺ binding domain of FNR was found to be cross-linked to the peptide “MGVTK” of the N-terminus of subIV. In this unique peptide pair, the cross-linking occurred between the residue K268 of FNR and T4 of subIV (Figure 4.15C); K5 of subIV could have not been cross-linked to the K268 since this was the cleavage site of the peptide.

Analysis of the constructed structural model of FNR and cytb $6f$ complex (Figure 4.15B) showed that the distance between the FADH₂ cofactor of FNR and the haem c_n is approximately 28 Å. However, distances exceeding 14 Å are not optimal for an electron transfer event to occur (Moser and Dutton, 1995).

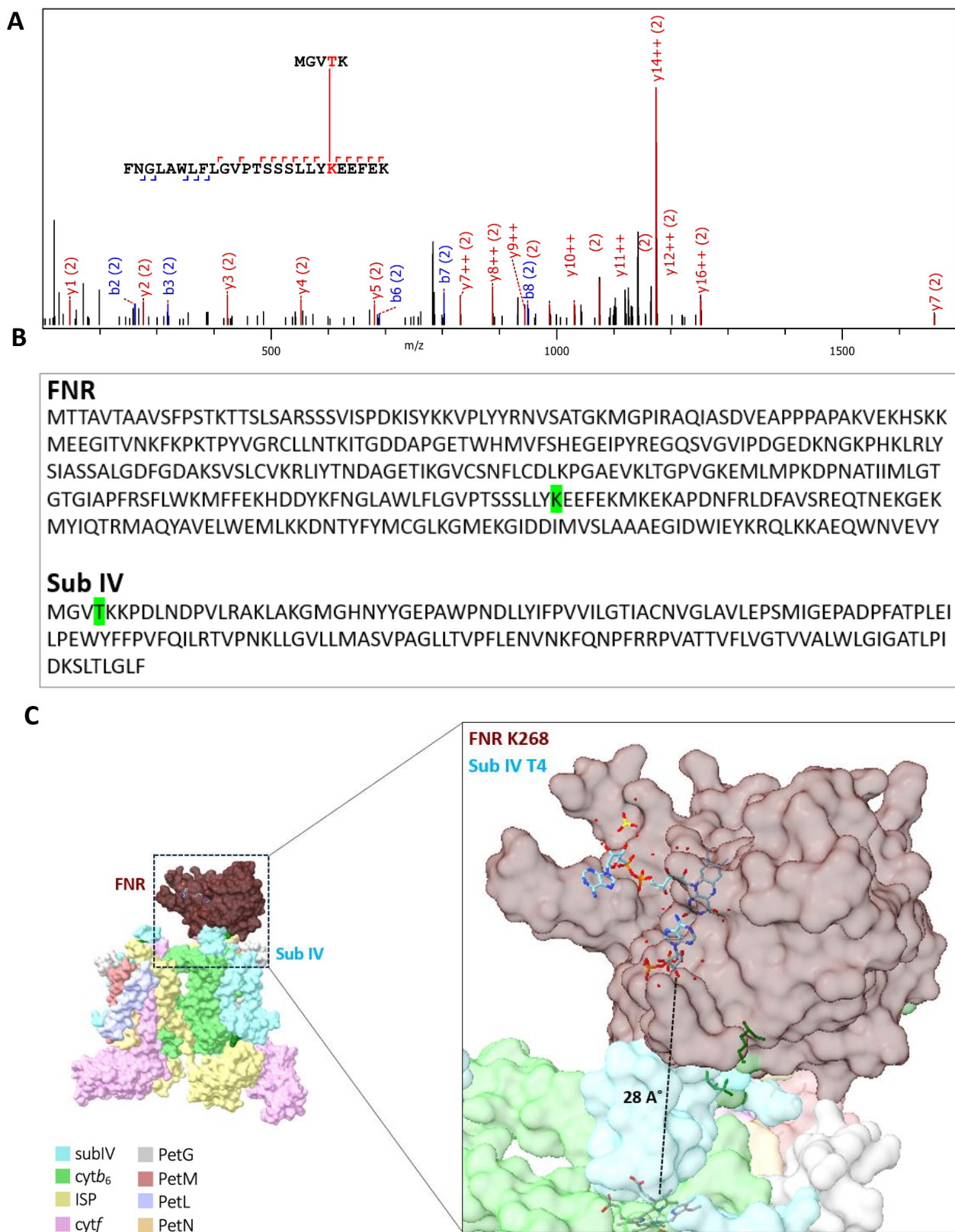


Figure 4.15 | Cross-linking between FNR and subIV.

A) Interlink product ion spectra of subIV and FNR. (B) FNR and subIV protein sequences. Highlighted in green the cross-linked residues of FNR (K268) and of subIV (T4). (C) Structural model of FNR cross-linked to subIV of the *cytb₆f* complex was constructed by constraining distances between the cross-linked residues to 11 Å or less while avoiding steric clashes. Within these constraints, the distance between the FADH₂ cofactor of FNR and haem *c_n* of the *cytb₆f* complex is of 28 Å PDB IDs: FNR (ID: P00455); *cytb₆f* complex (ID: 6RQF).

SubIV was also found to be cross-linked to PGR5. Either residues K5 or K6 in subIV were cross-linked to K53 of PGR5 (Figure 4.16A). For the construction of this model, PGR5 AlphaFold predicted structure was used, which is similar to the unstructured protein found in the NDH supercomplex in barley (Shen et al., 2022). The structural model depicted in Figure 4.16B suggests the potential of PGR5 to facilitate the binding of FNR to the *cyt_bef* complex. This possible role of PGR5 is also supported by the evidence of cross-links found between FNR and PGR5 (Figure 4.17A).

A

PGR5
MAMATSSIPTTGFKNAGLGTFSFASGENYGMVLKSVSSQARVPSRPTRAQPMMKNVNEGKGLFAPLVMVTRDI VGKKRFNQLRGKAIALHSQVITEFCKSIGADAKQRQGLIRLAKKNGEKLGFLA
Sub IV
MGVTKKPDLNDPVLRAKLAKGMGHNYGPAWPNDLLYIFPVVILGTIACNVGLAVLEPSMIGEPADPFATPLEI LPEWYFFPVFQILRTVPNKLLGVLLMASVPAGLLTVPFLENVNFQNPFRRPVATTVFLVGTVVALLWLGIGATLPI DKSLTLGLF

B

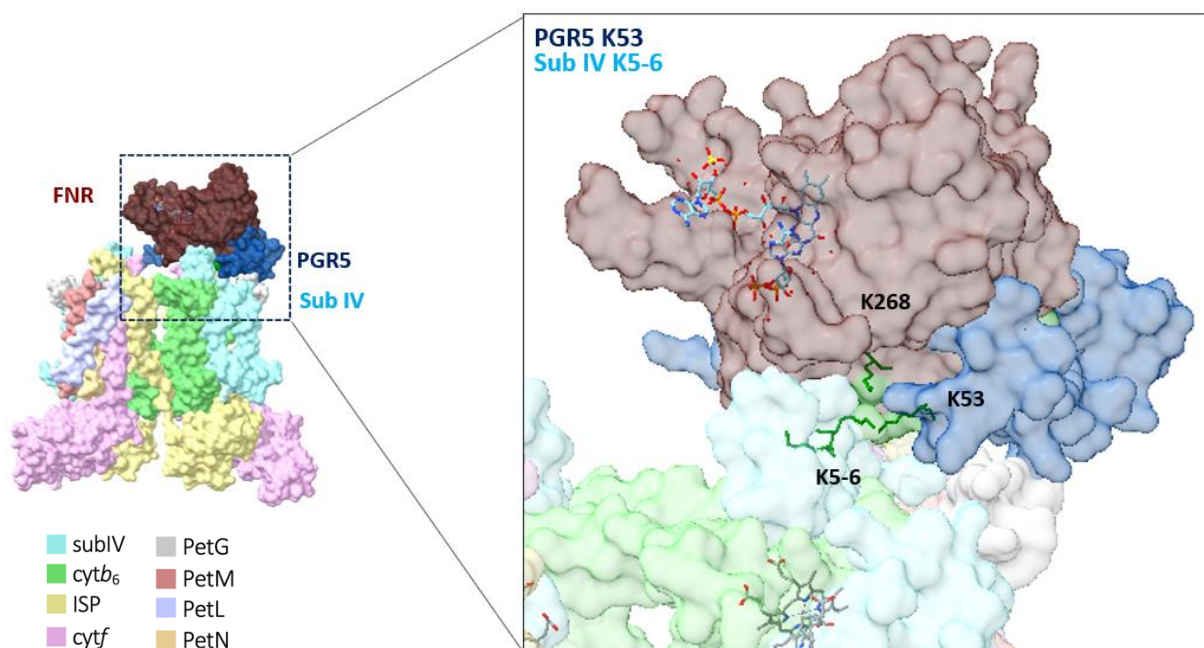


Figure 4.16 | Cross-linking between PGR5 and subIV.

(A) PGR5 and subIV protein sequences. Highlighted in green the cross-linked residues of PGR5 (K53) and of subIV (K5/6). (B) Structural model of PGR5 cross-linked to subunit IV of the *cyt_bef* complex was constructed by constraining distances between the cross-linked residues to 11 Å or less while avoiding steric clashes. The residue K268 of FNR cross-linked to the subIV of *cyt_bef* complex is also shown. PDB IDs: FNR (ID: P00455); *cyt_bef* complex (ID: 6RQF). UniProt entry PGR5: A0A0K9QIU2.

K195 of FNR was found to cross-linked to either K53 or K59 of PGR5 (4.17A). As previously shown, K53 was also found to interact with subIV of the *cyt_bf* complex. Therefore, it is likely that K59 is the residue interacting with K195 of FNR (Figure 4.17B).

A

<p>FNR MTTAVTAAVSPSTKTTSLSARSSSVISPDKISYKKVPLYRNVSATGKMGP IRAQIASDVEAPPAPAKVEKHSKK MEEGITVNFKFKPTPYVGRCLLNTKITGDDAPGETWHMVF SHEGEIPIYREGQSVGVIPDGEDKNGKPHKLRLY SIASSALGDFGDAKSVSLCVKRLIYTNDAGETIKGVCSNFLCDL KPGAEVKLTGPVGKEMLMPKDPNATIIMLGT GTGIAPFRSFLWKMF FEKHDDYKFNGLAWLFLGVPTSSSLLYKEEFEKMKEKAPDNFRLDFAVSREQTNEKGEK MYIQTRMAQYAVELWEMLKKNNTYFYMCGLKGMKGGIDDIMVSLAAAEGIDWIEYKRQLKKAEQWNVVEVY</p> <p>PGR5 MAMATSSIPTTGFKNAGLGT SFASGENY GMLVKS VSSQARVPSRPTRAQPM MKNVNEG KGLFAPLVMVTRDI VGKKRFNQLRGKAIALHSQVITEFCKSIGADAKQRQGLIRLAKKNGEKLGFLA</p>
--

B

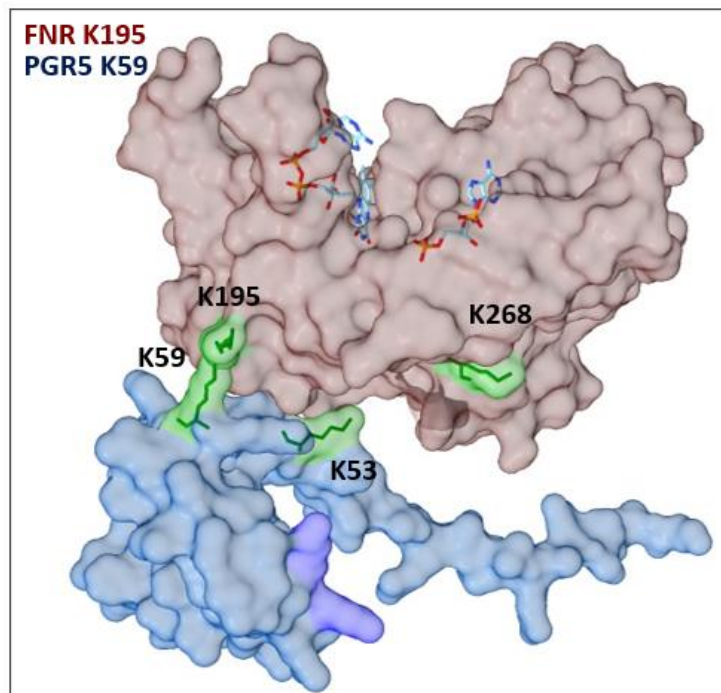


Figure 4.17 | Cross-linking between PGR5 and FNR.

(A) PGR5 and FNR protein sequences. Highlighted in green the cross-linked residues of PGR5 (K59) and of FNR (K195). (B) Structural model of PGR5 crosslinked to FNR and cross-linked residues highlighted in green are indicated. PGR5 K53 and FNR K268 cross-linked with subIV of the *cyt_bf* complex are also shown. PDB ID FNR: P00455. UniProt entry PGR5: A0A0K9QIU2.

Further searches were conducted to investigate the interaction between PGR5 and the other effector protein PGRL1. Despite many studies that show PGR5 to interact with PGRL1 (Hertle et al., 2013; Rühle et al., 2021), no cross-links were found between these two proteins.

However, PGRL1A was also found to be cross-linked with subIV of *cyt_bf* complex (Figure 4.18). The PGRL1A K164, located in one of the two transmembrane domains of the protein, is found to be cross-linked with the K94 of one of the three transmembrane α -helices of subIV. For the construction of this model, the PGRL1a structured predicted by AlphaFold was used.

A

<p>Sub IV MGVTKKPDLNDPVLRAKLAKGMGHNYGEPAWPNDLLYIFPVVILGTIACNVGLAVLEPSMIGEPADPFATPLEI LPEWYFFPVFQILRTVPN^KLLGVLLMASVPAGLLTVPFLENVNKFQNPFRRPVATTVFLVGTVVVALWLGIGATLPI DKSLTLGLF</p> <p>PGRL1A MASKLGVAALTSPRIFSAPRRKPLVTVSTASPLSFLKDASSQFMAVRRRLAVRRRFLLLAPNAATDKQGQTGGED ETIDSNMLQYCSIDKKAKKSIGDLEQDFLQALQSFYYEGKAVMSNEEFNLKEELMWEGSSIVMLSPDEQRFLE ASMAYVAGKPILSD^KEFDELKMNLKTGGSMIVVEGPRCSLSRQVSDLSVDYFKMFLNVPAAVVALGLFFFLD DLTGFEITVLELPEPFISFITWFAALPAILWLSQAITKLIVRDFLILKGTCPNCGTENLSFFGTILSVSSGGATNSVKC SDCGTKLEFDSSKRMLTIPEGSQA</p>
--

B

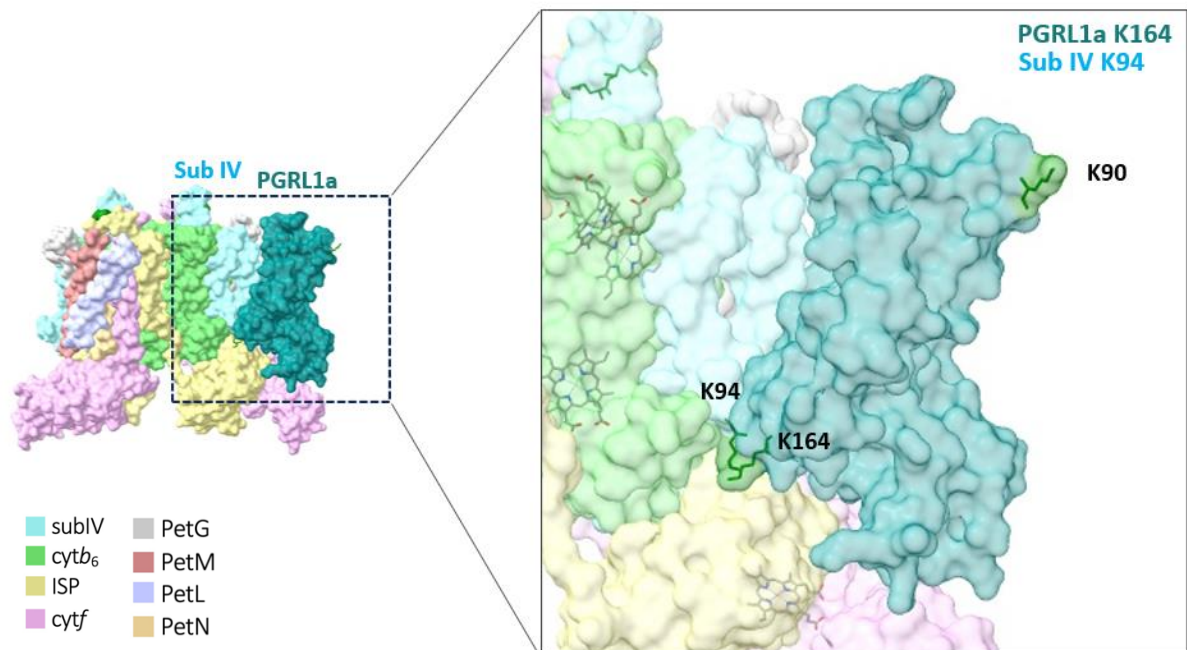


Figure 4.18 | Cross-linking between subIV and PGRL1a.

(A) SubIV and PGRL1a protein sequences. Highlighted in green the cross-linked residues of PGRL1A (K164) and of suBIV (K94). (B) Structural model of PGRL1A crosslinked to subIV of the *cyt_bf* complex; cross-linked residues are highlighted in green. PDB ID *cyt_bf* complex: 6RQF. UniProt entry PGRL1A: A0A0K9R7D6.

Cross-links were also identified between PGRL1A K90 and FNR residue K330 (Figure 4.19A). Analysis of the structural model revealed that FNR binds to the N-terminus of PGRL1A. This is

consistent with the topology of PGRL1A, as previous studies demonstrated that the N- and C-terminus of the protein are exposed to the stromal side of the thylakoid membrane, with two transmembrane domains separated by a loop of 19 amino acids (DalCorso et al., 2008). Furthermore, according to the cross-linking data, the active site of FNR is hindered by the binding with PGRL1a, thereby preventing its interaction with ferredoxin (Figure 4.19B).

A

<p>FNR MTTAVTAAVSFPSTKTTSL SARSSSVISPDKISYKKVPLYRNV SATGKMGP IRAQIASDVEAPPPAPAKVEKHSKK MEEGITV NKF PKTPYVGRCLLNTKITGDDAPGETWHMVF SHEGEIPYREGQSVGVIPDGEDKNGKPHKLRLY SIASSALGDFGDAKSVSLCVKRLIYTNDAGETIKGVCSNFLCDLKP GAEVKLTGPV GKEMLMPKDPNATIIMLGT GTGIAPFRSFLWKMFFEKHDDYKFNGLAWLFLGVPTSSSLLYKEEFEKMKEKAPDNFRLDFAVSREQTNEKGEK MYIQTRMAQYAVELWEMLKKNNTYFYMCGL K330 GMEKGIDDIMVSLAAAE GIDWIEYKRQLKKA EQWNVEVY</p> <p>PGRL1A MASKLGVAALTS PRIFSAPRRKPLVTVSTASPLSFLKDASSQFMAVRRRLAVRRRFLLLAPNAATDKQGQTGGED ETIDSNMLQYCSID K90 KAKKSIGDLEQDFLQALQSFY YEGKAVMSNEEFDNLKEELMWEGSSIVMLSPDEQRFL E ASMAYVAGKPI LSDKEFDELKMNLKTGGSMIVVEGPRCSLRSRKVYSDLSVDYFKMFLLNVPAAVVALGLFFFLD DLTGFEITVLELPEPFSFIFTWFAALPAILWLSQAITKLIVRDFLILKGTCPNCGTENLSFFGTILSVSSGGATNSVKC SDCGTKLEFDSSKRMLTIPEGSQA</p>

B

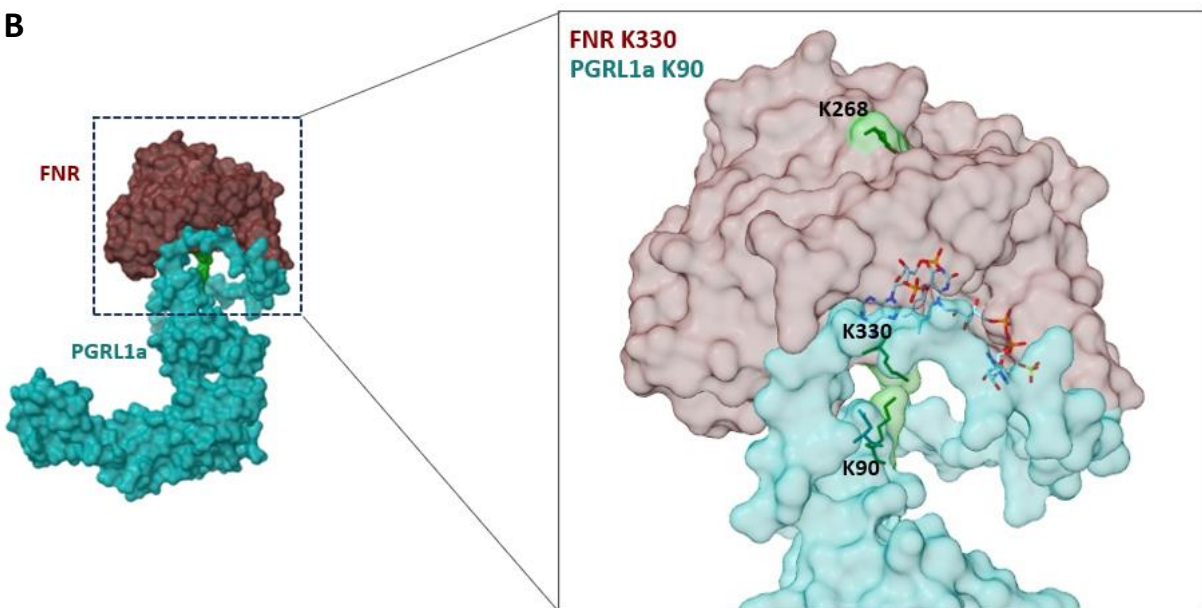


Figure 4.19 | Cross-linking between PGRL1a and FNR.

(A) PGRL1a and FNR protein sequences. Highlighted in green the cross-linked residues of PGRL1a (K90) and of FNR (K330). (B) Structural model of PGRL1a crosslinked to FNR; cross-linked residues are highlighted in green. FNR K268 cross-linked with subIV of the *cyt_bf* complex is also indicated. PDB ID FNR: P00455. UniProt entry PGRL1a: A0A0K9R7D6

Cross-links were also identified between FNR and the transmembrane protein TROL, via the residue K33/35 of FNR and K315 of TROL (Figure 4.20A). However, the FNR binding motif

identified in the Arabidopsis sequence of TROL is from residue 429 to 466; this sequence is also called ITEP binding motif, named after the first four amino acids of this region (Jurić *et al.*, 2009; Alte *et al.*, 2010). A previous study conducted by Alte *et al.*, al in 2010 demonstrated that the FNR binding motif induces the self-assembly of two FNR molecules. Several residues have been found to interact in the FNR interface region with the stroma-exposed C-terminus of TROL, in particular the residues 28-42; this is consistent with the identified cross-links.

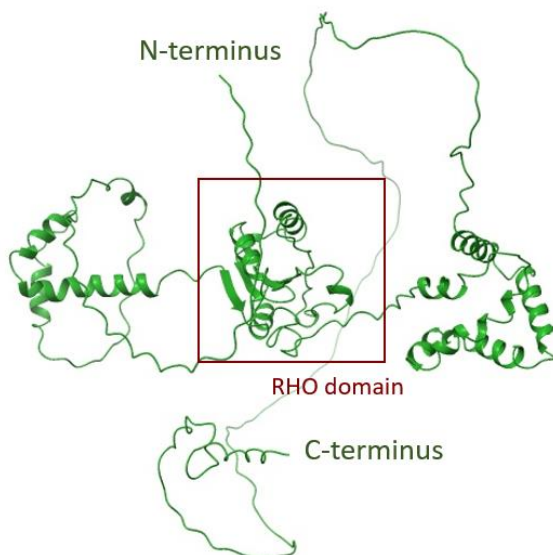
TROL is characterised by two transmembrane domains and an inactive RHO-domain faces the lumen (Vojta and Fulgosi, 2019). To this day, no cryo-EM structures of the protein have been published and the predicted structure generated by AlphaFold is too poorly defined for building a structural model on ChimeraX (Figure 4.20B). Hence, a simple schematic depiction of TROL is shown in figure 4.20C with FNR interacting with the C-terminus of the protein (Figure 4.20C).

A

TROL
 MEALNAVRLKPICGVDPDQIRGIPRKIPQIPTLPSLKFPQITINPPKFTEDFARKFHGSLLLLASSAFSANFAGALTYEE
 ALEQSVNADVGAEFDAGSVVETIVQNPPLIAGGVAVIAVPLVLSQVFGSKPKPFGVQSAKIAYAKIGEEPNAQLLD
 IRSLKESREVGSPDIRGLKKKAVSIVYRGEDKPGFLQKLSLKFKDPENTTLYILDKFDGNSELVAELVTANGFKSAYAI
 KDGAEGPRGWMNSKLPWILPKKTFSLDFSAALTEAFGESADGLPVLGIGAAAAAGFGLLAFTEMETLLQLLSAA
 IVQLLSKLLFAEDRKQTLGQLDEFLNPKVAPNELVSDIKKIGTALLPITVNDKALPAPEEAAPVAVAENSFQKTESV
 PAQPAPPEPQTEAEAPAQPAPPEPLAEAEAEAPAPEPLAEAEAPAPEPLAEAEAPAQPAPPEPLAEAPAEISSTPQKE
 VNTASHQRPLSPYAAYPDLKPPTSPCPSQP

FNR
 MTTAVTAAVSFPSTKTTLSARSSSVISPDKISYKVKVPLYRNVSATGKMGPPIRAQIASDVEAPPPAPAKVEKHSKK
 MEEGIVTNKFKPKTPYVGRCLLNTKITGDDAPGETWHMVFSEHEGIPYREGQSVGVIPDGEDKNGKPHKLRLY
 SIASSALGDFGDAKSVSLCVKRLIYTNDAGETIKGVCNFCDLKPGAEVKLTGPVKGKEMLMPKDPNATIIMLGT
 GTGIAPFRSFLWKMFFEKHDDYKFNGLAWLFLGVPTSSSLYKEEFKMKKEKAPDNFRDLFAVSREQTNEKGEK
 MYIQTRMAQYAVELWEMLKKDNTYFYMCGLKGMKGGIDDIMVSLAAAEIDWIEYKRQLKKAQWNVVEVY

B



C

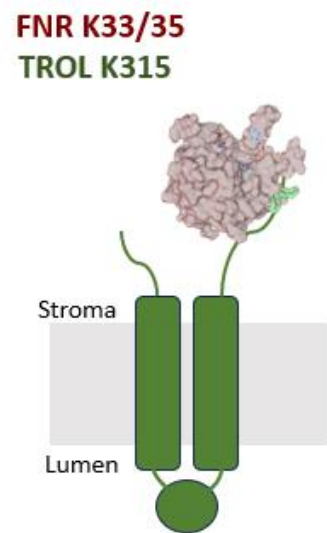


Figure 4.20 | Cross-linking between TROL and FNR.

(A) TROL and FNR protein sequences. Transmembrane α -helices are highlighted in yellow, while the RHO domain in red. Cross-linked residues of TROL (K315) and of FNR (K33/35) are highlighted in green. (B) AlphaFold predicted structure of TROL. UniParc entry: UPI0006BE88BE. (C) Structural model of FNR cross-linked to TROL C-terminus. PDB ID FNR: P00455.

Another interaction partner of FNR is Tic62. As in TROL, the FNR binding region in Tic62 is located at the C-terminus and is characterised by a highly conserved KPPSP motif (Balsera et al., 2007). FNR was also found cross-linked with Tic62; FNR K129 was cross-linked with either T678 or S679 (Figure 4.21A). Despite the cross-linked residue of Tic62 is located in the C-terminus of the protein, previous findings have identified with the use of Surface Plasmon Resonance (SPR) analysis a stretch of 58 amino acids from pea Tic62 which would interact with FNR (aa354-411), which differs from our cross-linking findings (Alte et al., 2010).

The AlphaFold predicted structure of Tic62 is not ideal for the construction of the model with the use of ChimeraX, as shown in figure 4.21B. In addition, the protein is characterised by a hydrophilic profile which suggests it faces the stromal side of the thylakoid membrane and a hydrophobic region which favours the attachment of Tic62 to the membrane or to other Tic complexes (Figure 4.21A) (Kekic et al., 2020). A simple schematic representation of Tic62 and its binding with FNR is shown in figure 4.21C.

A

Tic62
 MQNSLSISSQMELRSLQHSSSPLTNLPTSLLFRSNLVKRSYLYDQIIFSSSVKYPGARRFQNFQIKAQL
 SSGATRFSSSTVEATAESLDSKDEDVVFVAGATGKVGSRVRELLKLGVRVKAQVRSQAQRAESLVQSVKQLKV
 DTDATSARKPIEMLEIVECDLEKPGQIAPALGRASVVICCI GASEKEIFDVTGPYRIDFMATKNLIDAATVA
 KVDHFILLTSLGTNKVGFPAAILNLFWGVLCWKRKAEEALIASGLPYSIVRPGGMERPTDSFKETHNLTLA
 QDDTLFGGLVSNLQVAELLAFAFMAQNRSLSYCKIVEVVAETTAPLTPMAELLVKIPSKRKELQKPENQTPE
 APKTSRASPETSMVTEATSILKEEELSKEKLEEQDPTTKALEAESAKSFTTEVPTDVAIEESVLEGSMESE
 PLSPFTMYDDLKPPSSPCPTTPSFPSDQGKQTGPVSTEPGIPDTSTISIPETEADTAETATVELQKMQLS
 PYTAYEDLKPPSSPSPGNSRVSLETSKTVDGVPQNIDGNGALAEDVQQLIFHSPYSAYEDLKPPPTS
 PTPAAPSSLATSMTSADSESQTDSLNNGAVEPVQENDAEDQTSLQPKSRPLSPYTMIEDLKPPTSPTP
 TAPILATSITSAVAESQTASLSNNGAVEPVEGHDAEDKQTSIHPKPRPLSPYAMYEDLKPPTSPTPTAPILAS
 SITSVAESQTASLSNIGVVEPVEEHDAEDKQTSIQPKPRPLSPYTMYYDDMKPPSSPMPSPGNH

FNR
 MTTAVTAAVSPSTKTTSLARSSSVISPKISYKVKVPLLYRNVSATGKMGPRAQIASDVEAPPAPAKVEKHSKK
 MEEGITVNFKPKTPYVGRCLLNTKITGDDAPGETWHMVFSHEGEIPYREGQSVGVIPDGEDKNGKPHKLRLY
 SIASSALGDFGDAKSVSLCVKRLIYTNDAGETIIGVCSNFLCDLKPGAIEVKTGPVKGEMLMKDPNATIIMLGT
 GTGIAPFRSFLWKMFFEKHDDYKFNGLAWLFLGVPTSSSLYKEEFKMKKAPDNFRLDFAVSREQTNEKGEK
 MYIQTRMAQYAVELWEMLKDKNTYFYMCGLKGMKGGIDDIMVSLAAAEGLDWIEYKRQLKKAEQWNVEVY

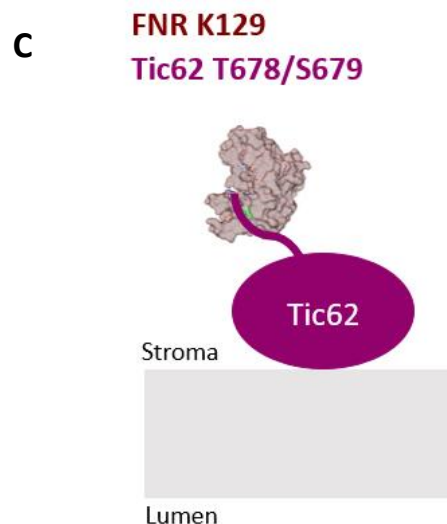
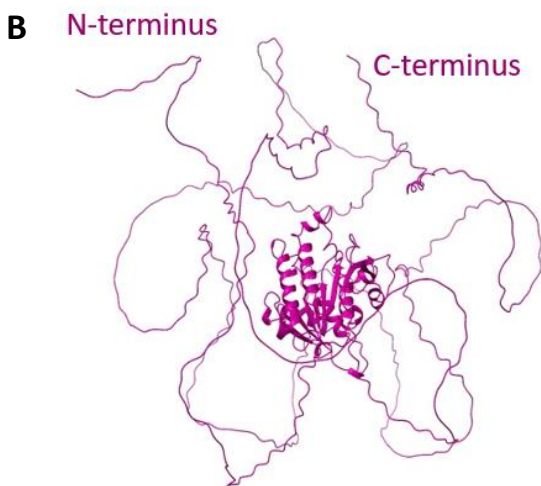


Figure 4.21 | Cross-linking between FNR and Tic62.

(A) Tic62 and FNR protein sequences. Cross-linked residues of Tic62 (T678/S679) and of FNR (K129) are highlighted in green. Residues of the hydrophobic region involved in membrane/Tic complex binding are shown in orange. (B) AlphaFold predicted structure of Tic62. UniProt entry: A0A0K9QTQ1. (C) Structural model of FNR crosslinked to Tic62 C-terminus. PDB ID FNR: P00455.

Furthermore, analysis of the sample by MS revealed the presence of NdhS, small stromal exposed subunit of the NDH complex. Recent studies have shown that NdhS interacts with the *cytb₆f* complex, specifically to subIV (Lan et al., 2023).

In addition, the protein TSP9 was also identified. TSP9 is a *cytb₆f* binding partner and it is involved in the regulation of state transitions. Recent cryo-EM structure of spinach *cytb₆f*

revealed the binding of TSP9 to *cytb₆* in a similar region where PetP is bound in the cyanobacterial *cytb_{6f}* (Proctor et al., 2022; Sarewicz et al., 2023). Both proteins could be involved in the regulation of LET and CET in plants and cyanobacteria. However, no cross-links were identified between NdhS, TSP9 and *cytb_{6f}*.

4.8 PetP pulldown

Since the cross-linking data showed the interaction between FNR and subIV, we hypothesised that FNR binding would prohibit the interaction with the cyanobacterial subunit PetP, which is absent from the genome of plants and green algae (Proctor et al., 2022).

To test this idea, we firstly investigated whether PetP would be able to pull-down *cytb_{6f}* complexes from spinach. C-terminal His₆-tagged PetP was bound to a charged Ni²⁺ resin and spinach thylakoid membranes were solubilised at 2mg/ml in 2% GDN for 1 hour at 4°C. Insolubilised material was pelleted and the supernatant was applied to columns with and without PetP, as negative control. After several washes, a significant amount of *cytb_{6f}* was retained by the column and co-eluted with PetP. The results from the SDS-PAGE analysis confirmed that the *cytb_{6f}* complexes were effectively purified from all species suggesting the binding site for PetP is conserved (Figure 4.22).

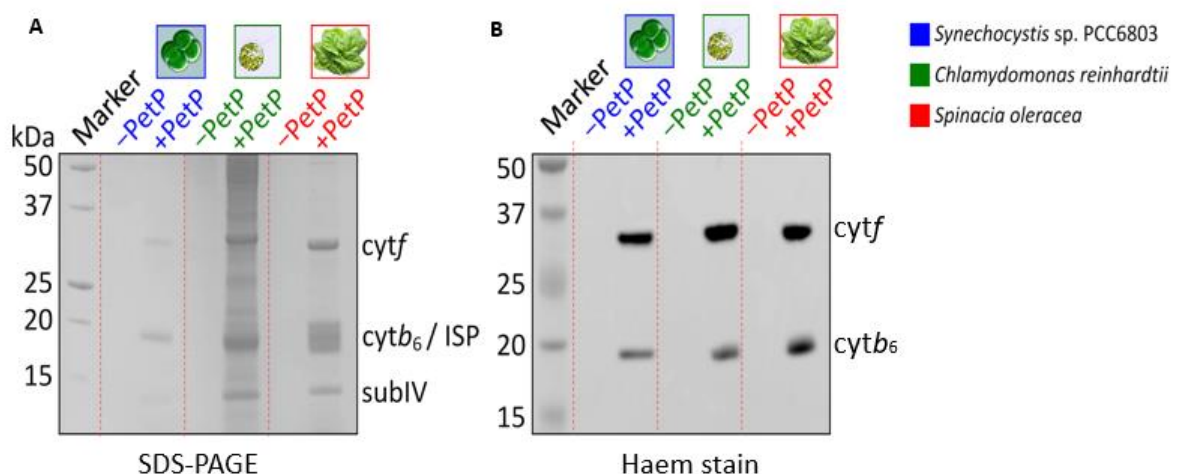


Figure 4.22 | PetP pulldown of *cytb_{6f}* complex from different photosynthetic organisms.

(A) Solubilised thylakoid membranes from *Synechocystis*, *Chlamydomonas* and spinach were applied to column with and without PetP. SDS-PAGE of the eluted samples confirmed the successful purification of *cytb_{6f}* complexes from the PetP pulldown. The four main subunits of *cytb_{6f}* are indicated. (B) Haem blot of the purified sample.

Once it was established that the *cytb₆f* from spinach could indeed interact with PetP, our next step involved investigating whether the binding of FNR to *cytb₆f* would inhibit its interaction with the PetP bound column. To do so, the FNR-*cytb₆f* supercomplex was purified using LMNG and then subjected to interaction with the PetP column (Figure 4.23A). Interestingly, the flow-through contained FNR and *cytb₆f*, whereas the eluted sample contained *cytb₆f* only, as confirmed by SDS-PAGE and FNR western blot analysis in figure 4.23B-C.

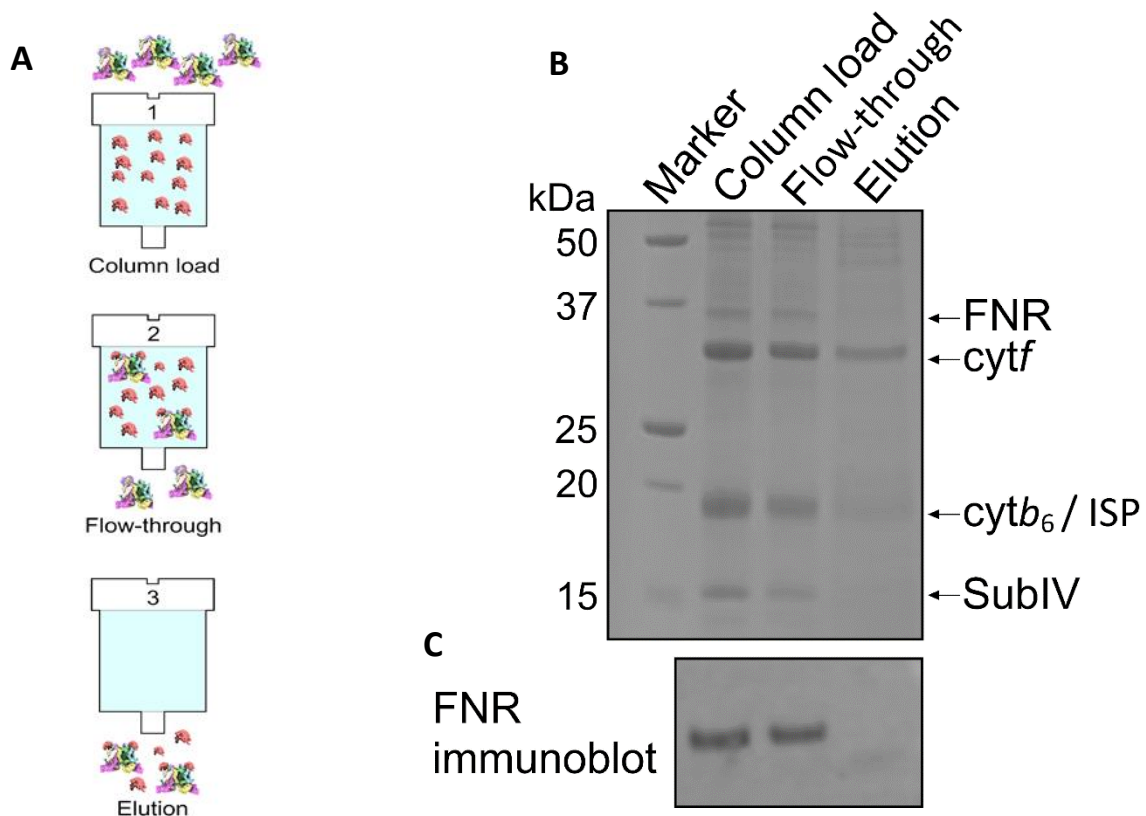


Figure 4.23 | Testing the interaction of the *cytb₆f*-FNR supercomplex with PetP.

(A) The LMNG purified supercomplex was loaded onto the PetP column and flow-through and elution samples were collected. (B) SDS-PAGE analysis showed the enrichment of FNR-*cytb₆f* supercomplex in the flow-through sample, while the elution was enriched in *cytb₆f* only. (C) This was also confirmed by analysis of the samples by western blot against FNR.

4.9 PGR5 pulldown

Since loss of PGR5 in *Arabidopsis* results in loss of CET phenotype and because of the cross-linking results with subIV of *cytb₆f*, we investigated its association with the *cytb₆f* complex using pulldown.

Recombinant spinach C-terminus Strep-tagged PGR5 was bound to a Strep column and spinach thylakoid membranes were solubilised at 1mg/ml in 0.8% GDN. Unsolubilized material

was pelleted by centrifugation and the supernatant was loaded onto columns with and without PGR5, as negative control. Analysis by SDS-PAGE of the eluted sample from the column revealed a similar composition to the FNR-cyt_{b6f} supercomplex purified in LMNG. Tic62 and TROL showed to have a high affinity to the Strep column, as it can be observed in the control column without bound PGR5 (Figure 4.24A). Western blot for ISP and haem blot of the purified samples confirmed the presence of cyt_{b6f} in the eluate from the PGR5 columns (Figure 4.24B-C).

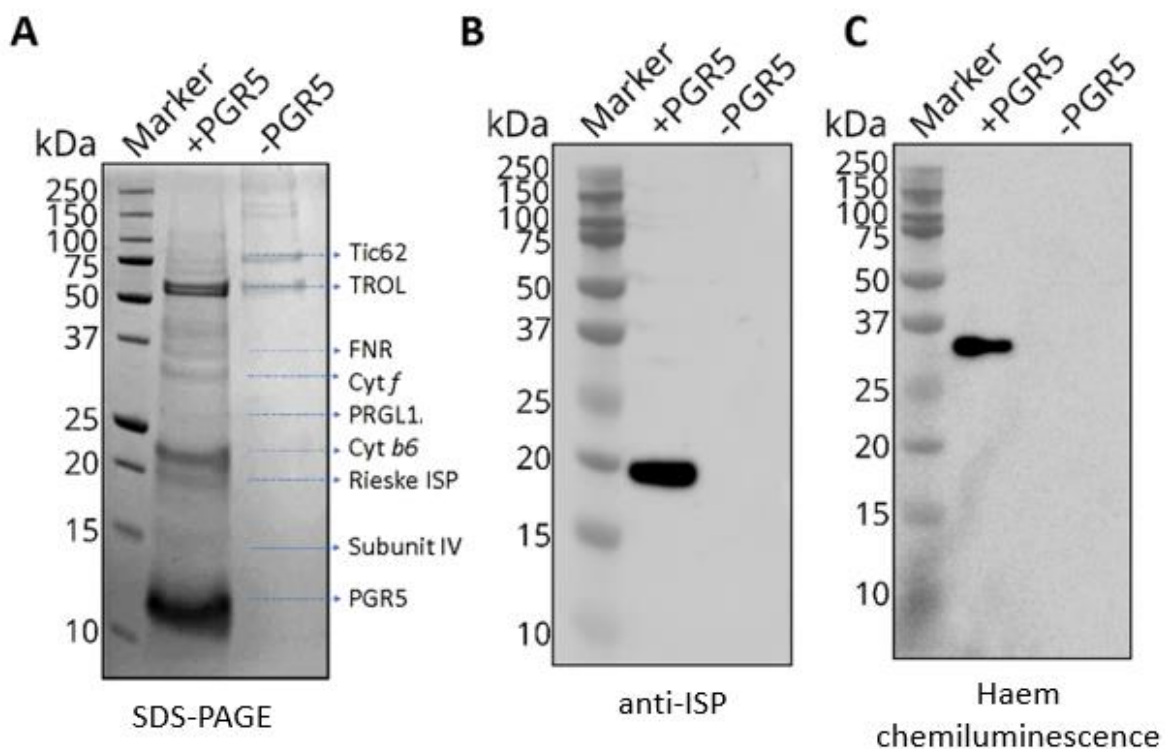


Figure 4.24 | PGR5 pulldown.

(A) Spinach thylakoid membranes solubilised in GDN were applied onto a PGR5 column. SDS-PAGE analysis of the eluted sample from the column revealed a similar composition to the CET supercomplex purified in LMNG. The ISP subunit was detected by western blot (B) and the presence of cyt_f was confirmed by the detection of haem *f* by haem chemiluminescence.

4.10 FQR activity of the FNR-cyt_{b6f} supercomplex

Activity of the purified FNR-cyt_{b6f} supercomplex was investigated by assessing the rate of PQ reduction, as outlined in section 2.12. Generation of PQH₂ was monitored by the increase of the emission signal at 330 nm (Kruk & Karpinski, 2006). When Fd and NADPH were added to the FNR-cyt_{b6f} supercomplex sample, a sharp rise of the signal was observed in the first 150 seconds of the measurement (Figure 4.25). Hence, the FNR-cyt_{b6f} supercomplex indeed

exhibits FQR activity. It can be observed that PQ reduction by the isolated FNR-*cytb_{6f}* supercomplex reaches a plateau, which can reflect either the limitation of reduced substrates (NADPH) or in the PQ molecules available.

As negative control, PQ reduction was also assessed by solely adding Fd and NADPH to PQ. Furthermore, pure *cytb_{6f}* complex without any additional CET effector proteins was also investigated. Upon addition of Fd and NADPH, the complex exhibited a notably slow rate of PQ reduction similar to the negative control one.

After the reduction of PQ from the FNR-*cytb_{6f}* complex and *cytb_{6f}* complex, PQ and PQH₂ molecules were extracted, details in section 2.12. HPLC analysis was conducted on the samples; the percentage of reduced PQH₂ in the sample was determined from the area of the corresponding peaks in the chromatograms to the same sample fully reduced by addition of 1 μ l NaBH₄. ~60% of total PQ molecules were reduced by the FNR-*cytb_{6f}* complex, in comparison to just ~20% by the *cytb_{6f}* complex. In addition, it was possible to calculate the rate of PQ reduction; 4 μ mol of PQ reduced per min per mg of FNR-*cytb_{6f}* complex, in comparison to 1 μ mol per min per mg of *cytb_{6f}* complex. Details on the calculations are found in the method section 2.12.

Previous studies have shown that FNR can efficiently reduce short-chain PQ and to a less extent PQ-9, which constitutes the PQ pool in thylakoid membrane; this is probably due to the high hydrophobicity of the molecules and on the detergent present in the solution (Bojko et al., 2003). Therefore, further experiments need to be carried out to exclude the possibility of PQ being directly reduced by FNR within the system.

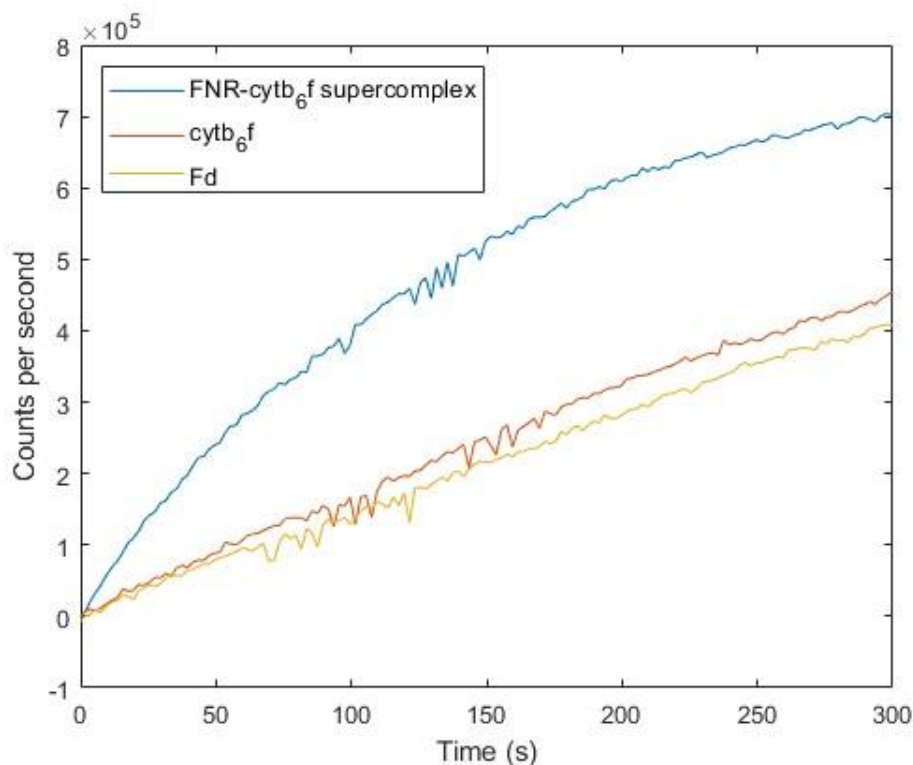


Figure 4.25 | FQR activity of the FNR- *cytb₆f* supercomplex.

PQ reduction was measured using FluoroLog FL3-22 spectrofluorometer. The sample was excited at 290 nm and emission was monitored at 330 nm, with a slip width of 5 nm. The FNR-*cytb₆f* supercomplex (*blue*) exhibits FQR activity, with a PQ reduction rate much higher than the one measured using the pure *cytb₆f* complex (*red*) and the negative control (*orange*, Fd+NADPH).

4.11 Discussion

As discussed in the previous chapter, the selection of the appropriate detergent is crucial for the preservation of labile interactions amongst membrane proteins. The most commonly used detergents for purification and structural determination of membrane proteins are non-ionic detergents, such as LMNG. In this chapter, the structural characterisation by cryo-EM of the FNR-*cytb₆f* supercomplex purified in LMNG was attempted; however, many problems were encountered as low contrast between the proteins and the micrograph background, detergent artefacts and dissociation of the supercomplex once applied onto the grid. It is worth noting that issues associated with the use of LMNG in cryo-EM have already been extensively documented and various strategies to overcome some of the problems have been proposed. It has been previously described that disassembly of supercomplexes can be caused by the denaturing effects at the air-water interface during the grid preparation. It has been shown

that the addition of secondary detergents with a high CMC value, as OG or CHAPS, would improve the ice thickness across the grid and prevented particles denaturing (Kampjut & Sazanov, 2020; Maeda et al., 2020).

In cryo-EM, the presence of excess of detergent micelles represents a problem for the background in the micrographs; this is a common problem encountered with LMNG and it has been proposed to lower the concentration of the detergent throughout the protein purification protocol. However, this leads to possible disassembly of the supercomplex. Therefore, another approach documented in the literature to address this problem is GradeR, which involves the centrifugation of the sample in a glycerol gradient, with high percentage of LMNG at the top that gradually decreases towards the bottom; this method would essentially spin the excess of micelles away (Hauer et al., 2015).

All these strategies to overcome problems encountered with the grid preparation using LMNG were tested in this study; however, no improvements were made. An alternative approach was tested involving the reconstitution of the sample into amphipols, following a similar approach used for the purification of PSII supercomplex in *Chlamydomonas* (Watanabe et al., 2019). However, the interactions between the different proteins of the supercomplex are extremely labile and this was also observed from the asymmetric peaks in the FPLC traces or the heterogeneity of the samples from the negative stain analysis. This is consistent also with previous studies in which they attempted the structural characterization of PetO-*cytb₆f* complex or of the PSI-LHCI- *cytb₆f* supercomplex from *Chlamydomonas* (Buchert et al., 2018; Steinbeck et al., 2018).

Indeed, the fragility of the FNR-*cytb₆f* supercomplex may reflect its transient formation under different conditions to balance LET and CET.

A suggested mechanism by which LET/CET balance is regulated is via state transitions, by which the excitation energy is distributed between PSII and PSI upon changes of light conditions. This process involves the reallocation of LHCII trimers between PSII and PSI. On preferential excitation of PSII by red/blue light, the PQ pool is reduced and it triggers the phosphorylation of LHCII trimers by STN7 kinase causing their association to PSI (State II).

Instead, under far-red light PSI is preferentially excited, which results in the PQ pool oxidation and the inactivation of the STN7 kinase. TAP38 dephosphorylates LHCII subunits which associate again with PSII (State I). Since CET necessitates an increased excitation of PSI over PSII, it has been proposed that State II would promote CET, balancing the ATP/NADPH ratio. In contrast, State I would lead to an enhancement of LET and an increase in NADPH generation (Hepworth et al., 2021; Wood et al., 2018).

In 2010, the putative CET supercomplex involving FNR and *cytb₆f* was purified from *Chlamydomonas*, reported to form under state II inducing conditions (Iwai et al., 2010). Recent findings have shown that STT7 (STN7 analogue) in *Chlamydomonas* interacts with the stromal side of *cytb₆f*, and it induces the autophosphorylation of the kinase. PetO is phosphorylated in State II and it could regulate the interaction between STT7 and *cytb₆f*. Similarly, this could occur in cyanobacteria with PetP and in plants with TSP9; PetP and TSP9 are both located on the stromal side of *cytb₆f* and they could be involved in the formation of supercomplexes (Riché et al. 2023; Proctor et al. 2022; Sarewicz et al. 2023). In future experiments, conditions as State I and II, dark or high light, could be tested in order to induce the formation of the FNR-*cytb₆f* supercomplex and stabilise those interactions between the CET effector proteins.

In the purified FNR-*cytb₆f* supercomplex, the proteins TROL and Tic62 were also identified. Previous studies have shown that TROL and Tic62 might also be involved in the control of photosynthetic pathways by tethering FNR to the membrane. It has been previously observed that TROL and Tic62 interaction with FNR is strong under dark conditions while it weakens under the exposure to high light. Furthermore, in Lintala et al. in 2014, it was shown that these proteins do not interact to *cytb₆f* by BN PAGE and immunoblotting analysis, which could suggest that Tic62, TROL and FNR are just co-purified with *cytb₆f* in our sample (Benz et al., 2009; Lintala et al., 2014). However, in their study the thylakoids were solubilised in β DDM, which is known to be a harsher detergent in comparison to LMNG.

Activity of the purified FNR-*cytb₆f* supercomplex was investigated. We expected that the association of the CET effector proteins to *cytb₆f* would accelerate PQ reduction. Indeed, measurements of the PQ reduction have demonstrated that the isolated FNR-*cytb₆f*

supercomplex displays FQR activity, characterised by a much faster PQ reduction compared to *cytb_{6f}* only and confirming our initial hypothesis. However, further experiments are necessary to exclude the possibility of PQ being directly reduced by FNR within the system.

Furthermore, analysis of particles sizes from negative stain and cryo-EM grids prepared with samples in both LMNG and amphipol indicate the presence of large complexes.

Cross-linking mass-spectrometry revealed interesting and novel insights of the potential interactions of the CET effector proteins to the *cytb_{6f}* complex. From these results, the stromal side of *cytb_{6f}* binds to FNR and PGR5. This interaction would also block the interaction of *cytb_{6f}* with PetP. In addition, from the PGR5 pull down experiment, it is possible to purify the FNR-*cytb_{6f}* supercomplex from solubilised thylakoids, indicating a strong interaction of PGR5 with *cytb_{6f}*, consistent also with a recent study carried out in cucumber leaves that showed the association of PGR5 with *cytb_{6f}* (Wu et al., 2021). Cross-links found between subIV, PGR5 and FNR could indicate that PGR5 could act as a glue between these proteins.

The cross-linking results also indicate that the interaction between FNR and subIV would be too far (>14Å) for a direct electron transfer from FAD to the haem *c_n*; however, the distance may be bridged by the binding of Fd to FNR. This would also be consistent with the fact that haem *c_n* requires just one electron donor.

PGRL1 was also found in the sample, and it could bring PGR5 in close proximity to *cytb_{6f}* and FNR for the formation of a supercomplex. Interestingly, cross-links were also found between FNR and PGRL1; in this case FNR active site is hindered by the interaction with PGRL1, blocking it from oxidising Fd. Another hypothesis is that PGRL1 binds to a FNR dimer, bringing it closer to the thylakoid membrane similarly to TROL and Tic62. Cross-links were also found between FNR and TROL and Tic62; it is possible that these interactions with FNR might increase the amount of FNR tethered to the membrane to bring it near *cytb_{6f}* when CET is activated (M. Kramer et al., 2021).

Indeed, the structural characterisation by cryo-EM of the FNR-*cytb_{6f}* supercomplex would allow an even better understanding of these interactions. The FNR-*cytb_{6f}* supercomplex purified from the PGR5 pull-down could be reconstituted in other polymers that would offer more stability to the complex. Another approach could also involve the use of a combination

of detergents. In a recent study, successful structural determination of a complex was obtained by using a mixture of LMNG, GDN and A8-35 (Bous et al., 2021).

Future experiments would also involve the search for optimal physiological conditions that promote CET and the purification of the supercomplex under these conditions. Perhaps, the use of high CET Arabidopsis mutants, like *hope 2* (hunger for oxygen in photosynthetic electron transport reaction 2). *Hope 2* carries a mutation of the amino acid Gly134 to Asp in the γ subunit; this causes a higher H⁺ efflux in the complex, a loss of photosynthetic control and high CEF activity (Degen et al., 2022; Takagi et al., 2017).

5. Relevance of FNR binding to the thylakoid membrane for photosynthesis and CET in vivo

5.1 Introduction

As discussed in the previous chapter, the purified supercomplex is characterised by the presence of *cytb₆f* interacting with the stromal proteins PGR5 and FNR and the transmembrane proteins PGRL1, TROL and Tic62 complex. Previous studies have shown the importance of these proteins in CET and their role in the photoprotection of the photosystems (DalCorso et al., 2008; Joliot & Johnson, 2011; D. M. Kramer & Evans, 2011; Munekage et al., 2004; Rodriguez-heredia et al., 2022; Suorsa et al., 2012). Therefore, it was logical to assess the extent to which the observed association might affect the capacity for CET and photoprotection *in vivo* in Arabidopsis plants. To this end we utilised the *fnr1* mutant of Arabidopsis, which lacks proper thylakoid membrane association for FNR (Lintala et al., 2007).

As described in the introduction, the *pgr5* mutant of Arabidopsis lacks PGR5-dependent CET and shows a photosensitive phenotype in fluctuating light (Munekage et al., 2002, 2004; Suorsa et al., 2012). Several diverse methods are consistent with PGR5-dependent pathway making the major contribution to CET in Arabidopsis (Degen et al., 2023; Munekage et al., 2004; Nandha et al., 2007; Strand et al., 2016; Wang et al., 2015). The photosensitivity of the *pgr5* mutant is mostly ascribed to a lower Δ pH causing a loss of photosynthetic control, which leaves PSI vulnerable to over-reduction in high light. Over-reduction of PSI causes the generation of reactive oxygen species (ROS) at the acceptor side and eventually PSI photoinhibition (Sonoike, 2011). Although, loss of Δ pH in *pgr5* also leads to a low NPQ phenotype, PSII has a very efficient repair machinery which allows a fast rescue in case of photodamage (Nixon et al., 2010). However, PSI recovery from photoinhibition can be extremely slow and even irreversible (Sonoike, 2011; Suorsa et al., 2012). It remains unclear the extent to which the loss of CET and *pmf* affect ATP levels in *pgr5*, though there is some evidence they are perturbed (Sato et al., 2019; Wang et al., 2018). In theory, a slowdown in NADPH oxidation due to an unbalanced ATP/NADPH ratio for operation of the Calvin cycle could also lead to acceptor side limitation and PSI damage. Indeed, recent studies suggest both acceptor and donor side regulation by PGR5 are crucial to PSI (Yamamoto & Shikanai,

2019). Another feature of *pgr5* is its high proton conductivity (g_{H^+}) of the ATP synthase (Avenson et al., 2005), though this appears not to be caused by low *pmf* per se (Yamamoto & Shikanai, 2019).

In contrast to the *pgr5* mutant, the *crr* or *ndho* mutants of Arabidopsis, which lack the NDH-dependent CET pathway do not have a growth or photosynthetic control phenotype (Munekage et al., 2004). Moreover, they only show a slight loss of *pmf* compared to the wild-type plants (Wang et al., 2015), and in some circumstances even a slight enhancement in NPQ (Rumeau & Peltier, 2005). However, several studies have highlighted a more important role for NDH-dependent CET in LL conditions (Degen et al., 2023; Yamori et al., 2015a). Moreover, in Arabidopsis plants with ATP deficits resulting from aberrant Calvin cycle or chloroplast protein synthesis activity, the NDH-dependent pathway was strongly upregulated (Livingston et al., 2010; Strand et al., 2016), perhaps consistent with the higher H^+/e^- ratio generated by this pathway (4 compared to 2 for the PGR5 pathway).

FNR has also been implicated in CET *in vivo* in both Arabidopsis and tobacco (Hald et al., 2008; Joliot & Johnson, 2011; M. Kramer et al., 2021; Lintala et al., 2007; Rodriguez-heredia et al., 2022). In Arabidopsis, two leaf FNR isoforms exist (*AtFNR1* and *AtFNR2*) and knockout of *AtFNR1* results in the complete dissociation of the remaining *AtFNR2* from the thylakoid membrane (Lintala et al., 2007, 2009). The *fnr1* plants were reported to show a decrease in CET (M. Kramer et al., 2021; Lintala et al., 2007) and increased PSI photosensitivity (Rodriguez-heredia et al., 2022).

In this chapter, we present a series of experiments to assess CET *in vivo* in Arabidopsis mutant *fnr1*, in which tethering of the FNR heterodimer to the thylakoid membrane is abolished. CET mutants defective in the PGR5 and NDH pathways were also tested and compared to the *fnr1* to elucidate the regulatory mechanisms of CET and understand whether the FNR binding to the thylakoid membrane is necessary for photosynthesis and CET.

5.1.1 Chlorophyll fluorescence

Chlorophyll pigments are present in PSI, PSII and the associated LHCs and act as sensitive reporters of the internal light harvesting and electron transfer functions. Upon absorption of a red photon (~600-700 nm), electrons within a chlorophyll molecule will be promoted to S_1 state, while in case of a blue photon (~400-500nm), electrons will jump to the S_2 state. These electrons will lose the energy quickly reaching S_1 . Electrons in S_1 then decay to the ground state S_0 via i) excitation energy transfer to another pigment via FRET, ii) dissipated as heat via internal conversion, or iii) re-emitted as light (fluorescence). Since i) and ii) compete with iii) by observing changes in chlorophyll fluorescence emission it is possible to extract information regarding the relative rates of i) and ii).

As chlorophyll measurements are very sensitive to light intensity changes, all the measurements are carried out using a pulse amplitude modulated (PAM) weak green measuring light (540 nm). Use of green light ensures the measuring light samples all layers of the leaf, since red or blue light is preferentially absorbed by the upper layers of the leaf. The PAM approach ensures the fluorescence signal can be isolated from the differences in fluorescence amplitude caused by using varying light intensity and thus provides a form of normalisation so quenching rates caused by varying light intensity may be straightforwardly compared. The minimal fluorescence level in the presence of the weak measuring light is known as F_0 .

To initiate changes in fluorescence a bright pulse is applied to stimulate the maximum rate of photochemistry. Upon light absorption or energy transfer to the P680 primary donor Chl molecules in PSII, electrons are transferred to the primary acceptor plastoquinone Q_A . Following this charge separation event the PSII RC may be considered temporarily 'closed', removing its competition as a de-excitation pathway and thereby increasing the fluorescence signal to the maximum (F_m) (Maxwell & Johnson, 2000). The difference between F_m and F_0 is known as the variable fluorescence F_v . The value F_v/F_m is therefore proportional to the PSII quantum yield, which for healthy dark-adapted material is normally ~0.82, meaning PSII converts photons into charge separation with ~82% efficiency.

To determine the effect of a particular light intensity a second actinic light of red or blue wavelength is applied. If the actinic light is sufficiently bright to initiate photochemistry, the

chlorophyll fluorescence signal will first rise as RCs are closed, before gradually being quenched by a combination of photochemical (qP) i.e. photosynthesis, and non-photochemical quenching (NPQ) i.e. heat dissipation (Figure 5.1). The contributions of qP and NPQ can be distinguished by application of another bright flash, which is sufficient to transiently close any remaining open PSII RCs and so demonstrate the extent of NPQ. Increases in NPQ lead to a decline in PSII quantum yield $Y(II)$.

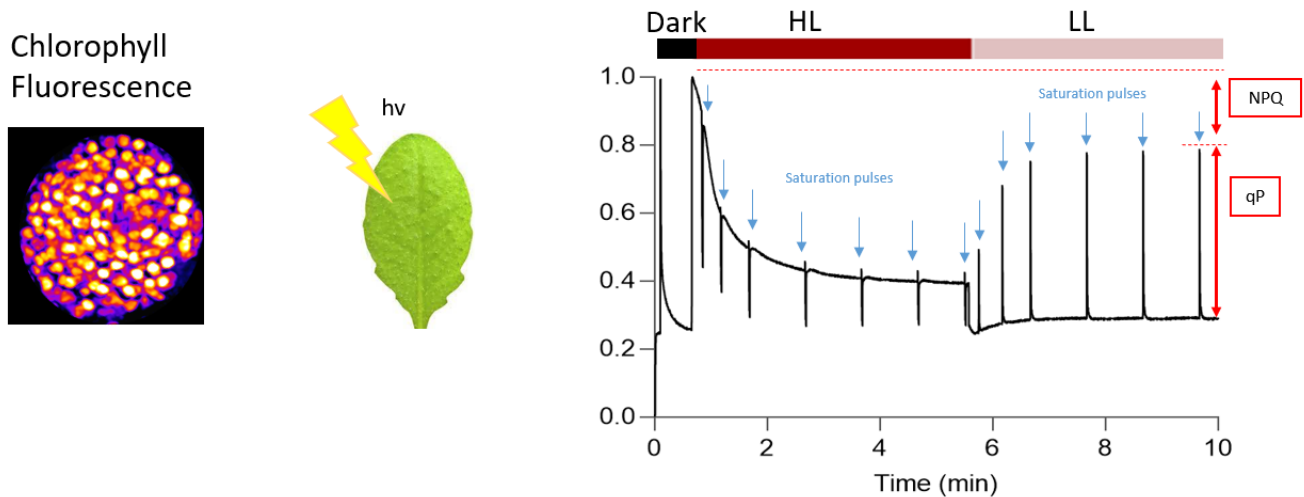


Figure 5.1 | Chlorophyll fluorescence.

Light energy absorbed by chl molecules can be either re-emitted as light (fluorescence), dissipated in form of heat (NPQ) or drive photosynthesis (qP). Here shown is a typical fluorescence trace of dark-adapted leaves exposed to a short period of darkness, high light (HL) and low light (LL), and application of several saturation pulses to obtain NPQ and qP values.

With the Dual/KLAS-NIR spectrophotometer it is possible to measure not only the chlorophyll fluorescence of leaves, but also simultaneously the absorption signals corresponding to the dynamics of PSI (P700), Pc and Fd. The actinic light provokes changes in the redox status of these electron transfer chain components, which can be monitored by their absorption changes in the near infra-red from 780-970 nm (Klughammer & Schreiber, 2016; Schreiber, 2017). The dual KLAS-NIR uses four dual-wavelength transmittance difference signals measured at 785-840 nm, 810-870 nm, 870-970 nm and 795-970 nm. Then following a procedure that utilises various physiological states of the plant to isolate the absorption signal belonging to each component (P700, Pc, Fd) a model spectrum is constructed for each defining their relative contribution to absorption at each wavelength pair. Combining the model spectra to produce a differential model plot (DMP) allows deconvolution of the

individual P700, Pc and Fd kinetics under normal physiological conditions where all three signals can change in parallel (Klughammer & Schreiber, 2016; Schreiber, 2017) (Figure 5.2).

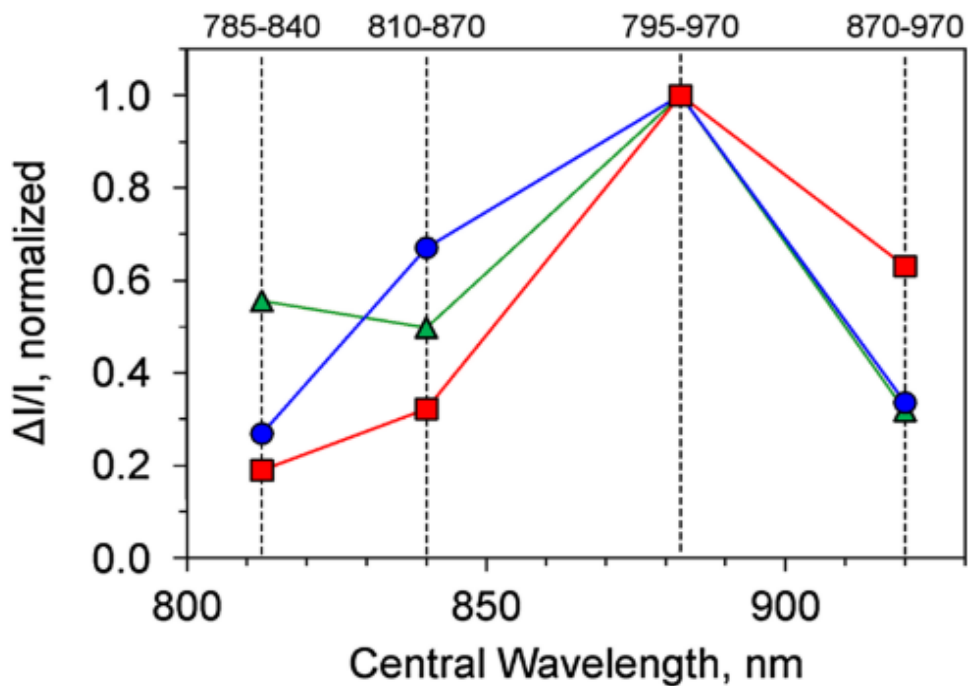


Figure 5.2 | Differential model plot (DMP) of P700, PC and Fd.

Dual-wavelength difference transmittance changes of Fd (*green*, 785-840 nm), P700 (*blue*, 810-870 nm), Pc (*red*, 870-970 nm) are measured. In this plot, the selective differential plots are shown with the maximal values of $\Delta I/I$ normalized to 1. The DMP is applied for deconvolution of redox changes of Fd, P700, and PC. Illustration adapted from (Klughammer & Schreiber, 2016; Schreiber, 2017).

The final challenge is to determine the maximum extent of the absorption signals associated with P700, Pc and Fd, so the kinetics can be framed within a scale of 0-100% oxidation/reduction. To achieve this a maximum signal routine is used that applies 3 s of bright actinic light to dark-adapted material to fully reduce Fd (prior to CBB cycle activation and its ensuing reoxidation). For Pc and P700 signals full oxidation is obtained via the application of bright far-red (FR) light (~720 nm) which preferentially excites PSI draining P700 and Pc of electrons, a short (10 ms) bright red flash (~650 nm) is applied in addition to the FR ensures any remaining P700 is photo oxidised.

For PSI, the quantum yields can be determined by a similar saturation pulse method are complementary and involves a similar short flash applied in addition to the actinic light as with PSII fluorescence:

-the quantum yield of PSI Y(I) corresponding to the P700 reduced fraction and open acceptor side,

-the quantum yield of non-photochemical energy dissipation due to the donor side limitation of PSI Y(ND), corresponding to the fraction of oxidised P700

- the quantum yield of non-photochemical energy dissipation due to the acceptor side of PSI Y(NA), corresponding to the fraction of reduced P700 and closed PSII RCs because of lack of oxidised electron acceptors (Schreiber & Klughammer, 2016).

Details on the calculations of the used fluorescence parameters in this chapter can be found in the method section 2.13.

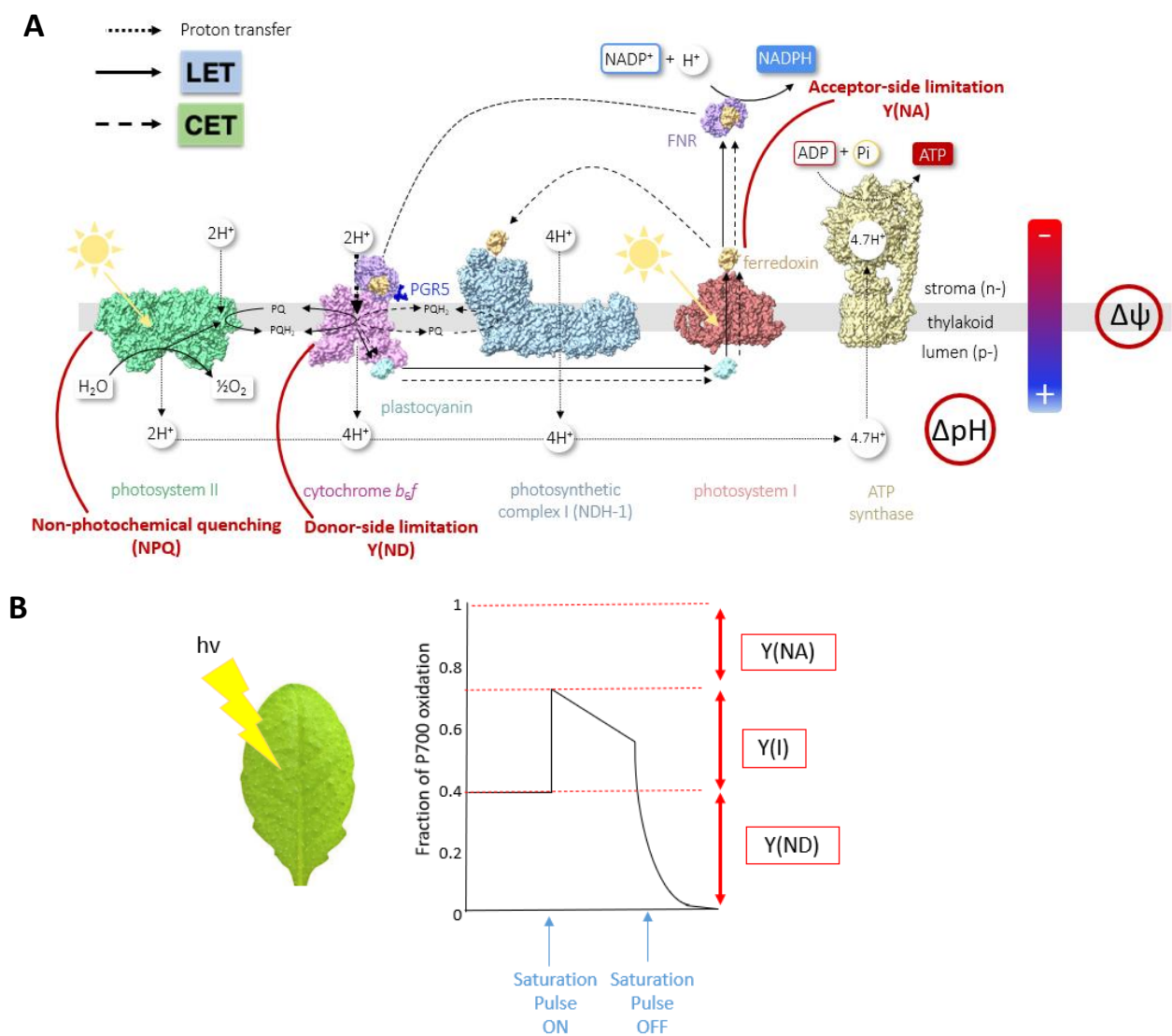


Figure 5.3 | Overview of the photosynthetic electron transport chain and the quantum yields of PSI. (A) Overview of the photosynthetic electron transport chain. PSII catalyses the initial water oxidation into oxygen, protons and electrons. Electrons are transferred through the photosynthetic components

of the chain and this is coupled to a proton translocation across the thylakoid membrane into the lumen (Mitchell, 1975b). This leads to the formation of an electric potential difference across the thylakoid membrane ($\Delta\Psi$), and proton concentration gradient (ΔpH), which together constitute the proton motive force (pmf) that allows ATP synthase to make ATP. Light absorption in PSI drives the oxidation of Pc and the reduction of ferredoxin (Fd), a water-soluble iron-containing protein in the stroma. Then, Fd is used by the enzyme Ferredoxin NADP(H) oxidoreductase (FNR) for the reduction of NADP^+ to NADPH. Reduced Fd returns electrons into the plastoquinol pool in CET. (B) Upon light absorption, P700 is reduced and the absorption change at 840 nm is measured. By a saturation pulse method it is possible to distinguish the PSI related quantum yields: $Y(\text{NA})$, $Y(\text{ND})$ and $Y(\text{I})$.

5.1.2 Electrochromic shift

Upon continuous light illumination of leaves it is also possible to observe several absorbance changes in the green spectral region peaking at the wavelengths 505 nm, 515-520 nm and 535 nm. Increase in the absorption at 505 nm is related to the formation of zeaxanthin in the xanthophyll cycle induced upon thylakoid lumen acidification by pmf (Bilger et al., 1989). While absorption changes at 515 to 520 nm are caused by the electrochromic shift (ECS) or Stark effect on carotenoid absorption. The ECS signal can be used as a measure of the electrical potential ($\Delta\Psi$) generated across the thylakoid membrane (Duysens L N M, 1954; Witt, 1979). On onset of light, movement of electrons across the membrane contributes to $\Delta\Psi$. During photochemistry in PSII and PSI, negative charges are moved towards the stroma, and similarly during the Q-cycle of $\text{cyt}b_6/f$ complex, where electrons are moved from the Q_p site on the luminal side to the stromal side of the thylakoid membrane via the low potential chain (Joliot & Joliot, 1986). Absorption changes at 535 nm are caused by conformational changes occurring within LHCII caused by NPQ (Ruban et al., 2002).

Upon illumination by actinic light the ECS signal (ΔA 515-550 nm) rises sharply, and this is defined as the A-phase (Figure 5.4). Subsequently, there is a slower rise in the signal which is referred as B-phase. This decays slowly in the C-phase. Constant illumination with actinic light results in a flat ECS signal, which reflects the balanced photosynthetic system; this is also defined as steady state. This state is characterised by the generation of $\Delta\Psi$ counter-balanced by the release of protons through ATP synthase.

Sacksteder and Kramer in 2000 introduced the DIRK (Dark Interval Relaxation Kinetic) technique, which involves brief dark intervals (<500 ms), to induce changes in the steady state of electrons and protons. When illumination is removed, the light driven reactions stop while

proton efflux continues via ATP synthase or ion channels; this causes the ECS signal to collapse. This phase is known as the D-phase and the initial rate of this ECS decay reflects the proton flux out of the lumen (vH^+), the amplitude of the decay is proportional to the *pmf*. The efflux via ATP synthase (vH^+) is related to its conductivity (gH^+). These parameters derived from the leaf ECS signal therefore provide sensitive reporters on the proton circuit of photosynthesis.

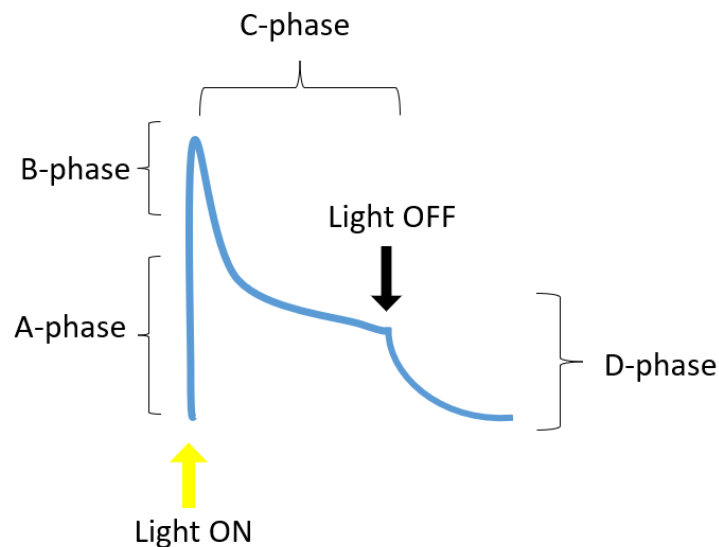


Figure 5.4 | Schematic illustration of the ECS decay

(A) Upon the first light illumination the ECS signal rises sharply (A-phase), followed by a slower rise (B-phase). Subsequently, the ECS signal decays and it reaches a steady state (C-phase). When light is turned off for the measurement of *pmf*, vH^+ and gH^+ , the ECS signal decays exponentially (D-phase).

5.2 A new *Arabidopsis thaliana* phenotype lacking CET

As previously discussed, the results in chapter 3 and 4 suggest that FNR binding to the *cytb₆f* complex may be involved in CET. Therefore, to test the *in vivo* relevance of these biochemical observations we examined the photosynthetic phenotype of the *fnr1* *Arabidopsis* mutant, in which FNR tethering to the membrane is abolished (M. Kramer et al., 2021; Lintala et al., 2007), in comparison with the wild type Col-0 and CET mutants *ndho*, *pgr5* and *pgr5 ndho*.

The original plan to utilise the *pgr5 crr double* mutant (*crr*, chlororespiratory reduction, which lacks the NDH complex) was thwarted by the failure of the seeds donated by Professor Shikanai (Kyoto University) to germinate. Therefore, a new double mutant crossing *pgr5* with *ndho* was created. NdhO is a NDH subunit exposed to the stromal side of the complex and it is involved in the regulation of ferredoxin binding and, therefore, in the function of the

complex and its absence leads to complete loss of NDH (Rumeau & Peltier, 2005; C. Zhang et al., 2020). The *pgr5 ndho* double mutants were screened by immunoblot with antibodies to PGR5 and NdhS which verified the successful cross (Figure 5.5).

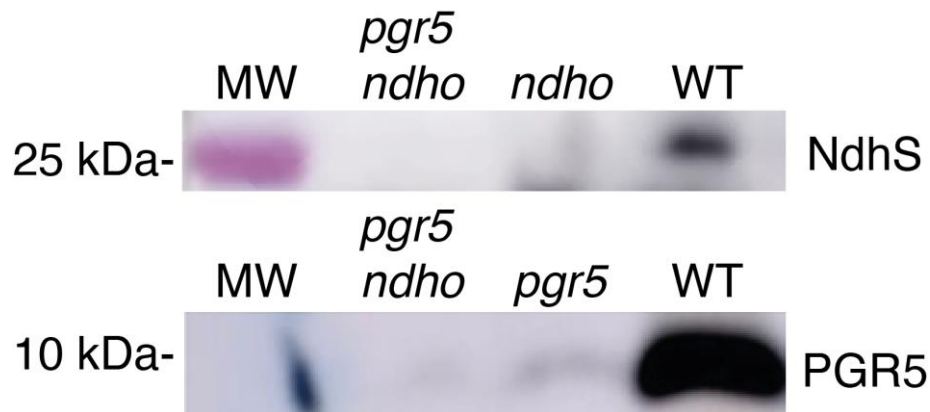


Figure 5.5|Generation of the double CET mutant *pgr5 ndho*.

(A) Immunodetection of PGR5 in *pgr5 ndho*, *pgr5* and WT using a PGR5 antibody. (B) Immunodetection of NdhS in *pgr5 ndho*, *ndho* and WT using NdhS antibody.

5.3 Analysis of the growth phenotype of CET mutants

Arabidopsis plants were grown for 3 weeks at light intensity of $180 \mu\text{mol photons m}^{-2} \text{s}^{-1}$, referred as “control light”, until first rosette area was measured (day 0). Following this period, plants were either maintained under control light or transferred to medium light ($400 \mu\text{mol photons m}^{-2} \text{s}^{-1}$, ML) for 6 days and then to high light ($685 \mu\text{mol photons m}^{-2} \text{s}^{-1}$, HL) for further 7 days. During the course of this growth experiment, the rosette areas were regularly measured via image analysis and measurements were plotted (Figure 5.6A); Asterisks were used to indicate statistical differences between genotypes grown under control and light treatment were also calculated using a two-way ANOVA test (alpha = 0.05), where *= $p < 0.05$, **= $p < 0.01$, ***= $p < 0.001$ and ****= $p < 0.0001$. Figure 5.6 B shows images taken at the end of the growth experiment (day 14). Generally, all Arabidopsis plants that were high light treated looked smaller in comparison to plants grown under control light (Figure 5.6B). Measurements of the rosette area taken on day 14 are also shown in a separate plot to facilitate the direct growth comparison between the mutants and the wild type. Statistical differences between the genotypes grown under control light or high light treated were calculated. The mutants *pgr5* and *pgr5 ndho* displayed a significant growth impairment when

compared to the plants grown under control light, as shown in Figure 5.6A. In addition, they displayed this growth impairment also under control light in comparison to Col-0 (Figure 5.6C). In contrast, the growth of the mutants *ndho* and *fnr1* was not severely impaired as shown in figure 5.6A-C.

At the end of the growth experiment, plants were harvested and fresh weight was also measured. In Figure 5.6D it can be observed that after light treatment the *fnr1* mutant suffers a loss in fresh weight in high light compared to the CET mutants and Col-0. In contrast, light treated Col-0, *pgr5* and *ndho* are characterised by a higher fresh weight compared to plants grown under control light. This is due to an enhancement of leaves thickness, and it is a well-known acclimation response that involves changes in the morphology of plants (Björkman, 1981; Pearcy, 1998).

These results indicate that the *fnr1* mutant was not affected by the light treatments, in comparison to the CET mutant *pgr5* and *pgr5 ndho* which displayed severe growth impairment.

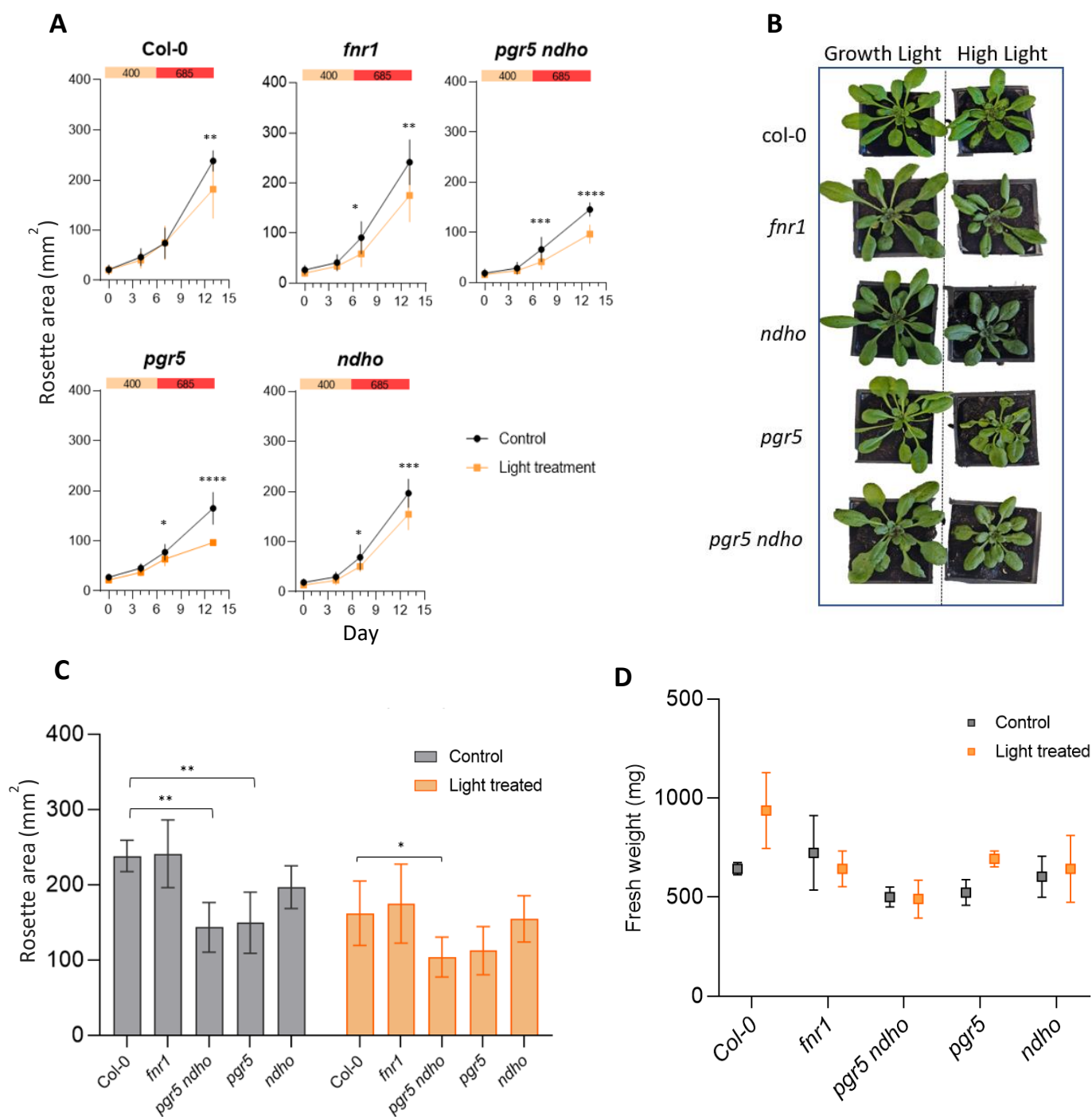


Figure 5.6 | Growth analysis of the genotypes under control and high light conditions.

(A) All plants were grown under control lights ($180 \mu\text{mol photons m}^{-2} \text{s}^{-1}$) for 3 weeks until first rosette area was measured (day 0). Half plants were moved to medium light ($400 \mu\text{mol photons m}^{-2} \text{s}^{-1}$) for 6 days and then to high light ($685 \mu\text{mol photons m}^{-2} \text{s}^{-1}$) for further 7 days. (B) Representative plants of all genotypes used in this study grown under control and high light. Images were taken at the end of the experiment. (C) Rosette area measurements on day 14 of all genotypes. (D) Fresh weight of plants was also measured at the end of the experiment ($n=3$).

Asterisks indicate statistical differences calculated using a two-way ANOVA test ($\alpha = 0.05$), where $*=p<0.05$, $**=p<0.01$, $***=p<0.001$ and $****=p<0.0001$.

5.4 Effects of light fluctuations in CET

To investigate the effect of each mutation on the overall photosynthetic efficiency and in photosynthetic regulation we measured changes in chlorophyll fluorescence in response to fluctuating light (FL), since these conditions have previously been shown to produce the greatest phenotype in CET mutants (Soursa *et al.*, 2012).

All plants were dark adapted prior to the measurements; this allows the minimum fluorescence level (F_0) to be recorded where all PSII RCs are open and oxidised before measuring a maximum fluorescence yield (F_m). Plants were then subjected to alternation of 5 minutes of high light ($800 \mu\text{mol photons m}^{-2} \text{s}^{-1}$, HL) and 5 minutes of low light ($30 \mu\text{mol photons m}^{-2} \text{s}^{-1}$, LL) for 30 minutes with saturation pulses to measure the maximum yields of photosystems every minute; further details on how these values were calculated are described in the method section 2.13.

The raw chlorophyll *a* fluorescence traces have been normalised between the genotypes by dividing them to the maximum fluorescence F_m (Figure 5.7B). By observing the chlorophyll fluorescence signal it is possible to assess the redox state of Q_A , the primary electron acceptor. The measurements showed that the steady-state fluorescence (F_s) was significantly higher in the mutants *pgr5* and *pgr5 ndho* in comparison to the other genotypes, indicating an overall decrease in photochemistry in these mutants compared to the other genotypes. The *ndho* mutant exhibited an initial increase in fluorescence, followed by a subsequent decrease during the course of the measurement. *fnr1* mutant instead displayed a similar behaviour to Col-0.

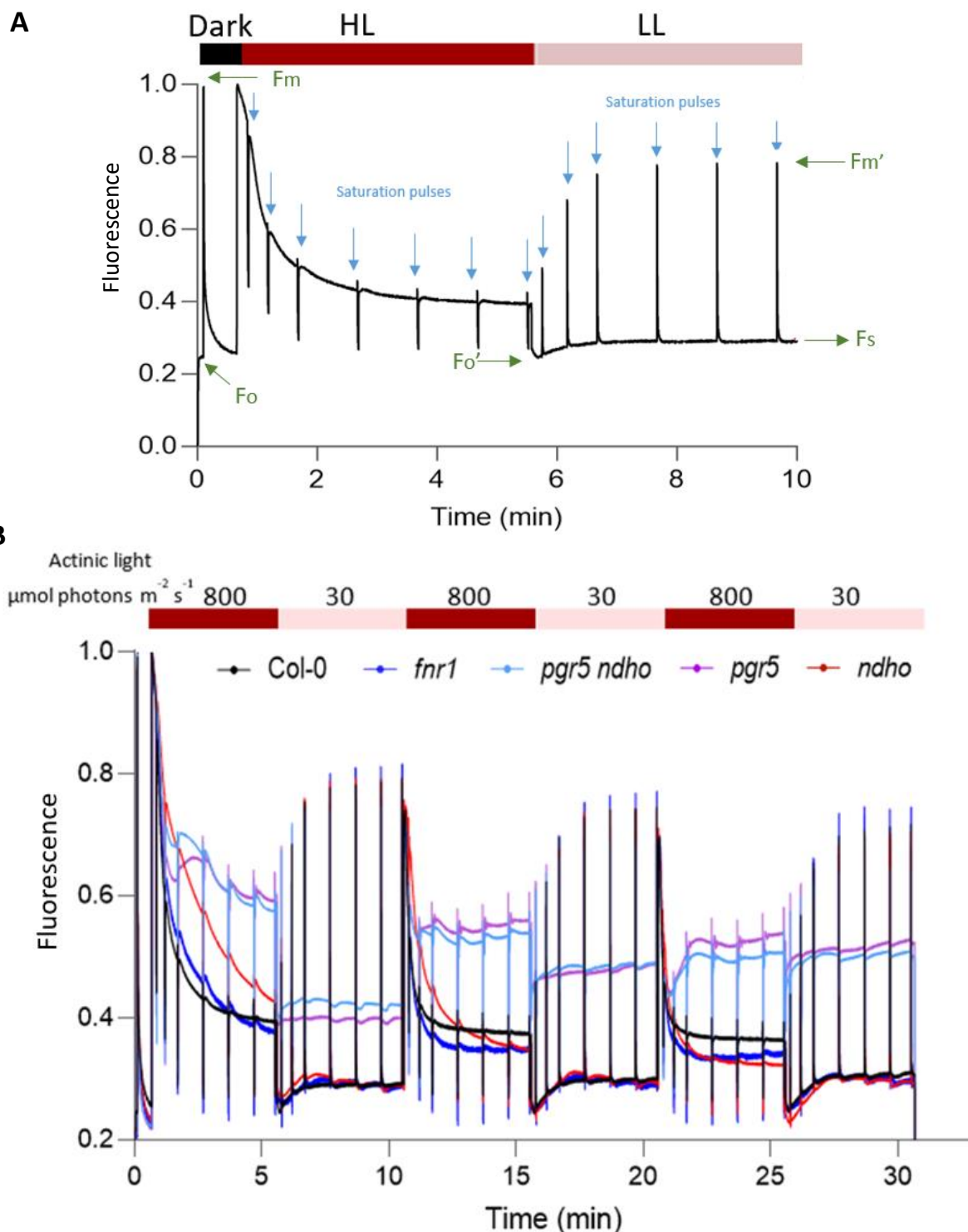


Figure 5.7| Chlorophyll *a* fluorescence measurement.

(A) Example of a Chlorophyll *a* fluorescence trace. The values indicated in the illustration are used for the estimation of the behaviour of the electron acceptor Q_A . After dark adaptation of the plants, F_o is measured. A saturation pulse is given to saturate the photosynthetic light reactions and maximum level of fluorescence is reached (F_m). Actinic light is then turned on, and saturation pulses are applied to estimate maximum yields of photosystems. (B) Chlorophyll *a* fluorescence trace recorded using the Dual/Klas-NIR spectrophotometer. Col-0, *fnr1*, *pgr5*, *ndho* and *pgr5 ndho* plants were all dark adapted before being subjected to alternation of 5 minutes of high light ($800 \mu\text{mol photons m}^{-2} \text{s}^{-1}$, HL) and low light ($30 \mu\text{mol photons m}^{-2} \text{s}^{-1}$, LL) for 30 minutes with saturation pulses every minute.

5.4.1 Fluctuating light effects on PSII photochemistry

PSII parameters were derived from the chlorophyll fluorescence measurement (Figure 5.7B) and calculated as described in the method section 2.13. Figure 5.8 shows the effect on alternating LL and HL on the photochemical quantum yield of PSII, $Y(II)$. In the HL phases, $Y(II)$ values were low in all genotypes reflecting the closure of PSII RCs due to light saturation of photosynthesis and the reduction of Q_A . However, upon the shift to LL, $Y(II)$ rapidly increases as Q_A is re-oxidised due to the lower rate of PSII RC turnover. In LL phases, $Y(II)$ in *pgr5* and *pgr5 ndho* was much lower compared to Col-0 and progressively reduces over the time of the experiment in the LL phases, indicative of damage suffered in the preceding HL phases (Figure 5.8A). In contrast, $Y(II)$ values *fnr1* and *ndho* were similar to Col-0 and are not affected by the subsequent HL periods (Figure 5.8 A).

The redox state of Q_A , a proxy for the plastoquinone pool, can be derived from the chlorophyll fluorescence data as 1- the photochemical quenching rate “1-qP”, with higher values indicating accumulation of Q_A^- and closure of PSII (Figure 5.8B). In HL phases, 1-qP rapidly increased in all genotypes, consistent with the low $Y(II)$ values in HL previously illustrated. In LL, 1-qP reached very low levels in Col-0, reflecting the re-opening of PSII RCs in this condition. On the other hand, in *pgr5* and *pgr5 ndho* a larger fraction of PSII remains acceptor side limited with reduced Q_A^- and the problem becomes worse with each low light phase. In *ndho* and *fnr1* 1-qP is only slightly increased compared to Col-0 in the LL phases (Figure 5.8B)

In the HL phases, NPQ increases in Col-0 as the increased rate of electron transfer causes acidification of the thylakoid lumen and induction of qE (Figure 5.8C). Return to LL causes NPQ to relax as the rate of coupled electron and proton transfer falls causing the lumen pH to rise once more. A decreased level of NPQ can be observed in *pgr5* and *pgr5 ndho* in comparison to all the other genotypes (Figure 5.8C) in HL. In contrast, while NPQ in *ndho* was slower to form compared to Col-0, the final amplitude was similar except in the third HL phase where the amplitude was slightly increased, consistent with previous reports (Rumeau et al., 2005; Degen et al., 2023) (Figure 5.8C). The *fnr1* plants showed similar NPQ kinetics to Col-0 in HL, although as with *ndho* the final amplitude was higher, in the second and third HL illumination periods (Figure 5.8C).

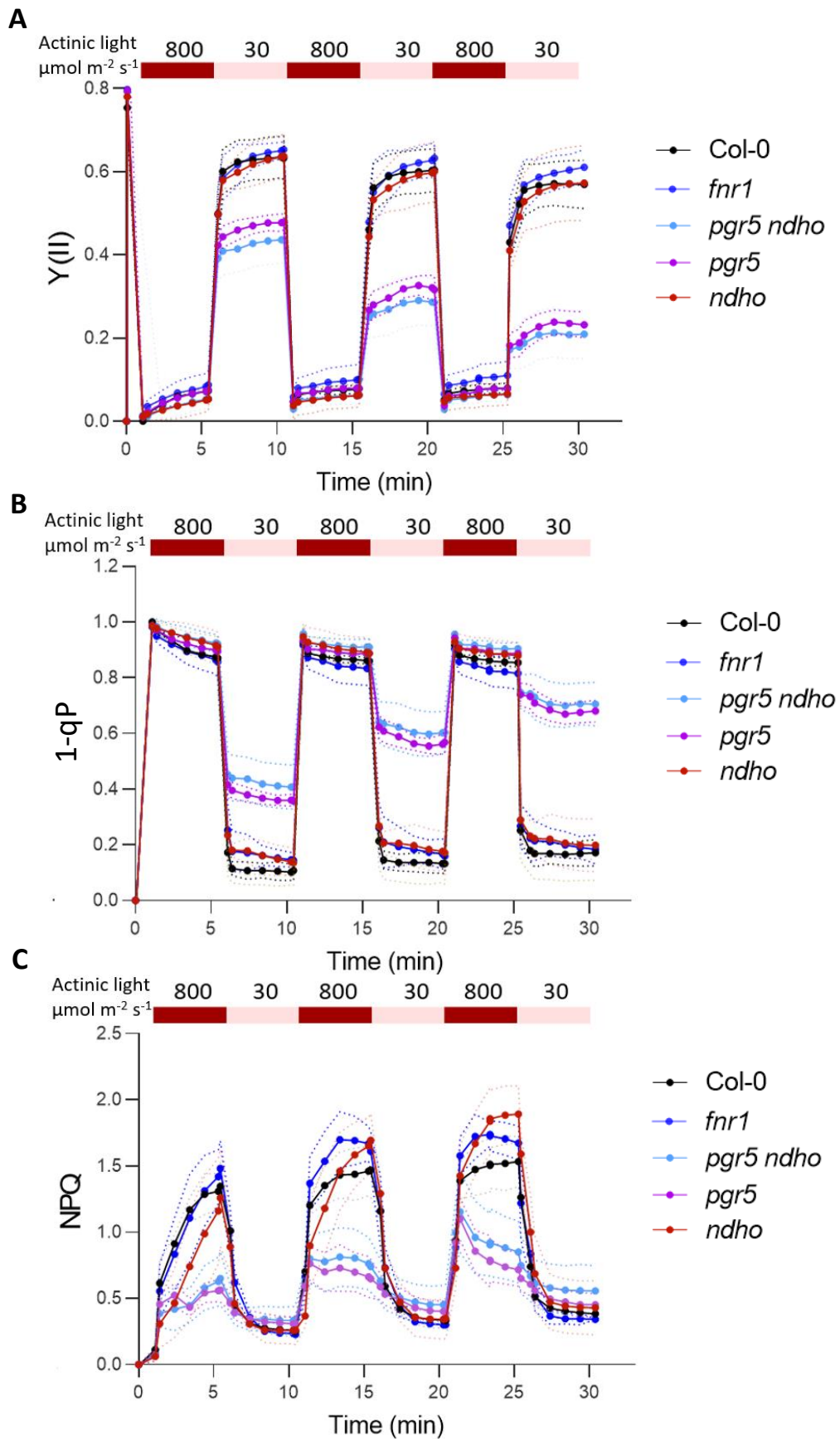


Figure 5.8 | PSII photochemistry.

Dark adapted plants were subjected to HL ($800 \mu\text{mol photons m}^{-2} \text{s}^{-1}$) and LL ($30 \mu\text{mol photons m}^{-2} \text{s}^{-1}$) fluctuations for 30 minutes. (A) Y(II) (B) 1-qP (C) NPQ (mean \pm SD) were derived from the fluorescence measurement in figure 5.7. Details on how these are calculated are described in method section 2.13.

Collectively these PSII fluorescence derived data indicate that the preceding HL phases cause a gradual increase in the proportion of PSII RCs that are closed in the LL phases in the *pgr5* and *pgr5 ndho* mutants. The lower NPQ observed in *pgr5* and *pgr5 ndho* mutants in HL was not however accompanied by a significant increase in NPQ in the LL phases, which would indicate PSII photoinhibition. Thus, the observed closure of PSII RCs reduction of the PQ pool instead reflects an inability of the downstream electron transfer chain components to re-oxidise PSII in the LL periods. This idea will be explored further in the next section. The other key observations here are similarity in *fnr1* phenotype to Col-0, suggesting that loss of FNR membrane binding does not adversely perturb PSII or NPQ under the conditions tested here, indeed there was evidence that NPQ may be enhanced in this mutant. It was also interesting to note a similar 1-qP and NPQ phenotype between *pgr5 ndho* and the single mutant *pgr5*. These data are consistent with the minor role described for NDH-dependent CET in Arabidopsis in HL (Yamori et al., 2015b).

5.4.2 Effects of fluctuating light on PSI photochemistry

From the chlorophyll fluorescence data, it can be observed that the mutants *pgr5* and *pgr5 ndho* are not capable of re-oxidising the PQ pool in the LL periods to the same extent as Col-0, *ndho* and *fnr1*. Therefore, we wanted to investigate how PSI was affected by examining its quantum yield $Y(I)$; this value represents the fraction of overall P700 that is active, i.e. not limited by the acceptor or donor sides.

In HL phases, all genotypes behaved similarly, and they were characterised by a low PSI yield consistent with the light saturation of photosynthesis. LL, instead, caused a rapid increase of $Y(I)$ in all genotypes, apart from in *pgr5* and *pgr5 ndho*, which gradually decreased overtime reaching almost 0 by the third LL phase (Figure 5.9 A). Therefore, as with PSII, PSI quantum yield is suppressed by the loss of PGR5. Compared to PSII, PSI is more affected in *fnr1* and *ndho* with a slightly lower $Y(I)$ in the LL phases, albeit much less severe than in *pgr5* and *pgr5 ndho*. Low $Y(I)$ may be caused by either donor side limitations ($Y(ND)$) on electron donation from Pc to PSI or alternatively by acceptor side limitations ($Y(NA)$) on electron donation from PSI to Fd.

The fraction of P700 under donor side limitation $Y(ND)$ is high in Col-0 in the HL phases consistent with the acidification of the lumen and induction of photosynthetic control at

cytb₆f driven by a high rate of coupled electron-proton transfer (Figure 5.9B). Y(ND) then falls as the lumen pH rises once more in the LL periods. Similar behaviour is seen in *ndho* albeit with slower kinetics of Y(ND) formation. In contrast, *fnr1* shows a similar Y(ND) kinetic to Col-0 but a slightly lower amplitude (Figure 5.9B). Y(ND) is very low in the mutants *pgr5* and *pgr5 ndho* in both HL and LL periods (Figure 5.9B), suggesting their inability to induce photosynthetic control.

Y(NA), the fraction of PSI that cannot be oxidised by a saturation pulse because of a shortage of electron acceptors, initially rises in HL in Col-0 as downstream sinks are transiently reduced, before activation of the Calvin cycle and reoxidation of electron sinks causes it to fall once more (Figure 5.9B). The mutants *ndho* and *fnr1* behaved similarly to Col-0 in the HL periods, although it took longer for Y(NA) to fall in *ndho*, mirroring the slower formation of Y(ND) in these plants (Figure 5.9C). Whereas Y(NA) values in *pgr5* and *pgr5 ndho* remained high without falling in HL and were also significantly increased in the LL phases compared to Col-0, and progressively increased in LL with each preceding HL phase.

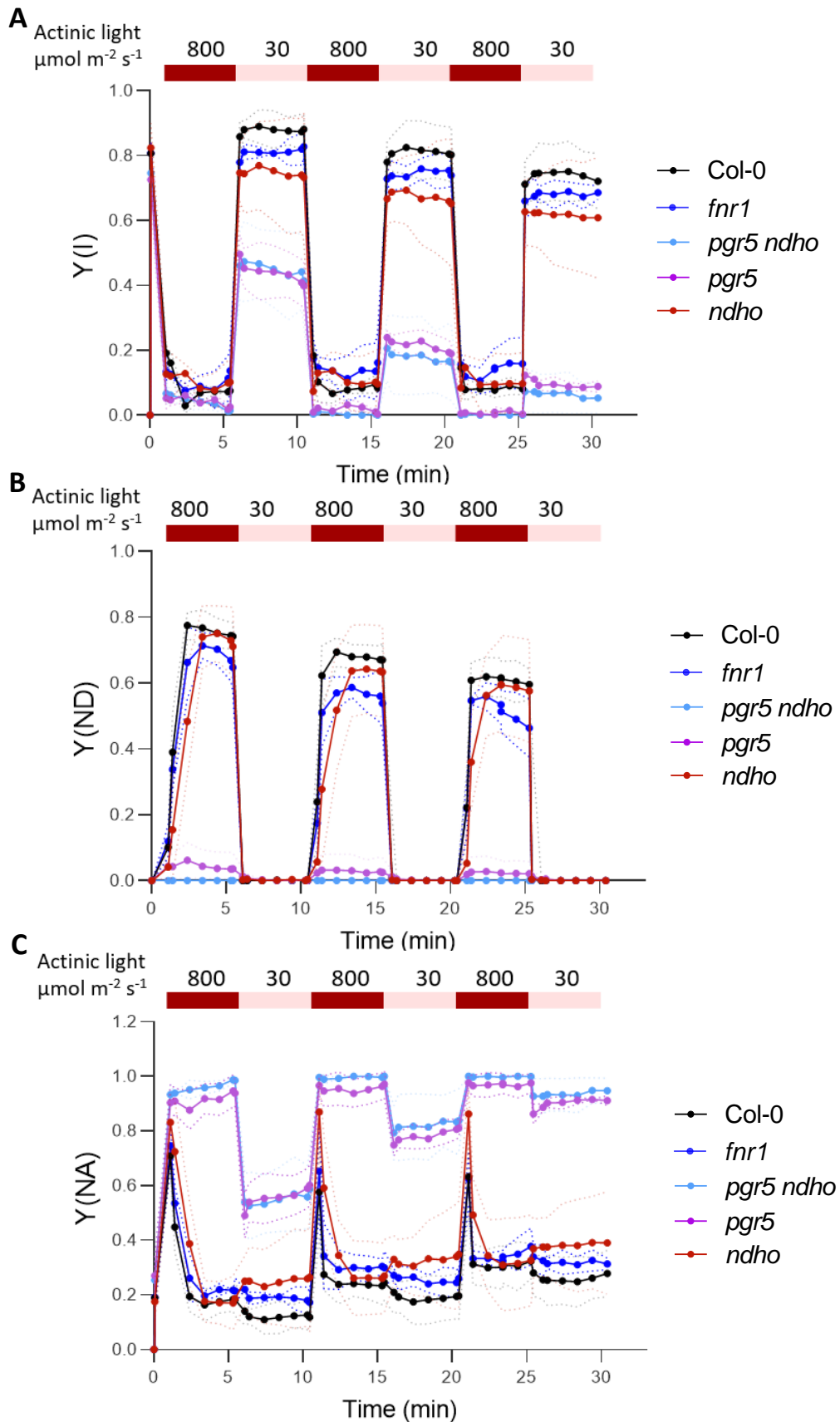


Figure 5.9 | PSI photochemistry.

Dark adapted plants were subjected to HL ($800 \mu\text{mol photons m}^{-2} \text{s}^{-1}$) and LL ($30 \mu\text{mol photons m}^{-2} \text{s}^{-1}$) fluctuations for 30 minutes. (A) Y(I), (B) Y(ND), (C) Y(NA).

Together these data indicate that in contrast to Col-0, PSI is acceptor side limited in *pgr5* and *pgr5 ndho* in HL and moreover this causes a progressive increase in the number of PSI RCs which suffer high Y(NA) in LL. The loss of photosynthetic control in *pgr5* has been previously reported (Munekage et al., 2004; Soursa et al., 2012), however as with NPQ, the double mutant *pgr5 ndho* does not suffer significantly more. This is consistent with the data we obtain on the *ndho* single mutant which shows NDH-dependent CET affects the kinetics of Y(ND) and NPQ formation but has little effect on its overall amplitude. In principle the rise in Y(NA) could be caused by damage to PSI and therefore an inability to transfer electrons onwards to Fd and downstream electron acceptors or alternatively a failure of the downstream metabolism to re-oxidise Fd. This will be further investigated in the next section. The *fnr1* mutant showed little phenotype with respect to PSI parameters under the conditions used here, showing only a slight decrease in Y(ND) and increase in Y(NA) compared to the WT.

5.4.3 Effects of fluctuating light on Fd and PC absorption changes

In addition to PSI parameters the Dual-KLAS NIR also provides information on the redox states of Pc and Fd. To date there has been no investigation in the literature about how these parameters are affected in the CET mutants by fluctuating light. In principle, since photosynthetic control acts at the *cytb₆f* complex upstream of Pc then it should be oxidised as with P700 in HL. Consistent with this Pc oxidation increases rapidly in the HL phases in Col-0 and *ndho*, albeit with slower kinetics in the latter consistent with slower formation of Y(ND) in this mutant (Figure 5.10A). In turn, Pc is partially re-reduced in LL in these plants as photosynthetic control relaxes but does not become completely reduced as P700 does, consistent with the redox potential difference (Pc = +370 mV, P700 +480 mV) favouring PSI reduction at equilibrium. In *ndho* in LL Pc was slightly more reduced than in Col-0. In contrast, in *pgr5* Pc oxidation is much restricted in HL, though interestingly it is not 0 as Y(ND), suggesting some restriction of Pc reduction by *cytb₆f* may still be active in this mutant (Figure 5.10A). The *fnr1* plants behaved similar to Col-0, however the *pgr5 ndho* plants showed unexpectedly increased Pc oxidation compared to *pgr5*.

The Fd absorption data showed that during HL this acceptor becomes largely reduced in Col-0 as photosynthesis becomes light saturated (Figure 5.10B). Indeed, in the HL phases, high levels of reduced Fd were observed in all genotypes, except *ndho* and *fnr1*. In *ndho* and *fnr1*,

HL intensity caused a sudden increase in Fd reduction, but that was shortly after followed by a re-oxidation. Interestingly, in the LL phases, levels of reduced Fd were the highest in Col-0 but much lower and almost completely re-oxidised in LL in all the remaining mutants (Figure 5.10B). Progressively with each HL phase the amount of reduced Fd falls in the WT, *pgr5* and *pgr5 ndho* mutants, although the amount of reduced Fd in the LL periods is more stable.

In summary, the Fd data favour the conclusion that Y(NA) remains high in LL in *pgr5* and *pgr5 ndho* due to photodamage to PSI as opposed to a lack of available Fd acceptor due to slower downstream metabolism. The low Pc oxidation in HL and low NPQ and Y(ND) observed in *pgr5* are consistent with low *pmf* and this was investigated in the next section using the ECS absorption changes.

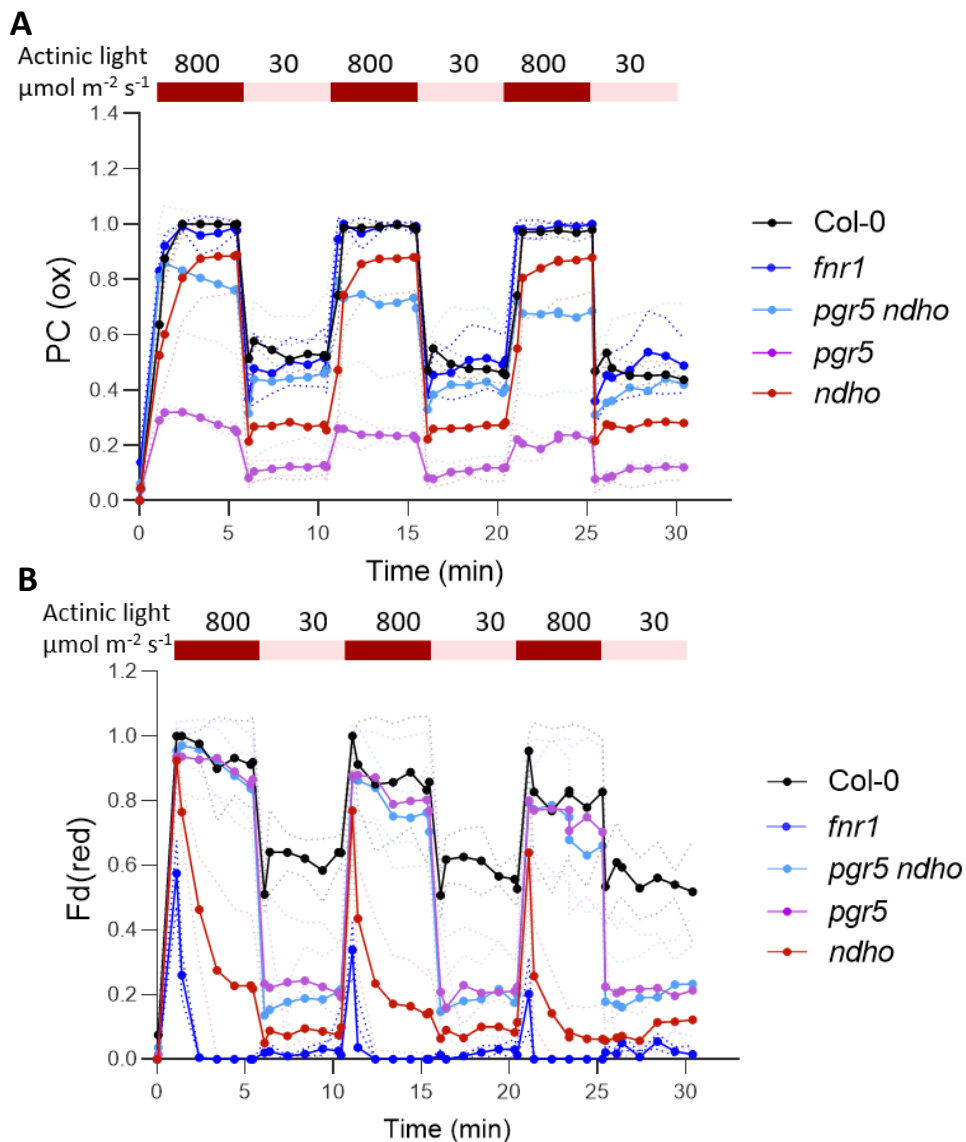


Figure 5.10 Redox state of Pc and Fd.

Dark adapted plants were subjected to HL ($800 \mu\text{mol photons m}^{-2} \text{s}^{-1}$) and LL ($30 \mu\text{mol photons m}^{-2} \text{s}^{-1}$) fluctuations for 30 minutes. (A), Pc oxidation, (B) Fd reduction.

5.5 Effects of light fluctuations on ECS signal

To investigate also the effect of fluctuating lights on the proton transfer across the thylakoid membrane ECS absorption data were recorded on the leaves. As expected the *pmf* increased in HL as the rate of coupled electron-proton transfer acidifies the lumen at a rate greater than its relaxation via the ATP synthase. Unfortunately, the signal amplitude in LL was too low to allow proper quantification of the ECS parameters in LL. The highest *pmf* values were observed in Col-0 and *fnr1* which were not significantly different (Figure 5.11A). On the other hand, the *ndho* mutant showed a small drop in *pmf* amplitude consistent with previous results (Wang et al., 2015). The *pmf* in HL was lowest in *pgr5*, especially in the second and third HL periods where it was only a third of the Col-0 level (Figure 5.11A). Interestingly, the *pgr5 ndho* mutant was no worse affected than *pgr5*, consistent with the similar Y(ND) and NPQ in these two mutants. As previously reported although *pmf* is lower in *pgr5*, the amplitude actually approaches the Col-0 level in the opening moments of HL illumination (Nikkanen et al., 2018; Degen et al., 2023).

The proton conductivity, gH^+ , which reflects the flux of protons through ATP synthase, is very high in *pgr5* as previously reported (Avenson et al., 2005) (Figure 5.11B). In the other mutants gH^+ is lower in the first HL phase yet still higher than in Col-0. In the subsequent HL periods the gH^+ in the mutants increases to near *pgr5* levels, while values in Col-0 are much more stable.

The lowest proton flux (vH^+) was observed in *pgr5 ndho* double mutant, similarly in *pgr5* the flux was lower than in Col-0 especially in the second and third HL periods (Figure 5.11C). Interestingly, while *ndho* behaved like Col-0 the proton flux in *fnr1* was higher. Since $pmf = vH^+/gH^+$, the lower *pmf* in *pgr5* and *pgr5 ndho* must be explained either by a lower vH^+ or higher gH^+ , the data favouring a combination of these two effects.

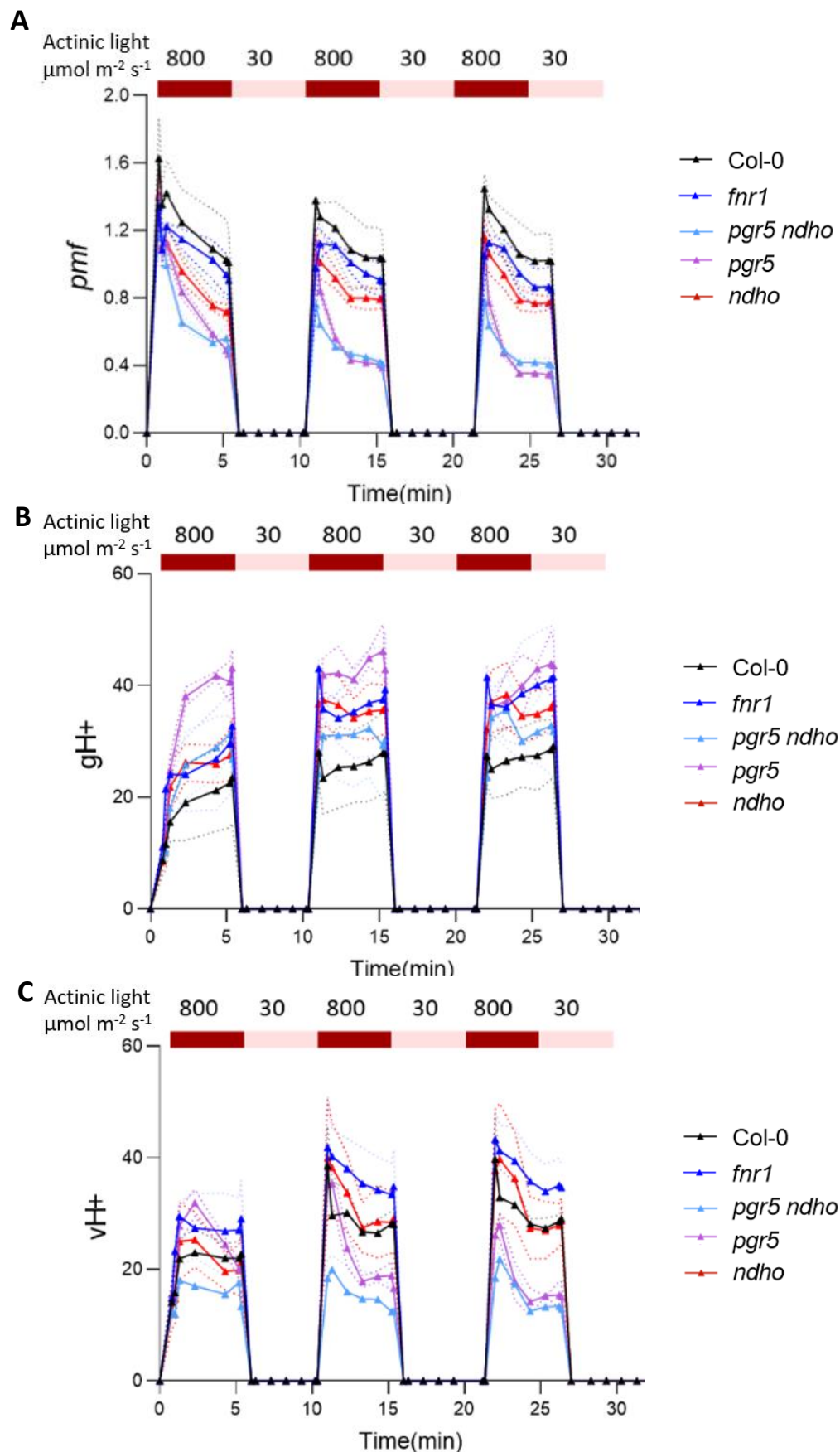


Figure 5.11 Proton motive force (pmf), proton conductivity (gH^+) and proton flux (vH^+).

Dark adapted plants were subjected to HL ($800 \mu\text{mol photons m}^{-2} \text{s}^{-1}$) and LL ($30 \mu\text{mol photons m}^{-2} \text{s}^{-1}$) fluctuations for 30 minutes. DIRK intervals of 300 ms were used to measure pmf (A), gH^+ (B) and vH^+ (C).

5.6 *In vivo* analysis of P700 oxidation activity

Given the lack of a strong phenotype in terms of PSI and PSII parameters and indeed *pmf* in *fnr1* it was interesting to quantify the extent to which CET is actually affected in this mutant. Past work indicated lower CET efficiency in *fnr1* (M. Kramer et al., 2021; Lintala et al., 2007). Here we used the Joliot method (Joliot & Joliot, 2002) which utilises far-red (FR) illumination of dark adapted leaves. Under these conditions the CBB cycle is inactive and CET should be maximal. CET activity was then measured in all mutants by observing the P700 oxidation; a slower P700 oxidation rate would reflect an enhanced CET activity since more electrons are cycled back to PSI via the PQ pool. Before these measurements, all plants were dark adapted and then exposed to a weak actinic light and a multiple turnover (MT) flash, causing the reduction of Fd and ensuring each system was poised in a similar way (Nandha et al., 2007). This was followed by 4 s of darkness in which Fd is re-oxidised and P700 reduced. Oxidation of P700 was then induced by 10 s of FR illumination.

Figure 5.12 shows the P700 oxidation measured in *fnr1*, *pgr5*, *ndho* and *pgr5 ndho* mutants compared to the wild type. It can be observed that P700 oxidation in the double mutant *pgr5 ndho* was much faster compared to all the genotypes, reflecting a strong impairment in the CET activity and consistent with the lack of both CET pathways. In contrast, P700 oxidation rate of the single mutants *pgr5* was still faster than *col-0* yet slower than *pgr5 ndho*, while *ndho* was similar to *Col-0*. Surprisingly, the *fnr1* mutant showed an extremely slow P700 oxidation rate suggesting enhanced CET activity.

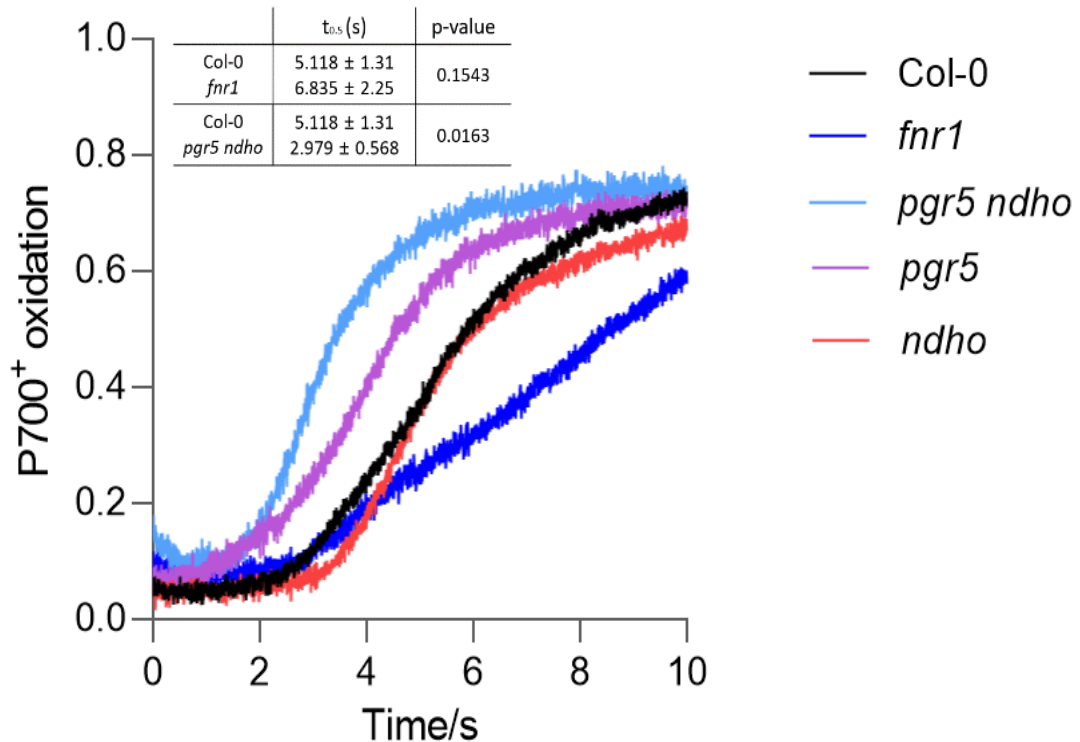


Figure 5.12 | P700 oxidation for CET determination.

To measure P700 oxidation, dark adapted leaves were exposed to a weak actinic light for 30 s, followed by a 30 ms MT flash and 4 s of darkness. P700 oxidation was then measured by turning on FR light for 10 s with final MT pulse. P700 oxidation was measured in *pgr5*, *ndho* and *pgr5 ndho*, *fnr1* in comparison to the wild-type Col-0. Insert: Half-life of P700 oxidation determined by fitting an allosteric sigmoidal function. Data points represent the average of 3 biological replicates \pm SD.

As an alternative means of estimating CET activity one can compare proton flux (vH^+) to the LET rate calculated from Y(II) values of chlorophyll fluorescence (Avenson et al., 2005) (Figure 5.13). Here, a higher ratio is consistent with an increased H^+/e^- ratio produced during photosynthesis. Using this method, we found similar relationships between vH^+ and LET in Col-0 and *ndho*, consistent with their similar CET activity reported by the Joliot method. Similarly, the *pgr5* and *pgr5 ndho* mutants showed much lower ratios consistent with the lower CET activity and lower *pmf* generation. Again, in line with the Joliot method the *fnr1* mutant showed a higher vH^+/LET ratio suggesting an increased capacity for CET compared to Col-0.

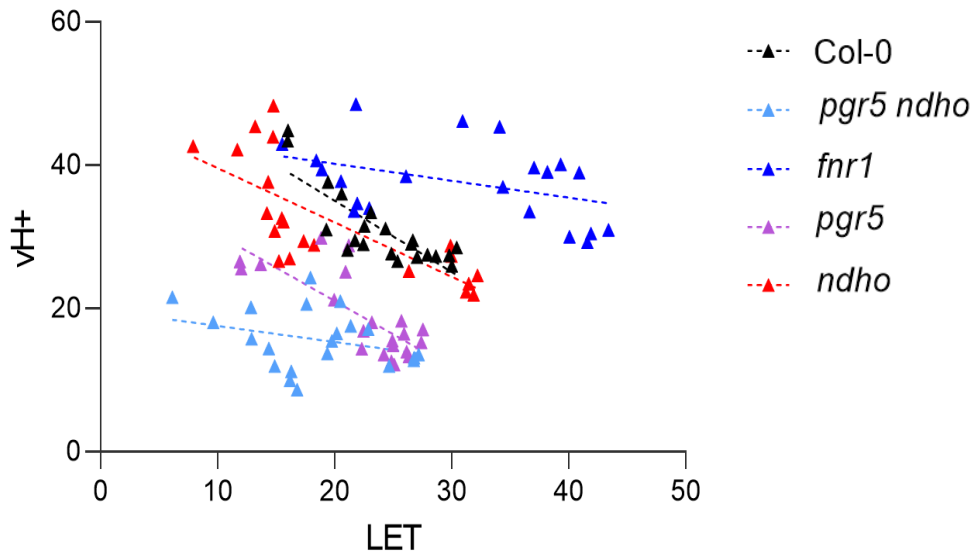


Figure 5.13 | vH+ versus LET.

To measure CET activity values of vH+ were compared to LET activity (derived from chlorophyll fluorescence measurement). The higher the proton flux relative to LET rate the larger the H⁺/e⁻ ratio.

5.7 Discussion

In this chapter the effect of loss of membrane binding of FNR in Arabidopsis on growth and photosynthesis in variable light environments was investigated. Surprisingly, we found that under the variable light experiments used here there was no strong phenotype for the *fnr1* mutant with regard to either growth or PSI/ PSII photosensitivity. This contrasts with previous results which showed *fnr1* plants grow more poorly than the wild-type (Lintala et al., 2007) and shows a greater extent of PSI photoinhibition (Rodriguez-heredia et al., 2022). The contrasting results may reflect the differences in the growth regimes / light intensities employed in these previous studies that were somewhat harsher than used here.

All Arabidopsis plants in this study were grown under 8h light/16h dark cycles. Previous works have either used the same light/dark cycle or 12h light/12h dark cycle. In addition, the light intensity under which our plants were grown was set to 200 $\mu\text{mol m}^{-2} \text{s}^{-1}$, in comparison to 120 $\mu\text{mol m}^{-2} \text{s}^{-1}$ and 100 $\mu\text{mol m}^{-2} \text{s}^{-1}$ (Lintala et al., 2007; Rodriguez-heredia et al., 2022). Furthermore, previous studies have reported a significant increase of PSI photoinactivation in the *fnr1* mutant at higher light intensities (>800 $\mu\text{mol m}^{-2} \text{s}^{-1}$) than the light intensity used in our experiments (M. Kramer et al., 2021; Rodriguez-heredia et al., 2022).

Based on the results presented in this chapter, it appears that CET activity is higher in *fnr1* than in Col-0, which contradicts previous results from other studies. In this study, CET was assessed based on the P700 oxidation rate and by plotting vH^+/LET (Livingston et al., 2010; Munekage et al., 2002; Nandha et al., 2007). It is possible that these discrepancies in the results may be reflect the different approaches used for measuring CET under different physiological circumstances.

Ipso facto, the high CET activity exhibited in *fnr1* appears to rule out the necessity for FNR supercomplex formation with *cytb₆f* and PGR5 for cyclic activity *in vivo*. However, there are several caveats, firstly Immuno gold-label (IGL) studies to investigate the localisation of FNR in the chloroplast have revealed that FNR association to the thylakoid membrane is not completely abolished in the *fnr1* mutant. Instead, it indicates that FNR is still associated to the thylakoid membrane by weak interactions (M. Kramer et al., 2021). This finding contradicts previous studies in which FNR interactions were considered to be completely disrupted, resulting in FNR being fully soluble in the mutant. It is worth noting that these previous conclusions were based on results obtained from experiments involving mechanical separation and centrifugation (Lintala et al., 2007, 2014).

This leaves open the possibility that the weakly-membrane bound FNR sub-population might represent the fraction of FNR found associated with the *cytb₆f* supercomplex presented in the previous chapters. This would also provide an explanation for the fragility of the interactions between FNR and *cytb₆f* and the difficulties encountered in preserving them. As discussed in previous chapters, it is evident that these interactions are more likely to be preserved when gentle detergents such as LMNG or amphipols are used; harsher detergents e.g. DDMs, are more likely to disrupt these as was observed in the solubilisation and Native PAGE studies of Lintala et al 2014.

One possibility is that the observed increase of CET in *fnr1* mutant may be attributed to an increased flow of electrons via *cytb₆f* resulting from the disruption of regular FNR associations with the thylakoid membrane. Future experiments should involve a gentle purification of the *cytb₆f* complex from *fnr1* and *tic62/trol* Arabidopsis mutants to assess FNR binding to the complex.

FNR interaction to the *cytb₆f* could also be regulated by PGR5. In Chapter 4, PGR5 was found to be cross-linked to subIV and FNR, leading to the hypothesis that PGR5 might play a structural role by providing a binding site for FNR to associate with *cytb₆f*. The lack of PGR5 *in vivo* leads to a decrease in CET under the conditions tested. The double mutant *pgr5 ndho* displayed the weakest CET phenotype, however they showed unexpectedly increased Pc oxidation compared to the *pgr5* mutant. These results should be further investigated since they might reflect errors for instance in the calculation of maximum oxidation of Pc.

The decrease of reduced Fd levels observed in LL in *pgr5* and *pgr5 ndho* suggests that the high Y(NA) values in LL are likely due to PSI photodamage, rather than the lack of downstream acceptors due to a slowdown in metabolic activity caused by disruptions to the ATP/NADPH ratio. Interestingly, the *fnr1* mutant presents very low levels of reduced Fd; this could potentially be attributed to the enhanced CET activity discussed in this chapter. Similarly, *ndho* mutant displayed a similar result. It has been shown that PGR5 could potentially associate to the NDH complex in barley (Shen et al., 2022). The loss of NDH in the *ndho* mutant could perhaps increase the binding of PGR5 to *cytb₆f* and therefore providing the binding site for FNR and Fd, finally enhancing CET activity and oxidation of Fd. Further work is now required to distinguish these possibilities.

6. Concluding remarks

The aim of the work described in this thesis was to investigate the mechanism of the AA-sensitive CET pathway in angiosperms. In Chapter 3, several different methods were tested for the isolation and purification of the FNR-*cytb_{6f}* supercomplex. An optimal purification method was developed for the successful preservation of the association of FNR to the *cytb_{6f}* complex, which involved the use of the gentle detergent LMNG. In addition, the CET effector proteins PGR5, PGRL1, TROL and Tic62 were also found in the sample. In Chapter 4, the FNR-*cytb_{6f}* supercomplex in LMNG and amphipol A8-35 was analysed by negative stain; the observed size of the particles confirmed the presence of other proteins associated with *cytb_{6f}*. Despite the stability of the supercomplex particularly in the detergent LMNG, structural characterisation by cryo-EM could not be achieved. The interactions occurring between *cytb_{6f}* and CET effector proteins are extremely labile and perhaps sensitive to physiological conditions. A supercomplex involving PSI, LHCII, *cytb_{6f}*, PGRL1 and FNR has been previously isolated from *Chlamydomonas* (Iwai et al., 2010), though subsequently proved highly unstable (Buchert et al., 2018). To this day, no cryo-EM structure has been resolved of this supercomplex, highlighting the difficulties to preserve the labile interactions between the proteins in a purified sample.

Therefore, in Chapter 4, successful stabilisation of the FNR-*cytb_{6f}* supercomplex was performed with the use of the cross-linker DSS. Through investigation of the cross-linked sample by MS, it was possible to gain novel insights regarding the interactions occurring in the FNR-*cytb_{6f}* supercomplex. Recent work demonstrated the interaction between purified FNR and *cytb_{6f}* is extremely weak (Zakharov et al., 2020). Yet here it was possible to observe cross-links between the stromal face of *cytb_{6f}* subunit IV and FNR suggesting a specific interaction does exist. These two results can be reconciled if one assumes that the interaction is dependent on the presence of the other components of the supercomplex such as PGR5, PGRL1, TROL and Tic62. However, since our MS based structural model suggests a minimum distance of ~28Å between haem *c_n* and the FAD cofactor of FNR it is unlikely that AA-sensitive CET depends on direct electron transfer between these species. Instead FNR may hold reduced Fd in close proximity to the haem *c_n* allowing electron transfer between it and the 2Fe-2S cofactor. The isolated *cytb_{6f}*-FNR supercomplex also exhibits FQR activity as shown in

the measurement of the rate of PQ reduction. These results suggest a key role for the CET effector proteins in promoting enzyme activity and represent an additional evidence of the proposed CET mechanism proposed in this thesis.

Amongst those proteins found in the supercomplex was PGR5, which was found to be cross-linked to the stromal side of *cytb_{6f}* subunit IV and also pulled-down a FNR-*cytb_{6f}* complex from a solubilised thylakoid mixture, corroborating previous reports (DalCorso et al., 2008; Wu et al., 2021). Since PGR5 has been found to affect FNR binding to the membrane in *Chlamydomonas* (Steinbeck et al., 2018) it is possible that it functions as the binding site for FNR-Fd on *cytb_{6f}*. By analysis of the structural model built based on these cross-linking data, PGR5 would bind in the same site of PetP in the cyanobacterial *cytb_{6f}* (Figure 6.1)(Proctor et al., 2022), and also of the protein TSP9 (Sarewicz et al., 2023). TSP9 was identified by MS in the FNR-*cytb_{6f}* supercomplex, suggesting its potential role in the recruitment of PGR5 to *cytb_{6f}*, perhaps in high light or when state II is induced, when TSP9 is phosphorylated by STN7.

The cross-linking results also revealed the interaction of PGRL1 to *cytb_{6f}*, although not to PGR5. Previous studies have shown that PGR5 is tethered to the thylakoid membrane by PGRL1, preventing its degradation by PGRL2 (Rühle et al., 2021). The cross-linking data support the idea of the involvement of PGRL1 in the regulation of the PGR5 in CET. I hypothesise that PGRL1/PGR5 complex interact with *cytb_{6f}*, consistent with past results (DalCorso et al., 2008; Hertle et al., 2013) thereby maintaining PGR5 in close proximity to the complex for it to interact (Figure 6.2B). The release of PGR5 and its subsequent interaction and the reverse would then be regulated by the stromal redox state .e.g through interactions with the m-type Trx (Okegawa et al., 2020, 2022).

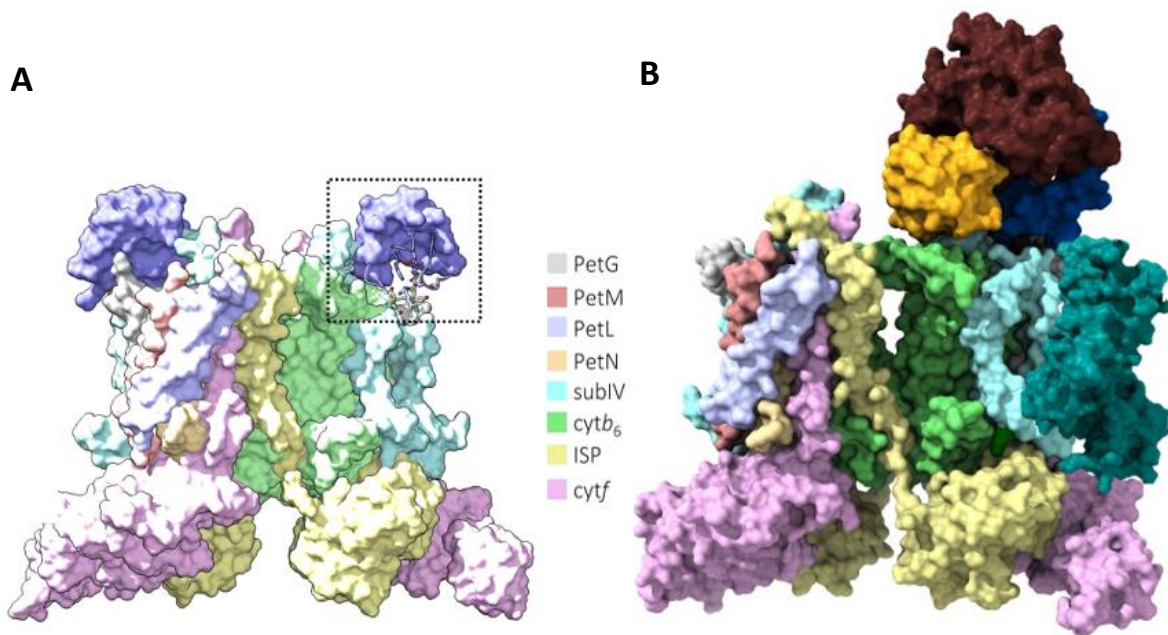


Figure 6.1 | Cryo-EM structure of the PetP-*cytb₆f* and structural model of the FNR-*cytb₆f* complex
 (A) Cryo-EM structure of the cyanobacterial *cytb₆f* complex interacting with PetP (indicated by the black box) (PDB:7ROW). (B) Structural model built of spinach *cytb₆f* interacting to PGR5, FNR, and PGRL1 based on the cross-linking data described in Chapter 4. PGR5 (*blue*) interacts to the spinach *cytb₆f* complex in the same site of PetP. PGRL1 (*teal*) interacts to the transmembrane region of subIV, FNR (*dark red*) interacts to PGR5 and the stromal side of *cytb₆f*. Fd (*gold*) bound to the complex is also shown.

The association of FNR to the thylakoid membrane via TROL and Tic62 proteins enhances CET (M. Kramer et al., 2021; Rodriguez-heredia et al., 2022). The absence of TROL and Tic62 leads to FNR to be more weakly associated with the membrane (M. Kramer et al., 2021). It is possible that the association between *cytb₆f*, FNR, Tic62 and TROL maintains a higher concentration of reduced Fd in close proximity to *cytb₆f*. Another possible function of TROL and Tic62 may be in the regulation of the relative rates of the forward and back reactions of FNR. It is possible that membrane binding favours the reduction of Fd by NADPH. It has been previously shown that FNR interaction with TROL and Tic62 depends on the chloroplast redox state. The pH of the chloroplast stroma varies from being acidic in the darkness to more alkaline in saturating light; interaction of FNR to the two proteins is stronger in the dark and weakened upon illumination (Benz et al., 2009).

Therefore, the attachment of FNR to the thylakoid membrane could provide a mechanism for the partitioning of LET and CET, with membrane association maintaining a higher

concentration of reduced Fd near to *cytb₆f* and so ensuring more electrons can enter the CET system (Figure 6.2).

Unlike maize, *Arabidopsis* has two FNR isoforms and in Chapter 5 we investigated the relevance of FNR binding to the thylakoid membrane by analysing the *fnr1* mutant. Surprisingly, the mutant exhibited a high CET activity. *Ipsa facto* these results cast some doubt on the relevance of FNR binding to *cytb₆f*, however other explanations are possible e.g. FNR2 binding to *cytb₆f* may be enhanced in the absence of FNR1. These ideas now need to be tested further by investigating the dependence of the FNR-*cytb₆f* interaction on specific FNR isoforms.

While this work contributed to the understanding of the CET mechanisms in angiosperms by providing novel insights in the potential interactions occurring between the CET effector proteins, further work is required to confirm these proposed mechanisms. FQR activity measurements could be carried out with the addition of also antimycin A, which inhibits the PGR5-dependent CET pathway in still in an unknown mechanism.

Without any doubts, the cryo-EM structural characterisation of the FNR-*cytb₆f* supercomplex would provide further insights. The research outlined in this thesis serves a strong foundation for future experiments that could be performed to structurally characterise this complex and elucidate the fascinating mechanisms of CET.

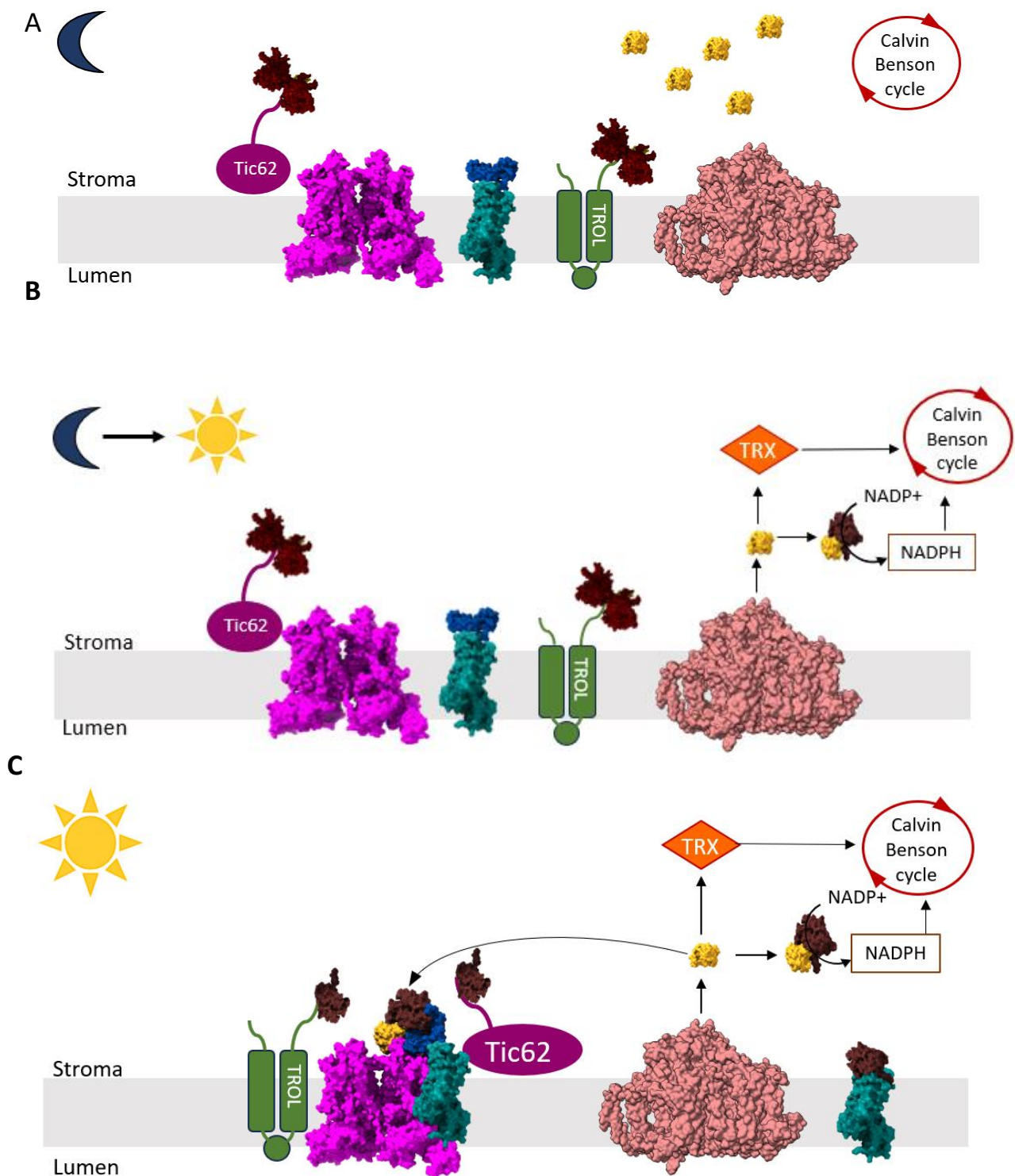


Figure 6.2 | Possible model of the regulation of the FNR-cyt b_6f supercomplex formation.

(A) In the dark FNR dimers are bound to the thylakoid membrane by TROL and Tic62. (B) Upon slight illumination, the Fd pool becomes more reduced and CBB enzymes are activated by the TRX system. NADPH is generated. (C) Upon high light illumination, PGR1/PGR5 interacts with cyt b_6f facilitating the PGR5 association to cyt b_6f . FNR interaction with TROL and Tic62 decreases; FNR:Fd complex interacts with cyt b_6f via PGR5.

7. Bibliography

Akiyama, K. et al. (2023) "Two specific domains of the γ subunit of chloroplast Fo F1 provide redox regulation of the ATP synthesis through conformational changes," *Proceedings of the National Academy of Sciences*, 120(6). Available at: <https://doi.org/10.1073/pnas.2218187120>.

Alexis Riché, Louis Dumas, Soazig Malesinski, Guillaume Bossan, Céline Madigou, Francesca Zito, J. A. (2023). The stromal side of cytochrome b6f complex regulates state transitions. *BioRxiv*.

Allen, J. F. (2003). Cyclic, pseudocyclic and noncyclic photophosphorylation: New links in the chain. *Trends in Plant Science*, 8(1), 15–19. [https://doi.org/10.1016/S1360-1385\(02\)00006-7](https://doi.org/10.1016/S1360-1385(02)00006-7)

Alte, F., Stengel, A., Benz, J. P., Petersen, E., Soll, J., Groll, M., & Bölder, B. (2010). *Ferredoxin : NADPH oxidoreductase is recruited to thylakoids by binding to a polyproline type II helix in a pH-dependent manner*. <https://doi.org/10.1073/pnas.1009124107>

Anderson, J. M. (1982). *thylakoids of higher plant chloroplasts possess a c-type cytochrome, cyt f(E, at pH 7.0, t 360 mV; h max of the cr band; 554 nm) and three b-type cyto- chromes, cyt. 138(1), 62–66.*

Arana, J. L., & Vallejos, R. H. (1982). Involvement of sulfhydryl groups in the activation mechanism of the ATPase activity of chloroplast coupling factor 1. *Journal of Biological Chemistry*, 257(3), 1125–1127. [https://doi.org/10.1016/s0021-9258\(19\)68159-7](https://doi.org/10.1016/s0021-9258(19)68159-7)

Asada, K. (1999). The water-water cycle in chloroplasts: Scavenging of active oxygens and dissipation of excess photons. *Annual Review of Plant Biology*, 50, 601–639. <https://doi.org/10.1146/annurev.arplant.50.1.601>

Avenson, T. J., Cruz, J. A., Kanazawa, A., & Kramer, D. M. (2005). *Regulating the proton budget of higher plant photosynthesis*. 102(27), 9709–9713. <https://doi.org/10.1073/pnas.0503952102>

Balsera, M., Stengel, A., Soll, J., & Bölder, B. (2007). Tic62: A protein family from metabolism to protein translocation. *BMC Evolutionary Biology*, 7, 1–12. <https://doi.org/10.1186/1471-2148-7-43>

Batie, C. J., & Kamins, H. (1984a). Electron Transfer by Ferredoxin : NADP + Reductase. *Journal of Biological Chemistry*, 259(19), 11976–11985. [https://doi.org/10.1016/S0021-9258\(20\)71306-2](https://doi.org/10.1016/S0021-9258(20)71306-2)

Batie, C. J., & Kamins, H. (1984b). *Ferredoxin : NADP + Oxidoreductase EQUILIBRIA IN BINARY AND TERNARY COMPLEXES WITH*. 259(14), 8832–8839. [https://doi.org/10.1016/S0021-9258\(17\)47229-2](https://doi.org/10.1016/S0021-9258(17)47229-2)

Benz, J. P., Lintala, M., Mulo, P., & Bo, B. (2010). *A new concept for ferredoxin – NADP (H) oxidoreductase binding to plant thylakoids*. 15(608). <https://doi.org/10.1016/j.tplants.2010.08.008>

Benz, J. P., Stengel, A., Lintala, M., Lee, Y. H., Weber, A., Philippar, K., Gügel, I. L., Kaieda, S., Ikegami, T., Mulo, P., Soll, J., & Bölder, B. (2009). Arabidopsis Tic62 and ferredoxin-NADP(H) oxidoreductase form light-regulated complexes that are integrated into the chloroplast redox poise. *Plant Cell*, 21(12), 3965–3983. <https://doi.org/10.1105/tpc.109.069815>

Berrisford, J. M., Baradaran, R., & Sazanov, L. A. (2016). Biochimica et Biophysica Acta Structure of bacterial respiratory complex I ☆. *BBA - Bioenergetics*, 1857(7), 892–901. <https://doi.org/10.1016/j.bbabi.2016.01.012>

- Bilger, W., Björkman, O., & Thayer, S. S. (1989). Light-Induced Spectral Absorbance Changes in Relation to Photosynthesis and the Epoxidation State of Xanthophyll Cycle Components in Cotton Leaves. *Plant Physiology*, 91(2), 542–551. <https://doi.org/10.1104/pp.91.2.542>
- Bojko, M., Kruk, J. and Więckowski, S. (2003) 'Plastoquinones are effectively reduced by ferredoxin:NADP⁺ oxidoreductase in the presence of sodium cholate micelles significance for cyclic electron transport and chlororespiration', *Phytochemistry*, 64(6), pp. 1055–1060. doi:10.1016/s0031-9422(03)00506-5.
- Bous, J., Orcel, H., Floquet, N., Leyrat, C., Lai-Kee-Him, J., Gaibelet, G., Ancelin, A., Saint-Paul, J., Trapani, S., Louet, M., Sounier, R., Déméné, H., Granier, S., Bron, P., & Mouillac, B. (2021). Cryo-electron microscopy structure of the antidiuretic hormone arginine-vasopressin V2 receptor signaling complex. *Science Advances*, 7(21), 1–19. <https://doi.org/10.1126/sciadv.abg5628>
- Boyer, P. D. (2000). *Catalytic site forms and controls in ATP synthase catalysis*. 1458, 252–262.
- Björkman O (1981) Responses to different quantum flux densities. In O Lange, Nobel PS, Osmond CB, Ziegler H, eds, *Physiological Plant Ecology I: Responses to the Physical Environment*. Springer-Verlag, Berlin, pp 57-107
- Buchert, F., Hamon, M., Gäbelein, P., Scholz, M., Hippler, M., & Wollman, F. A. (2018). The labile interactions of cyclic electron flow effector proteins. *Journal of Biological Chemistry*, 293(45), 17559–17573. <https://doi.org/10.1074/jbc.RA118.004475>
- Buchert, F., Mosebach, L., Gäbelein, P., & Hippler, M. (2020). PGR5 is required for efficient Q cycle in the cytochrome b6f complex during cyclic electron flow. *Biochemical Journal*, 477(9), 1631–1650. <https://doi.org/10.1042/BCJ20190914>
- Carrillo, N., & Ceccarelli, E. A. (2003). Open questions in ferredoxin-NADP⁺ reductase catalytic mechanism. *European Journal of Biochemistry*, 270(9), 1900–1915. <https://doi.org/10.1046/j.1432-1033.2003.03566.x>
- Caspy, I., Fadeeva, M., Kuhlger, S., Borovikova-Sheinker, A., Klaiman, D., Masrati, G., Drepper, F., Ben-Tal, N., Hippler, M., & Nelson, N. (2021). Structure of plant photosystem I-plastocyanin complex reveals strong hydrophobic interactions. *Biochemical Journal*, 478(12), 2371–2384. <https://doi.org/10.1042/BCJ20210267>
- Chae, P. S., Rasmussen, S. G. F., Rana, R. R., Gotfryd, K., Chandra, R., Goren, M. A., Kruse, A. C., Nurva, S., Loland, C. J., Pierre, Y., Drew, D., Popot, J., Picot, D., Fox, B. G., Guan, L., Gether, U., Byrne, B., Kobilka, B., & Gellman, S. H. (2010). *Maltose – neopentyl glycol (MNG) amphiphiles for solubilization , stabilization and crystallization of membrane proteins*. 7(12). <https://doi.org/10.1038/nmeth.1526>
- Charvolin, D., Picard, M., Huang, L. S., Berry, E. A., & Popot, J. L. (2014). Solution Behavior and Crystallization of Cytochrome bc 1 in the Presence of Amphipols. *Journal of Membrane Biology*, 247(9–10), 981–996. <https://doi.org/10.1007/s00232-014-9694-4>
- Chen, Y., Clarke, O. B., Kim, J., Stowe, S., Kim, Y. K., Assur, Z., Cavalier, M., Godoy-Ruiz, R., Von Alpen, D. C., Manzini, C., Blamer, W. S., Frank, J., Quadro, L., Weber, D. J., Shapiro, L., Hendrickson, W. A., & Mancina, F. (2016). Structure of the STRA6 receptor for retinol uptake. *Science*, 353(6302), 1–28. <https://doi.org/10.1126/science.aad8266>

- Chung, K. Y., Kim, T. H., Manglik, A., Alvares, R., Kobilka, B. K., & Prosser, R. S. (2012). Role of Detergents in Conformational Exchange of a G. *Journal of Biological Chemistry*, *287*(43), 36305–36311. <https://doi.org/10.1074/jbc.M112.406371>
- Clark, R. D., Hawkesford, M. J., Coughlan, S. J., Bennett, J., & Hind, G. (1984). Association of ferredoxin-NADP+ oxidoreductase with the chloroplast cytochrome b-f complex. *FEBS Letters*, *174*(1), 137–142. [https://doi.org/10.1016/0014-5793\(84\)81092-3](https://doi.org/10.1016/0014-5793(84)81092-3)
- Cox, R. P., & Andersson, B. (1981). Lateral and transverse organisation of cytochromes in the chloroplast thylakoid membrane. *Biochemical and Biophysical Research Communications*, *103*(4), 1336–1342. [https://doi.org/10.1016/0006-291X\(81\)90269-2](https://doi.org/10.1016/0006-291X(81)90269-2)
- Cramer, W. A., Hasan, S. S., & Yamashita, E. (2011). The Q cycle of cytochrome bc complexes: A structure perspective. *Biochimica et Biophysica Acta - Bioenergetics*, *1807*(7), 788–802. <https://doi.org/10.1016/j.bbabi.2011.02.006>
- Crofts, A; Meinhardt, S; Jones, K; Snozzi, M. (1983). THE ROLE OF THE QUINONE POOL IN THE CYCLIC ELECTRONTRANSFER CHAIN OF RHODOPSEUDOMONAS SPHAEROIDES: A MODIFIED Q-CYCLE MECHANISM. *Biochim Biophys Acta*. [https://doi.org/10.1016/0005-2728\(83\)90120-2](https://doi.org/10.1016/0005-2728(83)90120-2).THE
- DalCorso, G., Pesaresi, P., Masiero, S., Aseeva, E., Schünemann, D., Finazzi, G., Joliot, P., Barbato, R., & Leister, D. (2008). A Complex Containing PGRL1 and PGR5 Is Involved in the Switch between Linear and Cyclic Electron Flow in Arabidopsis. *Cell*, *132*(2), 273–285. <https://doi.org/10.1016/j.cell.2007.12.028>
- Darrouzet, E., Valkova-Valchanova, M., Moser, C. C., Dutton, P. L., & Daldal, F. (2000). Uncovering the [2Fe2S] domain movement in cytochrome bc1 and its implications for energy conversion. *Proceedings of the National Academy of Sciences of the United States of America*, *97*(9), 4567–4572. <https://doi.org/10.1073/pnas.97.9.4567>
- Degen, G. E., Jackson, P. J., Proctor, M. S., Zoulias, N., Casson, S. A., & Johnson, M. P. (2022). Supercharged PGR5-dependent cyclic electron transfer compensates for mis-regulated chloroplast ATP synthase 2. <https://doi.org/10.1101/2022.09.25.509416>
- Degen, G. E., Jackson, P. J., Proctor, M. S., Zoulias, N., Casson, S. A., & Johnson, M. P. (2023). High cyclic electron transfer via the PGR5 pathway in the absence of photosynthetic control. *Plant Physiology*, *192*(1), 370–386. <https://doi.org/10.1093/plphys/kiad084>
- Denison, M. S., Fine, J., & Wilkinson, C. F. (1984). Protamine sulfate precipitation: A new assay for the Ah receptor. *Analytical Biochemistry*, *142*(1), 28–36. [https://doi.org/10.1016/0003-2697\(84\)90512-8](https://doi.org/10.1016/0003-2697(84)90512-8)
- Dietrich, J., & Kühlbrandt, W. (1999). Purification and two-dimensional crystallization of highly active cytochrome b6f complex from spinach. *FEBS Letters*, *463*(1–2), 97–102. [https://doi.org/10.1016/S0014-5793\(99\)01609-9](https://doi.org/10.1016/S0014-5793(99)01609-9)
- Duysens L N M. (1954). *Reversible Changes in the Absorption Spectrum of Chlorella upon Irradiation*. 2.
- Endo, T., Mi, H., Shikanai, T., & Asada, K. (1997). Donation of Electrons to Plastoquinone by NAD(P)H Dehydrogenase and by Ferredoxin-Quinone Reductase in Spinach Chloroplasts. *Plant and Cell Physiology*, *38*(11), 1272–1277. <https://doi.org/10.1093/oxfordjournals.pcp.a029115>

- Flannery, S. E., Hepworth, C., Wood, W. H. J., Pastorelli, F., Hunter, C. N., Dickman, M. J., Jackson, P. J., & Johnson, M. P. (2021). Developmental acclimation of the thylakoid proteome to light intensity in *Arabidopsis*. *Plant Journal*, *105*(1), 223–244. <https://doi.org/10.1111/tpj.15053>
- Friedrich, T., Steinmüller, K., & Weiss, H. (1995). The proton-pumping respiratory complex I of bacteria and mitochondria and its homologue in chloroplasts. *FEBS Letters*, *367*(2), 107–111. [https://doi.org/10.1016/0014-5793\(95\)00548-N](https://doi.org/10.1016/0014-5793(95)00548-N)
- Hanke, G.T. *et al.* (2005) 'Multiple iso-proteins of FNR in *arabidopsis*: Evidence for different contributions to chloroplast function and nitrogen assimilation', *Plant, Cell & Environment*, *28*(9), pp. 1146–1157. doi:10.1111/j.1365-3040.2005.01352.x.
- Hahn, A., Vonck, J., Mills, D. J., Meier, T., & Kühlbrandt, W. (2018). Structure, mechanism, and regulation of the chloroplast ATP synthase. *Science*, *360*(6389). <https://doi.org/10.1126/science.aat4318>
- Hald, S., Nandha, B., Gallois, P., & Johnson, G. N. (2008). *Biochimica et Biophysica Acta Feedback regulation of photosynthetic electron transport by NADP (H) redox poise*. *1777*, 433–440. <https://doi.org/10.1016/j.bbabi.2008.02.007>
- Harbinson J., & Hedley, C. L. (1989). The kinetics of P-700+ reduction in leaves: a novel in situ probe of thylakoid functioning. *Plant, Cell & Environment*, *12*(4), 357–369. <https://doi.org/10.1111/j.1365-3040.1989.tb01952.x>
- Hauer, F., Gerle, C., Fischer, N., & Shinzawa-ito, K. (2015). *GraDeR : Membrane Protein Complex Preparation for Single-Particle Cryo-EM Resource GraDeR : Membrane Protein Complex Preparation for Single-Particle Cryo-EM*. November 2017. <https://doi.org/10.1016/j.str.2015.06.029>
- Havaux, M. (2020). Plastoquinone In and Beyond Photosynthesis. *Trends in Plant Science*, *25*(12), 1252–1265. <https://doi.org/10.1016/j.tplants.2020.06.011>
- He, Z., & Mi, H. (2016). Functional characterization of the subunits N, H, J, and O of the NAD(P)H dehydrogenase complexes in *Synechocystis* sp. strain PCC 68031. *Plant Physiology*, *171*(2), 1320–1332. <https://doi.org/10.1104/pp.16.00458>
- He, Z., Xu, M., Wu, Y., Lv, J., Fu, P., & Mi, H. (2016). NdhM subunit is required for the stability and the function of NAD(P)H dehydrogenase complexes involved in CO₂ uptake in *synechocystis* sp. strain PCC 6803. *Journal of Biological Chemistry*, *291*(11), 5902–5912. <https://doi.org/10.1074/jbc.M115.698084>
- Hepworth, C., Wood, W. H. J., Emrich-mills, T. Z., Proctor, M. S., Casson, S., & Johnson, M. P. (2021). Dynamic thylakoid stacking and state transitions work synergistically to avoid acceptor-side limitation of photosystem I. *Nature Plants*, *7*(January), 24–27. <https://doi.org/10.1038/s41477-020-00828-3>
- Hertle, A. P., Blunder, T., Wunder, T., Pesaresi, P., Pribil, M., Armbruster, U., & Leister, D. (2013). PGRL1 Is the Elusive Ferredoxin-Plastoquinone Reductase in Photosynthetic Cyclic Electron Flow. In *Molecular Cell* (Vol. 49, Issue 3, pp. 511–523). <https://doi.org/10.1016/j.molcel.2012.11.030>
- Hitchcock, A., Jackson, P. J., Chidgey, J. W., Dickman, M. J., Hunter, C. N., & Canniffe, D. P. (2016). Biosynthesis of Chlorophyll a in a Purple Bacterial Phototroph and Assembly into a Plant Chlorophyll-Protein Complex. *ACS Synthetic Biology*, *5*(9), 948–954. <https://doi.org/10.1021/acssynbio.6b00069>
- Huang, D., Everly, R. ., Cheng, R. H., Heymann, J. ., Schagger, H., Sled, V., Onishi, T., Baker, T. ., & Cramer, W. . (1994). *Characterization of the Chloroplast Cytochrome b6 f Complex as a Structural and Functional Dimer*. *33*(14), 4401–4409.

- HURT, E., & HAUSKA, G. (1981). A Cytochrome f/b6 Complex of Five Polypeptides with Plastoquinol-Plastocyanin-Oxidoreductase Activity from Spinach Chloroplasts. *European Journal of Biochemistry*, *117*(3), 591–599. <https://doi.org/10.1111/j.1432-1033.1981.tb06379.x>
- Ifuku, K., Endo, T., Shikanai, T., & Aro, E. M. (2011). Structure of the chloroplast NADH dehydrogenase-like complex: Nomenclature for nuclear-encoded subunits. *Plant and Cell Physiology*, *52*(9), 1560–1568. <https://doi.org/10.1093/pcp/pcr098>
- Iwai, M., Takizawa, K., Tokutsu, R., Okamuro, A., Takahashi, Y., & Minagawa, J. (2010). Isolation of the elusive supercomplex that drives cyclic electron flow in photosynthesis. *Nature*, *464*(7292), 1210–1213. <https://doi.org/10.1038/nature08885>
- Jahns, P., Graf, M., Munekage, Y., & Shikanai, T. (2002). Single point mutation in the Rieske iron-sulfur subunit of cytochrome b6/f leads to an altered pH dependence of plastoquinol oxidation in Arabidopsis. *FEBS Letters*, *519*(1–3), 99–102. [https://doi.org/10.1016/S0014-5793\(02\)02719-9](https://doi.org/10.1016/S0014-5793(02)02719-9)
- Jansen, T., Reildnder, H., Steppuhn, J., & Herrmann, R. G. (1988). Analysis of cDNA clones encoding the entire precursor-polypeptide for ferredoxin: NADP+ oxidoreductase from spinach. *Current Genetics*, *13*(6), 517–522. <https://doi.org/10.1007/BF02427758>
- Johnson, G. N. (2011). Physiology of PSI cyclic electron transport in higher plants. *Biochimica et Biophysica Acta - Bioenergetics*, *1807*(3), 384–389. <https://doi.org/10.1016/j.bbabi.2010.11.009>
- Johnson, M. P., & Wientjes, E. (2020). The relevance of dynamic thylakoid organisation to photosynthetic regulation. *Biochimica et Biophysica Acta - Bioenergetics*, *1861*(4), 148039. <https://doi.org/10.1016/j.bbabi.2019.06.011>
- Joliot, P., Barbier, G., & Chabaud, R. (1969). U N Nouveau Modele Des Centres. *Photochemistry and Photobiology*, *10*(16), 309–329.
- Joliot, P., & Johnson, G. N. (2011). Regulation of cyclic and linear electron flow in higher Plants. *Proceedings of the National Academy of Sciences of the United States of America*, *108*(32), 13317–13322. <https://doi.org/10.1073/pnas.1110189108>
- Joliot, P., & Joliot, A. (1986). Proton pumping and electron transfer in the cytochrome b6f complex of algae. *Biochimica et Biophysica Acta* *849* 211-222.
- Joliot, P., & Joliot, A. (2002). *Cyclic electron transfer in plant leaf*. *99*(15). <https://doi.org/10.1073/pnas.102306999>
- Junesch, U., & Gräber, P. (1987). Influence of the redox state and the activation of the chloroplast ATP synthase on proton-transport-coupled ATP synthesis/hydrolysis. *BBA - Bioenergetics*, *893*(2), 275–288. [https://doi.org/10.1016/0005-2728\(87\)90049-1](https://doi.org/10.1016/0005-2728(87)90049-1)
- Jurić, Hazler-pilepic, K., Tomas, A., Jelic, B., Vojta, L., Allen, J. F., Schleiff, E., & Fulgosi, H. (2009). *Tethering of ferredoxin: NADP + oxidoreductase to thylakoid membranes is mediated by novel chloroplast protein TROL*. 783–794. <https://doi.org/10.1111/j.1365-313X.2009.03999.x>
- Kamienietzky, A., & Nelson, N. (1975). Preparation and Properties of Chloroplasts Depleted of Chloroplast Coupling Factor 1 by Sodium Bromide Treatment. *Plant Physiology*, *55*(2), 282–287. <https://doi.org/10.1104/pp.55.2.282>
- Kampjut, D., & Sazanov, L. A. (2020). The coupling mechanism of mammalian respiratory complex I. *Science*, *370*(6516). <https://doi.org/10.1126/SCIENCE.ABC4209>

- Kekic, T., Fulgosi, H., Vojta, L., & Berto, B. (2020). *Molecular basis of ferredoxin : NADP (p) reductase interactions with FNR binding domains from TROL and Tic62 proteins*. 1215. <https://doi.org/10.1016/j.molstruc.2020.128281>
- Kim, Y. J., Lee, H. M., Wang, Y., Wu, J., Kim, S. G., Kang, K. Y., Park, K. H., Kim, Y. C., Choi, I. S., Agrawal, G. K., Rakwal, R., & Kim, S. T. (2013). Depletion of abundant plant RuBisCO protein using the protamine sulfate precipitation method. *Proteomics*, 13(14), 2176–2179. <https://doi.org/10.1002/pmic.201200555>
- Kim, Y. J., Wang, Y., Gupta, R., Kim, S. W., Min, C. W., Kim, Y. C., Park, K. H., Agrawal, G. K., Rakwal, R., Choung, M. G., Kang, K. Y., & Kim, S. T. (2015). Protamine sulfate precipitation method depletes abundant plant seed-storage proteins: A case study on legume plants. *Proteomics*, 15(10), 1760–1764. <https://doi.org/10.1002/pmic.201400488>
- Klughammer, C., & Schreiber, U. (2016). Deconvolution of ferredoxin , plastocyanin , and P700 transmittance changes in intact leaves with a new type of kinetic LED array spectrophotometer. *Photosynthesis Research*, 128(2), 195–214. <https://doi.org/10.1007/s11120-016-0219-0>
- Kono, M. *et al.* (2019) 'Far-red light accelerates photosynthesis in the low-light phases of fluctuating light', *Plant and Cell Physiology*, 61(1), pp. 192–202. doi:10.1093/pcp/pcz191.
- Kramer, D. M., & Evans, J. R. (2011). The importance of energy balance in improving photosynthetic productivity. *Plant Physiology*, 155(1), 70–78. <https://doi.org/10.1104/pp.110.166652>
- Kramer, M., Rodriguez-Heredia, M., Saccon, F., Mosebach, L., Twachtmann, M., Krieger-Liszkay, A., Duffy, C., Knell, R. J., Finazzi, G., & Hanke, G. T. (2021). Regulation of photosynthetic electron flow on dark to light transition by ferredoxin:Nadp(h) oxidoreductase interactions. *ELife*, 10, 1–32. <https://doi.org/10.7554/eLife.56088>
- Kruk, J., & Karpinski, S. (2006). *An HPLC-based method of estimation of the total redox state of plastoquinone in chloroplasts , the size of the photochemically active plastoquinone-pool and its redox state in thylakoids of Arabidopsis*. 1757, 1669–1675. <https://doi.org/10.1016/j.bbabi.2006.08.004>
- Küchler, M., Decker, S., & Heins, L. (2002). *Protein import into chloroplasts involves redox-regulated proteins*. 21(22).
- Kurisu, G., Kusunoki, M., Katoh, E., Yamazaki, T., Teshima, K., Onda, Y., Kimata-Arigo, Y., & Hase, T. (2001). Structure of the electron transfer complex between ferredoxin and ferredoxin-NADP+ reductase. *Nature Structural Biology*, 8(2), 117–121. <https://doi.org/10.1038/84097>
- Lamb, J., Røkke, G., and Hohmann-Marriott, M. (2018). Chlorophyll fluorescence emission spectroscopy of oxygenic organisms at 77 K. *Photosynthetica* 56, 105-124.
- Lan, Y., Chen, Q., & Mi, H. (2023). NdhS interacts with cytochrome b6f to form a complex in Arabidopsis. *Plant Journal*, 1–11. <https://doi.org/10.1111/tbj.16398>
- Laughlin, T. G., Bayne, A. N., Trempe, J. F., Savage, D. F., & Davies, K. M. (2019). Structure of the complex I-like molecule NDH of oxygenic photosynthesis. *Nature*, 566(7744), 411–414. <https://doi.org/10.1038/s41586-019-0921-0>
- Laughlin, T. G., Savage, D. F., & Davies, K. M. (2020). BBA - Bioenergetics Recent advances on the structure and function of NDH-1 : The complex I of oxygenic photosynthesis. *BBA - Bioenergetics*, 1861(11), 148254. <https://doi.org/10.1016/j.bbabi.2020.148254>

- Le Bon, C., Marconnet, A., Masscheleyn, S., Popot, J. L., & Zoonens, M. (2018). Folding and stabilizing membrane proteins in amphipol A8-35. *Methods*, 147(December 2017), 95–105. <https://doi.org/10.1016/j.ymeth.2018.04.012>
- Lee, H. J., Lee, H. S., Youn, T., Byrne, B., & Chae, P. S. (2022). Impact of novel detergents on membrane protein studies. *Chem*, 8(4), 980–1013. <https://doi.org/10.1016/j.chempr.2022.02.007>
- Lee, K., & O'Reilly, F. J. (2023). Cross-linking mass spectrometry for mapping protein complex topologies in situ. *Essays in Biochemistry*, 67(2), 215–228. <https://doi.org/10.1042/EBC20220168>
- Lee, Y. H., Ikegami, T., Standley, D. M., Sakurai, K., Hase, T., & Goto, Y. (2011). Binding energetics of ferredoxin-NADP + reductase with ferredoxin and its relation to function. *ChemBioChem*, 12(13), 2062–2070. <https://doi.org/10.1002/cbic.201100189>
- Lee, Y. H., Tamura, K., Maeda, M., Hoshino, M., Sakurai, K., Takahashi, S., Ikegami, T., Hase, T., & Goto, Y. (2007). Cores and pH-dependent dynamics of ferredoxin-NADP+ reductase revealed by hydrogen/deuterium exchange. *Journal of Biological Chemistry*, 282(8), 5959–5967. <https://doi.org/10.1074/jbc.M608417200>
- Lemaire, C., Girard-Bascou, J., Wollman, F. A., & Bennoun, P. (1986). Studies on the cytochrome b6/f complex. I. Characterization of the complex subunits in *Chlamydomonas reinhardtii*. *BBA - Bioenergetics*, 851(2), 229–238. [https://doi.org/10.1016/0005-2728\(86\)90130-1](https://doi.org/10.1016/0005-2728(86)90130-1)
- Li, S. (2022). *Detergents and alternatives in cryo-EM studies of membrane proteins*. 54(July), 1049–1056.
- Lintala, M., Allahverdiyeva, Y., Kangasja, S., Lehtima, N., Kera, M., & Rintama, E. (2009). *oxidoreductase isoforms in Arabidopsis thaliana*. 1103–1115. <https://doi.org/10.1111/j.1365-313X.2008.03753.x>
- Lintala, M., Allahverdiyeva, Y., Kidron, H., Piippo, M., Battchikova, N., Suorsa, M., Rintamäki, E., Salminen, T. A., Aro, E. M., & Mulo, P. (2007). Structural and functional characterization of ferredoxin-NADP +-oxidoreductase using knock-out mutants of Arabidopsis. *Plant Journal*, 49(6), 1041–1052. <https://doi.org/10.1111/j.1365-313X.2006.03014.x>
- Lintala, M., Schuck, N., Thormählen, I., Jungfer, A., Weber, K. L., Weber, A. P. M., Geigenberger, P., Soll, J., Bölder, B., & Mulo, P. (2014). Arabidopsis tic62 trol mutant lacking thylakoid-bound ferredoxin-NADP + Oxidoredu shows distinct metabolic phenotype. *Molecular Plant*, 7(1), 45–57. <https://doi.org/10.1093/mp/sst129>
- Liu, Z., Yan, H., Wang, K., Kuang, T., Zhang, J., Gui, L., An, X., & Chang, W. (2004). *Crystal structure of spinach major light- harvesting complex at 2.72 Å resolution*. 287–292.
- Livingston, A. K., Cruz, J. A., Kohzuma, K., Dhingra, A., & Kramer, D. M. (2010). *An Arabidopsis Mutant with High Cyclic Electron Flow around Photosystem I (hcef) Involving the NADPH Dehydrogenase Complex*. 22(January), 221–233. <https://doi.org/10.1105/tpc.109.071084>
- Maeda, S., Yamamoto, H., Kinch, L. N., Garza, C. M., Takahashi, S., Otomo, C., Grishin, N. V., Forli, S., Mizushima, N., & Otomo, T. (2020). Structure, lipid scrambling activity and role in autophagosome formation of ATG9A. *Nature Structural and Molecular Biology*, 27(12), 1194–1201. <https://doi.org/10.1038/s41594-020-00520-2>
- Malone, L. A., Proctor, M. S., Hitchcock, A., Hunter, C. N., & Johnson, M. P. (2021). Cytochrome b6f – Orchestrator of photosynthetic electron transfer. *Biochimica et Biophysica Acta - Bioenergetics*, 1862(5). <https://doi.org/10.1016/j.bbabi.2021.148380>

- Malone, L. A., Qian, P., Mayneord, G. E., Hitchcock, A., Farmer, D. A., Thompson, R. F., Swainsbury, D. J. K., Ranson, N. A., Hunter, C. N., & Johnson, M. P. (2019). Cryo-EM structure of the spinach cytochrome b₆ f complex at 3.6 Å resolution. *Nature*, *575*(7783), 535–539. <https://doi.org/10.1038/s41586-019-1746-6>
- Maxwell, K., & Johnson, G. N. (2000). *Chlorophyll fluorescence — a practical guide*. *51*(345), 659–668.
- Mayneord, G. E., Vasilev, C., Malone, L. A., Swainsbury, D. J. K., Hunter, C. N., & Johnson, M. P. (2019). Single-molecule study of redox control involved in establishing the spinach plastocyanin-cytochrome b₆f electron transfer complex. *Biochimica et Biophysica Acta - Bioenergetics*, *1860*(7), 591–599. <https://doi.org/10.1016/j.bbabi.2019.06.013>
- Mazor, Y., Borovikova, A., Caspy, I., & Nelson, N. (2017). Structure of the plant photosystem i supercomplex at 2.6 Å resolution. *Nature Plants*, *3*(March), 1–9. <https://doi.org/10.1038/nplants.2017.14>
- Mazor, Y., Borovikova, A., & Nelson, N. (2015). The structure of plant photosystem i super-complex at 2.8 Å resolution. *ELife*, *4*(JUNE2015), 1–18. <https://doi.org/10.7554/eLife.07433>
- Michelet, L., Zaffagnini, M., Morisse, S., Sparla, F., Pérez-Pérez, M. E., Francia, F., Danon, A., Marchand, C. H., Fermani, S., Trost, P., & Lemaire, S. D. (2013). Redox regulation of the Calvin-Benson cycle: Something old, something new. *Frontiers in Plant Science*, *4*(NOV), 1–21. <https://doi.org/10.3389/fpls.2013.00470>
- Mills, J., Crowther, D., Slovacek, R., Hind, G., & McCarthy, R. (1979). Electron Transport Pathways in Spinach Chloroplasts. *Biochimica et Biophysica Acta*, *547*, 127–137.
- Mitchell, P. (1975a). Protonmotive redox mechanism of the cytochrome b-c₁ complex in the respiratory chain: Protonmotive ubiquinone cycle. *FEBS Letters*, *56*(1), 1–6. [https://doi.org/10.1016/0014-5793\(75\)80098-6](https://doi.org/10.1016/0014-5793(75)80098-6)
- Mitchell, P. (1975b). *The protonmotive Q cycle: A general formulation*. *59*(2), 137–139.
- Mosebach, L., Heilmann, C., Mutoh, R., Gäbelein, P., Steinbeck, J., Happe, T., Ikegami, T., Hanke, G., Kurisu, G., & Hippler, M. (2017). Association of Ferredoxin:NADP⁺ oxidoreductase with the photosynthetic apparatus modulates electron transfer in *Chlamydomonas reinhardtii*. *Photosynthesis Research*, *134*(3), 291–306. <https://doi.org/10.1007/s11120-017-0408-5>
- Moss, D. A., & Bendall, D. S. (1984). Cyclic electron transport in chloroplasts. The Q-cycle and the site of action of antimycin. *BBA - Bioenergetics*, *767*(3), 389–395. [https://doi.org/10.1016/0005-2728\(84\)90036-7](https://doi.org/10.1016/0005-2728(84)90036-7)
- Munekage, Y., Hashimoto, M., Miyake, C., Tomizawa, K. I., Endo, T., Tasaka, M., & Shikanai, T. (2004). Cyclic electron flow around photosystem I is essential for photosynthesis. *Nature*, *429*(6991), 579–582. <https://doi.org/10.1038/nature02598>
- Munekage, Y., Hojo, M., Meurer, J., Endo, T., Tasaka, M., & Shikanai, T. (2002). PGR5 is involved in cyclic electron flow around photosystem I and is essential for photoprotection in *Arabidopsis*. *Cell*, *110*(3), 361–371. [https://doi.org/10.1016/S0092-8674\(02\)00867-X](https://doi.org/10.1016/S0092-8674(02)00867-X)
- Nakayama, K., Okamoto, F., & Harada, Y. (1956). Antimycin A: isolation from a new *Streptomyces* and activity against rice plant blast fungi. *The Journal of Antibiotics*, *9*(2), 63–66.

- Nalin, C. M., & McCarty, R. E. (1984). Role of a disulfide bond in the gamma subunit in activation of the ATPase of chloroplast coupling factor 1. *Journal of Biological Chemistry*, 259(11), 7275–7280. [https://doi.org/10.1016/s0021-9258\(17\)39868-x](https://doi.org/10.1016/s0021-9258(17)39868-x)
- Nandha, B., Finazzi, G., Joliot, P., Hald, S., & Johnson, G. N. (2007). The role of PGR5 in the redox poising of photosynthetic electron transport. *Biochimica et Biophysica Acta - Bioenergetics*, 1767(10), 1252–1259. <https://doi.org/10.1016/j.bbabi.2007.07.007>
- Nawrocki, W. J., Bailleul, B., Cardol, P., Rappaport, F., Wollman, F., & Joliot, P. (2019). *BBA - Bioenergetics Maximal cyclic electron flow rate is independent of PGRL1 in Chlamydomonas*. 1860(February), 425–432.
- Nawrocki, W. J., Bailleul, B., Picot, D., Cardol, P., Rappaport, F., Wollman, F. A., & Joliot, P. (2019). The mechanism of cyclic electron flow. In *Biochimica et Biophysica Acta - Bioenergetics* (Vol. 1860, Issue 5, pp. 433–438). Elsevier B.V. <https://doi.org/10.1016/j.bbabi.2018.12.005>
- Nelson, N., & Junge, W. (2015). Structure and energy transfer in photosystems of oxygenic photosynthesis. *Annual Review of Biochemistry*, 84, 659–683. <https://doi.org/10.1146/annurev-biochem-092914-041942>
- Nelson, N., & Neumann, J. (1972). Isolation of a cytochrome b 6 -f particle from chloroplasts. *Journal of Biological Chemistry*, 247(6), 1817–1824. [https://doi.org/10.1016/s0021-9258\(19\)45547-6](https://doi.org/10.1016/s0021-9258(19)45547-6)
- Nikkanen, L., Toivola, J. and Rintamäki, E. (2016) 'Crosstalk between chloroplast thioredoxin systems in regulation of photosynthesis', *Plant, Cell & Environment*, 39(8), pp. 1691–1705. doi:10.1111/pce.12718.
- Nikkanen L, Toivola J, Trotta A, Guinea Diaz M, Tikkanen M, Aro E, Rintamäki E (2018) Regulation of cyclic electron flow by chloroplast NADPH-dependent thioredoxin system. *Plant Direct* 2: 1–24
- Nishio, J. N., & Whitmarsh, J. (1993). Dissipation of the proton electrochemical potential in intact chloroplasts: II. The pH gradient monitored by cytochrome f reduction kinetics. *Plant Physiology*, 101(1), 89–96. <https://doi.org/10.1104/pp.101.1.89>
- Nixon, P. J., Michoux, F., Yu, J., Boehm, M., & Komenda, J. (2010). Recent advances in understanding the assembly and repair of photosystem II. *Annals of Botany*, 106(1), 1–16. <https://doi.org/10.1093/aob/mcq059>
- Noctor, G., & Foyer, C. H. (2000). Homeostasis of adenylate status during photosynthesis in a fluctuating environment. *Journal of Experimental Botany*, 51(SPEC. ISS.), 347–356. https://doi.org/10.1093/jexbot/51.suppl_1.347
- Okegawa, Y., Basso, L., Shikanai, T., & Motohashi, K. (2020). Cyclic electron transport around PSI contributes to photosynthetic induction with thioredoxin f. *Plant Physiology*, 184(3), 1291–1302. <https://doi.org/10.1104/pp.20.00741>
- Okegawa, Y., Sakamoto, W., & Motohashi, K. (2022). Functional division of f-type and m-type thioredoxins to regulate the Calvin cycle and cyclic electron transport around photosystem I. *Journal of Plant Research*, 135(4), 543–553. <https://doi.org/10.1007/s10265-022-01388-7>
- Paladini, D. H., Musumeci, M. A., Carrillo, N., & Ceccarelli, E. A. (2009). Induced fit and equilibrium dynamics for high catalytic efficiency in ferredoxin-NADP(H) reductases. *Biochemistry*, 48(24), 5760–5768. <https://doi.org/10.1021/bi9004232>

- Pan, X., Ma, J., Su, X., Cao, P., Chang, W., Liu, Z., Zhang, X., & Li, M. (2018). Structure of the maize photosystem I supercomplex with light-harvesting complexes I and II. *Science*, *360*(6393), 1109–1113. <https://doi.org/10.1126/science.aat1156>
- Pandey, A., Andersen, J. S., & Mann, M. (2000). Use of mass spectrometry to study signaling pathways. *Science's STKE: Signal Transduction Knowledge Environment*, *2000*(37), 1–13. <https://doi.org/10.1126/stke.2000.37.pl1>
- Pearcy RW (1998) Acclimation to sun and shade. In A Raghavendra, ed, *Photosynthesis*. Cambridge University Press, Cambridge, UK
- Peng, L., & Shikanai, T. (2011). Supercomplex formation with photosystem I is required for the stabilization of the chloroplast NADH dehydrogenase-like complex in Arabidopsis. *Plant Physiology*, *155*(4), 1629–1639. <https://doi.org/10.1104/pp.110.171264>
- Popot, J. (2010). *Amphipols, Nanodiscs and Fluorinated Surfactants: Three Nonconventional Approaches to Studying Membrane Proteins in Aqueous Solutions*. <https://doi.org/10.1146/annurev.biochem.052208.114057>
- Proctor, M. S., Malone, L. A., Farmer, D. A., Swainsbury, D. J. K., Hawkings, F. R., Pastorelli, F., Emrich-Mills, T. Z., Siebert, C. A., Hunter, C. N., Johnson, M. P., & Hitchcock, A. (2022). Cryo-EM structures of the Synechocystis sp. PCC 6803 cytochrome b6f complex with and without the regulatory PetP subunit. *Biochemical Journal*, *479*(13), 1487–1503. <https://doi.org/10.1042/BCJ20220124>
- Rodriguez-heredia, M., Saccon, F., Wilson, S., Finazzi, G., Ruban, A. V., & Hanke, G. T. (2022). *Protection of photosystem I during sudden light stress depends on ferredoxin : NADP (H) reductase abundance and interactions*. 1028–1042. <https://doi.org/10.1093/plphys/kiab550>
- Ruban, A. V. (2016). Nonphotochemical chlorophyll fluorescence quenching: Mechanism and effectiveness in protecting plants from photodamage. *Plant Physiology*, *170*(4), 1903–1916. <https://doi.org/10.1104/pp.15.01935>
- Ruban, A. V., Pascal, A. A., Robert, B., & Horton, P. (2002). Activation of Zeaxanthin Is an Obligatory Event in the Regulation of Photosynthetic Light Harvesting *. *Journal of Biological Chemistry*, *277*(10), 7785–7789. <https://doi.org/10.1074/jbc.M110693200>
- Rühle, T., Dann, M., Reiter, B., Schünemann, D., Naranjo, B., Penzler, J. F., Kleine, T., & Leister, D. (2021). PGRL2 triggers degradation of PGR5 in the absence of PGRL1. *Nature Communications*, *12*(1), 1–14. <https://doi.org/10.1038/s41467-021-24107-7>
- Rumberg, B., & Siggel, U. (1969). pH changes in the inner phase of the thylakoids during photosynthesis. *Die Naturwissenschaften*, *56*(3), 130–132. <https://doi.org/10.1007/BF00601025>
- Rumeau, D., & Peltier, G. (2005). *New Subunits NDH-M, -N, and -O, Encoded by Nuclear Genes, Are Essential for Plastid Ndh Complex Functioning in Higher Plants*. *17*(January), 219–232. <https://doi.org/10.1105/tpc.104.028282.1>
- Sarewicz, M., Szwałec, M., Pintscher, S., Indyka, P., Rawski, M., Pietras, R., Mielecki, B., Koziej, Ł., Jaciuk, M., Glatt, S., & Osyczka, A. (2023). High-resolution cryo-EM structures of plant cytochrome b6f at work. *Science Advances*, *9*(2), 1–13. <https://doi.org/10.1126/sciadv.add9688>
- Sato, R., Kawashima, R., Duy, M., Trinh, L., Nakano, M., Nagai, T., & Masuda, S. (2019). Significance of PGR5-dependent cyclic electron flow for optimizing the rate of ATP synthesis and consumption in

- Arabidopsis chloroplasts. *Photosynthesis Research*, 139(1), 359–365. <https://doi.org/10.1007/s11120-018-0533-9>
- Scheibe, R. (2004). Malate valves to balance cellular energy supply. *Physiologia Plantarum*, 120(1), 21–26. <https://doi.org/10.1111/j.0031-9317.2004.0222.x>
- Schreiber, U. (2017). Redox changes of ferredoxin , P700 , and plastocyanin measured simultaneously in intact leaves Chl Chlorophyll a. *Photosynthesis Research*, 134(3), 343–360. <https://doi.org/10.1007/s11120-017-0394-7>
- Schreiber, U., & Klughammer, C. (2016). Analysis of photosystem I donor and acceptor sides with a new type of online-deconvoluting kinetic LED-array spectrophotometer. *Plant and Cell Physiology*, 57(7), 1454–1467. <https://doi.org/10.1093/pcp/pcw044>
- Schuller, J. M., Birrell, J. A., Tanaka, H., Konuma, T., Lubitz, W., Sétif, P., Ikegami, T., & Engel, B. D. (2019). *Structural adaptations of photosynthetic complex I enable ferredoxin-dependent electron transfer*. 260(January), 257–260.
- Schwanhäusser, B., Busse, D., Li, N., Dittmar, G., Schuchhardt, J., Wolf, J., Chen, W., & Selbach, M. (2011). *Global quantification of mammalian gene expression control*. 1–8. <https://doi.org/10.1038/nature10098>
- Shahak, Y., Crowther, D., & Hind, G. (1981). THE INVOLVEMENT OF FERREDOXIN-NADP + REDUCTASE IN CYCLIC ELECTRON TRANSPORT IN CHLOROPLASTS. *Springs*, 636, 234–243.
- Shen, L., Tang, K., Wang, W., Wang, C., Wu, H., Mao, Z., An, S., Chang, S., Kuang, T., Shen, J., Han, G., & Zhang, X. (2022). *Architecture of the chloroplast PSI – NDH supercomplex in Hordeum vulgare*. 601(January). <https://doi.org/10.1038/s41586-021-04277-6>
- Shinozaki, K., Ohme, M., Tanaka, M., Wakasugi, T., Hayashida, N., Matsubayashi, T., Zaita, N., Chunwongse, J., Obokata, J., Yamaguchi-Shinozaki, K., Ohto, C., Torazawa, K., Meng, B. Y., Sugita, M., Deno, H., Kamogashira, T., Yamada, K., Kusuda, J., Takaiwa, F., ... Sugiura, M. (1986). The complete nucleotide sequence of the tobacco chloroplast genome: Its gene organization and expression. *EMBO Journal*, 5(9), 2043–2049. <https://doi.org/10.1002/j.1460-2075.1986.tb04464.x>
- Singh, S. K., & Sigworth, F. J. (2015). Previews Cryo-EM : Spinning the Micelles Away. *Structure/Folding and Design*, 23(9), 1561. <https://doi.org/10.1016/j.str.2015.08.001>
- Sonoike, K. (2011). Photoinhibition of photosystem I. *Physiologia Plantarum*, 142(1), 56–64. <https://doi.org/10.1111/j.1399-3054.2010.01437.x>
- Steinbeck, J., Ross, I. L., Rothnagel, R., Gäbelein, P., Schulze, S., Giles, N., Ali, R., Drysdale, R., Sierecki, E., Gambin, Y., Stahlberg, H., Takahashi, Y., Hippler, M., & Hankamer, B. (2018). Structure of a PSI-LHCI-cyt b6f supercomplex in Chlamydomonas reinhardtii promoting cyclic electron flow under anaerobic conditions. *Proceedings of the National Academy of Sciences of the United States of America*, 115(41), 10517–10522. <https://doi.org/10.1073/pnas.1809973115>
- Stock, D., Leslie, A. G. W., & Walker, J. E. (1999). Molecular architecture of the rotary motor in ATP synthase. *Science*, 286(5445), 1700–1705. <https://doi.org/10.1126/science.286.5445.1700>
- Strand, D. D., Fisher, N., Davis, G. A., & Kramer, D. M. (2016). Redox regulation of the antimycin A sensitive pathway of cyclic electron flow around photosystem i in higher plant thylakoids. *Biochimica et Biophysica Acta - Bioenergetics*, 1857(1), 1–6. <https://doi.org/10.1016/j.bbabi.2015.07.012>

- Stroebel, D., Choquet, Y., Popot, J. L., & Picot, D. (2003). An atypical haem in the cytochrome b6f complex. *Nature*, *426*(6965), 413–418. <https://doi.org/10.1038/nature02155>
- Su, X., Cao, D., Pan, X., Shi, L., Liu, Z., Osto, L. D., Bassi, R., Zhang, X., & Li, M. (2022). Supramolecular assembly of chloroplast NADH dehydrogenase-like complex with photosystem I from *Arabidopsis thaliana*. *Molecular Plant*, *15*(3), 454–467. <https://doi.org/10.1016/j.molp.2022.01.020>
- Su, X., Wei, X., Zhu, D., Chang, W., Liu, Z., Zhang, X., & Li, M. (2017). Structure and assembly mechanism of plant C2S2M2-type PSII-LHCII supercomplex. *Science*, *355*(August), 815–820. <http://link.springer.com/10.1007/s12551-017-0357-4>
- Sugimoto, K., Okegawa, Y., Tohri, A., Long, T. A., Covert, S. F., Hisabori, T., & Shikanai, T. (2013). A single amino acid alteration in PGR5 confers resistance to antimycin a in cyclic electron transport around PSI. *Plant and Cell Physiology*, *54*(9), 1525–1534. <https://doi.org/10.1093/pcp/pct098>
- Suorsa, M., Järvi, S., Grieco, M., Nurmi, M., Pietrzykowska, M., Rantala, M., Kangasjärvi, S., Paakkarinen, V., Tikkanen, M., Jansson, S., & Aro, E. M. (2012). PROTON GRADIENT REGULATION5 is essential for proper acclimation of *Arabidopsis* photosystem I to naturally and artificially fluctuating light conditions. *Plant Cell*, *24*(7), 2934–2948. <https://doi.org/10.1105/tpc.112.097162>
- Szwalec, M., Bujnowicz, Ł., Sarewicz, M., & Osyczka, A. (2022). Unexpected Heme Redox Potential Values Implicate an Uphill Step in Cytochrome b6f. *Journal of Physical Chemistry B*, *126*(47), 9771–9780. <https://doi.org/10.1021/acs.jpcc.2c05729>
- Szymańska, R., & Kruk, J. (2010). Plastoquinol is the main prenyllipid synthesized during acclimation to high light conditions in *Arabidopsis* and is converted to plastochromanol by tocopherol cyclase. *Plant and Cell Physiology*, *51*(4), 537–545. <https://doi.org/10.1093/pcp/pcq017>
- Tagawa, K., Tsujimoto, Y., & Arnon, D. I. (1963). *ROLE OF CHLOROPLAST FERREDOXIN IN THE ENERGY CONVERSION PROCESS OF PHOTOSYNTHESIS*. 567–572.
- Takabayashi, A., Ishikawa, N., Obayashi, T., Ishida, S., Obokata, J., & Endo, T. (2009). *Three novel subunits of Arabidopsis chloroplastic NAD (P) H dehydrogenase identified by bioinformatic and reverse genetic approaches*. 207–219. <https://doi.org/10.1111/j.1365-313X.2008.03680.x>
- Takagi, D., Amako, K., Hashiguchi, M., Fukaki, H., Ishizaki, K., Goh, T., Fukao, Y., Sano, R., Kurata, T., Demura, T., Sawa, S., & Miyake, C. (2017). Chloroplastic ATP synthase builds up a proton motive force preventing production of reactive oxygen species in photosystem I. *Plant Journal*, *91*(2), 306–324. <https://doi.org/10.1111/tpj.13566>
- Takahashi, H., Clowez, S., Wollman, F. A., Vallon, O., & Rappaport, F. (2013). Cyclic electron flow is redox-controlled but independent of state transition. *Nature Communications*, *4*. <https://doi.org/10.1038/ncomms2954>
- Trissl, H. W., & Wilhelm, C. (1993). Why do thylakoid membranes from higher plants form grana stacks? *Trends in Biochemical Sciences*, *18*(11), 415–419. [https://doi.org/10.1016/0968-0004\(93\)90136-B](https://doi.org/10.1016/0968-0004(93)90136-B)
- Van Bezouwen, L. S., Caffarri, S., Kale, R., Kouřil, R., Thunnissen, A. M. W. H., Oostergetel, G. T., & Boekema, E. J. (2017). Subunit and chlorophyll organization of the plant photosystem II supercomplex. *Nature Plants*, *3*(June), 1–11. <https://doi.org/10.1038/nplants.2017.80>
- Vojta, L. (2019). *Topology of TROL protein in thylakoid membranes of Arabidopsis thaliana*. 300–308. <https://doi.org/10.1111/ppl.12927>

- Voss, I., Sunil, B., Scheibe, R., & Raghavendra, A. S. (2013). *Emerging concept for the role of photorespiration as an important part of abiotic stress response*. *15*, 713–722. <https://doi.org/10.1111/j.1438-8677.2012.00710.x>
- Wang, C., Takahashi, H., & Shikanai, T. (2018). BBA - Bioenergetics PROTON GRADIENT REGULATION 5 contributes to ferredoxin-dependent cyclic phosphorylation in ruptured chloroplasts. *BBA - Bioenergetics*, *1859*(10), 1173–1179. <https://doi.org/10.1016/j.bbabi.2018.07.011>
- Wang, C., Yamamoto, H., & Shikanai, T. (2015). Role of cyclic electron transport around photosystem I in regulating proton motive force. *Biochimica et Biophysica Acta - Bioenergetics*, *1847*(9), 931–938. <https://doi.org/10.1016/j.bbabi.2014.11.013>
- Watanabe, A., Kim, E., Burton-Smith, R. N., Tokutsu, R., & Minagawa, J. (2019). Amphipol-assisted purification method for the highly active and stable photosystem II supercomplex of *Chlamydomonas reinhardtii*. *FEBS Letters*, *593*, 1072–1079. <https://doi.org/10.1002/1873-3468.13394>
- Wei, X., Su, X., Cao, P., Liu, X., Chang, W., Li, M., Zhang, X., & Liu, Z. (2016). Structure of spinach photosystem II-LHCII supercomplex at 3.2 Å resolution. *Nature*, *534*(7605), 69–74. <https://doi.org/10.1038/nature18020>
- Whatley, F. R., Allen, M. B., & Arnon, D. I. (1955). Photosynthetic phosphorylation as an anaerobic process. *BBA - Biochimica et Biophysica Acta*, *16*(C), 605–606. [https://doi.org/10.1016/0006-3002\(55\)90294-8](https://doi.org/10.1016/0006-3002(55)90294-8)
- Witt, H. T. (1979). *ENERGY CONVERSION IN THE FUNCTIONAL MEMBRANE OF PHOTOSYNTHESIS. A ANALYSIS BY LIGHT PULSE AND ELECTRIC PULSE METHODS THE CENTRAL ROLE OF THE ELECTRIC FIELD*. *505*, 355–427.
- Wood, W. H. J., MacGregor-Chatwin, C., Barnett, S. F. H., Mayneord, G. E., Huang, X., Hobbs, J. K., Hunter, C. N., & Johnson, M. P. (2018). Dynamic thylakoid stacking regulates the balance between linear and cyclic photosynthetic electron transfer. *Nature Plants*, *4*(2), 116–127. <https://doi.org/10.1038/s41477-017-0092-7>
- Wu, X., Wu, J., Wang, Y., He, M., He, M., Liu, W., Shu, S., Sun, J., & Guo, S. (2021). The key cyclic electron flow protein PGR5 associates with cytochrome b6f, and its function is partially influenced by the LHCII state transition. *Horticulture Research*, *8*(1). <https://doi.org/10.1038/s41438-021-00460-y>
- Yamamoto, H., Peng, L., Fukao, Y., & Shikanai, T. (2011). An Src homology 3 domain-like fold protein forms a ferredoxin binding site for the chloroplast NADH dehydrogenase-like complex in *Arabidopsis*. *Plant Cell*, *23*(4), 1480–1493. <https://doi.org/10.1105/tpc.110.080291>
- Yamamoto, H., & Shikanai, T. (2019). *PGR5-Dependent Cyclic Electron Flow Protects Photosystem I under Fluctuating Light at Donor and*. *179*(February), 588–600. <https://doi.org/10.1104/pp.18.01343>
- Yamori, W., & Shikanai, T. (2016). Physiological Functions of Cyclic Electron Transport Around Photosystem i in Sustaining Photosynthesis and Plant Growth. *Annual Review of Plant Biology*, *67*, 81–106. <https://doi.org/10.1146/annurev-arplant-043015-112002>
- Yamori, W., Shikanai, T., & Makino, A. (2015a). Corrigendum : Photosystem I cyclic electron flow via chloroplast NADH dehydrogenase-like complex performs a physiological role for photosynthesis at low light. *Nature Publishing Group*, 15593. <https://doi.org/10.1038/srep15593>

Yamori, W., Shikanai, T., & Makino, A. (2015b). Photosystem I cyclic electron flow via chloroplast NADH dehydrogenase-like complex performs a physiological role for photosynthesis at low light. *Nature Publishing Group, August*, 1–10. <https://doi.org/10.1038/srep13908>

Yan, J., & Cramer, W. A. (2003). Functional insensitivity of the cytochrome b6f complex to structure changes in the hinge region of the Rieske iron-sulfur protein. *Journal of Biological Chemistry*, 278(23), 20925–20933. <https://doi.org/10.1074/jbc.M212616200>

Zakharov, S., Misumi, Y., Kurisu, G., & Cramer, W. A. (2020). Interaction of FNR with the Cytochrome b6f Complex: Thermodynamic Parameters. *Biophysical Journal*, 118(3), 132a. <https://doi.org/10.1016/j.bpj.2019.11.852>

Zbierzak, A. M., Kanwischer, M., Wille, C., Vidi, P. A., Giavalisco, P., Lohmann, A., Briesen, I., Porfirova, S., Bréhélin, C., Kessler, F., & Dörmann, P. (2010). Intersection of the tocopherol and plastoquinol metabolic pathways at the plastoglobule. *Biochemical Journal*, 425(2), 389–399. <https://doi.org/10.1042/BJ20090704>

Zhang, C., Shuai, J., & Ran, Z. (2020). Structural insights into NDH-1 mediated cyclic electron transfer. *Nature Communications*, 1–13. <https://doi.org/10.1038/s41467-020-14732-z>

Zhang, H., Whitelegge, J. P., & Cramer, W. A. (2001). Ferredoxin:NADP+ Oxidoreductase Is a Subunit of the Chloroplast Cytochrome b6f Complex. *Journal of Biological Chemistry*, 276(41), 38159–38165. <https://doi.org/10.1074/jbc.m105454200>

Appendix

Supplementary Figure 1 | Total proteins analysis of the sample purified in LMNG by MS.

Proteins identified in the sample purified in LMNG are here displayed based on their relative abundance in the sample. The order of the proteins in the table was based on the median of the iBAQ values from triplicate analyses. Proteins that are part of the FNR-cyt_{b6f} supercomplex are highlighted in yellow.